Development of simple, ultrasensitive electrochemical biosensors for the detection of miRNAs associated with neurological diseases

Amanda Carrico M. Sc.

Thesis submitted for the award of PhD

Supervisor

Prof. Robert J. Forster

Dublin City University

School of Chemical Science

March 2024

Ollscoil Chathair Bhaile Átha Cliath
Dublin City University

DCU

DECLARATION

I hereby certify that this material, which I now submit for assessment on the programme of study leading to the award of Doctor of Philosophy is entirely my own work, and that I have exercised reasonable care to ensure that the work is original, and does not to the best of my knowledge breach any law of copyright, and has not been taken from the work of others save and to the extent that such work has been cited and acknowledged within the text of my work.

Signed:  Student ID No.:19212740 Date:09/08/23

ACKNOWLEDGMENTS

I would like to express my heartfelt gratitude to my supervisor, Prof. Robert Forster, for his unwavering guidance, invaluable feedback, and countless insightful meetings throughout the development of my project. His patience and mentorship over the course of these four years have been instrumental in shaping the trajectory of my research.

I would like to offer my sincere appreciation to FutureNeuro and Science Foundation Ireland for their funding and steadfast belief in my potential as a researcher, enabling the realization of this intricate and impactful project. Their support has played an indispensable role in realizing the fruition of my research efforts.

I am thankful to Professor Loanda Cumba and my fellow colleagues at the lab, namely Miren, Fionn, and Angelo, for their camaraderie, encouragement, and support along this journey. Your collective efforts have truly made this endeavour a collaborative and enriching experience.

I humbly acknowledge the support of God, my parents, and my cherished husband. To my parents, your constant encouragement and belief in my abilities have been a driving force. To my husband, you have been more than a partner – you have been my rock. Your patient ear for my research reflections, your role as a sounding board for doubts and ideas, and your steadfast presence in navigating challenges have been indispensable .Your support helped me persevere through the ups and downs of pursuing a PhD, and your nourishing meals during intense writing spells provided sustenance for both body and mind. From the depths of my heart, I hold you in profound gratitude and love.

This achievement would not have been possible without the collective support and inspiration of all those mentioned and many others who contributed to my journey in ways both seen and unseen. Thank you.

TABLE OF CONTENTS

Declaration ii
Acknowledgments iii
List of Abbreviations viii
List of Tables xii
List of Figures xv
Abstract xxiii
Publications and presentations xxiv
Chapter 1. Introduction and Literature Review 1
1 Literature Review 2
1.1 miRNA and Cognitive diseases: Alzheimer and Epilepsy 2
1.1.1 miRNA: An Overview 2
1.1.2 Biogenesis of the miRNA 2
1.1.3 miRNA in epilepsy 4
1.1.3.1 Epilepsy: triggers, definitions, symptoms 4
1.1.3.2 Epilepsy in numbers 6
1.1.3.3 miRNAs as biomarkers of epilepsy 6
1.1.3.4 Circulating microRNAs 10
1.1.3.5 Challenges among the use of miRNA as a theranostic molecule 14
1.1.3.5.1 Use of antagomirs or mimics to treat epilepsy 14
1.1.3.5.2 Differences in microRNA expression levels 14
1.1.3.6 Limitations in the currently detection system 14
1.1.3.6.1 The use of EEG 14
1.1.3.6.2 qRT-PCR 15
1.1.4 miRNA in Alzheimer's Disease 17
1.1.4.1 Definitions and Symptoms 17
1.1.4.2 Detection of Alzheimer's disease: Currently methodologies and biomarkers of disease 18
1.1.4.3 miRNAs as biomarkers of Alzheimer Disease 19
1.1.5 Limitations and challenges among the use of miRNAs as a neurodegenerative biomarker 21
1.2 Electrochemical Biosensors for miRNA Detection: Revealing Their Competitive Edge 23
1.2.1 Electrochemical Techniques vs. Traditional Analysis 23
1.2.2 Using Electrochemical Biosensors as an Alternative to Optical-Based Methods 24
1.2.3 Electrochemical biosensors: Main formats 24
1.2.4 Bioreceptors 25
1.2.5 Electrode Substrates 25
1.2.5.1 Gold Electrodes 26
1.2.5.2 Carbon-Based Electrodes 27
1.2.6 Electrochemical Techniques 27
1.2.6.1 Electrochemical Impedance Spectroscopy (EIS) 27
1.2.6.2 Amperometry 28
1.2.7 Use of the nanomaterials in biosensing: Overview 28
1.2.8 Nanoparticles for catalytic signal amplification 29
1.3 Multianalyte detection 38
1.3.1 Classification of Electrochemical Biosensors for Multi-analyte Detection 39
1.3.1.1 Multi-label Platform 39

1.3.1.2 Multi-electrode Platform 40
1.3.2 Examples of electrochemical platforms for multi-analyte detection (multi-miRNA detection) 41
1.3.2.1 Sequential detection of multi microRNAs using the same biosensor 43
1.3.3 Future prospects on the multi-analytes field 46
1.4 Conclusion and Thesis Outline 48
1.5 References 51
Chapter 2. Development of a label-free electrochemical biosensor for the detection of miRNA-206 in plasma of Alzheimer disease patients. 58
2 Introduction 59
2.1 Experimental Procedures 61
2.1.1 Materials: Chemicals and Solutions 61
2.1.2 Instrumentation 62
2.1.3 Procedures 62
2.1.3.1 Electrode Cleaning and surface preparation 62
2.1.3.2 Construction of the label-free sensor 63
2.1.3.3 Electrochemical follow up of the modification steps 64
2.1.3.4 Calculation of capacitance from CV 64
2.1.3.5 Estimation of the heterogeneous electron transfer (k_0) and the diffusion coefficient (D) from CV 64
2.1.3.6 Impedance analysis 65
2.1.3.7 Calculation of capacitance 66
2.1.3.8 Calculation of the monolayer thickness 68
2.1.3.9 Calculation of miRNA surface density 69
2.2 Results and Discussion 71
2.2.1 Electrochemical follow-up of the gold surface modifications 71
2.2.2 Insights on the integrity of the monolayer and validation of the proposed adsorption model 80
2.2.3 Optimization of the hybridization time between miRNA capture-probe and miRNA target 82
2.2.4. Co-immobilization of miRNA capture-probe and MCH 85
2.2.3.1 Determination of the surface coverage using Chronocoulometry 86
2.2.3.1.1 Calculation of surface coverage: general considerations 86
2.2.3.2 The effect of a low ion- pairing electrolyte on chronocoulometric curves 87
2.2.3.2.1 miRNA surface Coverage 89
2.2.3.3 Analysis of the binding properties of target in different molar fractions of miRNA: total thiol 92
2.2.3.4 Correlation of charge transfer resistance with hybridization efficiency at different surface densities 96
2.2.4 Validation of the developed biosensor 99
2.2.5 Analytical performance of the impedimetric biosensor 99
2.2.5.1 Specificity of the miRNA detection 104
2.2.5.2 Stability and reproducibility of the fabricated biosensor 107
2.2.5.3 Quantitative detection of miRNA-206 in plasma samples 109
2.3 Conclusion 112
2.4 References 114
Chapter 3. Development of an electrochemical biosensor using amperometry and gold nanorod labels. 121
3 Introduction 121
3.1 Experimental Procedures 123

3.1.1 Materials and Chemicals 123
3.1.2 Instrumentation 124
3.1.2.1 Electrochemical instrumentation 124
3.1.2.2 Spectroscopic Instrumentation: UV-vis 124
3.1.3 Experimental Procedures 124
3.1.3.1 Labelling of miRNA reporter-probe with AuNRDs 124
3.1.3.2 Development of miRNA assay at conventional gold electrodes 125
3.1.3.3 Limit of Blank and Limit of detection 126
3.1.4 Electrochemical Analysis 127
3.1.4.1 Amperometric detection of miRNA-206 127
3.2 Results and Discussion 127
3.2.1 Optimal mole ratio of oligo molecules to gold nanorods 127
3.2.2 Optimum hybridisation time between miRNA reporter-probe and target 134
3.2.3 Influence of the hydrogen peroxide concentration on the electrocatalysis of miRNA assay 137
3.2.4 Amperometric response of the biosensor 141
3.2.5 Comparison between label-free and labelled amperometric biosensor 146
3.2.6 Control Studies 148
3.2.7 Selectivity studies 150
3.3 Conclusion 156
3.4 References 157
Chapter 4. Development of labelled amperometric biosensors based on screen-printed carbon electrodes (SPCE) that contain different gold microstructures within the carbon ink. 159
4 Introduction 161
4.1 Experimental Procedures 162
4.1.1 Materials and Chemicals 162
4.1.2 Synthesis of PdNCBs (50 nm in size) 163
4.1.3 Labelling of miRNA reporter-probes with PdNCBs and PtNPs 164
4.1.4 Labelling of miRNA reporter-probe with AuNRDs 165
4.1.5 Development of miRNA assay at screen printed electrodes 165
4.1.6 Drop-casting of metal nanoparticles 167
4.1.7 Electrochemical Analysis 167
4.1.7.1 Voltametric Analysis 167
4.1.7.2 Amperometric detection of miRNA-206 167
4.1.8 Instrumentation 168
4.1.9 Microscopic measurements 169
4.1.9.1 TEM and SEM 169
4.1.10 Spectroscopic measurements 169
4.1.10.1 DLS and Zeta potential 169
4.1.11 Estimation of the heterogeneous electron transfer (k_0) and the diffusion coefficient (D) from CV: 169
4.2 Results and Discussion 170
4.2.1 Evaluation of the Electrochemical Behaviour of SPCE with different gold structures mixed to the carbon ink 170
4.2.2 Analytical Performance of the 10% AuS SPCE and 10% AuF SPCE 178
4.2.3 Enhancement of the analytical performance of AuS SPCEs 182
4.2.4 Optimisation of the studied conditions 185
4.2.4.1 Studies of the optimal potential for hydrogen peroxide reduction 185
4.2.5 Characterization of Metal nanomaterials 192

4.2.5.1 Morphology of AuNRDs: Correlation between TEM, DLS and zeta potential 192
4.2.6 Fabrication and Characterization of Pd Nanocubes labels 193
4.2.6.1 SEM of PdNCBs 194
4.2.6.2 XRD of Palladium nanocubes 195
4.2.7 Characterisation of PdNCBs— reporter probe conjugates on 20% AuS SPCE 196
4.2.8 Characterisation of 20% AuS SPCE 198
4.2.8.1 Thickness of the electrode surface 198
4.3 Conclusion 199
4.4 References 201
Chapter 5. A sandwich electrochemical biosensor for miRNA-206, miRNA-135a and let-7b detection based on metal nanoparticles labelled SPEs 203
5 Introduction 205
5.1 Experimental Procedures 207
5.1.1 Materials and Chemicals 207
5.1.2 Development of functionalized miRNA assay at 20% (w/w) AuS SPCE 208
5.1.3 Electrochemical Analysis 211
5.1.3.1 Amperometric detection of miRNAs target 211
5.1.4 Instrumentation 211
5.2 Results and Discussion 212
5.2.1 Principle of the proposed electrochemical biosensor 212
5.2.2 Analytical performance of the biosensor 213
5.2.3 Selectivity of the biosensor 224
5.2.4 Non-specific binding of BSA 234
5.2.5 Stability of the biosensor 239
5.3 Conclusion 242
5.4 References 244
Chapter 6. Conclusions and Future Direction 247
6 summary 249
Appendix A 257
Appendix B 258

LIST OF ABBREVIATIONS

A	Adenine
AA	Ascorbic acid
AD	Alzheimer Disease
Ag-NCs	Silver nanoclusters
APP	Amyloid precursor proteins
AFM	Atomic force microscopy
Au	Gold
AuF	Gold microflakes
AuNPs	Gold nanoparticles
AuNRDs	Gold nanorods
AuS	Gold microspheres
BBB	Blood brain barrier
BDNF	Brain-derived neurotrophic factor
BSA	Bovine serum albumin
C	Cytosine
CSF	Cerebrospinal fluid protein assays
CTAB	Cetyltrimethylammonium bromide
CPE	Constant phase elements
CV	Cyclic voltammetry
ds	Double stranded
di.	Monolayer thickness
DNA	Deoxyribonucleic acid
DPBS	Dulbecco's phosphate buffer saline
DPV	Differential pulse voltammetry
EA	Electrochemical area
ELS	Early life stress
EDX	Energy dispersive X-ray spectroscopy
EDTA	Ethylenediaminetetraacetic acid
EIS	Electrochemical impedance spectroscopy
ELISA	Enzyme-linked immunosorbent assay
EtOH	Ethanol
ε_i	Dielectric constant of the layer
$[Fe(CN)_6]^{3-/4-}$	Ferri/ferro cyanide
FcMeOH	Ferrocenemethanol
FCD	Focal cortical dysplasia

G	Guanine
GC	Glassy carbon
GCE	Glassy carbon electrode
GE	Gold electrode
GSPE	Gold screen-printed electrode
HQ	Hydroquinone
HRP	Strep-Horseradish peroxidase polymer
LOD	Limit of detection
MBs	Magnetics beads
MCH	6-Mercapto-1-hexanol
MCI	Mild cognitive impairment
miRNA	Micro ribonucleic acid
MoS_2	Molybdenum Disulfide
mTLE	Mesial temporal lobe epilepsy
NA	Nucleic acid
NP	Nanoparticle
OMCNTs	oxidized multi-walled carbon nanotube
PBS	Phosphate buffer saline
PdNCBs	Palladium nanocubes
PET	Positron emission tomography
PEG	Polyethylene glycol
PtNPs	Platinum nanoparticles
P2ABA	Poly(2-amino-benzylamine)
RCA	Rolling circle amplification
rGO	reduced graphene oxide
RNAt	RNA total
RF	Roughness factor
RNA	Ribonucleic acid
RT-PCR	Reverse-transcriptase polymerase chain reaction
ss	Single stranded

SAM	Self-assembled monolayer
Scr	Scrambled sequence
SEM	Scanning electron microscopy
SPCE	Screen printed carbon electrode
SWV	Square wave voltammetry
T	Thymine
TCEP	Tris[2-carboxyethyl]phosphine
TE buffer	10mM Tris and 1 mM EDTA
Thi	Thionine
TEM	Transmission electron microscopy
TSNP	Triangular silver nanoplates
Tris-HCl	Tris-hydrochloric acid
U	Uracil
WHO	World Health Organization
χ^2	Chi-square
Zf	Faradaic impedance
Zw	Warburg impedance

Symbols

A	Area of the working electrode (cm^2)
AG	Geometrical area of the electrode (cm^2)
AM	Microscopic Area (cm^2)
Ap	Area under the peak (cm^2)
α	Transfer coefficient
aM	attomoles per litre
C	Capacitance (F)
Cdl	Double layer capacitance (F)
cm	Centimetre
D	Diffusion coefficient ($cm^2\ s^{-1}$)
e^-	Electron
E	Electrochemical potential (V)
E_0	Standard electrochemical potential (V)
F	Faraday constant (V)
fM	femtomoles per litre

ΔG	Gibbs free energy (eV)
Hz	frequency, Hertz
i	current (Amps)
ipc	catodic peak current (Amps)
ipa	anodic peak current (Amps)
kg	kilograms
k_0	heterogeneous electron transfer rate constant ($cm^2\ s^{-1}$)
L	Litre
M	moles per litre
mA	milliamps
mL	millilitres
mM	millimoles per litre
mV	millivolts
µA	microamps
µL	microlitre
µM	micromoles per liter
nM	nanomoles per litre
n	number of electrons
pM	picomoles per litre
Qdl	Charge of the double layer (C)
Γ	Surface coverage (molecules cm^{-2})
R	Universal gas constant ($J\ K^{-1}\ mol^{-1}$)
Rct	Charge transfer resistance
Ω	Resistance (Ohms)
Φ	Phase shift
s	Second
t	Time
T	Temperature
V	Volts
v	Scan rate ($V\ s^{-1}$)
ω	Radial frequency

LIST OF TABLES

Table 1.1. Clinical studies on blood miRNA biomarkers of epilepsy. Adapted from ref. [15] Avansini, S. H., de Sousa Lima, B. P., Secolin, R., Santos, M. L., Coan, A. C., Vieira, A. S., Torres, F. R., Carvalho, B. S., Alvim, M. K., Morita, M. E., Yasuda, C. L., Pimentel-Silva, L. R., Dogini, D. B., Rogerio, F., Cendes, F., & Lopes-Cendes, I. (2017). MicroRNA hsa-miR-134 is a circulating biomarker for mesial temporal lobe epilepsy. *PloS one*, *12*(4), e0173060.. 13
Table 1.2. Determination of miRNA-155 added in human blood serum (n=3) with the proposed miRNA biosensor. Reproduced from ref. [65] Wu, X., Chai, Y., Yuan, R., Su, H., & Han, J. (2013). A novel label-free electrochemical microRNA biosensor using Pd nanoparticles as enhancer and linker. *The Analyst*, *138*(4), 1060–1066. 38
Table 2.1. From the voltammogram in Figure 2.4 it is possible to extract the potentials of the anodic and cathodic peak. Also, the difference between them, ΔE, for each time of the immobilization. The average values and standard deviations are based on n=3. 73
Table 2.2. Variations on the double-layer capacitance (C_{dl}) , heterogeneous charge transfer (k_0) and diffusion coefficients (D) values of a gold electrode immobilized with 10 μM of miRNA capture-probe at different times. The average values and standard deviation are calculated based on n=3. 75
Table 2.3. Summary of the impedance parameters obtained by fitting (with Randles circuit) the experimental results of a gold electrode immobilized with 10 μM of miRNA capture-probe at different times. Each value was reported with its standard deviation obtained from equivalent circuit modelling. 77
Table 2.4. Summary of the microscopic area and roughness factor calculated from the integration of the reduction current of the chemisorbed oxygen during the electrode cleaning process. The standard deviations represent the spread of the results performed in triplicate. 87
.**Table 2.5.** Rct values before and after hybridization according to the molar fraction of [miRNA]: [total thiol] in the immobilization solution. The average values and standard deviation represent are calculated based on n=3.....94
Table 2.6. Variation of the target hybridization density and miRNA capture-probe surface density in accordance to the molar fraction of [miRNA]: [total thiol] in the immobilization solution. The standard deviation represent the spread of the results performed in triplicate. 97
Table 2.7. Comparison of the developed biosensor with different label-free electrochemical biosensors reporter in the literature for the detection of miRNAs. The current sensitive electrochemical biosensors selected here, performed the measurements under the same redox probe used at this work. 103
Table 2.8. Comparison between the resistance to the charge transfer of a fully complementary nucleic acid strand in and without an environment of BSA. 104
Table 2.9. Comparison between the resistance to the charge transfer of a fully complementary nucleic acid strand and a 4-base mismatch. The average values and standard deviation are calculated based on n=3. 107
Table 2.10. Detection of miRNA-206 in healthy (control) and disease plasma (AD positive) samples (n = 3) by the developed biosensor. 111
Table 3.1. Overview of the initial miRNA reporter-probe concentration used for quantitative adsorption onto AuNRDS based on its loading capacity. The effects of the different [$miRNA_{reporter\text{-}probe}$] $_I$ / [AuNRDs] ratios in the amperometric signal response are also displayed at this table. 131
Table 3.2. Variation in current signal (Δi) in a functionalized fully complementary sandwich assay as a over hybridisation time, considering three independent electrodes. The concentration

of miRNA targets studied was nM and pM. Average values and standard deviation were calculated based on triplicate measurements (n=3). 136
Table 3.3. Change in the current before and after the addition of different concentrations of hydrogen peroxide in a non-functionalized miRNA sandwich assay. The average values and standard deviation are calculated based on n=3..... 139
Table 3.4. Summary of average current response of the system in accordance with different concentrations of hydrogen peroxide. The variation in current is given by Δi assay (variation in current of functionalized assay)- Δi background (variation in current of blank, non-functionalized assay)..... 141
Table 3.5. Average variation of the current response before and after the injection of hydrogen peroxide (Δi) on a functionalized fully complementary miRNA assay..... 144
Table 3.6. Comparison of the current response before and after the injection of hydrogen peroxide (Δi) on a functionalized fully complementary assay and a label-free functionalized sandwich assay. Average values and standard deviations were calculated from triplicate measurements (n=3)..... 147
Table 3.7. Change in the current before and after the injection of hydrogen peroxide for varying stages of the hybridisation process. Average values and standard deviations were calculated from triplicate measurements (n=3)..... 149
Table 3.8. Comparison of the current response before and after the injection of hydrogen peroxide (Δi) on a functionalized fully complementary nucleic acid strand (miRNA-206) to functionalized, non-complementary sandwich assay (1-base mismatch). Average values and standard deviations were calculated based on n=3. 152
Table 3.9. Comparison of the current response before and after the addition of hydrogen peroxide (Δi) on a functionalized fully complementary nucleic acid strand (miRNA-206) to functionalized, non-complementary sandwich assay (4 base mismatch, miRNA-1). Average values and standard deviations were calculated from triplicate measurements (n=3)..... 155
Table 4.1. Average of the peak-to-peak potentials obtained from scan rate studies of conventional gold electrode, 10% AuF SPCE and 10% AuS SPCE in FcMeOH and 0.01 M PBS. 173
Table 4.2. Average heterogeneous electrons transfer rate (k_0) for conventional gold electrode, 10% AuS SPCE and 10% AuF SPCE. Average values and standard deviations were calculated from triplicate measurements (n=3)..... 174
Table 4.3. Changes in the current before and after the injection of 400 μM hydrogen peroxide in **10% AuS SPCE** and **10% AuF SPCE** functionalised with a full sandwich assay and **PdNCBs**. Average values and standard deviations were calculated from triplicate measurements (n=3)..... 181
Table 4.4. Changes in the current before and after the injection of 400 μM hydrogen peroxide in **10% AuS SPCE** and **10% AuF SPCE** functionalised with a full sandwich assay and **AuNRDs.** Average values and standard deviations were calculated from triplicate measurements (n=3)..... 181
Table 4.5. Changes in the current before and after the injection of hydrogen peroxide of **10% AuS SPCE** and **20% AuS SPCE** with full sandwich assay functionalised with **PdNCBs**. Average values and standard deviations were calculated from triplicate measurements. 184
Table 4.6. Changes in the current before and after the injection of hydrogen peroxide of **10% AuS SPCE** and **20% AuS SPCE** with full sandwich assay functionalised with **AuNRDs**. Average values and standard deviations were calculated from triplicate measurements. 184
Table 4.7. Summary of the changes in the current before and after the injection of hydrogen peroxide in a blank 20% AuS SPCE and in 20% AuS SPCE functionalised with a full sandwich assay and PdNCBs; AuNRDs or PtNPs at different applied potentials. Average and standard deviations were calculated from triplicate measurements. 191

Table 5.1. Performances of the proposed electrochemical biosensor for miRNA detection compared with those of previous studies. 222
Table 5.2. Average variation of the current response before and after the injection of H2O2 (Δi) on functionalized fully complementary miRNA assays. These data were obtained from the calibration curves depicted in Figure 5.2 A-C. Average values and standard deviations were calculated based in the measurements performed in triplicate. 223
Table 5.3. Comparison between the current of a fully complementary nucleic acid strand and 1-base mismatch. Average values and standard deviations were calculated by measurements performed in triplicate.....226
Table 5.4. Comparison between the currents observed for a fully complementary nucleic acid strand and 4-bases mismatches. Average values and standard deviations were calculated by measurements performed in triplicate (n=3). 227
Table 5.5. Comparison between the current of a fully complementary let-7b assay and 1-base and 2 base mismatches. Average values and standard deviations were calculated by measurements performed in triplicate. 230
Table 5.6. Comparison between the current of a fully complementary nucleic acid strand and 1-base mismatch. Average values and standard deviations were calculated by measurements performed in triplicate.....233
Table 5.7. Comparison between the current of a functionalized fully complementary miRNA-206 assay with and without an environment of BSA. Average values and standard deviations were calculated by measurements performed in triplicate. 237
Table 5.8. Comparison between the current of a functionalized fully complementary miRNA-135a assay with and without an environment of BSA. Average values and standard deviations were calculated by measurements performed in triplicate. 237
Table 5.9. Comparison between the current of a functionalized fully complementary let-7b assay with and without an environment of BSA. Average values and standard deviations were calculated by measurements performed in triplicate. 238
Table 6.1. Variation of the double layer capacitance (Cdl) and dielectric constants (εi) at different surface moieties of [miRNA]: [total thiol]. 258
Table 6.2. Variation of the doble layer capacitance (Cdl), dielectric (εi) and association constant through the hybridisation of 1[miRNA]:4[total thiol] to a range of miRNA-206 target (from aM to μM). Cdl values was obtained through the modelling of the surface to a modified Randles circuit using ZView Software. Ka was obtained by the modelling of the calibration curve to a Langmuir like isotherm. 258

LIST OF FIGURES

Figure 1.1 Schematic representation of microRNA biogenesis in animal cells. Reproduced from ref. [63] Novák, J., Kružliak, P., Bienertová-Vašků, J., Slabý, O., & Novák, M. (2014). MicroRNA-206: a promising theranostic marker. *Theranostics*, *4*(2), 119–133.....3
Figure 1.2. Schematic illustrating the structure of the BBB in normal conditions (A), and following exposure to BSWs of lower intensity (B) or higher intensity (C). Reproduced from ref. [24] Shetty, A. K., Mishra, V., Kodali, M., & Hattiangady, B. (2014). Corrigendum: Blood brain barrier dysfunction and delayed neurological deficits in mild traumatic brain injury induced by blast shock waves. *Frontiers in cellular neuroscience*, *8*, 404. 5
Figure 1.3 . (A) qPCR analysis of Ago2-eluted P2rx7 mRNA, 8 h after SE (n = 5/group). (B) RISC profiling. Heat map lists miRNAs in order of abundance in the Contra hippocampus. (C) qPCR analysis of miRNA-22 from pulldowns 8h after SE (n = 6; each sample was a pool of 2 hippocampi). (D) Graph showing temporal course of miRNA-22 down-regulation in hippocampal tissue after Ant22 i.c.v. injection (d, day; w, week; n = 4/group). (E) Graphs show transcript levels of proinflammatory cytokines are elevated in the contralateral hippocampus of Ant22 treated mice at 12 h after SE (n = 5 – 6/group). (F) Western blot (n = 1/lane) and graph show increased IL-1β in the contralateral hippocampus of Ant22 mice 12 h after SE (n = 4/group). *p < 0.05; **p < 0.01 compared to indicated group/control. (G,H) Increased Arc and c-Fos in the contralateral hippocampus of epileptic Ant22 mice at the end of recordings compared to epileptic Scr mice and non-kainic acid controls (n = 11 (Ant22 Cont), 12 (Scr Cont), 16 (Ant22 SE) 13 (Scr SE). (I) Immunoblot (n = 1/lane) and corresponding graph showing increased P2X7R levels in the contralateral hippocampus of epileptic Ant22-treated mice when compared to epileptic Scr mice at the end of epilepsy monitoring (n = 4–5/group). (J) Time course showing injection of 0.5 pmol Mi22 results in a transient increase in miR-22 levels in the hippocampus (n = 4–7/group). (K) Mi22 treated mice (Mi22; 0.5 pmol injected at 1, 8 and 24 h post-SE) show reduced spontaneous seizures during the first 4 days after status epilepticus (n = 7/group). *p < 0.05; **p < 0.01; ***p < 0.001 compared to indicated group/control. Adapted from ref. [12] Jimenez-Mateos, E. M., Arribas-Blazquez, M., Sanz-Rodriguez, A., Concannon, C., Olivos-Ore, L. A., Reschke, C. R., Mooney, C. M., Mooney, C., Lugara, E., Morgan, J., Langa, E., Jimenez-Pacheco, A., Silva, L. F., Mesuret, G., Boison, D., Miras-Portugal, M. T., Letavic, M., Artalejo, A. R., Bhattacharya, A., Diaz-Hernandez, M., Engel, T. (2015). microRNA targeting of the P2X7 purinoceptor opposes a contralateral epileptogenic focus in the hippocampus. *Scientific reports*, *5*, 17486.....9
Figure 1.4. Conserved brain and blood miRNA responses following epileptogenic brain injuries (A) Profiling data show unique as well as common up- and down-regulated miRNAs 24 h after different epileptogenic insults to the brain. (B) Blood profiling data show each insult produces unique as well as shared miRNA expression responses in blood suggesting a set of common miRNAs that could represent biomarkers of epileptogenic brain injury. Boxes list the conserved miRNAs. Note, -3p and -5p denote mature miRNAs that originate from opposite arms of the same miRNAs. Adapted from ref. [14] Liu, D. Z., Tian, Y., Ander, B. P., Xu, H., Stamova, B. S., Zhan, X., Turner, R. J., Jickling, G., & Sharp, F. R. (2010). Brain and blood microRNA expression profiling of ischemic stroke, intracerebral hemorrhage, and kainate seizures. *Journal of cerebral blood flow and metabolism*, *30*(1), 92–101. 11
Figure 1.5. DPV curves of silver-nanoclusters modified Au electrodes in N_2- saturated PBS (100 mM, pH 7.0) containing H_2O_2 (3 mM) at 10 fM, 100 fM, 1 pM, 10 pM, 100 pM, 1 nM, 10 nM, and 100 nM target miRNA (from a to h). Inset: plot of the peak current versus the logarithm of target concentration. Reproduced from ref. [63] Dong, H., Jin, S., Ju, H., Hao, K., Xu, L. P., Lu, H., & Zhang, X. (2012). Trace and label-free microRNA detection using

oligonucleotide encapsulated silver nanoclusters as probes. *Analytical chemistry*, *84*(20), 8670–8674.....31
Figure 1.6. DPV curves of Ag-NCs modified Au electrodes in N_2- saturated PBS (100 mM, pH 7.0) containing H_2O_2 (3 mM) for detection of 100 pM complementary target, single-base mismatched strand, and three-base mismatched strand. Inset shows the corresponding peak currents. Reproduced from ref. [63] Dong, H., Jin, S., Ju, H., Hao, K., Xu, L. P., Lu, H., & Zhang, X. (2012). Trace and label-free microRNA detection using oligonucleotide encapsulated silver nanoclusters as probes. *Analytical chemistry*, *84*(20), 8670–8674. 32
Figure 1.7. Schematic diagram of the platinum nanoparticle formation and regio-selective miRNA functionalization. Reproduced from ref. [64] Spain, E., Jimenez-Mateos, E. M., Raoof, R., et al. (2015). Direct, non-amplified detection of microRNA-134 in plasma from epilepsy patients. *RSC Advances, 5*, 90071–90078.....34
Figure 1.8. Dependence of the difference in current before and after addition of H_2O_2 on log[RNA] for a 2 mm diameter bare electrode following hybridization with reporter-probe DNA that is labelled with PtNPs and where the probe is unlabelled (n=3). In both cases, the solution contains 2mM H_2O_2 at an applied potential of -0.250V. Where error bars are not visible, they are smaller than or comparable to, the size of the symbols and range of 1.1% to 3.5%. Reproduced from ref. [50] Spain, E., Jimenez-Mateos, E. M., Raoof, R., et al. (2015). Direct, non-amplified detection of microRNA-134 in plasma from epilepsy patients. *RSC Advances, 5*, 90071–90078. 35
Figure 1.9. Calibration plots of peak current response vs. logarithm of concentration of miRNA with the biosensor under optimal conditions. Inset shows the typical CV plots upon the addition of varying amounts of miRNA: 5.6; 56; 280; 560; $5.6x10^3$; 2.8 $x10^4$; 5.6 $x10^5$ pM. All potentials are given vs. SCE and the scan rate is 50 mVs^{-1}.Reproduced from ref. [65] Wu, X., Chai, Y., Yuan, R., Su, H., & Han, J. (2013). A novel label-free electrochemical microRNA biosensor using Pd nanoparticles as enhancer and linker. *The Analyst*, *138*(4), 1060–1066. .37
Figure 1.10. Schematic representation for simultaneous electrochemical biosensors. Multi-analyte can be detected either by multi-label systems (panel a) or multi-electrode systems (panel b). Reproduced from ref. [52] Pakchin, P. S., Nakhjavani, S. A., Saber, R., Ghanbari, H., & Omidi, Y. (2017). Recent advances in simultaneous electrochemical multi-analyte sensing platforms. *TrAC-Trends in Analytical Chemistry, 92* (1), 32–41. 41
Figure 1.11. Schematic display of the fundamentals involved in the development of the disposable dual magnetosensor for the simultaneous determination of miRNA-21 and miRNA-205 (a). Picture showing the dual SPCE and the homemade magnet holding block (up), and the modified MBs on the dual SPCE assembled on the magnetic holding block and (b) the specific cable connector (down). Reproduced from ref. [75] Torrente-Rodríguez, R. M., Campuzano, S., López-Hernández, E., Montiel, V. R., Barderas, R., Granados, R., Sánchez-Puelles, J. M., & Pingarrón, J. M. (2015). Simultaneous detection of two breast cancer-related miRNAs in tumor tissues using p19-based disposable amperometric magnetobiosensing platforms. *Biosensors & bioelectronics*, *66*, 385–391.....42
Figure 1.12. Schematic representation of the 3-mode electrochemical sensor (HPD-SENS) for detection of miRNAs. (a) A thiol-modified complementary probe for miRNA-21 was self-assembled onto a gold nanoparticles-modified screen-printed carbon electrode (GNPs-SPCE) followed by backfilling the surface with 0.1 mM 2-mercaptoethanol. (b) A hybridization-based sensor (H-SENS) where the binding of the target miRNA-21 caused an increase in the current intensity, measured by square wave voltammetry (SWV). The linear detection range of the H-SENS is from 1 fM to 10 pM. (c) A p19 protein-based sensor (P-SENS) where the binding of the p19 protein caused a large decrease in current density and thus improved the detection range. The linear detection range of the P-SENS is from 10 aM to 10 fM. (d) A displacement-based sensor (D-SENS) where the hybridization product of miRNA-200 and its complementary

probe forced the p19 protein to dissociate from the previous immobilized hybrid, causing a shift-back in the signal. The linear detection range of the D-SENS is from 100 pM to 1 μM Figure reproduced from ref. [76] Labib, M., Khan, N., Ghobadloo, S. M., Cheng, J., Pezacki, J. P., & Berezovski, M. V. (2013). Three-mode electrochemical sensing of ultralow microRNA levels. *Journal of the American Chemical Society*, *135*(8), 3027–3038.....45
Figure 2.1.Schematic of a gold electrode (a) immobilized with miRNA through specific and non-specific adsorption, (b) co-immobilized with miRNA/MCH, (c) with oriented miRNA passivated with MCH and hybridized with miRNA target.....60
Figure 2.2. (A) Standard Randle's equivalent circuit model used to fit the electrochemical impedance spectroscopy data and (B) the corresponding Nyquist Diagram. 66
Figure 2.3. Representative experimental chronocoulometric curves for gold electrodes modified with ssDNA probes (red, Q_{ss}); electrodes after hybridization with 1 μM target DNA (green, Q_{ds}) and electrodes after hybridization with 10 pM target DNA and with the amplification of AuNPs (black, Q_{AuNPs}). Redox charges of RuHex bound to DNA are obtained from chronocoulometric intercepts at t=0. The signal is defined as the increment of the redox charge, i.e., signal = Qds-Qss, or signal = QAuNPS-Qss. Figure adapted from [18]. 70
Figure 2.4. Representative cyclic voltammograms of the gold electrode modified with 10 μM solution of miRNA capture-probe at different immobilization times, such as: 0, 10, 30, 40, 80 min and 17 h. Electrochemical species: 1 mM $[Fe(CN)_6]^{3-/4-}$ with 0.01 M PBS. Scan rate: 500 mV/s. The analysis was performed in triplicate.....72
Figure 2.5. Cyclic voltammograms of the gold electrode modified with 10 μM of miRNA during 10 min at various scan rates (10, 20, 50, 70, 100, 150, 200, 250, 300, 350, 400, 450, 500 mV/s from outer to inner). Inset: Dependence of reduction and oxidation peak currents on the square root of scan rate ($\nu^{1/2}$). Electrochemical species: 1 mM $[Fe(CN)_6]^{3-/4-}$ with 0.01 M PBS. The analysis was performed in triplicate. 74
Figure 2.6. (A) Nyquist plot of the impedance spectra obtained by the gold electrode immobilized with 10 μM of miRNA capture-probe over different times. Inset: modified equivalent Randles circuit used to model impedance data, where R_1 is the electrolyte resistance; WS_1 is the Warburg impedance; R_2 is the charge-transfer resistance; and CPE_1 is the double-layer capacitance. Electrolyte used: 1mM $[Fe(CN)_6^{3-/4-}]$ in 0.01 M PBS. Biasing potential: 0.231V. Amplitude: 25 mV. Frequency range: 0.1 Hz to 10^5 Hz. (B) Fitting of the Nyquist plots presented in (A) using the equivalent Randles circuit (inset) obtained through the ZView program. The analysis was performed in triplicate.....76
Figure 2.7. The monolayer thickness of the miRNA capture-probe immobilized onto the gold surface was estimated at multiple time points spanning from 0 to 1200 minutes. Error bars, indicative of the variability in results obtained from three independent measurements, are displayed on the graph. In cases where error bars are not discernible, they either reflect minimal variability or are comparable in size to the plotted symbols. 79
Figure 2.8. (A) Cyclic voltammograms and (B) Nyquist plots of impedance spectra obtained by the miRNA modified electrode after hybridization with 10 μM of miRNA target at times: 5, 20, 40 and 60 min. Electrochemical species: 1 mM $[Fe(CN)_6]^{3-/4-}$ with 0.01 M PBS. Scan rate: 50 mV/s. Potential: 0.231V. Amplitude: 25mV. Frequency range 0.1 Hz to 10^5 Hz. The analysis was performed in triplicate. 83
Figure 2.9. Chronocoulometric response curves for the miRNA: MCH functionalized at the gold electrode at 1[miRNA]:2[total thiol] molar ratio. Parameters: -0.3V to -0.8 V during 0.5 s. Sample interval: 0.0025 s and numbers of steps: 2. 88
Figure 2.10. Chronocoulometric response curves for the miRNA: MCH functionalized at the gold electrode at 1[miRNA]:[total thiol] molar ratio. The dashed line represents the extrapolation of the linear part of the Anson plot by least square fit. Parameters: -0.3V to -0.8V during 0.5 s. Sample interval: 0.0025s and number of steps:2. 90

Figure 2.11. Relation between miRNA surface density and different molar ratios of miRNA: total thiol in the immobilization solution. The solid line is the least square fit where the [miRNA]/[Total thiol]=1 data point has been excluded. The error bars represent the spread of the results performed in triplicate. 91
Figure 2.12. (A) Nyquist plots of the impedance spectra obtained by the gold electrode immobilized with different molar ratios of [miRNA]:[total thiol] and **(B)** Nyquist plot curve response upon the hybridization event of the gold electrode immobilized with different mixed SAM ratios and 1 μM of miRNA target. Electrolyte used: 1 mM [Fe $(CN)_6^{3-/4-}$] in 0.01 M PBS. Biasing potential: 0.231V. Amplitude: 25 mV. Frequency range: 0.1 Hz to 10^5Hz. The analysis was performed in triplicate. 95
Figure 2.13. Correlation between the hybridization efficiency and the surface density of miRNA capture-probe. Hybridization event occurs using 1 μM of miRNA target during 20 min at 37°C. The error bars represent the spread of the results performed in triplicate. 98
Figure 2.14. (A) Nyquist plots of impedance spectra obtained by the miRNA capture-probe electrode after hybridization with different concentrations of miRNA-206 during 20 min at 37°C and (B) the corresponding calibration curve based on the variation of charge transfer and log concentration of the miRNA-206. The error bars were indicated on the curve (n = 3). Electrochemical species: 1 mM $[Fe(CN)_6]^{3-/4-}$ with 0.01 M PBS. Scan rate: 50 mV/s. Biasing potential: 0.231 V. Amplitude: 25 mV. Frequency range 0.1 Hz to 10^5 Hz. Numbers 1-10 correspond to 1aM to 1μM of miRNA-206. 100
Figure 2.15. Calibration curves of a miRNA capture-probe hybridized with different concentrations of miRNA-206 (from μM to aM) without any interfering assay (black line) and in an environment where BSA is present (red line). The variations of charge transfer resistance were obtained from the response of the Nyquist plots at the different concentrations. The error bars were indicated on the curve (n = 3). The parameters used were scan rate: 50 mV/s, biasing potential: 0.231 V, amplitude: 25 mV and frequency range: 0.1Hz to 10^5 Hz. The analysis was performed at 0.01 M PBS containing 1 mM $[Fe(CN)_6]^{3-/4-}$ as a redox probe. 105
Figure 2.16. Impedimetric curves (Nyquist plots) showing the variation of the charge transfer resistance between miRNA capture-probe and a fully complementary target strand (black and grey line) and a 4-base mismatched strand (red and pink line). Electrochemical species: 1 mM $[Fe(CN)_6]^{3-/4-}$ with 0.01 M PBS. Scan rate: 50 mV/s. Potential applied: 0.231 V, amplitude: 25 mV and frequency range: 0.1Hz to 10^5Hz. 106
Figure 2.17. Impedimetric response of the biosensor toward miRNA-206 at different concentrations after storage in the immobilization buffer at 4 °C. The number next to each data point represents the average percent of response compared to the freshly prepared biosensors. The error bars were calculated based on standard deviation of the measurements performed in triplicate (n=3). 108
Figure 2.18. (A) Calibration curves of a miRNA capture-probe electrode hybridized with different concentrations of standard miRNA-206 (from μM to aM) in a healthy female control sample and (B) in a healthy male control sample. The variations of charge transfer resistance were obtained from the response of the Nyquist plots at the different concentrations. The error bars were indicated on the curve and were calculated based on standard deviation of the measurements performed in triplicate (n = 3). The parameters used were: scan rate: 50 mV/s, biasing potential: 0.231 V, amplitude: 25 mV and frequency range: 0.1 Hz to 10^5 Hz. The analysis was performed at 0.01 M PBS containing 1 mM $[Fe(CN)_6]^{3-/4-}$ as a redox probe. 110
Figure 3.1. Amperometric i-t curves for gold electrode functionalized with 10 μM miRNA capture-probe, 1μM of miRNA target strands and different ratios of the conjugate $[miRNA_{reporter\text{-}probe}]_I$/[AuNRDs], such as 640:1 (black line), 960:1 (pink line), 1280:1 (red line) and 6400: 1 (blue line). Potential applied is -0.25 V in 0.1M PBS. The difference in current before and after the addition of 400 μM of hydrogen peroxide is displayed.....130

Figure 3.2. UV-vis absorption spectrum of 50 nm AuNRDs modified at different [$miRNA_{reporter-probe}$]$_I$ /[AuNRDs] ratios. 133
Figure 3.3. Amperometric i-t curves for gold electrodes functionalized with 10 μM miRNA capture-probe strands, (A) 1 nM and (B) 1 pM of miRNA target strands and 6.8 μM miRNA reporter-probe strands labelled with gold nanorods. The hybridization between the target and reporter-probe strands was allowed to occur for various durations, ranging from 30 minutes to 17 hours. Potential applied is -0.25 V in 0.1 M PBS. The difference in current before and after the addition of 400 μM of hydrogen peroxide is displayed. 135
Figure 3.4. Representative chronoamperometric curves of a non-functionalized fully complementary miRNA sandwich assay ([miRNAtarget = 1nM) at sequential additions of hydrogen peroxide to form a final concentration ranging from 200 μM to 10000 μM. The electrolyte used was 0.1 M PBS. Inset depicts the chronoamperometric behaviour of the same assay at longer reaction times and at hydrogen peroxide concentration of 10 mM. Measurements were conducted in triplicate. 138
Figure 3.5. Chronoamperometric curves of a functionalized fully complementary miRNA sandwich assay ([miRNA target= 1nM) at different hydrogen peroxide concentrations, such as 400 μM (purple curve), 600 μM (green curve), 800 μM (blue curve), 1000 μM (red curve) and 2000 μM (black curve). Potential applied is -0.25V in 0.1 M PBS. Measurements were conducted in triplicate. 140
Figure 3.6.Amperometric i-t curves for gold electrodes functionalized with 10 μM miRNA capture-probe strands, varying concentrations of miRNA target stands (as shown in subtitle) and 6.8μM miRNA reporter-probe strands labelled with gold nanorods. Potential applied is -25V in 0.1M PBS. The difference in current before and after the addition of 400μM is displayed. 142
Figure 3.7. Chronoamperometric current response of a functionalized fully complementary sandwich assay as a function of target concentrations. The Y-axis is the difference in current before and after the addition of 400 μM hydrogen peroxide. The applied potential is -0.25V in 0.1M PBS. Measurements were conducted in triplicate, and therefore, error bars depicts the data spread (n=3). Where error bars are not visible, it means they are either very small or about the same size as the symbols used. 145
Figure 3.8. Comparison of the current response of miRNA-206 at different concentrations (aM- μM) in a full sandwich assay functionalized with AuNDRs (black line) and without AuNRDs (red line). The Y-axis is the difference in current before and after the addition of 400 μM of hydrogen peroxide. The applied potential is -0.25 V in 0.1M PBS. Measurements were conducted in triplicate, and therefore, error bars depicts the data spread (n=3). Where error bars are not visible, it means they are either very small or about the same size as the symbols used. 146
Figure 3.9. Amperometric i-t curves for a bare gold electrode (black line), a gold electrode functionalized with 10 μM capture-probe miRNA/40 μM MCH (red line), a gold electrode functionalized with capture-probe and hybridised to 1 nM target miRNA (pink line), and a gold electrode functionalized with full sandwich assay (blue line). Potential applied is -0.25 V in 0.1M PBS. The difference in current before and after the addition of 400 μM of hydrogen peroxide is displayed. Measurements were performed in triplicate. 149
Figure 3.10. Comparison of the chronoamperometric current response of a functionalized fully complementary sandwich assay (miRNA-206, black line) to a non-complementary, 1 base mismatch assay (red line) as a function of target concentrations. The Y-axis is the difference in current before and after the addition of 400 μM hydrogen peroxide. The applied potential is -0.25 V in 0.1M. Measurements were conducted in triplicate, and therefore, error bars depicts the data spread (n=3).....151

Figure 3.11. Comparison of the chronoamperometric current response of a functionalized fully complementary sandwich assay (miRNA-206, black line) to a non-complementary, 4-base mismatched assay (miRNA-1, red line) as a function of target concentrations. The Y-axis is the difference in current before and after the addition of 400 μM of hydrogen peroxide. The applied potential is -0.25 V in 0.1 M. Measurements were conducted in triplicate, and therefore, error bars depicts the data spread (n=3). Where error bars are not visible, it means they are either smaller or comparable to the same size of the symbols used. 154
Figure 4.2. Cyclic voltammograms of (A) a conventional gold disk electrode, (C) 10% AuF SPCE and (E) 10% AuS SPCE in 0.01 M PBS with 1mM FcMeOH at scan rates from 0.005 V/s to 0.5 V/s. Graphs of peak current vs. square root of scan rate are depicted in (B), (D) and (F). Error bars were estimated as triple of the standard deviation. 172
Figure 4.3. SEM images of a 10% AuF SPCE surface made with secondary electrons. Magnification and accelerating voltage used was of (a) 25 k, 1 kV (b), 25 k, 5 kV and (b) 22 k, 20 kV.....176
Figure 4.4. SEM image of a 10% AuS SPCE surface generated by secondary electrons. Magnification and accelerating voltage used was of (a) 60 k, 1 kV.The gold nanoparticle were highlighted for clarity. 177
Figure 4.5. SEM images of 10% AuS SPCE surface made with magnification and accelerating voltage of 5 k and 10 kV using (A) secondary electrons (B) secondary electrons (LA1000) and SEM images of 10% AuF SPCE surface made with magnification and accelerating voltage used of (C)1.3 K, 1 kV using secondary electrons and (D) 1.3 k, 5 kV using SE (LA100)..178
Figure 4.6. Amperometric i-t curves for 10% AuF and AuS SPCEs functionalised with (A) 10 µM miRNA capture-probe strands, 1 µM of miRNA target stands, and 1 µM miRNA reporter-probe strands labelled with palladium nanocubes at an applied potential of -0.375 V in 0.01 M PBS and (B) 10 µM miRNA capture-probe strands, 100 nM of miRNA target strands and 4.6 μM miRNA reporter-probe strands labelled with AuNRDs at an applied potential of -0.250 V in 0.01 M PBS. The difference in current before and after the addition of 400 µM hydrogen peroxide is displayed in the graphs. Measurements were conducted in triplicate. 180
Figure 4.7. Representative amperometric i-t curves for 10% AuS and 20% AuS SPCEs functionalised with (A)10 µM miRNA capture-probe strands, 1 µM of miRNA target strands, and 1 µM miRNA reporter-probe strands labelled with PdNCBs at -0.375 V in 1 mM PBS and (B) 10 µM miRNA capture-probe strands, 100 nM of miRNA target strands and 4.6 µM miRNA reporter-probe strands labelled with gold nanorods at -0.25 V in 0.01M PBS. The difference in current before and after the addition of 400 µM hydrogen peroxide is displayed. Measurements were conducted in triplicate.....183
Figure 4.8. Cyclic voltammograms of a 20% AuS SPCE without any modification over the surface (black curve). Cyclic voltammograms of a 20% AuS SPCE with 2 µL of (a) palladium nanocubes, (b) gold nanorods and (c) platinum nanoparticles drop-casted on its surface. Electrolyte: 0.01 M of PBS with 400 μM of hydrogen peroxide. Scan rate: 0.05 V/s. Measurements were conducted in triplicate.....188
Figure 4.9. Amperometric i-t curves of 20% AuS SPCEs functionalised with (A) 10 µM miRNA capture-probe strands, 1 µM of miRNA target stands and 1 µM miRNA reporter-probe strands labelled with PdNCBs ; (B) 10 µM miRNA capture-probe strands, 100 nM of miRNA target strands, and 4.6 µM miRNA reporter-probe strands labelled with AuNRDs and (C) 10 µM miRNA capture-probe strands, 1 µM of miRNA target stands and 1 µM miRNA reporter-probe strands labelled with PtNPs (n=3). The studied potential window ranged from -0.1 to -0.5 V in 0.01 M PBS. The difference in current before and after the addition of 400 µM hydrogen peroxide is displayed in the graphs.....190
Figure 4.10. TEM image of AuNRDs in citrate. Magnification and accelerating voltage used was 700k and 20kV, respectively. 193

Figure 4.11. SEM image made with secondary electrons. Magnification of 90 k was used. Accelerating voltage of 25 kV. 194
Figure 4.12. XRD pattern of Pd nanocubes with average size of 48.9 nm. 195
Figure 4.13.SEM images of (A) 20% AuS SPCE without modification of the surface and (B) 20% AuS SPCE functionalised with full miRNA assay and PdNCBs labels. Magnification and accelerating voltage used is described in the respective images.....197
Figure 5.1. Assembly of the Labelled miRNA Biosensor: Schematic Diagram and Specific Parameters. For the functionalization of the electrode to AuNRDs, 4.6 μM reporter-probe solution were utilized. Alternatively, when functionalized with PtNPs and PdNCBs, a 1 μM miRNA reporter-probe solution were employed. 210
Figure 5.2. Amperometric i-t curves for 20% AuS SPEs functionalized with 10 μM miRNA capture-probe strands following hybridisation with the indicated concentration of the target. The concentration of the reporter-probe labelled nanoparticles is 1 μM. The reporter-probe labelled nanoparticles are (A) gold nanorods, (B) palladium nanocubes, and (C) platinum nanoparticles. The applied potentials were (A) - 0.25V, (B) - 0.375V, and (C) - 0.5 V. The electrolyte was 0.01 M PBS and hydrogen peroxide was added at 300 s to give a final concentration of 400 μM. Measurements were conducted in triplicate,.....215
Figure 5.3. Calibration curves of the functionalized fully sandwich assay based on the amperometric variation of current and log concentration of the (A) miRNA-206, (B) miRNA-135a and (C) let-7b. Error bars were estimated as triple of the standard deviation (n = 3)...220
Figure 5.4. Chronoamperometric curves show the current difference between a fully complementary strand at nM and pM (red and blue line, respectively) and a 1-base mismatch strand (pink and green line) at the same concentrations. The fully complementary assay was labelled with gold nanorods. Potential applied is -0.25 V in 0.01 M PBS. The difference in current before and after the addition of 400 μM H_2O_2 is displayed. Measurements were performed in triplicate.....225
Figure 5.5. Chronoamperometric curves showing the current difference between a fully complementary strand at 1 nM and 1 pM (red and blue line) and a 4-base mismatches strand (pink and green line) at the same concentrations. The fully complementary assay was labelled with gold nanorods. Potential applied is -0.25 V in 0.01 M PBS. The difference in current before and after the addition of 400 μM hydrogen peroxide is displayed. Measurements were performed in triplicate.....227
Figure 5.6. Representative chronoamperometric curves of the current difference between a fully complementary strand at nM and pM and a (A)1-base mismatches strand (and (B) 2-base mismatches at the same concentrations (n=3). The fully complementary assay was labelled with platinum nanoparticles. Potential applied is -0.50 V in 0.01 M PBS. The difference in current before and after the addition of 400 μM hydrogen peroxide is displayed.....229
Figure 5.7. Chronoamperometric curves show the current difference between a fully complementary strand at nM and pM (red and blue line) and a 1-base mismatch strand (pink and green line) at the same concentrations (n=3). The fully complementary assay was labelled with palladium nanocubes. Potential applied is -0.375 V in 0.01 M PBS.The difference in current before and after the addition of 400 μM H_2O_2 is displayed. 233
Figure 5.8. Calibration curves of functionalized assays at a range of concentrations (from 1μM to aM) of (A) miRNA-206; (B) miRNA-135a; (C)let-7b and 1 μM of miRNA reporter-probe without any interfering assay (black line) and in an environment where BSA is present (red line). The error bars were indicated on the curve (n = 3). Potential applied is (A) -0.25V; (B) -0.375 V; (C) -0.5V in 0.01M PBS. 236
Figure 5.9. Time dependence of the amperometric current response of the biosensor to two different concentrations (1 nM and 1 pM) of (A)miRNA-206; (B) miRNA-135a; (C) let-7b after storage at 4 °C for 21 days. The number next to each data point represents the average

percent of response compared to the freshly prepared biosensors. Errors bars estimated as triple of the standard deviations (n=3). 241

ABSTRACT

Amanda Carrico

Development of ultrasensitive electrochemical biosensors for the detection of miRNAs associated with neurological diseases.

An impedance-based biosensor was developed to detect miRNA-206, associated with Alzheimer's disease, with remarkable sensitivity (LOD 0.15 aM). By modulating surface coverage and hybridization efficiency, the biosensor achieved a reduced dielectric constant and smaller association constant between miRNA capture-target. This phenomenon enhanced the biosensors' dynamic range (μM to aM), while maintaining high selectivity, low non-specific binding, and sensing phase stability. The biosensor was also validated in the clinical settings by accurately quantification of miRNA-206 in real plasma samples.

To enhance biosensor sensitivity, miRNA reporter-probes were modified with gold nanorods (AuNRDs).The study employed chronoamperometry analysis, emphasizing hydrogen peroxide reduction by gold nanorods confined to the gold electrode via miRNA target hybridization. Optimization steps, including [miRNA $_{\text{reporter-probe}}]_I$ to [AuNRDs] ratios, optimal hydrogen peroxide concentration for electrocatalysis, and refinement of target—reporter-probe hybridization time, improved detection accuracy. The biosensor detected miRNA-206 across a broad dynamic range (fM to μM) with high sensitivity (LOD 0.46 fM), selectivity against base mismatches, and rapid response time (5 to 25 minutes).

Screen printed carbon electrodes (SPCE) offered a cost-effective and biocompatible alternative for mass-producing miRNA detection platforms. Two SPCE, containing different gold structures within their carbon ink as 10%(w/w) microflakes (AuF) and 10%(w/w) microspheres (AuS), were developed. Comparative analysis involving chronoamperometry revealed that SPCEs with AuS exhibited superior charge transfer process, higher peak currents and reduced potential for hydrogen peroxide reduction. Further assessments evaluated SPCE with an enhanced sensing phase (i.e. 20% (w/w) AuS). An additional of 10% AuS onto the matrix ink led to an expressive (i.e 56-fold) signal amplification of the platform when using AuNRDs as labels.

In a proof-of-concept study, the innovative 20% (w/w) AuS SPCE demonstrated its potential as a multiplex platform. It successfully detected potential biomarkers for Alzheimer disease (miRNA-206) and epilepsy (let-7b and miRNA-135a) using various nanomaterial labels. Platinum nanoparticles showed the highest electrocatalytic activity, followed by PdNCBs and AuNRDs, catering to different miRNA requirements. The biosensor exhibited a wide dynamic range (fM-uM), ultralow LODs (fM), high selectivity against mismatches and stable sensing phase. The successful detection of multiples miRNAs and absence of cross-reactivity between assays position it as a promising candidate for multiplexed analysis.

Publications and Presentations

Carrico, A., Cumba, L., Medina, M., Engel, T., & Forster, R. J. (2023). Ultrasensitive, Label-free Electrochemical Detection of the Alzheimer Disease Biomarker miR-206 in Human Plasma. **Manuscript in preparation.**

Carrico, A., Cumba, L., & Forster, R. J. (2023). Development of labelled amperometric biosensors based on screen printed electrodes that contain different gold microstructures within the carbon ink. **Manuscript in preparation.**

Carrico, A., Cumba, L., & Forster, R. J. (2023). A sandwich electrochemical biosensor for miRNA-206, miRNA-135a and let-7b detection based on metal nanoparticles labelled SPEs. **Manuscript in preparation.**

Conference Contributions

Poster Presentation

Carrico A.; Cumba L.; Medina M.; Engel T.; Forster R.J. Ultrasensitive, Labelled and label-free detection of miRNAs. Presented at FutureNeuro Research Day on 13th October 2022, Dublin.

Carrico A.; Cumba L.; Medina M.; Engel T.; Forster R.J. Ultrasensitive, Label-free Electrochemical Detection of the Alzheimer Disease Biomarker miR-206 in Human Plasma. Presented at 2022 Satellite Early Career Researcher Regional Symposium on Electrochemistry. 4th November 2022, Queen's University Belfast.

Carrico A.; Cumba L.; Medina M.; Engel T.; Forster R.J. Ultrasensitive, Label-free Electrochemical Detection of the Alzheimer Disease Biomarker miR-206 in Human Plasma. Presented at 46ª RASBQ Reunião Annual da SBQ (Annual Meeting of SBQ), 28 May 2023-31 May 2023, São Paulo, Brazil

Oral Presentation

"Labelled and label-free ultrasensitive electrochemical biosensors for the detection of miRNA associated with neurological diseases". Presentation delivered as a short talk (5 min) at FutureNeuro Annual Science Meeting, 19th October 2021, Dublin, Ireland.

"Labelled and label-free ultrasensitive electrochemical biosensors for the detection of miRNA associated with neurological diseases". Presentation delivered as a long talk (15 min) at Chemistry Day, May 2022, DCU, Dublin, Ireland.

"Development of Companion Diagnosis: electrochemical biosensors for detection of miRNAs associated to epilepsy" at Epilepsy Ireland, August 2022, Dublin, Ireland.

CHAPTER 1

Introduction and Literature Review.

1 LITERATURE REVIEW

1.1 miRNA and Cognitive diseases: Alzheimer and Epilepsy

1.1.1 miRNA: An Overview

MicroRNAs, also known as miRNAs, are a non-coding, single stranded RNA that range in length 18-25 oligonucleotides and can be found in tissues or body fluids of animals, microorganisms, humans, and plants. This large class of small RNAs has several biological functions, such as embryonic development, proliferation, apoptosis, and haematopoiesis [1]. Moreover, specific alterations in their expression are often linked to human diseases, as well as genetic neurological disorders and the onset of cancers.

Although, miRNAs were first described as a post-transcriptional gene regulator in 1993 when Lee *et al.* [2] investigated the role of small RNAs in lin-4 and lin-14 genes, it was only considered an evolutionary key to gene regulation and, therefore, a possible biomarker of diseases years later. Among the advantages presented by miRNAs, the interest of use is due to its high stability in extracellular environments (e.g. binding in exomes or microvesicles), resistance to defrost cycles and its easy quantification (e.g., direct measurements via RT-qPCR or via electrochemical system of detection) [3]. In addition, the relatively easy accessibility of these molecules in patient samples in a non-invasive manner, characterized by its abundance in body fluids and tissue, made the study of miRNAs gain significant attention.

1.1.2 Biogenesis of the miRNA

The biogenesis of miRNAs can be described by its transcription process in the cell nucleus, exportation to the cytoplasm and subsequent processing and maturation. Following the process described in Figure 1.1, initially, a long primary transcript (pri-miRNA) in the form of a hairpin structure is transcribed by RNA polymerase II in the nucleus. The pri-miRNA is then processed into pre-miRNA by the action of the enzyme Drosha which cleaves the ends of the RNAs leaving it in the form of a hairpin with a 3' overhang end. This overhang end causes the pre-miRNA to be exported to the cytoplasm by the protein Exportina 5. Subsequently, the pre-miRNA has its loop region cleaved by the Dicer enzyme, generating a double-stranded RNA (dsRNA) [4]. This process recruits' proteins from the argonaut family (Ago) to form the RNA-induced silencing complex (RISC), where the two RNA strands are separated. RISC binds to

the active part of one of the two strands of dsRNA to generate mature miRNA (canonical miR or miR-5p), while the inactive part of the strand (miR * or miR-3p) dissociates and is degraded [5].

Regarding the genetic regulation of a target mRNA in the cytoplasm, it can occur by direct or indirect paths. The direct path occurs through the cleavage of the mRNA by the mature miRNA. The indirect path occurs through the repression of translation. The type of genetic regulation that will be processed will depend exclusively on the complementarity between the three-prime untranslated (3'UTR) of the target mRNA and the miRNA. The perfect pairing (fully complementarity) between the miRNA and the 3 'UTR region of the target mRNA promotes the cleavage of the mRNA and its subsequent degradation. On the other hand, partial pairing between the miRNA and the 3 'UTR region of the mRNA inhibits translation [5].

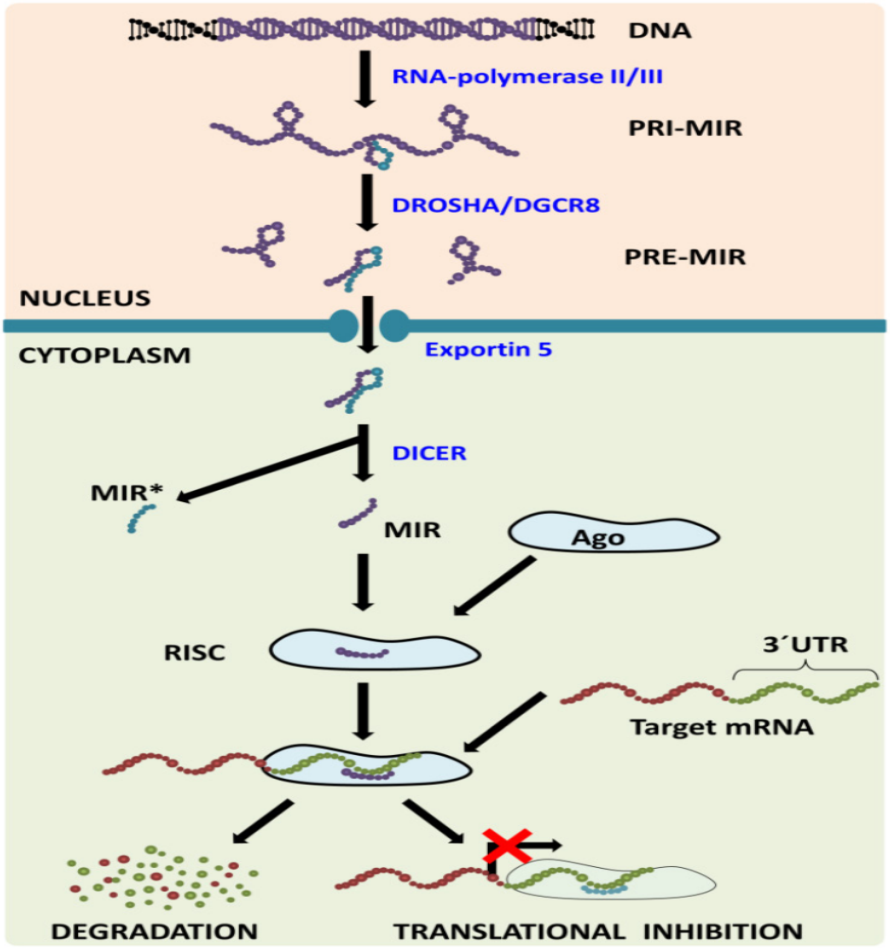


Figure 1.1 Schematic representation of microRNA biogenesis in animal cells. Reproduced from ref. [63] Novák, J., Kružliak, P., Bienertová-Vašků, J., Slabý, O., & Novák, M. (2014). MicroRNA-206: a promising theranostic marker. *Theranostics*, *4*(2), 119–133..

1.1.3 miRNA in epilepsy

1.1.3.1 Epilepsy: triggers, definitions, symptoms

Epilepsy is a severe neurological dysfunction that causes a "shut down" of a patient's normal brain for a few seconds or minutes. This interruption of neurological signals is caused by a paroxysmal disturbance of brain electrical activity, caused by sudden, excessive, and hypersynchronous discharges of neurons [6].

Epilepsy can be classified as genetic or acquired. Genetic epilepsy involves mutations of crucial neural genes, while acquired epilepsy, also known as temporal lobe epilepsy, mostly involves changes in the properties of neurons (e.g., neural loss, synaptic reorganization, altered neuronal metabolism) [7].

Although epilepsy cause seizures in large scale, there are a range of other symptoms that are also correlated with the disease. Significant neuropathological changes in the hippocampus, variations in consciousness, impaired motor coordination skills, automatism and impaired cognition are some of the other common symptoms generated by this disorder [8].

Epileptic seizures can be classified according to their onset and symptoms. A seizure is considered partial / focal (simple or complex) when the neurological dysfunction is restricted to a single location in the brain. However, generalized seizures occur when the dysfunction involves both brain hemispheres. So, when an epileptic crisis compromises the motor system in a generalized and habitual way ensues an epileptic seizure.

Due to the heterogeneity of the disease, different factors are identified as causing epileptic seizures. Some studies in epileptic tissue in humans show that epileptic seizures can be caused by factors such as enhanced micro-pinocytosis, basal membrane thickening, fewer mitochondria in endothelial cells, and presence of abnormal tight junctions [9][12]. However, blood brain barrier (BBB) disruption is still one of the main investigated causes of epileptic seizures.

In general, studies indicate that BBB modification can contribute to the development of epilepsy by direct or indirect mechanisms. The disease unfolds directly, for example, when the BBB rupture generates neural depolarization via influx of potassium. On the other hand, the development of epilepsy may be an indirectly response to a cascade of events triggered by

leakage of serum proteins that leads to glial activation, impaired potassium buffering, inflammation, and synaptogenesis [9].

Figure 1.2. presents depicts the structure of the blood-brain barrier (BBB) under normal conditions (A) and after exposure to either lower-intensity (B) or higher-intensity (C) blast shock waves (BSWs). Exposure to lower-intensity BSWs is expected to lead to the disruption of tight junction (TJ) proteins, damage to or alterations in the capillary basement membrane (BM), detachment or loss of pericytes, and swelling of astrocyte end-feet in brain microvessels (B). In contrast, exposure to higher-intensity BSWs is likely to directly rupture brain microvessels, resulting in the loss of TJ proteins, BM, pericytes, and endothelial cells, along with swelling of astrocyte end-feet and the leakage of blood (hemorrhage) into perivascular areas (C).

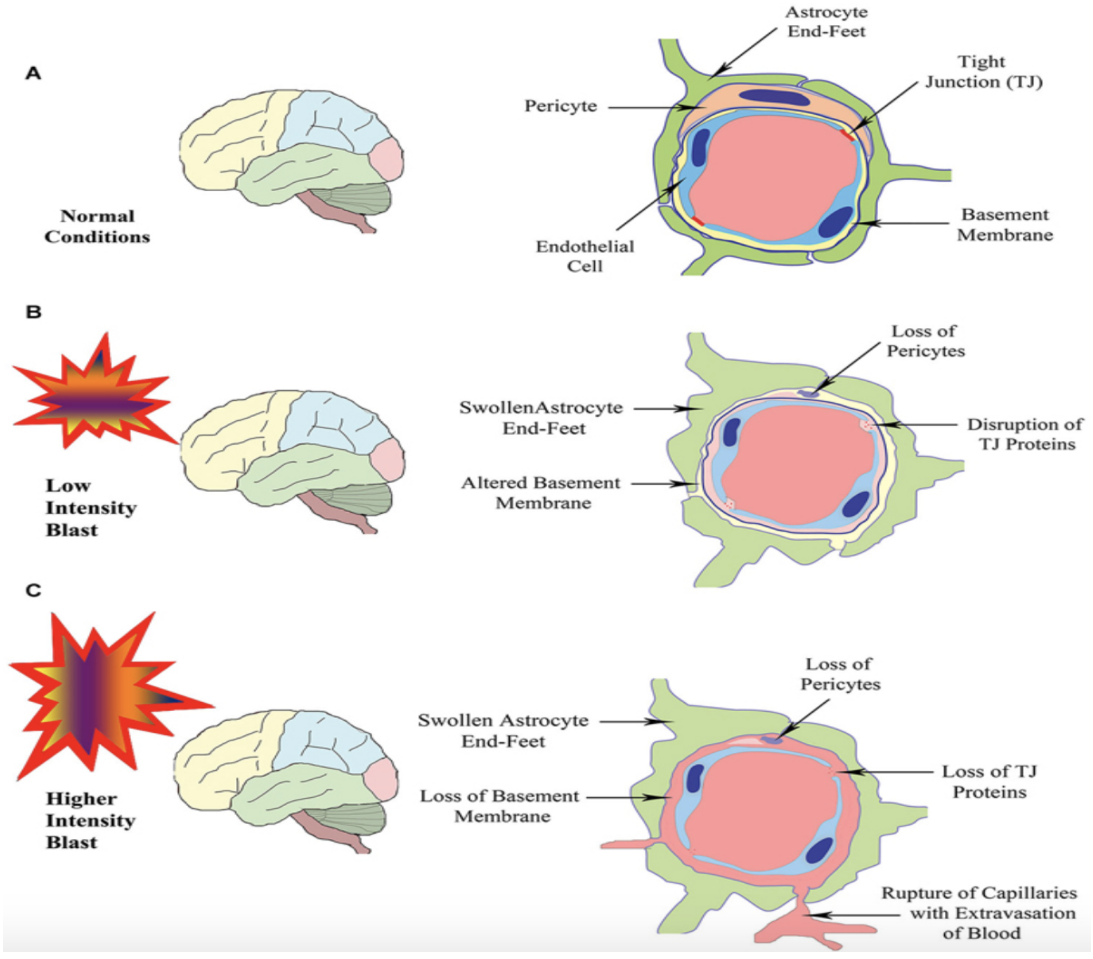


Figure 1.2. Schematic illustrating the structure of the BBB in normal conditions (A), and following exposure to BSWs of lower intensity (B) or higher intensity (C). Reproduced from ref. [24] Shetty, A. K., Mishra, V., Kodali, M., & Hattiangady, B. (2014). Corrigendum: Blood brain barrier dysfunction and delayed neurological deficits in mild traumatic brain injury induced by blast shock waves. *Frontiers in cellular neuroscience*, *8*, 404.

1.1.3.2 Epilepsy in numbers

Epilepsy is one of the most studied diseases worldwide because of its high incidence in the population and due to the drastic decrease in quality of life of those affected by the disease in its most severe form.

According to the World Health Organization (WHO), approximately 1% of the world population has epilepsy. It accounts for over 50 million people affected in which approximately one third do not respond to antiepileptic drugs. Furthermore, WHO estimates that 70% of people living with epilepsy could live seizure free if properly diagnosed and treated [10].

Thus, these numbers can be translated into the need of new techniques for detecting and monitoring imminent seizures which could enable prophylactic actions to the person living with the disease. As epilepsy is a disease that damages the central nervous system in each new seizure, detecting seizures is also extremely important to control the possible unfolding of the disease in its most severe form. In addition, preventive diagnosis for people who have suffered seizures once in their lives is extremely necessary as they are more susceptible to develop the disease.

1.1.3.3 miRNAs as biomarkers of epilepsy

For approximately ten years, miRNAs have been showing promising evidence as a possible biomarker of epilepsy [6]. This is due to three main factors: (1) studies of miRNAs as controllers of gene expression in the epileptic brain; (2) miRNA and its multi-targeting capability; (3) advances in the field of RNA-based therapeutics [11].

The initial correlation between miRNA and epilepsy arose in studies on genetic epilepsy. It was observed that gene mutations affected not only the crucial brain genes, but also their expression and consequently their regulation. Moreover, the events that triggered epileptogenesis have shown to disrupt global transcriptional and post-transcriptional regulatory function [11]. It was later observed that this conclusion also covered temporal lobe epilepsy, since miRNAs regulate approximately 30% of the entire human genome and, therefore, cellular processes involving neuronal death, gliosis and inflammation.

The multi-targeting ability of miRNA can be directly related to its wide range of genetic regulation. This causes a single miRNA to have many targets within a cell, impacting different

outcomes in the human body [8]. Therefore, this multi-targeting ability can impact repairing functions thereby leading to seizures, thus bringing an advantage or a challenge for the use of miRNA as biomarkers of the disease.

The advantage of multi-targeting presented by miRNAs occurs when a regulation of a single miRNA has the effect of interrupting several pathological processes simultaneously. On the other hand, the multi-targeting process can become a challenge, when a regulation of a disease-generating miRNA deregulates other important genes, causing the appearance of other disorders in a larger or smaller scale.

An intriguing example showcasing the beneficial potential of multi-targeting miRNAs is presented in a study conducted by Jimenez-Mateos *et al.* [12]. This research delved into a mouse model of focal-onset status epilepticus, where it explored the relationship between the expression of the P2X7R gene and the levels of miRNA-22. The investigation encompassed both the damaged, ipsilateral hippocampus, and the intact, contralateral hippocampus, drawing insightful comparisons.

Specifically, the authors divided their work into three phases. An overview of the pertinent findings from these phases is illustrated in Figure 1.3. Initially, a group of 6 mice were induced to status epilepticus by the addition of an intra-amygdala microinjection of kainic acid. Then, it was observed that prolonged seizures were confined to the ipsilateral hippocampus of the brain while the contralateral hippocampus was spared of damage. Herein this unilateral feature, occurred a reduction of functional responses from P2X7R in the contralateral hippocampus and a possible correlation between the suppression of this gene by microRNAs and the preservation of that part of the brain was hypothesized. In order to test whether P2rx7 mRNA was targeted to the RISC, Ago2 from mice hippocampus was immunoprecipitated and a 4 fold increase of RISC-loaded P2rx7 mRNA was detected in the contralateral hippocampus of the brain 8 h after status epilepticus. In addition, analysis of RISC-loaded microRNAs confirmed a 6-fold increase of miRNA-22 levels in Ago2-eluted samples in the contralateral part of the brain 8 h after status epilepticus, thus leading to the conclusion that P2X7R was a target regulated by miRNA-22.

In order to confirm the effect of the up and down regulation of the microRNA-22 on P2X7R, in a second phase of the project, studies using an antagonist that had the function of blocking

miRNA-22 (Ant 22) were carried out. After that, a 2 μL of 0.5 nmol Ant 22 (sequence: CTTCAACTGGCAGCT) were injected into the lateral ventricle of 5 mice, resulting in a 65–70% reduction in miRNA-22 levels when compared to a scrambled sequence (Scr). Furthermore, it was noted that silencing miRNA-22 increased P2X7R markers of inflammation in the contralateral hippocampus. Compared to Scr mice, levels of Il-1β and another key inflammatory cytokine, TNFα, increased in 4-fold after status epilepticus in the contralateral hippocampus of Ant22-treated mice. Moreover, levels of c-Fos, Arc and P2X7R protein increased in 2, 0.55, and 1.2 fold (respectively) in the contralateral hippocampus of Ant22-treated epileptic mice, when compared to Scr mice. Therefore, the major pro-inflammatory and hyperexcitability effects of microRNA-22 silencing were only prevented in P2rx7 mice or by treatment with a specific P2X7R antagonist.

The third part of the project investigated whether over-expression of miRNA-22 would suppress P2X7R protein levels in the contralateral hippocampus and reduce spontaneous seizures. The injection of 2μL of 0.5 pmol of a miRNA-22 mimic (Mi22) after status epilepticus reduced the occurrence of spontaneous seizures during the first 4 days of epilepsy monitoring. However, later seizure rates (days 5–9) were similar to Scr mice, perhaps because of the transient ability of Mi22 to enhance hippocampal miRNA-22 levels.

This study successfully demonstrated that while epileptogenesis is typically governed by a set of miRNAs that target shared pathways, there is potential for a single miRNA to independently regulate this pathological process. Furthermore, the experimental data from this research elucidated the molecular mechanism through which an individual miRNA controls epileptic seizures.

However, it's important to note that although Jimenez-Mateos *et al.* [12] established a robust experimental model, the absence of validation studies, such as the calculation of receiver operating characteristic (ROC), prevents us from confirming the effectiveness of miRNA-22 as a reliable biomarker.

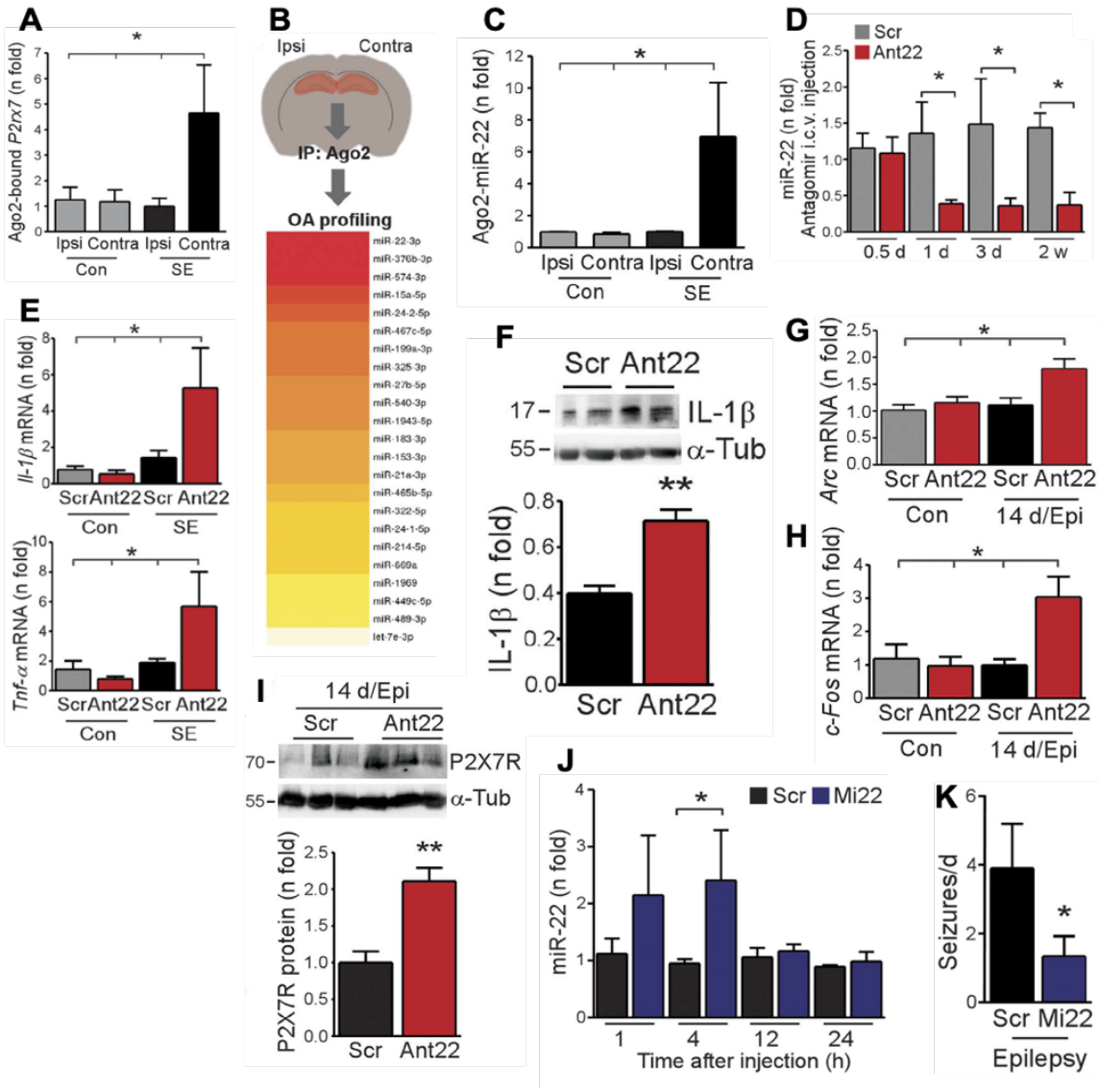


Figure 1.3 . (A) qPCR analysis of Ago2-eluted P2rx7 mRNA, 8 h after SE (n = 5/group). (B) RISC profiling. Heat map lists miRNAs in order of abundance in the Contra hippocampus. (C) qPCR analysis of miRNA-22 from pulldowns 8h after SE (n = 6; each sample was a pool of 2 hippocampi). (D) Graph showing temporal course of miRNA-22 down-regulation in hippocampal tissue after Ant22 i.c.v. injection (d, day; w, week; n = 4/group). (E) Graphs show transcript levels of proinflammatory cytokines are elevated in the contralateral hippocampus of Ant22 treated mice at 12 h after SE (n = 5 – 6/group). (F) Western blot (n = 1/lane) and graph show increased IL-1β in the contralateral hippocampus of Ant22 mice 12 h after SE (n = 4/group). *p < 0.05; **p < 0.01 compared to indicated group/control. (G,H) Increased Arc and c-Fos in the contralateral hippocampus of epileptic Ant22 mice at the end of recordings compared to epileptic Scr mice and non-kainic acid controls (n = 11 (Ant22 Cont), 12 (Scr Cont), 16 (Ant22 SE) 13 (Scr SE). (I) Immunoblot (n = 1/lane) and corresponding graph showing increased P2X7R levels in the contralateral hippocampus of epileptic Ant22-treated mice when compared to epileptic Scr mice at the end of epilepsy monitoring (n = 4–5/group). (J) Time course showing injection of 0.5 pmol Mi22 results in a transient increase in miR-22 levels in the hippocampus (n = 4–7/group). (K) Mi22 treated mice (Mi22; 0.5 pmol injected at 1, 8 and 24 h post-SE) show reduced spontaneous seizures during the first 4 days after status epilepticus (n = 7/group). *p < 0.05; **p < 0.01; ***p < 0.001 compared to indicated group/control. Adapted from ref. [12] Jimenez-Mateos, E. M., Arribas-Blazquez, M., Sanz-Rodriguez, A., Concannon, C., Olivos-Ore, L. A., Reschke, C. R., Mooney, C. M., Mooney, C., Lugara, E., Morgan, J., Langa, E., Jimenez-Pacheco, A., Silva, L. F., Mesuret, G.,

Boison, D., Miras-Portugal, M. T., Letavic, M., Artalejo, A. R., Bhattacharya, A., Diaz-Hernandez, M., Engel, T. (2015). microRNA targeting of the P2X7 purinoceptor opposes a contralateral epileptogenic focus in the hippocampus. *Scientific reports*, *5*, 17486.

1.1.3.4 Circulating microRNAs

Currently, most studies found in the literature explore microRNAs as biomarkers of epilepsy in brain tissue of humans and animals. However, with new knowledge about the possible mechanisms that permeate epileptic seizures and with the amplification of knowledge about the intrinsic properties of microRNAs, questions, and investigations about the presence of cerebral miRNAs circulating in the blood began to arise.

Based on the assumption that an external brain trauma will result in the direct physical injury of the brain parenchyma (disruption of the BBB), it is possible to comprehend the presence of cerebral microRNAs in the blood since BBB rupture will generate a lytic release of the microRNAs in circulation. Furthermore, the possibility of binding microRNAs to proteins or encapsulating them in microvesicles generates high stability to these small molecules in extracellular medium, justifying their presence at the most diverse environments (e.g. plasma, serum and CSF), varying pH (acid or base) and a wide variation in temperature [13].

In 2010, Liu et al. [14] published groundbreaking research on circulating microRNAs, marking the inception of studies exploring the relationship between various brain injuries associated with epilepsy and alterations in blood miRNA levels in rats. This pioneering work was the first to establish a correlation between miRNA profiles in both the blood and the brain. In this study, they examined groups of 6 rats each (totalling 48 rats) subjected to sham surgeries, ischemic strokes, brain hemorrhage (including lysed blood, fresh blood, or thrombin-induced), or kainate-induced seizures, comparing them to healthy control rats. After 24 hours, total RNA, including miRNA, was extracted from both the brain and blood samples, and miRNA expression patterns were analysed using TaqMan. Rodent miRNA arrays were employed, with fold-change criteria applied to identify miRNAs exhibiting more than a 1.5- or 2-fold regulation.

Figure 1.4 displays Venn diagrams illustrating the numbers of miRNAs that were upregulated or downregulated by more than twofold in both the brain and blood 24 hours after brain ischemia, brain hemorrhage (LB, lysed blood), and kainate-induced seizures (status

epilepticus), in comparison to control samples. Notably, the figure also highlights a common set of miRNAs that have the potential to serve as biomarkers for epileptogenic brain injuries. Liu et al. [14] reported that 45 miRNAs exhibited significant regulation, exceeding 1.5-fold, in both brain and blood following each type of brain injury ($p < 0.05$). Furthermore, miRNA-155 and miRNA-362-3p were consistently downregulated by more than 2-fold in both brain and blood across all experimental conditions, while miRNA-298 exhibited consistent upregulation of more than 2-fold in both the brain and blood across all pathologies.

In the research conducted by Liu *et al.* [14], it's important to note that they did not include additional studies to assess sensitivity and selectivity. Furthermore, despite the limited sample size used to measure miRNAs, this study holds significant importance in establishing foundational knowledge for future investigations regarding the potential use of blood miRNAs as biomarkers for epileptogenic injuries.

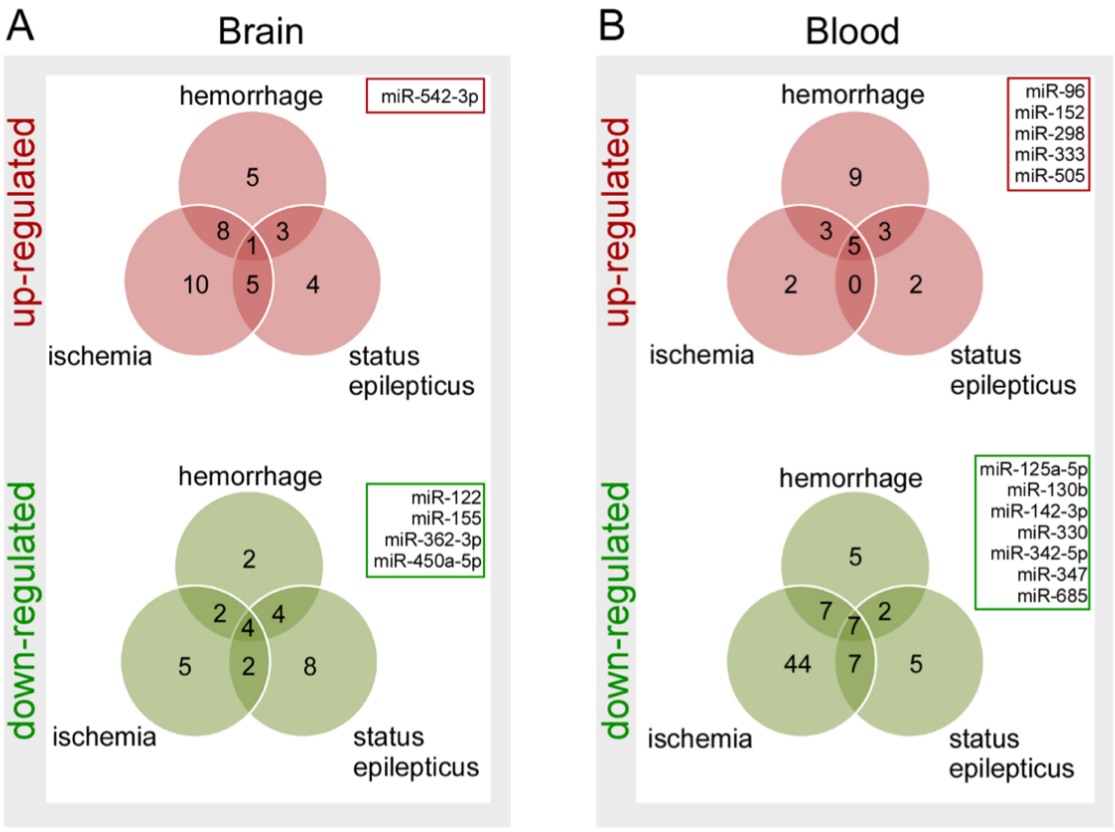


Figure 1.4. Conserved brain and blood miRNA responses following epileptogenic brain injuries (A) Profiling data show unique as well as common up- and down-regulated miRNAs 24 h after different epileptogenic insults to the brain. (B) Blood profiling data show each insult produces unique as well as shared miRNA expression responses in blood suggesting a set of common miRNAs that could represent biomarkers of epileptogenic brain injury. Boxes list the conserved miRNAs. Note, -3p and -5p denote

mature miRNAs that originate from opposite arms of the same miRNAs. Adapted from ref. [14] Liu, D. Z., Tian, Y., Ander, B. P., Xu, H., Stamova, B. S., Zhan, X., Turner, R. J., Jickling, G., & Sharp, F. R. (2010). Brain and blood microRNA expression profiling of ischemic stroke, intracerebral hemorrhage, and kainate seizures. *Journal of cerebral blood flow and metabolism*, *30*(1), 92–101.

A study conducted by Avansini *et al.* [15] was presented as one of the trailblazers in the investigation of miRNAs linked to epilepsy in human plasma. In this study, three different microRNAs (miRNA-134, miRNA-31 and miRNA-23a) formerly associated with different types of epilepsy, such as mesial temporal lobe epilepsy (mTLE), focal cortical dysplasia (FCD) and temporal lobe epilepsy were investigated for a possible correlation between aetiology and changes in plasma levels of microRNA. Thus, RNA isolated from plasma was obtained through quantitative real-time PCR in 14 patients with mTLE, 13 with FCD type II and 16 controls.

As miRNA-134 was the only microRNA that was shown to be downregulated in plasma when compared to controls ($p = 0.018$ versus $p = 1$ for miRNA-23 a and miRNA-31), validation studies followed only with this small class of molecules. The validation cohort was constituted from an independent group of 65 patients with mTLE and 83 controls. Results show that plasma levels of microRNA-134 could discriminate patients with mTLE from control individuals with an AUC of 0.75 with acceptable sensitivity (65%) and specificity (75%).

Complementary studies on the robustness of miRNA-134 and its ability to identify patients with mTLE independent of specific clinical characteristics, including response to treatment with AEDs, were performed. An independent cohort of 65 patients with mTLE was evaluated, in which 27 mTLE patients were responsive to pharmacotherapy, 38 patients were pharmacoresistant and 83 were controls. It was found that miRNA-134 was downregulated in patients with AED-responsive mTLE ($p = 0.0026$) and AED-resistant mTLE ($p = 0.044$) when compared to control subjects. Therefore, miRNA-134 was considered capable of identifying patients with mTLE regardless of their response to pharmacotherapy or the presence of MRI signs of hippocampal sclerosis, being an attractive diagnostic biomarker for mTLE.

The promising results found by Liu *et al.* [14] and Avancini *et al.* [15] encouraged further studies regarding levels of miRNAs in human biofluids. Table 1.1, presented below, is a

summary of the latest clinical studies on circulating miRNA cited in literature in terms of patients with temporal lobe epilepsy (TLE), mesial lobe epilepsy (mTLE) and focal dysplasia (CDF) [16].

Table 1.1. Clinical studies on blood miRNA biomarkers of epilepsy. Adapted from ref. [15] Avansini, S. H., de Sousa Lima, B. P., Secolin, R., Santos, M. L., Coan, A. C., Vieira, A. S., Torres, F. R., Carvalho, B. S., Alvim, M. K., Morita, M. E., Yasuda, C. L., Pimentel-Silva, L. R., Dogini, D. B., Rogerio, F., Cendes, F., & Lopes-Cendes, I. (2017). MicroRNA hsa-miR-134 is a circulating biomarker for mesial temporal lobe epilepsy. *PloS one*, *12*(4), e0173060..

miRNA	Biofluid	Patient type	No. of patients	Validation cohort?	ROC curve	Other findings	References
let-7d-5p	Serum	Mixed	n = 147	Yes	AUC = 0.79	No correlations found with clinical variables including seizure frequency	Wang, Yu *et al.* (2015)[17]
miRNA-106b-5p					AUC = 0.88		
miRNA-130a-3p					AUC = 0.78		
miRNA-146a-5p					AUC = 0.78		
miRNA-15a-5p					AUC = 0.84		
miRNA-301a-3p	Serum	Mixed	n = 218	Yes	AUC = 0.89	Serum miRNA-301a-3p correlated with seizure frequency (NHS3 score)	Wang, *Tan et al.* (2015)[18]
miRNA-4446-3p					AUC = 0.70		
miRNA-194-5p					AUC = 0.74		
miRNA-106b	Serum	Mixed	n = 90	No	AUC = 0.79	Correlated with seizure severity score	An *et al.* (2016)[19]
miRNA-129-2-3p	Plasma	TLE	n = 25	No	AUC = 0.78		Sun *et al.* (2016)[20]
miRNA-134-5p	Plasma	mTLE	n = 65	Yes	AUC = 0.67	Levels differed in drug-responsive and drug-resistant patients but no relation to seizure frequency	Avansini *et al.* (2017)[15]
miRNA-323a-5p	Plasma	FCD	n = 30	No	AUC = 0.74	Correlated with duration of epilepsy and seizure frequency	Che *et al.* (2017)[21]
miRNA-4521	Serum	FCD	n = 30	No	AUC = 0.72		Wang *et al.* (2016)[22]
miRNA-3613-5p	Plasma exosomes)	mTLE	n = 43	Yes	AUC = 0.84		Yan *et al.* (2017)[23]
miRNA-8071					AUC = 0.93		

-3p and -5p strands were not specified in some studies.

AUC, area under the curve; FCD, Focal cortical dysplasia; mTLE, mesial temporal lobe epilepsy; ROC, receiver operating characteristic.

1.1.3.5 Challenges among the use of miRNA as a theranostic molecule

1.1.3.5.1 Use of antagomirs or mimics to treat epilepsy

Although the use of mimics or antagomirs for the up or down-regulation of miRNAs presents as a potent antiseizure effect in the animal model, as illustrated in the work of Jimenez-Mateos *et al.* [12], it presents limitations to treat epilepsy when the subject of study changes to humans. Due to the size of their molecules, inhibitors (antagomirs) and mimics (mimic) of oligonucleotides are functional only in situations where the blood-brain barrier (BBB)is degraded [7]. Hence, a direct injection of antagomirs or mimics into the ventricle or the hippocampus would not be suitable for human patients, except if injections could be performed as an alternative to surgical resection of seizure foci.

1.1.3.5.2 Differences in microRNA expression levels

Evaluating studies presented by Liu *et al.* [14], Avansini et al. [15], Jimenez-Mateos *et al.* [12] among others mentioned here, it is possible to state that there are no standard values (range or fold changes) used to classify a microRNA as differentially expressed and, therefore, dysregulated. It is worth mentioning that, according to some authors, a change of two to three-fold [12], could be considered a moderate change that will not necessarily be successful in a clinical context. However, this gap in the literature of fixed values for the levels of biomarkers of disease is due to the heterogeneity of the pathology. Thus, it would be important that future research in therapeutics be conducted with dichotomous microRNAs or at least with microRNAs that are presented in the literature with "higher than the average" levels of expression.

1.1.3.6 Limitations in the currently detection system

1.1.3.6.1 The use of EEG

As demonstrated in the studies of Jimenez-Mateos *et al.* [12] and Avancini et al. [15] electroencephalography (EEG) recordings provide important support in the detection and diagnosis of neuronal diseases such as epilepsy. Despite this technique being considered a “gold standard”, and its intracranial and scalp detections in focal seizure have a good sensitivity (80- 98.8%) [8], the rates of misdiagnosis performed by this type of detection are considered high [15].

Another disadvantage presented by this technique is the use of complex parameters for detection (skull radius and specific electro-conductivity), in addition to being extremely invasive. Therefore, there is a clinical need for the development of new detection systems that could provide more accessible, faster, and non-invasive methods to theranostics.

1.1.3.6.2 qRT-PCR

qPCR is a powerful molecular biology technique used to analyze nucleic acid samples and quantify gene expression levels. To ensure the accuracy of qPCR results, it's essential to consider factors like PCR efficiency and normalization methods, as these can significantly impact the final outcome [24]. Additionally, incorporating intra- and inter-assay controls is vital to minimize technical variations in qPCR experiments.

Regardless of whether researchers are attempting relative or absolute quantification, constructing a standard curve is always necessary for accurate data analysis. This standard curve serves as a reference point for assessing target concentrations in the samples.

For the standardized and quality-controlled execution of qPCR experiments, researchers can rely on the MIQE (Minimum Information for Publication of Quantitative Real-Time PCR Experiments) guidelines [25]. These guidelines offer a systematic framework for designing, conducting, and reporting qPCR experiments, making them an invaluable resource for scientists working with this technique.

Here are several key reasons why adherence to the MIQE guidelines is fundamental for qPCR studies:

1. Enhancing Reproducibility and Reliability: A primary objective of the MIQE guidelines is to enhance the reproducibility and reliability of qPCR experiments. Factors such as variations in master mix components, the use of low reference dye concentrations, and amplifications with suboptimal efficiency (ideally between 90% - 110%) can introduce errors in Ct values, reducing confidence in distinguishing small differences in target concentrations [26]. By adopting a standardized approach, researchers can ensure consistent experiment execution, enabling other laboratories to replicate results more accurately [24].

2. Transparent Reporting: MIQE emphasizes the importance of transparent reporting of all experimental details. This includes comprehensive descriptions of experimental design, sample preparation, qPCR protocols, and data analysis. Such transparency allows other researchers to assess the study's validity and facilitates meaningful comparisons across different experiments.

3. Quality Control Measures: The MIQE guidelines advocate for stringent quality control measures at every stage of the qPCR workflow. Researchers are encouraged to provide detailed information about instrument calibration, assay validation, and the use of appropriate controls. These measures are essential for identifying and mitigating potential sources of error.

4. Proper Sample Handling and Preparation: MIQE offers specific recommendations for sample handling, including RNA extraction and storage. Ensuring the integrity of nucleic acids through proper sample preparation is a critical step in obtaining accurate qPCR results.

5. Assay Validation: Researchers are urged to perform comprehensive validation of their qPCR assays. This includes assessing primer specificity, amplification efficiency, and dynamic range. Robust assay validation ensures that the qPCR assays accurately represent the target of interest and reliably cover a range of concentrations.

6. Standardized Normalization and Data Analysis: MIQE guidelines underscore the importance of employing appropriate normalization strategies and data analysis methods. Researchers should detail how they normalize data and handle outliers or technical variations to draw valid conclusions from their qPCR experiments.

While real-time PCR is renowned for its high sensitivity, it is an advanced technique that involves the use of miRNA-specific fluorescent probes, making it relatively costly [27]. Consequently, qPCR may not be the most suitable choice for high-throughput analysis of numerous miRNAs. Alternative methods like next-generation sequencing may prove more cost-effective and efficient for such endeavours.

1.1.4 miRNA in Alzheimer's Disease

1.1.4.1 Definitions and Symptoms

Alzheimer's disease was first described in 1909 by the neurologist Alois Alzheimer as a neurodegenerative dysfunction that affects individuals silently, progressively, and irreparably. Among the symptoms caused by the disease are difficulty in maintaining a clear and objective communication, loss of memory, disorientation in time and space, impairment of abstract thinking, difficulty in learning, mood swings and difficulty in discerning and judging everyday actions [28].

As the symptoms of the disease appear particularly in senile people, with statistics pointing to 1 in 14 individuals over 65 years old and 1 in 4 individuals over 85 years old [29], for a long time it was thought that the disease was a neurological decline caused by age. Although the pathomechanism of the disease is not yet fully understood, it is known that nutritional factors, smoking, high blood pressure, diabetes, genetic inheritance, and sociological factors can help or even cause the onset of the disease.

A study performed by Lemche *et al.* [30] in rodents model showed that an epigenetic factor known by the term "early life stress (ELS)" can interact with the genome, altering the brain lipid metabolism, brain insulin resistance, myelin disintegration and causing neuro-inflammations that lead to AD-associated histopathology. Another study presented by the Norton *et al.* [31] points to a sedentary lifestyle as an aggravating factor of the disease. According to statistics, 1 in 3 cases can be avoided with simple changes in lifestyle, such as participation in sports.

Therefore, Alzheimer's disease is categorized according to pathological factors and time of neural decline (sporadic or continuous). The Early-stage Alzheimer's disease (or familial Alzheimer's disease) occurs when a person presents the symptoms of the disease sporadically, which adds to other health problems already described here (e.g. diabetes mellitus (type 1 and 2), obesity, hypercholesterolemia, metabolic syndrome). Late-onset Alzheimer's disease, on the other hand, is characterized by an irreversible neurodegeneration caused by neuroinflammation, mitochondrial impairment, synaptic dysfunction, oxidative stress, and disruption in the blood–brain barrier [32], thus raising Aβ-42 fragment levels and generating

an accumulation of neuronal hyperphosphorylated tau protein in intracellular neurofibrillary tangles (NFTs).

1.1.4.2 Detection of Alzheimer's disease: Currently methodologies and biomarkers of disease

Considered as a disease of stages, Alzheimer's disease (AD) presents itself long before its most abrupt symptoms, moving from the early-preclinical stage to mild cognitive impairment (MCI) and ending in dementia. Therefore, reports in the literature point to the gap between the early diagnosis of the disease and its recognition in an advanced state, as the biggest contributor to the failure of treatment of the disease [33]. The irreversibility of the disease, causing permanent cognitive damage, justifies the limitation of the impact of gene therapy, setting precedents for the need to implement therapies at early stages of the disease, as well as for effective detection of the disease at an early stage.

Among the methods used nowadays to the detection of Alzheimer's disease are the use of neuropsychological tests, neurological imaging of AD biomarkers and detection via cerebrospinal fluid (CSF) protein assays. Although accurate, disease monitoring using these techniques sometimes becomes costly, invasive, and inefficient. Evaluating the neuroimaging techniques as magnetic resonance imaging and fluorodeoxyglucose (FDG)–positron emission tomography (PET), despite having the advantage of visualizing brain abnormalities and atrophies, it is a time-consuming, costly, and complex technique [34]. Moreover, it can only be evaluated and performed by specialized professionals, limiting the possibility of clinical trials to be done in a large number of patients.

The detection of the biomarkers β-amyloid peptides ($A\beta_{1-40}$, $A\beta_{1-42}$), Tau proteins (t-tau) and/or phosphorylated tau (p-tau) protein in samples of cerebrospinal fluid, has a high specificity and sensitivity, but must be obtained through invasive and painful practices, such as lumbar puncture [35]. Consequently, this technique can be stated as impractical due not only the negative perception of patients who commonly refuse to undergo the procedure, but by the successive sampling needed to monitor the disease.

Neuropsychological tests, such as Mini-Mental State Examination (MMSE), are used as a cognitive test to assess the progression of Alzheimer's disease. Despite being validated as a

good standard of analysis, this method is a sum of many variables such as the patient's education level, familiarity with the test and access to the health system (due the need of continuous assessment of the patient) [35]. Therefore, the methodology has its specificity and sensitivity wildly limited to external factors, being considered by some researchers a method that achieves inaccurate results.

1.1.4.3 miRNAs as biomarkers of Alzheimer Disease

The interest in blood circulating biomarkers has grown in recent years due to the advantages of promoting a detection system in this medium. The blood collection, in addition to being less invasive, presents a simple and low-cost method, which can help in the scientific investigation of the mechanism of Alzheimer's disease by increasing the feasibility of analysis. Moreover, as previously mentioned at this work, circulating blood miRNAs are stable in cell-free environments and robust even under defrost cycles [36], presenting as excellent surrogate markers for AD.

To better understand the relation between expressed miRNA levels and Alzheimer's disease, we can cross-reference the complementary work of Hebert *et al.* [37] and Perreira *et al.* [38].

In the study performed by Hebert *et al.* [37] the increased expression of the enzyme BACE1(β-site amyloid precursor protein cleaving enzyme 1), as well as the regulation of APP (amyloid precursor proteins) in post-mortem brains of patients suffering from sporadic AD was examined. The investigation into the decline in the level of specific miRNAs (miRNA-29a, miRNA-29b-1, and miRNA -9) to the increased expression of BACE-1 was based in the role of this enzyme in cleaving proteins that contribute to the accumulation of neuritic platelets in the neuropil, the AD hallmark. Through *in vitro* analysis of functional assays the authors confirmed the specificity and contribution of miRNA-29 a/b-1 in modulating the action of the BACE-1 enzyme, as well as the mechanism of enzymatic action.

The assertiveness about the correlation of miRNA-29 a/b-1 and the possibility of regulation of BACE-1 presented by the modulation of the Aβ1-42 protein, can be confirmed by the evaluation in the work of Pereira *et al.* [38]. In this study, the validation of the action of miRNA was illustrated by the development of a technology capable of delivering the recombinant pre-miRNA-29b into the cytoplasm in vitro. Together, these results suggest insights into the pathology (AD), gene regulation pathways and miRNA levels present in the clinical samples

evaluated, as well as the levels of an enzyme responsible for the accumulation of a histological hallmark of the disease. Moreover, this study presents the development/ possibilities needed to successfully deliver a therapy based in miRNAs.

The treatment of Alzheimer's disease through circulating miRNAs becomes important due to the high level of specificity, precision, and sensitivity that these biomarkers promote to the detection system when combined with each other in analysis or combined with neuroimaging techniques. Reports in the literature [39, 40] have shown that the use of miRNA-based signatures, where there is a combination of one to two pairs of miRNAs, can generate discrimination between control and AD positive samples with an accuracy ranging from 75-82%, reaching a greater sensitivity and/or compatible with neuroimaging techniques.

A study about this relationship can be examined by evaluating the work of Sandau *et al.* [41]. A crossover between 17 microRNAs hypothesized as prodromal markers of AD in MCI and neurological tests considered consolidated standards for detection of the disease was performed. This study assumed that the main biomarker validated for detection of AD in asymptomatic phase is the Aβ1–42/Tau protein present in cerebrospinal fluid and that positron emission tomography (PET) is the neuroimaging technique fundamentally used to detect the accumulation of this protein. Among the miRNAs studied, five of these biomarkers (miRNA-142-3p, miRNA-146a-5p, miRNA-146b-5p, miRNA-193a-5p, miRNA-365 - 3p) were shown to be highly capable of differentiating cognitively normal controls from MCI and AD through their decreasing levels of expression. The detection of the selected miRNAs combined with the assessment of the levels of Aβ42:T-Tau, was also presented as an effective technique capable of exponentially improving the classification performance (relative to protein biomarkers alone) for MCI diagnosis.

Therefore, a significant benefit offered by miRNAs as a biomarker for Alzheimer's disease is the potential to utilize them as a prognostic indicator, aiding in the assessment of the disease's progression. As was already described in this work, the high level of amyloid beta protein ($A\beta_{1-40}$; $A\beta_{1-42}$) in the form of neuritic plaques are the standard requisition for the diagnosis of AD in neuroimaging techniques, however, this marker is incapable to represent the severity of the disease. The possibility to assess the onset of the disease by miRNAs could help the population in risk of acquiring it, to pursue treatments capable of slowing cognitive loss.

In a five-year longitudinal study, Kenny *et al.* [42] examined the correlation between miRNA-206 plasma levels and the rate of neurological decline from controls to mild cognitive impairment (MCI) to Alzheimer's disease. For a more complete assessment of the precedents that lead to the development of the disease, genetic, neurological, and neuropsychological data from the patients in the discovery cohort — of which comprised 31 AD negative patients and 30 patients with minimal cognitive impairment — and in the longitudinal cohort — formed by 18 patients with variable progression from AD negative to AD or MCI — were also evaluated in this work. The analyses performed in the longitudinal studies were collected at intervals of 1 to 2 years during the 5 years of studies, allowing to observe the rate of increase in miRNA-206 levels as the disease progressed. As described in the literature, miRNA-206 regulates memory by targeting brain-derived neurotrophic factor (BDNF), so the elevation of this miRNA concomitantly with the decrease of this protein in individuals with AD justifies the observed pathomechanism of the disease, characterized by synaptic loss and cell death. Therefore, over this work, miRNA-206 has been shown as a highly potential predictor of the different stages that predispose to Alzheimer's disease.

1.1.5 Limitations and challenges among the use of miRNAs as a neurodegenerative biomarker

As any other emerging class, miRNAs present gaps and challenges needed to overcome before its implementation as an extremely reliable biomarker to predict epilepsy and/or Alzheimer disease. The lack of standardization in the methodology applied to selected cohort groups for clinical trials, in the usage of controls references, the miRNA extraction/ isolation procedures, the source of sample collection (CSF, plasma, serum), the diverse quantification techniques and statistical protocols [43] are some of the factors indicated as responsible for the reproducibility issue that arises among performed studies. The absence of consolidated standard protocols to detect miRNAs related to Alzheimer’s disease generates small experimental modifications and, consequently, generates results that cannot be compared. This makes the detection limit of the biosensor, to become dependent on the nature of the fluid and the processing pattern.

The confounding element between analyses is generated not only by the profiling miRNA that exists in each type of sample, but also, the actual levels of the molecule present in each environment. When comparing biofluids to neural exosomes, for example, the last one can be directly transported from the blood-brain barrier to CSF, while in biofluids, the mature

miRNAs need to be initially absorbed into microvesicles- in a path of specific membrane proteins- before being released to the medium [33,34]. The type (active or passive) of miRNAs transportation gathered with the stability of this molecule in the proposed environment brings the higher difference in the expressed levels. Therefore, some studies [44,45] suggest that a well-planned choice of sample is the key to guarantee a better quality and diagnostic efficiency to the biomarker during all the pathological states.

Regarding the profiling miRNAs, the issue is generated by the sequences being highly homologous to members of their family e.g. proteins and among other nucleic acids. Thus, one of the detection challenges is the ability of the biosensor to quantify the miRNAs present in the sample without interference from molecules similar to the target.

Another critical factor that impacts the accurate diagnosis of neurodegeneration is associated with the multi-targeting properties of miRNAs. Since a unique miRNA can regulate different targets (different proteins), the prediction of which target is directly related to epilepsy not only becomes arduous, but it also creates issues of misdiagnosis. Furthermore, this property makes the off-target effect difficult to avoid and, therefore, can bring unforeseen effects to the use of miRNAs in therapies. However, this multi-targeting challenge can be overcome by the development of multi-analyte detection platforms. In this type of platform, more than one microRNA could be detected, as well as different proteins related to the disease under study, thus bringing greater specificity in theranosis.

So, in conclusion, during the analyses provided by the scope of this literature review, one can assume that the usage of miRNAs as biomarkers of disease goes beyond the monitoring and detection of AD or epilepsy, it can also be used as an important tool in clinical trials. The feasibility of screen a large population suffering from the disease by the construction of a non-invasive, sample- to- answer electrochemical device, derived from blood circulating miRNAs would permit an incredible progress over the knowledge of the pathomechanism of the disease, directly improving the possibility of treatment of patients at early stage of the disease, as well as enhance the percentage of clinic trials for the search of a cure.

1.2 Electrochemical Biosensors for miRNA Detection: Revealing Their Competitive Edge

This section briefly delves into the unique attributes, key formats, bioreceptors, electrode substrates, and underlying electrochemical techniques highlighting the effectiveness of electrochemical biosensors in miRNA detection.

1.2.1 Electrochemical Techniques vs. Traditional Analysis

In the field of biomolecular analysis, electrochemical biosensors have emerged as powerful tools for the sensitive and specific determination of miRNAs, offering several distinct advantages over traditional techniques such as PCR-based assays and microarray methods, In general these advantages encompass [46][47][48]:

1. **High Sensitivity:** Electrochemical biosensors exhibit exceptional sensitivity, enabling the detection of miRNAs at ultralow concentrations. This attribute is critical when dealing with trace amounts of miRNAs in complex biological samples.

2. **Selectivity:** These biosensors offer outstanding selectivity, distinguishing between closely related miRNA sequences and differentiating them from other interfering species present in the sample. This selectivity is vital for precise miRNA profiling.

3. **Real-time Monitoring:** Electrochemical biosensors enable real-time monitoring of miRNA levels, providing dynamic insights into miRNA expression changes over time. This feature is particularly valuable for studying dynamic biological processes and disease progression.

4. **Cost-effectiveness:** Compared to traditional methods like PCR-based assays or microarray techniques, electrochemical biosensors often require fewer reagents and have lower operational costs, making them an economically viable choice for routine analysis.

5. **Portability:** Many electrochemical biosensors are compact and portable, facilitating their use in point-of-care diagnostics and field applications where immediate results are essential.

1.2.2 Using Electrochemical Biosensors as an Alternative to Optical-Based Methods

While optical biosensors have been extensively utilized for DNA or miRNA hybridization detection, there are compelling reasons to consider electrochemical biosensors as an alternative for such applications.

One significant drawback of optical methods is the complexity associated with designing dyes for labelling, which necessitates an additional synthetic step. Moreover, integrating a light source in point-of-care devices makes optical methods costlier and less physically robust [49].

In contrast, electrochemical biosensors offer environmental insensitivity due to their use of electroactive labels and exhibit remarkable versatility, making them applicable across a wide spectrum of fields, including healthcare, environmental monitoring, and food safety [46]. Additionally, biosensors have been strategically designed to achieve high selectivity through the inherent properties of the immobilized bio-components [49]. The biological recognition element attached to the transducer surface selectively interacts with the target analyte within a complex sample matrix, eliminating the need for pre-concentration steps. This means that oligonucleotide-based biosensors can offer simplicity and cost-effectiveness while delivering rapid and accurate results.

1.2.3 Electrochemical biosensors: Main formats

Electrochemical biosensors for miRNA detection come in various formats, each tailored to specific applications:

1. **Label-Free Sensors:** These sensors directly detect miRNAs without the need for labelled probes, simplifying the assay and reducing costs. This approach demands careful consideration of parameters responsible for the binding event generating the signal-to-noise ratio [50]. Optimization of the transducer platform plays a pivotal role in this regard.

2. **Enzyme-Based Sensors:** Enzymes are employed to amplify the electrochemical signal, enhancing sensitivity and allowing for the detection of miRNAs at lower concentrations. A prime example of this technique involves the utilization of horseradish peroxidase [51][52], showcasing the power of enzymatic enhancement..

3. **Nanomaterial-Based Sensors:** Nano-sized metals possess unique advantages, including enhanced mass transport, high effective surface area, and size-controlled electrical, chemical, and optical properties [53]. Hence, transition metals can be used due to their catalytic properties, as they can adsorb other substances onto their surface and activate them in various processes to improve the surface-to-volume ratio of the biosensor surface. Integration of nanomaterials, such as gold nanoparticles or carbon nanotubes, enhances the sensor's surface area, conductivity, and binding efficiency, improving both sensitivity and selectivity [54]. A more detailed explanation of this system can be found in Section 1.2.7.

1.2.4 Bioreceptors

Bioreceptors are essential components of electrochemical biosensors, responsible for the specific recognition and binding of miRNAs. Common bioreceptors used in miRNA detection include [46] :

1. **DNA Probes:** Single-stranded DNA probes that complementarily bind to target miRNA sequences.
2. **RNA Probes:** Similar to DNA probes, RNA probes are employed for specific binding to miRNAs.
3. **Aptamers:** Short single-stranded DNA or RNA sequences selected for their high affinity and specificity to miRNAs.
4. **Enzymes:** Enzymes can act as bioreceptors when they catalyse reactions involving miRNAs, amplifying the electrochemical signal.

1.2.5 Electrode Substrates

Electrode materials play a pivotal role in the performance of electrochemical biosensors. Common electrode substrates for miRNA detection include:

1.2.5.1 Gold Electrodes

Gold electrodes serve as excellent substrates for miRNA biosensors, offering a multitude of advantages that have made them a preferred choice in electrochemical biosensor applications. These advantages include [46][55]:

1. **High Conductivity:** Gold electrodes have excellent electrical conductivity, allowing for efficient electron transfer during redox reactions. This high conductivity is crucial for achieving sensitive and rapid electrochemical measurements of miRNAs.

2. **Biocompatibility:** Gold is inherently biocompatible and does not react with many biological molecules. This property makes it ideal for immobilizing biomolecules like DNA probes or antibodies used in miRNA detection, ensuring minimal interference with the biological components of the sample.

3. **Stability:** Gold electrodes are known for their stability and resistance to corrosion, which is essential for maintaining the integrity and longevity of the biosensor during repeated use.

4. **Ease of Functionalization:** Gold surfaces are easily functionalized with various molecules, making it straightforward to attach capture probes or recognition elements specific to miRNAs. This functionalization versatility enhances the specificity and sensitivity of the biosensor.

5. **Signal Amplification:** Gold electrodes can be used in conjunction with signal amplification strategies, such as gold nanoparticles or enzymatic amplification, to enhance the electrochemical signal generated upon miRNA binding. This amplification increases the sensitivity of the biosensor, allowing for the detection of low concentrations of miRNAs.

6. **Low Background Current:** Gold electrodes typically exhibit low background current levels, reducing noise in electrochemical measurements and improving the signal-to-noise ratio, leading to better detection limits.

7. **Compatibility with Miniaturization:** Gold electrodes can be easily integrated into microfluidic or lab-on-a-chip devices, making them suitable for miniaturized biosensor platforms. This miniaturization enables point-of-care and on-site miRNA analysis.

8. **Wide Applicability:** Gold electrodes are versatile and can be adapted for use in various electrochemical techniques, including cyclic voltammetry, amperometry, impedance spectroscopy, and more, depending on the specific requirements of the miRNA biosensor.

1.2.5.2 Carbon-Based Electrodes

Carbon-based materials, such as glassy carbon electrodes and screen-printed carbon electrodes (SPCEs), provide versatility and affordability in biosensing. Notably, SPCEs offer distinct advantages over traditional platforms for miRNA detection. Apart from their cost-effectiveness and biocompatibility, SPCEs are disposable, possess low toxicity, can be tailored to meet end-users' specific requirements, and enable miniaturization [56]. Miniaturization involves downsizing the electrode, reducing sample and reagent volumes in production, and facilitating potential integration into compact or handheld devices. While the conductivity and electron transfer properties of SPCEs may not match those of traditional electrodes, their surfaces remain customizable to address precise analytical needs, and their cost-effectiveness allows for large-scale testing.

1.2.6 Electrochemical Techniques

Various electrochemical techniques are employed for miRNA detection, including Electrochemical Impedance Spectroscopy (EIS), Cyclic Voltammetry (CV), and Amperometry. Since amperometry and impedance are the most studied techniques in the field of nucleic acid biosensors, a brief description of how these detection models function is provided herein.

1.2.6.1 Electrochemical Impedance Spectroscopy (EIS)

The alterations in surface properties can be effectively detected by monitoring the changes in electrical resistance and capacitance, which, in turn, serve as sensitive markers for oligonucleotide hybridization detection [57]. Hence, AC impedance analysis, conducted using

a potentiostat, is a tool to understand how an electrical system responds to tiny, alternating electric signals at different frequencies. Overall, the impedance between the miRNA layer and an outer-sphere redox probe can be valuable for understanding the electrical behaviour of the system.

1.2.6.2 Amperometry

In amperometric biosensors, the current generated due to miRNA-induced reactions is measured, allowing for quantitative detection. Amperometry is an electrochemical technique used to measure the current flowing through an electrochemical cell or electrode as a result of a redox (oxidation-reduction) reaction [58]. It is commonly used for the quantitative analysis of analytes in various fields. The process involves applying a constant potential to the working electrode, which results in a measurable current proportional to the concentration of the analyte.

In summary**,** electrochemical biosensors for miRNA determination offer a compelling array of advantages, including high sensitivity, selectivity, real-time monitoring, cost-effectiveness, and portability. With diverse formats, bioreceptors, electrode substrates, and electrochemical techniques at their disposal, these biosensors are poised to revolutionize the field of miRNA analysis, enabling a deeper understanding of biological processes and facilitating early diagnosis in clinical settings.

1.2.7 Use of the nanomaterials in biosensing: Overview

RNAs, e.g., miRNAs, t-RNA and m-RNA, present in the blood are useful for diagnosis and monitoring of neurological diseases. However, detecting circulating miRNAs can be a challenge due to their low concentration inside the cells (e.g. femtomolar to picomolar levels) [13] and, therefore, improving the sensitivity of the miRNA assay platform is highly important.

One of the most common methods to amplify the signal of miRNAs assays, is through RT-qPCR, which increases the concentration of the target. Despite being a "gold standard" technique, the long processing time and costly probes, which often suffer from high and variable background noise [13], makes the technique unsuitable for screening a large population suffering from neurological disease.

One approach is to use functional nanomaterials to enhance the sensitivity and specificity of biosensors. The signal amplification and reduction of the detection limit provided by nanomaterials may occur due to its direct contact with the sensing area of the electrode, boosting the signal transduction [59] or, excellent catalytic ability.

Among the many advantages that the use of nanomaterials offers, its small size (from 100 nm to 10 nm) which leads to a high surface area to volume ratio and its easily mouldable and flexible structure which enables miniaturization of diagnostic platforms, leading to small, inexpensive, portable, and low-cost tools in point-of-care diagnostics [59]. In addition, these materials have significant advantages in the diagnosis of diseases due to their optical and electrochemical properties, their low toxicity, their favourable biocompatibility, their large surface-to-volume ratio and their super- paramagnetic behaviour [60].

Therefore, the unique characteristics of nanomaterials bring many functions to electrochemical sensing applications, which can be classified according to their *modus operandi*, such as: (i) enhancement of electron transfer by directly increasing the surface area; (ii) acting directly as a redox couple; (iii) acting indirectly through catalysis; (iv) acting indirectly by attaching to multiple redox couples or enzymes, and (v) acting to concentrate samples [13].

1.2.8 Nanoparticles for catalytic signal amplification

The most used nanomaterials in amplified electrochemical miRNA bioassays include metallic / magnetic nanoparticles, carbon-based nanostructures, quantum dots and nanostructured electrodes [59]. Among these nanomaterials, noble metal nanoparticles are widely used for the electrocatalytic detection of nucleic acid biomarkers since, together with its intrinsic catalytic activity and optimal characteristic of the material (e.g. rapid mass transport, facilitated electron transfer, high surface area) it is easy to synthetise, to characterize and functionalize onto the surface [61].

Metal nanoparticles can be used to amplify the detection of nucleic acids, such as DNA and miRNA, through enhanced reduction of hydrogen peroxide [62]. More specifically, the noble metal nanoparticles, which are labelled with a nucleic acid probe complementary to the target, electro-catalyse the reduction of hydrogen peroxide producing a signal proportional to the quantity of nanoparticles present in the reaction and consequently the amount of target present.

The nanoparticles act as ultramicroelectrodes that perform the electrocatalysis of a substrate to produce an electrochemical signal, as long as they are close to the electrode surface to allow an efficient transfer of electrons [62]. Therefore, through the complementary binding of the nucleic acid probe with the target, the nanoparticles approach the electrode surface, and the reduction of hydrogen peroxide can be quantified.

One example of a nanomaterial which displays an efficient catalytic property towards hydrogen peroxide reduction, was explored in the work of Dong *et al.* [63]. In this project, the detection of a miRNA was done through the development of a simple, sensitive, selective and label-free method, where DNA encapsulated silver nanoclusters (Ag-NCs) were used as an electrocatalytic reporter-probe. A miRNA sandwich assay was developed on a gold electrode, where the immobilized capture-probe was a molecular beacon, in the form of a hairpin probe, selective to the target. When the target and the functional reporter-probe hybridise, the AgNCs nanoclusters were brought close to the electrode surface. Then, the electrochemical signal correlated to H_2O_2 reduction was observed. Figure 1.5 depicts the DPD response of the sensor across a miRNA target concentration range from 10 fM to 100 nM. The limit of detection was found to be 67 fM, exhibiting a linear current-concentration relationship within the range of 100 fM to 10 nM and amplifying the electrochemical signal in direct proportion to the target concentration. Furthermore, the method's selectivity was assessed by comparing the biosensor's performance with three types of miRNA sequences, including a complementary target, a single-base mismatched strand, and a three-base mismatched strand (refer to Figure 1.6) The biosensor exhibited remarkable selectivity and high sequence specificity, successfully discriminating a perfect complementary target with a current approximately four times higher than that of a single-base mismatched sequence.

This work was therefore a pioneering study demonstrating the synergistic effect of the intrinsic properties of functional nanomaterials (e.g., catalytic activity, conductivity, and biocompatibility) as being responsible for increasing the sensitivity and amplification of the miRNA signal. Although this biosensor is highly sensitive, it is presented only as a proof-of-concept demonstration since no study on the detection of circulating miRNA of blood from humans or animals has been carried out. Consequently, there was no validation of the performance, especially in terms of selectivity, of the electrode in this medium. Hence, additional studies on the interaction of proteins (e.g., BSA) that are commonly present in biofluids and can compete with the target would provide a better assessment over the selectivity

of the sensor. Therefore, this biosensor presents itself as highly dependent on laboratory-based setup and is far from being suitable for point-of-care analysis.

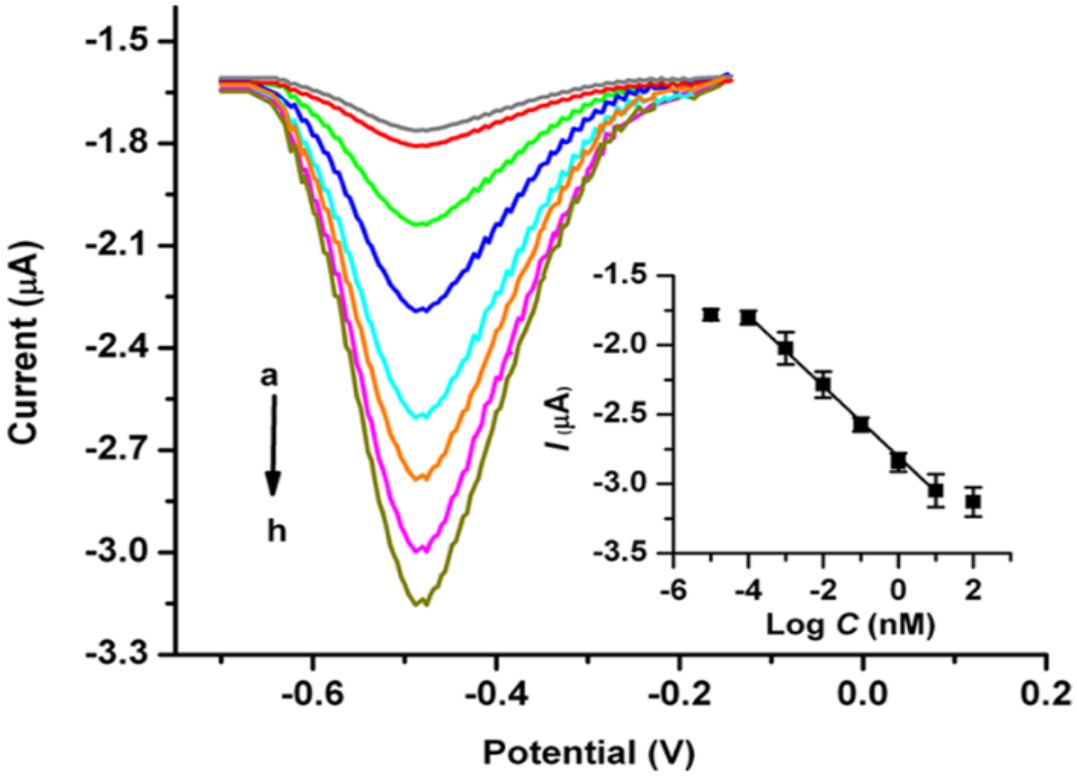


Figure 1.5. DPV curves of silver-nanoclusters modified Au electrodes in N_2- saturated PBS (100 mM, pH 7.0) containing H_2O_2 (3 mM) at 10 fM, 100 fM, 1 pM, 10 pM, 100 pM, 1 nM, 10 nM, and 100 nM target miRNA (from a to h). Inset: plot of the peak current versus the logarithm of target concentration. Reproduced from ref. [63] Dong, H., Jin, S., Ju, H., Hao, K., Xu, L. P., Lu, H., & Zhang, X. (2012). Trace and label-free microRNA detection using oligonucleotide encapsulated silver nanoclusters as probes. *Analytical chemistry*, *84*(20), 8670–8674.

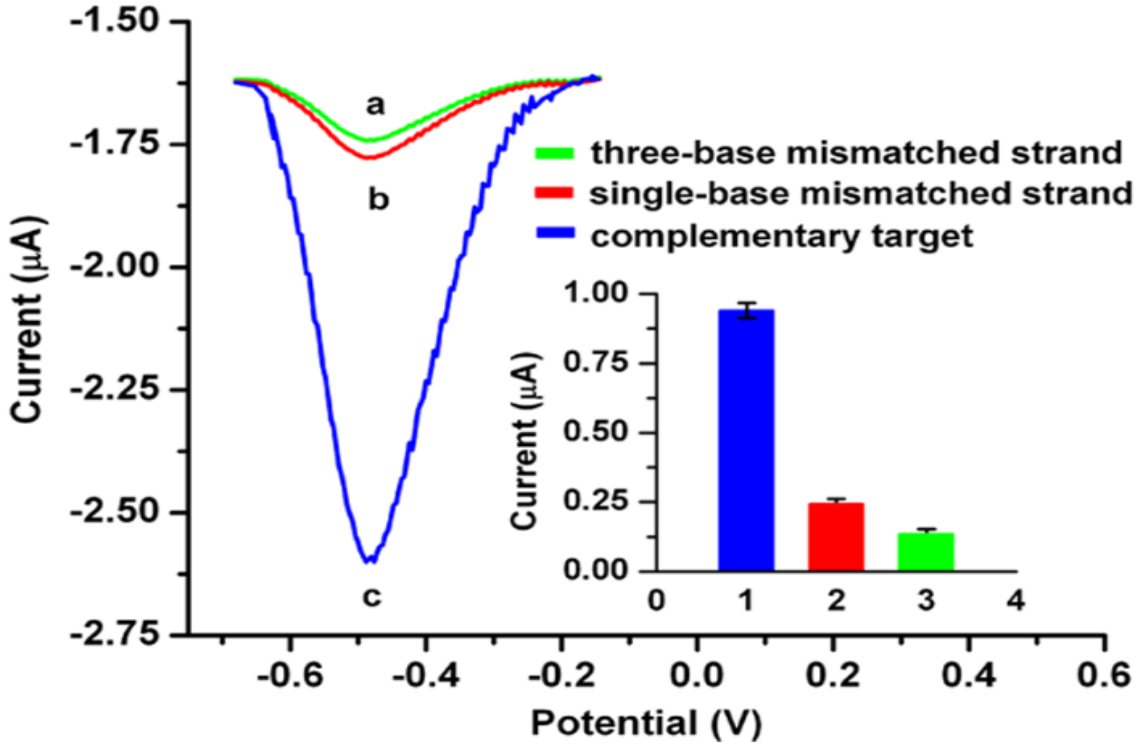


Figure 1.6. DPV curves of Ag-NCs modified Au electrodes in N_2- saturated PBS (100 mM, pH 7.0) containing H_2O_2 (3 mM) for detection of 100 pM complementary target, single-base mismatched strand, and three-base mismatched strand. Inset shows the corresponding peak currents. Reproduced from ref. [63] Dong, H., Jin, S., Ju, H., Hao, K., Xu, L. P., Lu, H., & Zhang, X. (2012). Trace and label-free microRNA detection using oligonucleotide encapsulated silver nanoclusters as probes. *Analytical chemistry*, *84*(20), 8670–8674.

Figure 1.7 shows a similar strategy developed by Spain *et al.* [64], where platinum nanoparticles (PtNPs) were decorated with reporter-probe strand nucleic acid in a region selective manner and used for the detection and monitoring of miRNA-134 towards the reduction of hydrogen peroxide in undiluted patient serum and clean buffer. In this work, two different gold electrode (GE) platforms were needed. In the first GE electrode, which was already immobilized within self-assembled monolayers of dodecanethiol, the platinum nanoparticles were produced by electrodeposition using the nanoscale defects of the monolayer as templates. Subsequently, PtNPs were functionalized with a thiolate reporter- probe oligo and desorbed by the application of a reductive current. Further, in the second electrode, a sandwich assay was constructed by the immobilization of oligonucleotide capture-probe strand to the gold surface, followed by the hybridization of the target miRNA-134 and hybridization

with the nanoparticle labelled probe miRNA sequence. The modified electrode was placed in a solution with hydrogen peroxide and the signal responsive to its reduction was measured.

Figure 1.8 presents the chronoamperometric response of the biosensor (Δi) both before and after addition of hydrogen peroxide, showcasing the behaviour of the fully complementary sandwich assay when hybridized at different miRNA target concentrations ranging from 1 aM to 1 μM. The current presented to be proportional to the logarithm of the [miRNA $_{target}$], with a remarkably low limit of detection of 0.0263 aM. In addition, the sensitivity of the electrochemical sensor in detecting miRNA-134 in human plasma samples was compared to standard Taqman PCR-based measurement. Notably, the measurement of miRNA-134 in the same set of samples collected from both healthy volunteers and epilepsy patients yielded a highly linear correlation with the Taqman assay, resulting in an R^2 value of 0.95. Regarding the sensor's selectivity, the electrocatalytic current experienced a reduction of approximately 4-fold in the presence of only a single-base mismatch, underscoring the sensor's exceptional selectivity.

This study validated the method developed by correlation with RT-qPCR. However, great care must be taken when using this technique as a high standard of confidence, since it has associated risks such as contamination, errors and sensing probes with high and variable background noise. Furthermore, it would be ideal if an appropriate statistical assessment of biomarker potential (ROC curve analysis) was studied to assess the sensitivity and specificity of the biomarker correlated for the first time in this study to focal epilepsy.

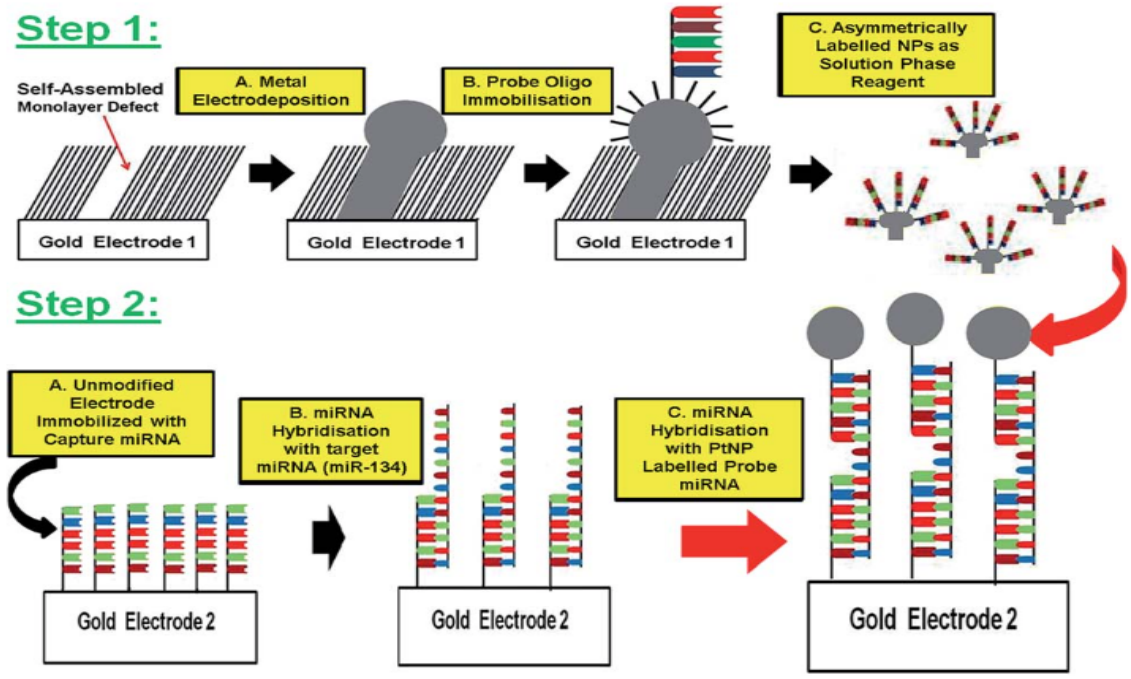


Figure 1.7. Schematic diagram of the platinum nanoparticle formation and regio-selective miRNA functionalization. Reproduced from ref. [64] Spain, E., Jimenez-Mateos, E. M., Raoof, R., et al. (2015). Direct, non-amplified detection of microRNA-134 in plasma from epilepsy patients. *RSC Advances, 5*, 90071–90078.

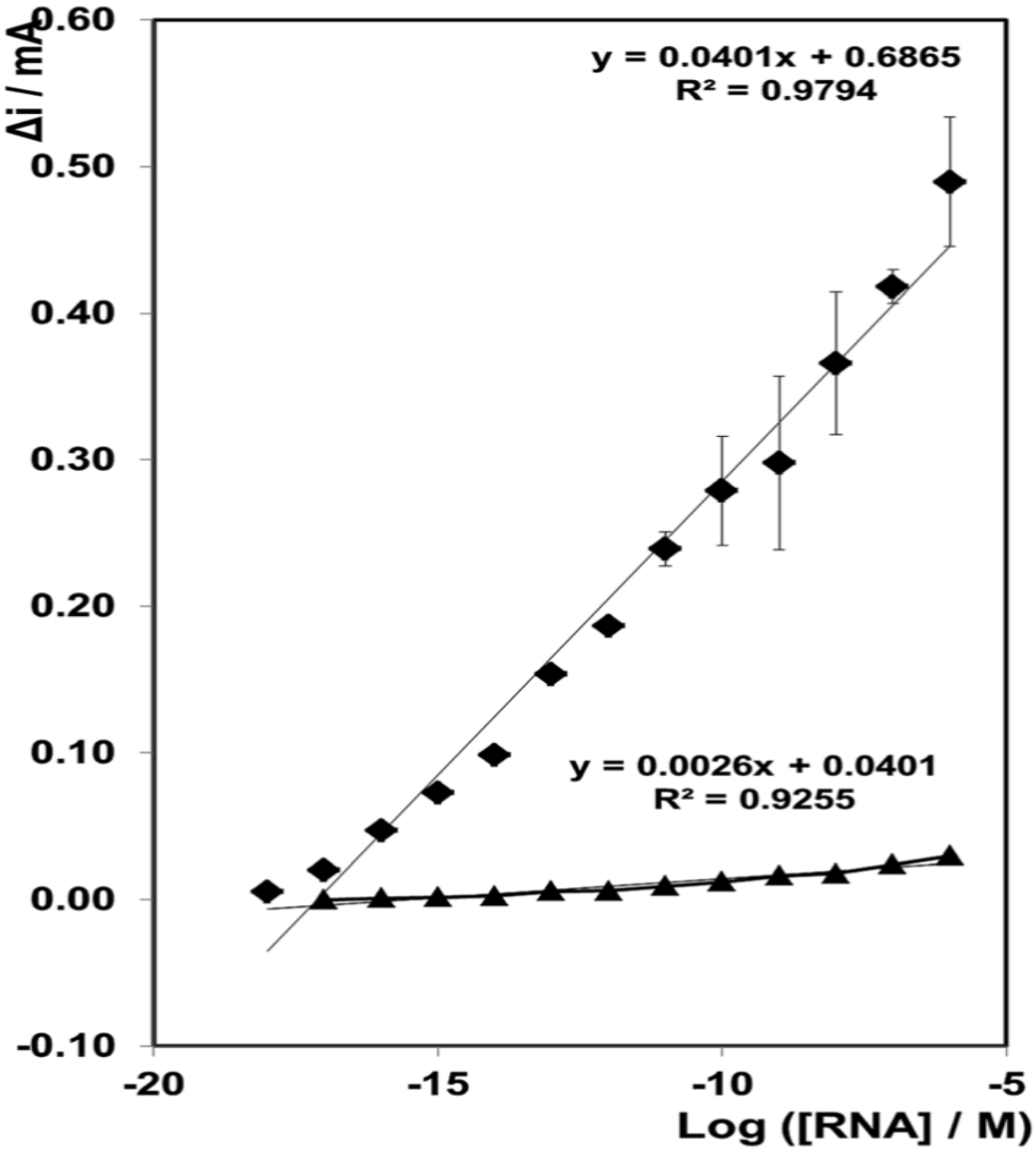


Figure 1.8. Dependence of the difference in current before and after addition of H_2O_2 on log[RNA] for a 2 mm diameter bare electrode following hybridization with reporter-probe DNA that is labelled with PtNPs and where the probe is unlabelled (n=3). In both cases, the solution contains 2mM H_2O_2 at an applied potential of -0.250V. Where error bars are not visible, they are smaller than or comparable to, the size of the symbols and range of 1.1% to 3.5%. Reproduced from ref. [50] Spain, E., Jimenez-Mateos, E. M., Raoof, R., et al. (2015). Direct, non-amplified detection of microRNA-134 in plasma from epilepsy patients. *RSC Advances, 5*, 90071–90078.

Wu *et al.* [65] developed a label-free amperometric biosensor for the detection of miRNA-155 based on the change of the faradaic current associated with reduction of hydrogen peroxide by a multilayer comprised of Nafion, thionine and Pd nanoparticles. In this work, a glassy carbon

(GCE) surface was covered with a Nafion film, which through its electronic exchange function absorbed thionine (Thi). Subsequently, palladium nanoparticles were immobilized on the electrode surface by the interaction between nano-Pd and the amino group of Thi. Further, miRNA-155 capture-probe modified with thiol group was immobilized on the nano-Pd layer and, in a final immobilisation step, the modified electrode was blocked with the spacer hexanethiol (HT). The prepared electrode was hybridized with the target and the signal of miRNA-155 was measured toward the reduction of hydrogen peroxide.

Figure 1.9 illustrates the biosensor's current response during the detection of varying concentrations of miRNA-155. This data was acquired using cyclic voltammetry after introducing 1.8 mM of hydrogen peroxide into a 0.1 M Hac-NaAc buffer solution (pH 5.5). Notably, the recorded currents exhibited an inverse relationship with the concentration of miRNA-155 in the working buffer. The biosensor demonstrated good sensitivity, boasting a limit of detection at 1.87 pM and a linear response range spanning from 5.6 pM to 5.6 x 10^5 pM. Furthermore, it exhibited commendable reproducibility, as evidenced by a negligible relative standard deviation of 0.74% (n = 6) at 560 pM. The sensor's stability was also noteworthy, maintaining its performance over an extended 25-day incubation period at 4°C with less than a 10% deviation from its initial current response. In a short-term analysis involving 40 consecutive cycles in cyclic voltammetry (potential range -0.5V to 0.1V at 50 mV/s), the biosensor demonstrated a modest relative standard deviation of 4.2% between analyses.

Lastly, the analytical application of miRNA was assessed by introducing various concentrations of miRNA-155 into human blood serum. Although the specific miRNA target concentrations were not specified at this periodic, the biosensor's current responses (refer to Table 1.2) indicate its capability to recover (between 95.93% and 101.52%) with a relative standard deviation ranging from 1.25% to 4.76%, well within the clinically acceptable range. Furthermore, this study underscores the biosensor's excellent selectivity and cross-selectivity, as demonstrated by its minimal response when paired with (or when substituting) the target with non-complementary tumour markers, such as TBA and PBA.

This study has demonstrated good results with the biosensor, showcasing its satisfactory sensitivity, reproducibility, and selectivity. However, its practical utility for diagnosing miRNA associated with neurological diseases is limited due to the significant disparity between

the miRNA concentrations tested here (in the μM range) and the actual levels found in real blood samples (picomolar to femtomolar levels, as indicated in the literature [3][78]). Additionally, the complex, time-consuming electrode surface preparation process, including nanoparticle immobilization and miRNA hybridization, poses challenges for point-of-care biosensor development.

Furthermore, this research sheds light on the potential of an emerging class of nanomaterials: palladium nanoparticles (nano-Pd). These nano-Pd exhibit remarkable electroactive and catalytic properties, making them promising candidates for signal amplification in bioanalysis. Nevertheless, it is worth noting that their application in this field remains underexplored, emphasizing the need for further investigation into their capabilities and potential contributions to advancing biosensing technologies.

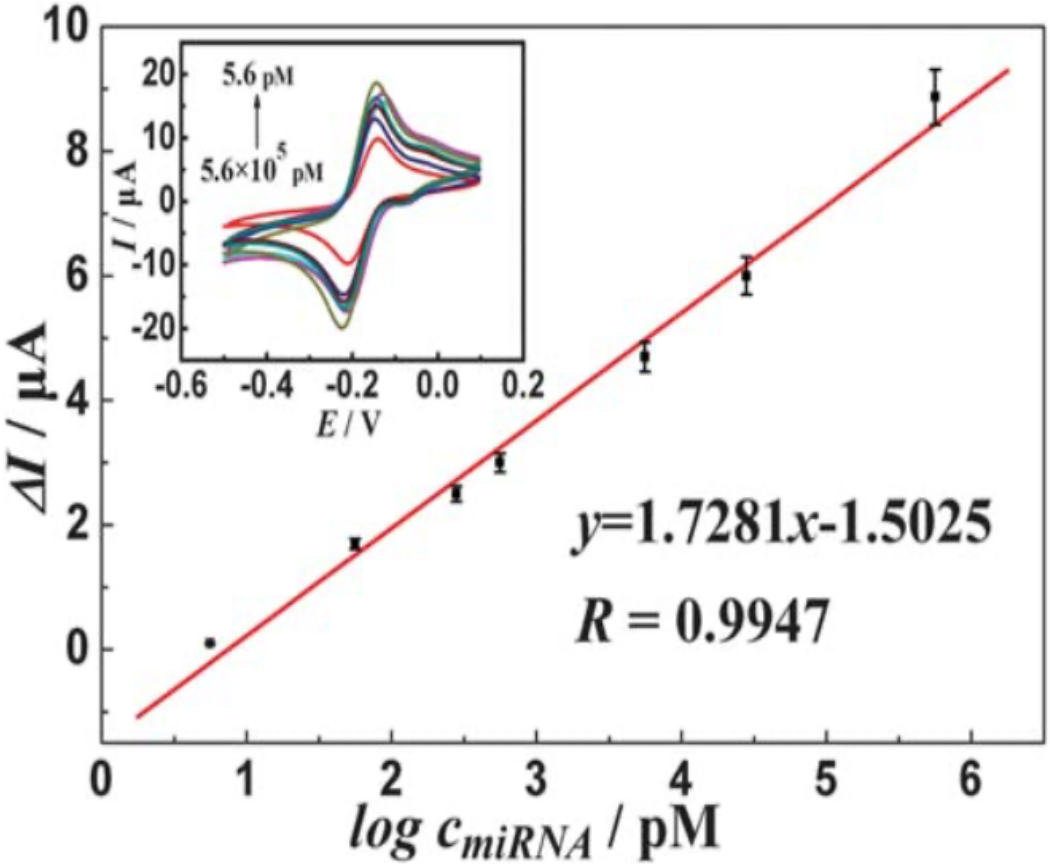


Figure 1.9. Calibration plots of peak current response vs. logarithm of concentration of miRNA with the biosensor under optimal conditions. Inset shows the typical CV plots upon the addition of varying amounts of miRNA: 5.6; 56; 280; 560; $5.6x10^3$; 2.8 $x10^4$; 5.6 $x10^5$ pM. All potentials are given vs. SCE and the scan rate is 50 mVs^{-1}.Reproduced from ref. [65] Wu, X., Chai, Y., Yuan, R., Su, H., &

Han, J. (2013). A novel label-free electrochemical microRNA biosensor using Pd nanoparticles as enhancer and linker. *The Analyst*, *138*(4), 1060–1066.

Table 1.2. Determination of miRNA-155 added in human blood serum (n=3) with the proposed miRNA biosensor. Reproduced from ref. [65] Wu, X., Chai, Y., Yuan, R., Su, H., & Han, J. (2013). A novel label-free electrochemical microRNA biosensor using Pd nanoparticles as enhancer and linker. *The Analyst*, *138*(4), 1060–1066.

Sample	Standard value/μA (I_0)	Found value/μA (I)	Recovery (%) (I/I_0)	RSD (%)
1	15.83	16.07	101.52	1.65
2	15.52	15.55	100.19	1.25
3	14.42	14.35	99.51	4.40
4	11.87	12.62	106.32	4.76
5	10.81	10.37	95.93	3.93

1.3 Multianalyte detection

As it has already been described, only occasionally can a single biomarker characterize a disease or a dysfunction in humans or animals. Typically, more than one biomarker directly associated with the disease is required. Solid tumours are an example of a disease that can have different molecular markers that provide insights into disease intensity and final diagnosis [66]. Therefore, the possibility of creating a detection system that allows the identification of a panel of biomarkers simultaneously, quickly, and accurately is extremely important for the prognosis and diagnosis of diseases, as well as for monitoring patient responses when undergoing treatment [67].

In contrast to conventional single-plex techniques, where a single analyte is detected, multiplexing technologies make the detection of multiple biomarkers more efficient, since the greater screening of biological information obtained from a single sample allows to minimize false negatives and false positives in diagnoses [68]. In addition, a multiplex assay can be performed with smaller sample volumes when compared to the detection of each analyte inserted in individual samples. This feature is particularly important for cases where sample

volumes are limited, such as when analysing samples containing cerebrospinal fluid (CSF) or blood samples from infants [68].

For point of care applications, multi-analyte detection platforms involving electrochemical detection can lead to high-performance sample-to-answer devices capable of reducing the cost and complexity of assays. Electrochemical biosensors have high sensitivity, simplicity of use and automation, rapid test development and low detection limit. Therefore, its combination with a multiplexed system will lead to an increase in the statistical power, e.g., confidence in true positive and true negative rates [69].

Analysing multiplexed electrochemical immunosensors, a multi-analyte platform widely studied and present in the literature, one can understand a critical challenge related to the simultaneous detection of antigens, antibodies, or aptamers. Primary, it may require different assay formats within a single device and the relative concentrations of each analyte may be significantly (>1 million fold) different from one another. Thus, differentiating the signal corresponding to each analyte even from multiple antigen-antibody reactions [70] can become difficult. For example, different electrochemical peaks can be obtained for each discrete analyte, but they can coalesce when several labels are present. The so-called “cross-talk” is a potential disadvantage of type of platform if the detection potentials of the different redox tags are not sufficiently separated [71]. Therefore, multiple transductors and / or detection tags that act independently for each specific analyte may be required to guarantee the success of this system [66].

1.3.1 Classification of Electrochemical Biosensors for Multi-analyte Detection

Electrochemical biosensors for simultaneous detection of multi-analyte can be classified into (i) multi-label and (ii) multi-electrode platforms [6]. The multiple electrode platforms can be subclassified as (a) branched electrodes and (b) paper-based electrodes. In addition, the branched electrodes can be sub-grouped as chip-based and disposable electrodes.

1.3.1.1 Multi-label Platform

Multi-label platforms are based on sandwich assays where the detection mechanism can be compared to the enzyme-linked immunosorbent assay (ELISA) for a better understanding.

Briefly, the biosensor platform consists of a biomolecular receptor immobilized on the electrode surface (capture-probe strand), which is hybridized to a target analyte which, in turn, hybridizes to a probe strand that is functionalized with a label such as a metal ion, quantum dot, redox agent, redox active polymer or enzymes [72]. If the properties of the labels for each analyte are different, e.g., each has a different redox potential, this detection system can distinguish different target analytes, since the intensity of different resultant electrochemical peaks can be correlated to the concentration of each target analyte [73]. An intrinsic advantage of using this detection platform is that electrochemical responses can be monitored in a single amperometric or voltammetric scan [66].

1.3.1.2 Multi-electrode Platform

In theory, multi-electrode platforms feature individual, independent electrodes for detecting each target, and when compared to multi-label platforms, they generally exhibit greater robustness, sensitivity, accuracy, and user-friendliness [66]. This detection system relies on a single label and effectively circumvents "cross-talk" between adjacent transduction elements, given their physical and electrochemical separation [74]. However, it necessitates the utilization of more intricate sensor platform electrochemical instrumentation, resulting in higher costs. Figure 1.10 provides a schematic summary of the various types of detection methods and their classifications employed in simultaneous electrochemical multi-analyte sensing platforms.

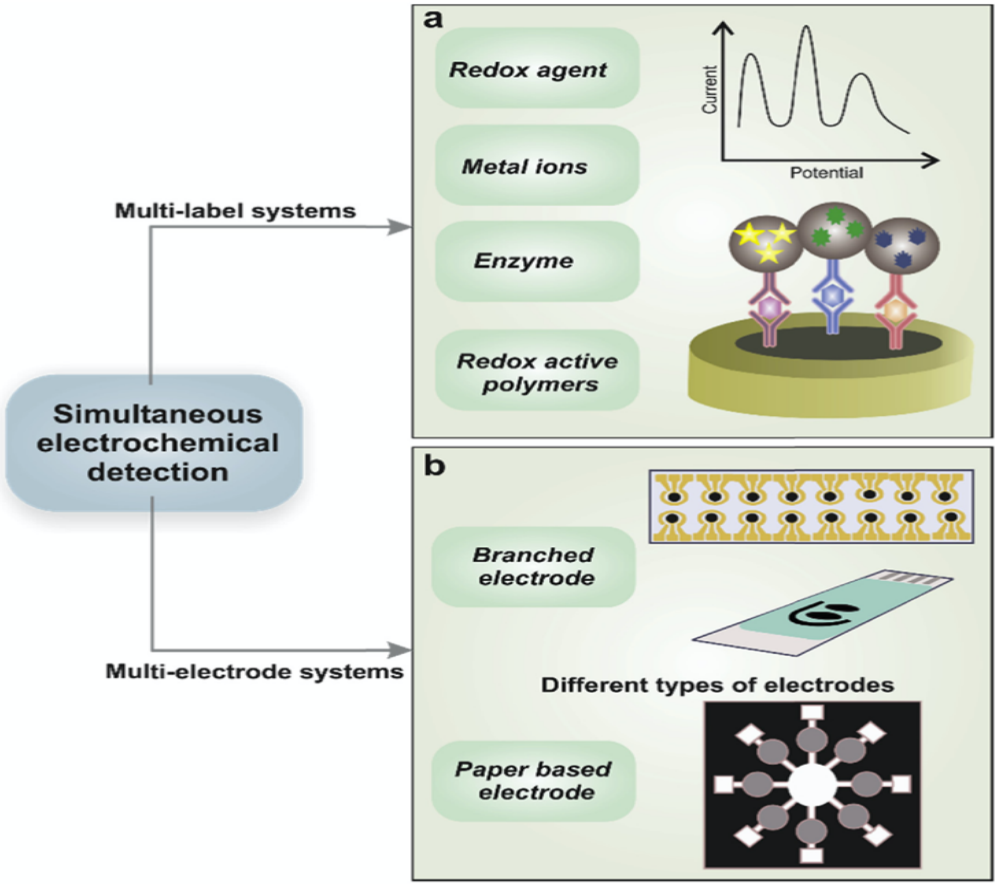


Figure 1.10. Schematic representation for simultaneous electrochemical biosensors. Multi-analyte can be detected either by multi-label systems (panel a) or multi-electrode systems (panel b). Reproduced from ref. [52] Pakchin, P. S., Nakhjavani, S. A., Saber, R., Ghanbari, H., & Omidi, Y. (2017). Recent advances in simultaneous electrochemical multi-analyte sensing platforms. *TrAC-Trends in Analytical Chemistry, 92* (1), 32–41.

1.3.2 Examples of electrochemical platforms for multi-analyte detection (multi-miRNA detection)

Although both platforms for detecting multi-analytes have well-structured examples in the literature, when the purpose is to develop a high-performance method for detecting multiple miRNAs capable to be integrated in point of care devices, the most promising ones involve the use of a combination of multi-label and multi-electrode platforms.

Torrente-Rodriguez *et al.* [75] integrated multiplex platforms (multi-label and multi-electrode) to simultaneously detect and quantify two different microRNAs associated with breast cancer (miRNA-21 and miRNA-205). Multiplexing arises from the composition between chitin-

modified magnetic beads (MB), a dual screen-printed carbon electrode (SPCEs) and a Strep-Horseradish peroxidase polymer, as a label.

Figure 1.11 illustrates the procedure that involves four stages. In the first stage, the targets miRNA-21 and miRNA-205 were hybridized to their respective biotinylated anti-miR probe (anti-miR-21 and anti-miR-205). Then, the hybrids were labelled with the polymer Strep-Horseradish peroxidase. In the second stage, magnetic beads were functionalized with chitin to immobilize the viral protein p19 on its surface. Subsequently, p19 acted as a selective capture-probe bioreceptor for the hybridized microRNA duplexes (miRNA-21-antimiR-21 and miRNA205-antimiR-205) prepared in the previous step. In the third stage, the magnetics beads (MBs) with the dsRNA / p19 complex for each target miRNA were captured magnetically in the corresponding working electrode (WE 1 and WE 2) of the SPCE. In the fourth and last stage, amperometric detection of the catalytic current produced after the addition of H_2O_2 occurred using hydroquinone (HQ) as a redox mediator.

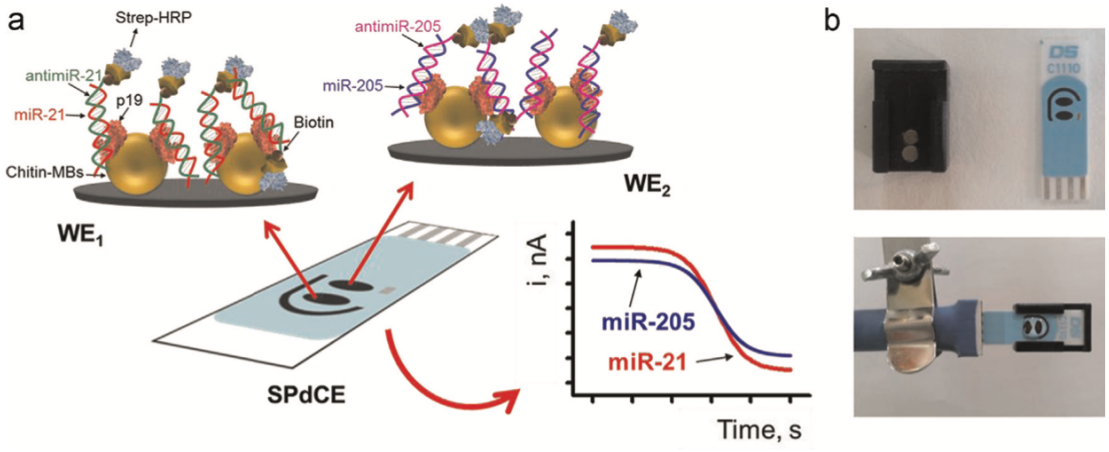


Figure 1.11. Schematic display of the fundamentals involved in the development of the disposable dual magnetosensor for the simultaneous determination of miRNA-21 and miRNA- 205 (a). Picture showing the dual SPCE and the homemade magnet holding block (up), and the modified MBs on the dual SPCE assembled on the magnetic holding block and (b) the specific cable connector (down). Reproduced from ref. [75] Torrente-Rodríguez, R. M., Campuzano, S., López-Hernández, E., Montiel, V. R., Barderas, R., Granados, R., Sánchez-Puelles, J. M., & Pingarrón, J. M. (2015). Simultaneous detection of two breast cancer-related miRNAs in tumor tissues using p19-based disposable amperometric magnetobiosensing platforms. *Biosensors & bioelectronics*, *66*, 385–391.

These p19-based strategies provided LODs of 0.6 nmol of the target miRNA-21 and miRNA-205 with a dynamic range from 2.0 to 10 nM without prior amplification, preconcentration or purification steps in about 2 h at clean buffer. The magnetosensor proved to be reproducible through the analysis of 8 different sensors built using the same protocol with relative standard deviation (RSD) values of 6.3% and 6.4%, for miRNA-21 and miRNA-205, respectively. Furthermore, the sensor showed high specificity allowing the detection and quantification of the endogenous levels of both target miRNAs in total RNA (RNAt) extracted from metastatic breast cancer cell lines and human tissues.

This assay concept is highly attractive from a workflow point of view. This is mainly due to the magnetosensor design, which gives advantages to the system, such as: enhanced capture of the target throughout the sample volume (provides less transport problems than bringing the analyte to the electrode surface), relatively low cost detection (mainly due to the use of SPCEs as working electrode), amplification of the amperometric signal (due to the composition between affinity bioreceptors to enzymatic labels (HRP) and hydroquinone mediator (HQ)) and provide a less time consuming assay (due to the optimization of experimental parameters that guarantee low hybridization time and temperature of the miRNA-anti-miR duplexes). However, this system needs further optimization to meet the requirements of routine laboratory tests. In particular, improved limit of detection, since if the device is to be an incisive / reliable detector it should also cover low abundant concentrations of miRNAs.

1.3.2.1 Sequential detection of multi microRNAs using the same biosensor

The ideal multi-analyte detection platforms should apply the measurements simultaneously because the analysis of a set of miRNAs is often decisive for the diagnosis of disease. However, there are relatively few reports in the literature of electrochemical sensors for simultaneous detection of multiple microRNAs at ultralow levels. This is probably due to the fact that microRNAs have highly homologous sequences and have extremely low concentrations in biological samples, requiring the development of more sensitive and creative technologies. Also, the cost of the reagents is significant (approximately €3000-6000 per analyte) which means that researchers tend to demonstrate their approach for a single analyte.

Breaking this paradigm, Labib *et al.* [76] presented in 2013, for the first time, a biosensor capable of ultrasensitive detection of two miRNAs associated not simultaneously, but sequentially. In this work, the goal was to develop a three-mode electrochemical sensor for

detection and quantitation of miRNAs associated with the onset of cancers by exploring the non-sequence specific binding of p19 RNA protein to small dsRNA (21−23 bp) with nanomolar affinity.

As shown in Figure 1.12, the first modality, called H-SENS, is based on the direct hybridization of thiolated miRNA capture-probe to the target microRNA, assembled onto the gold nanoparticles modified screen-printed carbon electrode (AuNPs-SPCE). The second modality, P-SENS, is based on the binding of the viral protein p19 to the duplex miRNA capture probe-miRNA target formed on the electrode surface. The third and last modality is based on the displacement of p19 connected to the electrode by incubating a mixture of miRNA targets with a non-thiolated miRNA probe at high concentration.

Figure 1.12 shows the modulation of the electrical signal generated by the hybridization between miRNA capture-probe and miRNA target (H-SENS, Figure 1.12b), as well as, the amplification of the hybrid signal caused by the blocking assay based on the binding of the bulky p19 protein with consequent shielding the electrode surface (P-SENS, Figure 1.12c) and the shift-back of the hybrid signal (formerly present on the electrode surface) based on the competitive assay generated by displacement of the p19 protein to a new hybrid with relatively higher concentration (D-SENS, Figure 1.12d).

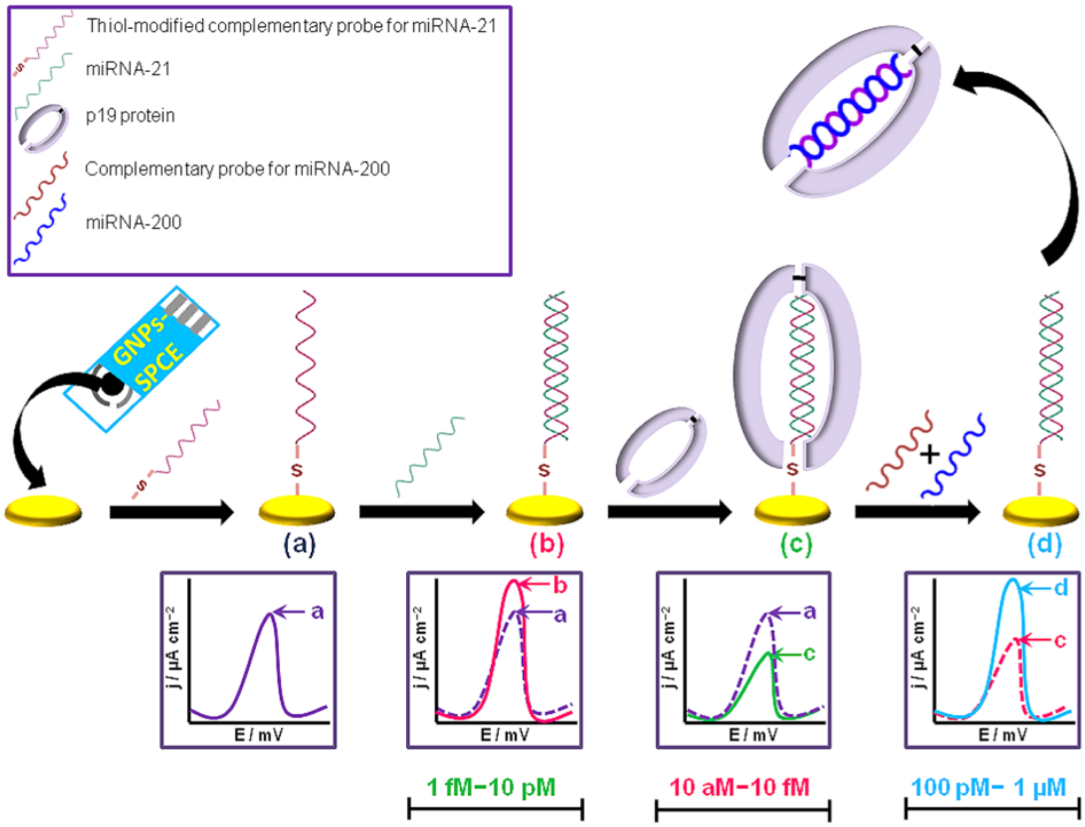


Figure 1.12. Schematic representation of the 3-mode electrochemical sensor (HPD-SENS) for detection of miRNAs. (a) A thiol-modified complementary probe for miRNA-21 was self-assembled onto a gold nanoparticles-modified screen-printed carbon electrode (GNPs-SPCE) followed by backfilling the surface with 0.1 mM 2-mercaptoethanol. (b) A hybridization-based sensor (H-SENS) where the binding of the target miRNA-21 caused an increase in the current intensity, measured by square wave voltammetry (SWV). The linear detection range of the H-SENS is from 1 fM to 10 pM. (c) A p19 protein-based sensor (P-SENS) where the binding of the p19 protein caused a large decrease in current density and thus improved the detection range. The linear detection range of the P-SENS is from 10 aM to 10 fM. (d) A displacement-based sensor (D-SENS) where the hybridization product of miRNA-200 and its complementary probe forced the p19 protein to dissociate from the previous immobilized hybrid, causing a shift-back in the signal. The linear detection range of the D-SENS is from 100 pM to 1 μM Figure reproduced from ref. [76] Labib, M., Khan, N., Ghobadloo, S. M., Cheng, J., Pezacki, J. P., & Berezovski, M. V. (2013). Three-mode electrochemical sensing of ultralow microRNA levels. *Journal of the American Chemical Society*, *135*(8), 3027–3038.

This sensing strategy was also implemented using combinations on one electrode (HPD-SENS) as well as on different electrodes (H-SENS, P-SENS and D-SENS). Thus, H-SENS and P-SENS proved to be adept at detecting and profiling three endogenous miRNAs at similar

concentrations (hsa-miRNA-21, hsa-miRNA-32, and hsa-miRNA-122) in human serum. In addition, H-SENS alone was able to recognize miRNAs with different A / U and G / C content and distinguish between a fully matched miRNA and a miRNA comprising either a terminal or a middle single base mutation.

The approach delivers high sensitivity, excellent selectivity, broad dynamic range (11 orders of magnitude, from 10 aM to 1 μM) and a double simultaneous detection of microRNA concentration. In addition, the sensor is clinically relevant since the extremely low limit detection of miRNAs in biological fluids (down to 90 molecules per 30 μL sample or 5 aM) can be reached without complex and time-consuming amplification steps. Furthermore, the developed sensors are based on nanoparticle-modified screen-printed electrodes that are cheap and commercially available bringing the possibility of implementing this system to portable point-of-care devices thus significantly impacting on early detection of disease.

1.3.3 Future prospects on the multi-analytes field

The alternate expression (i.e. up and down-regulation) of multiple microRNAs can be used to fingerprint disease characteristics. Therefore, the integration of miRNA detection into clinical practice can be facilitated with the capacity of multiplex systems to monitor concentration changes of different biomarkers related to the same disease.

Multiplexed devices based on electrochemical detection are extremely promising for improving the reliability and speed of diagnostics and therapy monitoring. This could lead to more rapid clinical decision making and corresponding reductions in patient stress and healthcare costs as well as improved patient outcomes. Therefore, the improvement of this technique is extremely relevant in the future clinical field.

One of the most suitable performances of label-free electrochemical multiplex sensors reported by the literature, uses the combination of nanomaterials-based assays and screen-printed electrodes. As presented in the work of Labib *et al.* [76] gold nanoparticles with screen- printed carbon platforms meet the required sensitivity specification for miRNA analysis even in complex biological matrices and using low miRNA amounts. This is due to the fact that nanomaterials play a fundamental role not only as a receptor for immobilizing molecules, but also as a signal amplifier capable of improving the sensitivity and response of the system. In addition, SPEs possess additional advantages derived not only from the good electrical

properties, but also from their small size and the possibility to be fabricated with different and less expensive materials. Therefore, nanomaterials in conjunction with screen printed electrodes are an attractive system paving the way for the development of point-of-care (POCs) testing devices.

In addition, another efficient method for electrochemical detection of multiple microRNAs derives from the implementation of hybrid strategies to improve multiplexing capability. As shown by Torrente- Rodríguez *et al.* [75] the use of more than one detection platform (multi-electrode and multi-label) generates a system with relatively low cost of manufacture, possibility of miniaturization (characteristics derived from the use of SPCEs), and good sensitivity (guaranteed by amplification of the signal via viral protein p19 and an enzyme label). In this type of detection, the use of two platforms generates an improvement in the sensitivity and selectivity of the system without the need to use more complex technologies (such as signal amplification by PCR or preconcentration of samples).

Regarding the future of multi-analyte electrochemical detection platforms, two pillars must be considered (i) the need for additional studies aiming the **development of simultaneous detections** and (ii) **expanding the applicability** of the technique. Considering that many of the multi-analyte detection platforms presented in the literature claim to detect several biomarkers with high differences in the threshold levels, additional efforts should be focused on developing strategies suitable to simultaneously determine biomarkers at very different concentration levels. In addition, the applicability of multi-analyte platforms could be expanded if, in addition to multi-analyte detection, these platforms could guarantee the validation of microRNAs.

Although the literature presents a good collection of multi-analyte detections in general, the development of electrochemical biosensors with the ability to analyse multiple microRNAs still have a long way ahead before becoming a competitive technology for development of point of care tests. Most of the multiplex platforms described in the literature are still at the proof-of-principle level. This is due to the fact that there is no standardization in the pre-analytical preparation for detection (sampling the different sources: synthetic miRNA, miRNA from real patients and miRNAs from spiked-in samples) and in the methodology for detecting miRNAs, making it difficult to compare cross-platform performance.

1.4 Conclusion and Thesis Outline

Epilepsy is a complex neurological disorder characterized by intermittent neuronal discharges that temporarily disrupt normal brain function for brief periods, ranging from seconds to minutes. Its diverse nature results in a wide spectrum of symptoms, ranging from seizures to impaired motor skills. Among the myriad factors implicated in its onset, the literature consistently highlights the disruption of the blood-brain barrier as a key player.

Alzheimer's disease is a neurodegenerative disorder, that affects individuals progressively and irreparably. However, in contrast to epilepsy, Alzheimer disease develops insidiously and ranks as the seventh leading cause of death worldwide. On average, a person can live with the disease for about twenty years before symptoms become apparent. The exact mechanisms behind the disease are still under investigation, with potential contributing factors ranging from early-life stress and lifestyle choices to neuroinflammation caused by blood-brain barrier disruption.

Epilepsy and Alzheimer's disease rank among the most thoroughly studied medical conditions worldwide. This extensive research is driven not only by their high prevalence on a global scale and their profound negative impact on the quality of life of afflicted individuals but also by the potential for epileptic seizures or neuroinflammation to inflict irreversible harm upon the central nervous system. Hence, early disease detection assumes paramount significance, not only for prognosis but also for effective intervention.

Current methods for detecting these neurological disorders mainly rely on neuroimaging and cerebrospinal fluid protein analysis. While these techniques are considered accurate, they often fall short in terms of feasibility for use in clinical trials. They are often complex, invasive, time-consuming, and typically only detectable in the late stages of the disease. Consequently, there is a pressing need for a user-friendly, cost-effective detection device suitable for clinical and primary care settings to screen large populations of patients.

In contrast to the current diagnostic strategies, the use of electrochemical sensors capable of detecting specific nucleic acid sequences, such as miRNAs, presents a revolutionary approach with great potential for improving the prognosis, diagnosis, and treatment of neurological diseases. miRNAs are stable gene regulators found in biofluids, and their quantification in blood plasma can indicate irregularities associated with neurological diseases. Furthermore,

the analysis of different miRNA sequences in biological fluids allows for differentiation between patients with mild cognitive impairment or epilepsy and those with other related brain diseases. This differentiation is vital for tailoring appropriate treatments and improving success rates in disease management.

The unique physical and chemical properties of electrochemical sensors make them a viable alternative to complex and expensive standard detection methods. Factors such as easy access to cost-effective materials for electrode development, high selectivity for analytes, and compatibility with microfabrication technology make electrochemical sensors promising for point-of-care devices. Additionally, the real-time detection capabilities of electrochemical sensors enable faster, more cost-effective, and reliable analyses.

This thesis focuses on two key approaches to enhance miRNA detection. The first approach involves the development of a *label-free* impedance-based biosensor with sub-attomolar sensitivity for detecting miRNA-206, which is associated with Alzheimer disease. This approach changes the interfacial microenvironment of the biosensor's interface through modulation of miRNA capture-probe surface coverage and hybridization efficiency, resulting in a wide dynamic range and high selectivity of the platform. The biosensor's performance has been validated using clinical plasma samples, demonstrating accurate quantification and excellent stability.

The second approach introduces gold nanorods (AuNRDs) as electrocatalytic *labels* in a chronoamperometric biosensor, achieving ultrasensitive detection across a broad dynamic range. In this approach, the biosensor's signal is generated by the reduction of hydrogen peroxide by the gold nanorods confined to the gold electrode surface through hybridization with miRNA targets. Building upon the results of the preceding chapter, the transducer platform was optimised to 1 : 4 mole ratio of capture-probe to mercaptohexanol (MCH). Additional optimization steps include adjusting the $[\text{miRNA}_{\text{reporter-probe}}]_I$ to [AuNRDs] ratio , fine-tuning the hybridization time for miRNA target—reporter-probe, and optimizing the concentration of hydrogen peroxide for electrocatalysis of the metal label. This biosensor excels in sensitivity, selectivity and rapid response time.

To address the high cost associated with conventional gold electrodes in mass production, modifications were made to the developed amperometric biosensor. Screen-printed carbon

electrodes (SPCEs) were chosen for their cost-effectiveness, biocompatibility, disposability, and customizability. Different gold structures were mixed with the carbon ink, resulting in the development of SPCE with 10% (w/w) gold microspheres (AuS) and 10% (w/w) gold microflakes (AuF). SPCEs with microspheres exhibited superior electrochemical behaviour, higher electron transfer process , and reduced overpotential for hydrogen peroxide reduction. Sensitivity was assessed using gold nanorods and palladium nanocubes (PdNCBs) as labels. Further enhancements of the platform with 20% (w/w) microspheres significantly amplified the biosensor's signal when using AuNRDs. This study offers valuable insights into optimizing SPCE design for advanced biosensing applications.

Multiplexed electrochemical biosensors have the potential to detect a panel of disease-specific miRNAs. This capability is highly desirable in diagnostics, as it can provide a more accurate characterization of the disease. In a proof-of-concept study, the novel 20% (w/w) microsphere SPCE demonstrated multiplex capabilities, successfully detecting miRNAs associated with both Alzheimer disease (miRNA-206) and epilepsy (let-7b and miRNA-135a) using various nanoparticle labels. Platinum nanoparticles proved to be the most effective, followed by PdNCBs and AuNRDs, catering to different miRNA requirements. The biosensor exhibited wide dynamic ranges, ultralow limits of detection, high selectivity, and stability.

Future directions in this research include miniaturization, microfluidic integration, and expanded clinical validation studies. The study underscores the potential of electrochemical biosensors to revolutionize the detection, diagnosis, and treatment of neurological diseases. Multiplexed detection offers a comprehensive view of disease states and opens the door to continuous monitoring systems, although challenges such as cross-reactivity and sample complexity must be addressed. The thesis anticipates further advancements in personalized medicine and improved patient care for neurological diseases.

1.5 References

[1] Zhang C. (2009). Novel functions for small RNA molecules. *Current opinion in molecular therapeutics*, *11*(6), 641–651.

[2] Lee, R. C., Feinbaum, R. L., & Ambros, V. (1993). The C. elegans heterochronic gene lin-4 encodes small RNAs with antisense complementarity to lin-14. *Cell*, *75*(5), 843–854. https://doi.org/10.1016/0092-8674(93)90529-y

[3] Kenny, A., McArdle, H., Calero, M., Rabano, A., Madden, S. F., Adamson, K., Forster, R., Spain, E., Prehn, J. H. M., Henshall, D. C., Medina, M., Jimenez-Mateos, E. M., & Engel, T. (2019). Elevated Plasma microRNA-206 Levels Predict Cognitive Decline and Progression to Dementia from Mild Cognitive Impairment. *Biomolecules*, *9*(11), 734. https://doi.org/10.3390/biom9110734

[4] Gillespie, P., Ladame, S., & O'Hare, D. (2018). Molecular methods in electrochemical microRNA detection. *The Analyst*, *144*(1), 114–129. https://doi.org/10.1039/c8an01572d

[5] Kilic, T., Erdem, A., Ozsoz, M., & Carrara, S. (2018). microRNA biosensors: Opportunities and challenges among conventional and commercially available techniques. *Biosensors & bioelectronics*, *99*, 525–546. https://doi.org/10.1016/j.bios.2017.08.007

[6] Stafstrom, C. E., & Carmant, L. (2015). Seizures and epilepsy: an overview for neuroscientists. *Cold Spring Harbor perspectives in medicine*, *5*(6), a022426. https://doi.org/10.1101/cshperspect.a022426

[7] Henshall, D. C., Hamer, H. M., Pasterkamp, R. J., Goldstein, D. B., Kjems, J., Prehn, J. H. M., Schorge, S., Lamottke, K., & Rosenow, F. (2016). MicroRNAs in epilepsy: pathophysiology and clinical utility. *The Lancet Neurology*, *15*(13), 1368–1376. https://doi.org/10.1016/S1474-4422(16)30246-0

[8] Tiwari, S., Sharma, V., Mujawar, M., Mishra, Y. K., Kaushik, A., & Ghosal, A. (2019). Biosensors for Epilepsy Management: State-of-Art and Future Aspects. *Sensors (Basel, Switzerland)*, *19*(7), 1525. https://doi.org/10.3390/s19071525

[9] van Vliet, E. A., da Costa Araújo, S., Redeker, S., van Schaik, R., Aronica, E., & Gorter, J. A. (2007). Blood-brain barrier leakage may lead to progression of temporal lobe epilepsy. *Brain: a journal of neurology*, *130* , 521–534. https://doi.org/10.1093/brain/awl318

[10] Henshall D. C. (2014). MicroRNA and epilepsy: profiling, functions and potential clinical applications. *Current opinion in neurology*, *27*(2), 199–205. https://doi.org/10.1097/WCO.0000000000000079

[11] Martinc, B., Grabnar, I., & Vovk, T. (2012). The role of reactive species in epileptogenesis and influence of antiepileptic drug therapy on oxidative stress. *Current neuropharmacology*, *10*(4), 328–343. https://doi.org/10.2174/157015912804143504

[12] Jimenez-Mateos, E. M., Arribas-Blazquez, M., Sanz-Rodriguez, A., Concannon, C., Olivos-Ore, L. A., Reschke, C. R., Mooney, C. M., Mooney, C., Lugara, E., Morgan, J., Langa,

E., Jimenez-Pacheco, A., Silva, L. F., Mesuret, G., Boison, D., Miras-Portugal, M. T., Letavic, M., Artalejo, A. R., Bhattacharya, A., Diaz-Hernandez, M., … Engel, T. (2015). microRNA targeting of the P2X7 purinoceptor opposes a contralateral epileptogenic focus in the hippocampus. *Scientific reports*, *5*, 17486. https://doi.org/10.1038/srep17486

[13] Gillespie, P., Ladame, S., & O'Hare, D. (2018). Molecular methods in electrochemical microRNA detection. *The Analyst*, *144*(1), 114–129. https://doi.org/10.1039/c8an01572d

[14] Liu, D. Z., Tian, Y., Ander, B. P., Xu, H., Stamova, B. S., Zhan, X., Turner, R. J., Jickling, G., & Sharp, F. R. (2010). Brain and blood microRNA expression profiling of ischemic stroke, intracerebral hemorrhage, and kainate seizures. *Journal of cerebral blood flow and metabolism*, *30* (1), 92–101. https://doi.org/10.1038/jcbfm.2009.186

[15] Avansini, S. H., de Sousa Lima, B. P., Secolin, R., Santos, M. L., Coan, A. C., Vieira, A. S., Torres, F. R., Carvalho, B. S., Alvim, M. K., Morita, M. E., Yasuda, C. L., Pimentel-Silva, L. R., Dogini, D. B., Rogerio, F., Cendes, F., & Lopes-Cendes, I. (2017). MicroRNA hsa-miR-134 is a circulating biomarker for mesial temporal lobe epilepsy. *PloS one*, *12* (4), e0173060. https://doi.org/10.1371/journal.pone.0173060

[16] Enright, N., Simonato, M., & Henshall, D. C. (2018). Discovery and validation of blood microRNAs as molecular biomarkers of epilepsy: Ways to close current knowledge gaps. *Epilepsia open*, *3* (4), 427–436. https://doi.org/10.1002/epi4.12275

[17] Wang, J., Yu, J. T., Tan, L., Tian, Y., Ma, J., Tan, C. C., Wang, H. F., Liu, Y., Tan, M. S., Jiang, T., & Tan, L. (2015). Genome-wide circulating microRNA expression profiling indicates biomarkers for epilepsy. *Scientific reports*, *5*, 9522. https://doi.org/10.1038/srep09522

[18] Wang, J., Tan, L., Tan, L., Tian, Y., Ma, J., Tan, C. C., Wang, H. F., Liu, Y., Tan, M. S., Jiang, T., & Yu, J. T. (2015). Circulating microRNAs are promising novel biomarkers for drug-resistant epilepsy. *Scientific reports*, *5*, 10201. https://doi.org/10.1038/srep10201

[19] An, N., Zhao, W., Liu, Y., Yang, X., & Chen, P. (2016). Elevated serum miR-106b and miR-146a in patients with focal and generalized epilepsy. *Epilepsy research*, *127*, 311–316. https://doi.org/10.1016/j.eplepsyres.2016.09.019

[20] Sun, Y., Wang, X., Wang, Z., Zhang, Y., Che, N., Luo, X., Tan, Z., Sun, X., Li, X., Yang, K., Wang, G., Luan, L., Liu, Y., Zheng, X., Wei, M., Cheng, H., & Yin, J. (2016). Expression of microRNA-129-2-3p and microRNA-935 in plasma and brain tissue of human refractory epilepsy. *Epilepsy research*, *127*, 276–283. https://doi.org/10.1016/j.eplepsyres.2016.09.016

[21] Che, N., Zu, G., Zhou, T., Wang, X., Sun, Y., Tan, Z., Liu, Y., Wang, D., Luo, X., Zhao, Z., Zhang, Y., Wei, M., & Yin, J. (2017). Aberrant Expression of miR-323a-5p in Patients with Refractory Epilepsy Caused by Focal Cortical Dysplasia. *Genetic testing and molecular biomarkers*, *21* (1), 3–9. https://doi.org/10.1089/gtmb.2016.0096

[22] Wang, X., Sun, Y., Tan, Z., Che, N., Ji, A., Luo, X., Sun, X., Li, X., Yang, K., Wang, G., Luan, L., Liu, Y., Wei, M., & Yin, J. (2016). Serum MicroRNA-4521 is a Potential Biomarker for Focal Cortical Dysplasia with Refractory Epilepsy. *Neurochemical research*, *41* (4), 905–912. https://doi.org/10.1007/s11064-015-1773-0

[23] Yan, S., Zhang, H., Xie, W., Meng, F., Zhang, K., Jiang, Y., Zhang, X., & Zhang, J. (2017). Altered microRNA profiles in plasma exosomes from mesial temporal lobe epilepsy with hippocampal sclerosis. *Oncotarget*, *8* (3), 4136–4146. https://doi.org/10.18632/oncotarget.13744

[24] Shetty, A. K., Mishra, V., Kodali, M., & Hattiangady, B. (2014). Corrigendum: Blood brain barrier dysfunction and delayed neurological deficits in mild traumatic brain injury induced by blast shock waves. *Frontiers in cellular neuroscience*, *8*, 404. https://doi.org/10.3389/fncel.2014.00404

[25] Bustin, S. A., Benes, V., Garson, J. A., Hellemans, J., Huggett, J., Kubista, M., Mueller, R., Nolan, T., Pfaffl, M. W., Shipley, G. L., Vandesompele, J., Wittwer, C. T. (2009). The MIQE Guidelines: Minimum Information for Publication of Quantitative Real-Time PCR Experiments. *Clinical Chemistry*, 55(4), 611–622. https://doi.org/10.1373/clinchem.2008.112797

[26] Schmittgen, T. D., Lee, E. J., Jiang, J., Sarkar, A., Yang, L., Elton, T. S., & Chen, C. (2008). Real-time PCR quantification of precursor and mature microRNA. *Methods (San Diego, Calif.)*, *44* (1), 31–38. https://doi.org/10.1016/j.ymeth.2007.09.006

[27] Kilic, T., Erdem, A., Ozsoz, M., & Carrara, S. (2018). microRNA biosensors: Opportunities and challenges among conventional and commercially available techniques. *Biosensors & bioelectronics*, *99*, 525–546. https://doi.org/10.1016/j.bios.2017.08.007

[28] Alzheimer's Society. (n.d.). What is Alzheimer's disease. Retrieved from http://www.alzheimers.org.uk/site/scripts/documents_info.php?documentID=100. Accessed on June 15, 2021.

[29] Qiu, C., Kivipelto, M., & von Strauss, E. (2009). Epidemiology of Alzheimer's disease: occurrence, determinants, and strategies toward intervention. *Dialogues in clinical neuroscience*, *11* (2), 111–128. https://doi.org/10.31887/DCNS.2009.11.2/cqiu

[30] Lemche E. (2018). Early Life Stress and Epigenetics in Late-onset Alzheimer's Dementia: A Systematic Review. *Current genomics*, *19* (7), 522–602. https://doi.org/10.2174/1389202919666171229145156

[31] Norton, S., Matthews, F. E., Barnes, D. E., Yaffe, K., & Brayne, C. (2014). Potential for primary prevention of Alzheimer's disease: an analysis of population-based data. *The Lancet Neurology*, *13* (8), 788–794. https://doi.org/10.1016/S1474-4422(14)70136-X

[32] Kandel E. R. (2012). The molecular biology of memory: cAMP, PKA, CRE, CREB-1, CREB-2, and CPEB. *Molecular brain*, *5*, 14. https://doi.org/10.1186/1756-6606-5-14

[33] Schneider, L. S., Mangialasche, F., Andreasen, N., Feldman, H., Giacobini, E., Jones, R., Mantua, V., Mecocci, P., Pani, L., Winblad, B., & Kivipelto, M. (2014). Clinical trials and late-stage drug development for Alzheimer's disease: an appraisal from 1984 to 2014. *Journal of internal medicine*, *275* (3), 251–283. https://doi.org/10.1111/joim.12191

[34] Siedlecki-Wullich, D., Miñano-Molina, A. J., & Rodríguez-Álvarez, J. (2021). microRNAs as Early Biomarkers of Alzheimer's Disease: A Synaptic Perspective. *Cells*, *10* (1), 113. https://doi.org/10.3390/cells10010113

[35] Wei, W., Wang, Z. Y., Ma, L. N., Zhang, T. T., Cao, Y., & Li, H. (2020). MicroRNAs in Alzheimer's Disease: Function and Potential Applications as Diagnostic Biomarkers. *Frontiers in molecular neuroscience*, *13*, 160. https://doi.org/10.3389/fnmol.2020.00160

[36] Kanach, C., Blusztajn, J. K., Fischer, A., & Delalle, I. (2021). MicroRNAs as Candidate Biomarkers for Alzheimer's Disease. *Non-coding RNA*, *7* (1), 8. https://doi.org/10.3390/ncrna7010008

[37] Hébert, S. S., Horré, K., Nicolaï, L., Papadopoulou, A. S., Mandemakers, W., Silahtaroglu, A. N., Kauppinen, S., Delacourte, A., & De Strooper, B. (2008). Loss of microRNA cluster miR-29a/b-1 in sporadic Alzheimer's disease correlates with increased BACE1/beta-secretase expression. *Proceedings of the National Academy of Sciences of the United States of America*, *105* (17), 6415–6420. https://doi.org/10.1073/pnas.0710263105

[38] Pereira, P. A., Tomás, J. F., Queiroz, J. A., Figueiras, A. R., & Sousa, F. (2016). Recombinant pre-miR-29b for Alzheimer´s disease therapeutics. *Scientific reports*, *6*, 19946. https://doi.org/10.1038/srep19946

[39] Lusardi, T. A., Phillips, J. I., Wiedrick, J. T., Harrington, C. A., Lind, B., Lapidus, J. A., Quinn, J. F., & Saugstad, J. A. (2017). MicroRNAs in Human Cerebrospinal Fluid as Biomarkers for Alzheimer's Disease. *Journal of Alzheimer's disease*, *55* (3), 1223–1233. https://doi.org/10.3233/JAD-160835

[40] Denk, J., Boelmans, K., Siegismund, C., Lassner, D., Arlt, S., & Jahn, H. (2015). MicroRNA Profiling of CSF Reveals Potential Biomarkers to Detect Alzheimer`s Disease. *PloS one*, *10* (5), e0126423. https://doi.org/10.1371/journal.pone.0126423

[41] Sandau, U. S., Wiedrick, J. T., Smith, S. J., McFarland, T. J., Lusardi, T. A., Lind, B., Harrington, C. A., Lapidus, J. A., Galasko, D. R., Quinn, J. F., & Saugstad, J. A. (2020). Performance of Validated MicroRNA Biomarkers for Alzheimer's Disease in Mild Cognitive Impairment. *Journal of Alzheimer's disease*, *78* (1), 245–263. https://doi.org/10.3233/JAD-200396

[42] Kenny, A., McArdle, H., Calero, M., Rabano, A., Madden, S. F., Adamson, K., Forster, R., Spain, E., Prehn, J. H. M., Henshall, D. C., Medina, M., Jimenez-Mateos, E. M., & Engel, T. (2019). Elevated Plasma microRNA-206 Levels Predict Cognitive Decline and Progression to Dementia from Mild Cognitive Impairment. *Biomolecules*, *9* (11), 734. https://doi.org/10.3390/biom9110734

[43] Piscopo, P., Lacorte, E., Feligioni, M., Mayer, F., Crestini, A., Piccolo, L., Bacigalupo, I., Filareti, M., Ficulle, E., Confaloni, A., Vanacore, N., & Corbo, M. (2019). MicroRNAs and mild cognitive impairment: A systematic review. *Ageing research reviews*, *50*, 131–141. https://doi.org/10.1016/j.arr.2018.11.005

[44] Lugli, G., Cohen, A. M., Bennett, D. A., Shah, R. C., Fields, C. J., Hernandez, A. G., & Smalheiser, N. R. (2015). Plasma Exosomal miRNAs in Persons with and without Alzheimer

Disease: Altered Expression and Prospects for Biomarkers. *PloS one*, *10* (10), e0139233. https://doi.org/10.1371/journal.pone.0139233

[45] Valadi, H., Ekström, K., Bossios, A., Sjöstrand, M., Lee, J. J., & Lötvall, J. O. (2007). Exosome-mediated transfer of mRNAs and microRNAs is a novel mechanism of genetic exchange between cells. *Nature cell biology*, *9* (6), 654–659. https://doi.org/10.1038/ncb1596

[46] Wang, J. (2002). Electrochemical nucleic acid biosensors. Analytica Chimica Acta, 469(1), 63-71. https://doi.org/10.1016/S0003-2670(01)01399-X.

[47] Gooding, J. J. (2002). Electrochemical DNA hybridization biosensors. Electroanalysis, 14 (17), 1149-1156. https://doi.org/10.1002/1521-4109(200209)14:17<1149::AID-ELAN1149>3.0.CO;2-8

[48] Drummond, T., Hill, M., & Barton, J. (2003). Electrochemical DNA sensors. *Nature Biotechnology, 21*, 1192-1199. https://doi.org/10.1038/nbt873.

[49] Esmaeilzadeh, A. A., Yaseen, M. M., Khudaynazarov, U., Al-Gazally, M. E., Opulencia, M. J. C., Jalil, A. T., & Mohammed, R. N. (2022). Recent advances on the electrochemical and optical biosensing strategies for monitoring microRNA-21: A review. *Analytical Methods, 14,* 4449-4459. https://doi.org/10.1039/D2AY01384C.

[50] Kafka, J., Pänke, O., Abendroth, B., & Lisdat, F. (2008). A label-free DNA sensor based on impedance spectroscopy. *Electrochimica Acta, 53* (25), 7467-7474. https://doi.org/10.1016/j.electacta.2008.01.031.

[52] Zhao, J., Henkens, R. W., Stonehuerner, J., O'Daly, J. P., & Crumbliss, A. L. (1992). Direct electron transfer at horseradish peroxidase—colloidal gold modified electrodes. *Journal of Electroanalytical Chemistry, 327* (1-2), 109-119. https://doi.org/10.1016/0022-0728(92)80140-Y.

[53] Teranishi, T., Hosoe, M., Tanaka, T., & Miyake, M. (1999). Size Control of Monodispersed Pt Nanoparticles and Their 2D Organization by Electrophoretic Deposition. Journal of Physical Chemistry, 103, 3818-3827. http://dx.doi.org/10.1021/jp983478m.

[54] Zhang, L., Su, W., Liu, S., Huang, C., Ghalandari, B., Divsalar, A., & Ding, X. (2022). Recent Progresses in Electrochemical DNA Biosensors for MicroRNA Detection. *Phenomics (Cham, Switzerland)*, *2* (1), 18–32. https://doi.org/10.1007/s43657-021-00032-z

[55] Levicky, R., Herne, T., Tatlov, M., & Satija, S. (1998). Using self-assembly to control the structure of DNA monolayers on gold: A neutron reflectivity study. *Journal of the American Chemical Society, 120* (38), 9787-9792. https://doi.org/10.1021/ja981897r

[56] Paimard, G., Ghasali, E., & Baeza, M. (2023). Screen-Printed Electrodes: Fabrication, Modification, and Biosensing Applications. *Chemosensors, 11* (2), 113. https://doi.org/10.3390/chemosensors11020113

[57] Pänke, O., Balkenhohl, T., Kafka, J., Schäfer, D., & Lisdat, F. (2008). Impedance Spectroscopy and Biosensing. *Advances in Biochemical Engineering/Biotechnology*, 109, 195.

[58] Zouari, M., Campuzano, S., Pingarrón, J. M., & Raouafi, N. (2018). Amperometric Biosensing of miRNA-21 in Serum and Cancer Cells at Nanostructured Platforms Using Anti-DNA–RNA Hybrid Antibodies. *ACS Omega, 3* (8), 8923–8931. https://doi.org/10.1021/acsomega.8b00986

[59] Masud, M. K., Umer, M., Hossain, M. S. A., Yamauchi, Y., Nguyen, N. T., & Shiddiky, M. J. A. (2019). Nanoarchitecture Frameworks for Electrochemical miRNA Detection. *Trends in biochemical sciences*, *44* (5), 433–452. https://doi.org/10.1016/j.tibs.2018.11.012

[60] Xia, N., & Zhang, L. (2014). Nanomaterials-Based Sensing Strategies for Electrochemical Detection of MicroRNAs. *Materials (Basel, Switzerland)*, *7*(7), 5366–5384. https://doi.org/10.3390/ma7075366

[61] Chen, S., Yuan, R., Chai, Y., et al. (2013). Electrochemical sensing of hydrogen peroxide using metal nanoparticles: A review. *Microchimica Acta, 180*, 15–32. https://doi.org/10.1007/s00604-012-0904-4

[62] Katz, E., & Willner, I. (2004). Integrated nanoparticle-biomolecule hybrid systems: synthesis, properties, and applications. *Angewandte Chemie (International ed. in English)*, *43*(45), 6042–6108. https://doi.org/10.1002/anie.200400651

[63] Dong, H., Jin, S., Ju, H., Hao, K., Xu, L. P., Lu, H., & Zhang, X. (2012). Trace and label-free microRNA detection using oligonucleotide encapsulated silver nanoclusters as probes. *Analytical chemistry*, *84*(20), 8670–8674. https://doi.org/10.1021/ac301860v

[64] Spain, E., Jimenez-Mateos, E. M., Raoof, R., et al. (2015). Direct, non-amplified detection of microRNA-134 in plasma from epilepsy patients. *RSC Advances, 5*, 90071–90078. https://doi.org/10.1039/C5RA16352H

[65] Wu, X., Chai, Y., Yuan, R., Su, H., & Han, J. (2013). A novel label-free electrochemical microRNA biosensor using Pd nanoparticles as enhancer and linker. *The Analyst*, *138*(4), 1060–1066. https://doi.org/10.1039/c2an36506e

[66] Pakchin, P. S., Nakhjavani, S. A., Saber, R., Ghanbari, H., & Omidi, Y. (2017). Recent advances in simultaneous electrochemical multi-analyte sensing platforms. *TrAC-Trends in Analytical Chemistry, 92* (1), 32–41. https://doi.org/10.1016/j.trac.2017.04.010

[67] Yáñez-Sedeño, P., Campuzano, S., & Pingarrón, J. M. (2017). Multiplexed Electrochemical Immunosensors for Clinical Biomarkers. *Sensors (Basel, Switzerland)*, *17*(5), 965. https://doi.org/10.3390/s17050965

[68] Ramnani, P., Gao, Y., Ozsoz, M., & Mulchandani, A. (2013). Electronic detection of microRNA at attomolar level with high specificity. *Analytical chemistry*, *85*(17), 8061–8064. https://doi.org/10.1021/ac4018346

[69] D'Agata, R., & Spoto, G. (2019). Advanced methods for microRNA biosensing: a problem-solving perspective. *Analytical and bioanalytical chemistry*, *411*(19), 4425–4444. https://doi.org/10.1007/s00216-019-01621-8

[70] Keshavarz, M., & Ra, H. (2015). Recent trends in electrochemical microRNA biosensors for early detection of cancer. *RSC Advances*, *5* (45), 35651–35660. https://doi.org/10.1039/C5RA01726B

[71] Chikkaveeraiah, B. V., Bhirde, A. A., Morgan, N. Y., Eden, H. S., & Chen, X. (2012). Electrochemical immunosensors for detection of cancer protein biomarkers. *ACS nano*, *6*(8), 6546–6561. https://doi.org/10.1021/nn3023969

[72] Li, X. M., Fu, P. Y., Liu, J. M., & Zhang, S. S. (2010). Biosensor for multiplex detection of two DNA target sequences using enzyme-functionalized Au nanoparticles as signal amplification. *Analytica chimica acta*, *673*(2), 133–138. https://doi.org/10.1016/j.aca.2010.05.034

[73] Zhu, Q., Chai, Y., Yuan, R., Zhuo, Y., Han, J., Li, Y., & Liao, N. (2013). Amperometric immunosensor for simultaneous detection of three analytes in one interface using dual functionalized graphene sheets integrated with redox-probes as tracer matrixes. *Biosensors & bioelectronics*, *43*, 440–445. https://doi.org/10.1016/j.bios.2012.12.030

[74] Escamilla-Gómez, V., Hernández-Santos, D., González-García, M. B., Pingarrón-Carrazón, J. M., & Costa-García, A. (2009). Simultaneous detection of free and total prostate specific antigen on a screen-printed electrochemical dual sensor. *Biosensors & bioelectronics*, *24*(8), 2678–2683. https://doi.org/10.1016/j.bios.2009.01.043

[75] Torrente-Rodríguez, R. M., Campuzano, S., López-Hernández, E., Montiel, V. R., Barderas, R., Granados, R., Sánchez-Puelles, J. M., & Pingarrón, J. M. (2015). Simultaneous detection of two breast cancer-related miRNAs in tumor tissues using p19-based disposable amperometric magnetobiosensing platforms. *Biosensors & bioelectronics*, *66*, 385–391. https://doi.org/10.1016/j.bios.2014.11.047

[76] Labib, M., Khan, N., Ghobadloo, S. M., Cheng, J., Pezacki, J. P., & Berezovski, M. V. (2013). Three-mode electrochemical sensing of ultralow microRNA levels. *Journal of the American Chemical Society*, *135*(8), 3027–3038. https://doi.org/10.1021/ja308216z

[77] Novák, J., Kružliak, P., Bienertová-Vašků, J., Slabý, O., & Novák, M. (2014). MicroRNA-206: a promising theranostic marker. *Theranostics*, *4*(2), 119–133. https://doi.org/10.7150/thno.7552

[78] Aziz, N. B., , Mahmudunnabi, R. G., , Umer, M., , Sharma, S., , Rashid, M. A., , Alhamhoom, Y., , Shim, Y. B., , Salomon, C., , & Shiddiky, M. J. A., (2020). MicroRNAs in ovarian cancer and recent advances in the development of microRNA-based biosensors. *The Analyst*, *145*(6), 2038–2057. https://doi.org/10.1039/c9an02263e

CHAPTER 2

Development of a label-free electrochemical biosensor for the detection of miRNA-206 in plasma of Alzheimer disease patients.

2 INTRODUCTION

miRNAs act as fingerprints of many neurological diseases and, therefore, the detection of their levels in circular blood, in a precise and sensitive way, is highly important as it can enable early detection of disease, lead to more efficient treatment, and enhance the patients' quality of life [1]. To achieve this objective, label-free biosensors based on electrochemical impedance spectroscopy have gained attention since they can be low cost, have impressive sensitivity, high compatibility with advanced detection devices and applicability to point of care systems [2].

The construction of a label-free biosensor based on a direct hybridization format with good sensitivity is extremely important and requires that hybridization between miRNA capture-probe and miRNA target to be maximised. Some factors that contribute to the optimization of this detection system are: (1) immobilization time of the miRNA capture-probe on the electrode surface, (2) control of the miRNA capture-probe surface density immobilized on the electrode surface, (3) minimizing electrostatic interactions between the chemisorb miRNA chains and the gold electrode (non-specific interactions) and (4) time of hybridization between capture-probe and target.

The importance of controlling the surface density of the capture-probe is directly related to the intrinsic charge of the miRNA, e.g. of its phosphate backbone. Hybridization between miRNAs causes an increase in the negative charge on the electrode surface, which, when immersed in a solution containing negatively charged redox ions, undergoes electrostatic repulsion, and hinders the charge transfer between electrode-electrolyte. This causes a change in electron transfer barrier, and consequently, a charge transfer resistance that can be detected using electrochemical impedance spectroscopy (EIS) [3]. Detection of this change requires that the miRNA charge is not significantly screened by counterions presents at the immobilization buffer and that probes are closely spaced compared to the Debye charge screening length in the solution, allowing an optimal performance of the sensor. Thus, an accurate control of the surface density and orientation of the immobilized miRNA probe is necessary since a high density can, due to steric impedance and electrostatic repulsion, prevent its hybridization with the target and, in contrast, a very small amount of capture-probe will be insufficient to produce a high-quality analytical response.

The steric effect generated by a high density of miRNA capture-probes on the electrode surface can be minimized or avoided by co-adsorption of a diluent such as mercaptohexanol (MCH) at the surface. These molecules can also help prevent non-specific adsorption. The hydrophilic nature of MCH helps the lateral movement of the oligonucleotides, reducing van der Waals interactions between molecules and promoting an upright conformation of miRNA strands [4]. Studies presented by Herne and Tarlov [5] suggested that the density of miRNA capture-probe on the surface can be optimised by forming a significantly compact self-assembled monolayer (SAM) which is then backfilled with MCH. However, Keighley et. al [6] reported that it is the co-adsorption of the capture-probe with the diluent that generates an improvement in the capture efficiency and reproducibility of hybridization systems.

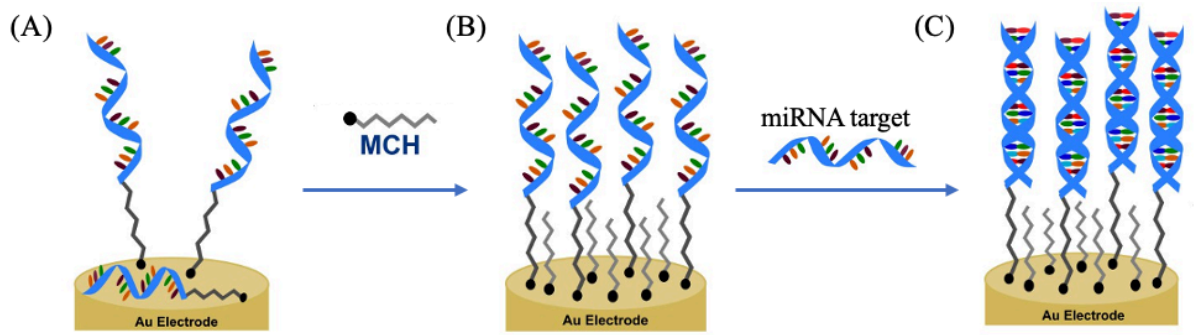


Figure 2.1.Schematic of a gold electrode (a) immobilized with miRNA through specific and non-specific adsorption, (b) co-immobilized with miRNA/MCH, (c) with oriented miRNA passivated with MCH and hybridized with miRNA target.

Although spacers and capture-probe co-immobilization has been reported in the literature for better control of surface coverage, this work explores the competitive reaction between miRNA capture-probe and alkanethiols under different ratios and their consequences on surface density, as well as investigating the immobilization time of the capture-probe and hybridization time of capture probe-target under different surface densities. Moreover, the procedure used for the formation of a mixed monolayer was based on the reported by Estrela *et al.* [6] with significant modifications, specifically: (1) the co-immobilization of MCH and miRNA capture-probe at 37 °C and (2) the removal of an extra step of backfilling with MCH after complete formation of SAM.

Overall, the aim of this work is to contribute significantly to improvement (enhancement of the sensitivity and selectivity) of the transducer surface which is a key element in the construction

of biosensors. For that, the formation of a stable monolayer of well-oriented captures highly accessible to the target was investigated, as well as the degree of non-specific adsorptions.

2.1 Experimental Procedures

2.1.1 Materials: Chemicals and Solutions

A 2mm diameter of a conventional gold disc working electrode was purchased from IJ Cambria, Wales, UK. The alpha alumina with a particle size of 0.3 μm and 0.05 μm used to polish the working electrode was obtained from Buehler, USA.

Sulphuric acid (H_2SO_4, 95-98%), phosphate buffer saline (PBS), hexa-amine ruthenium(III) chloride ($[Ru(NH_3)_6]Cl_3$), TCEP (tris[2-carboxyethyl]phosphine), 6-mercapto-1-hexanol (MCH), Trizma-HCl (pH =7.4), BSA (Bovine Serum Albumin), and potassium ferro/ferricyanide ($K_3Fe(CN)_6$; $K_4Fe(CN)_6$) were obtained by Sigma-Aldrich.

All the aqueous solutions described in this work, if it was not stated otherwise, were prepared using Milli-Q water (Millipore Core, 18 MΩ cm^{-1}).

The oligonucleotides (100 μM, purity ≥98%), RNase free water and TE buffer (10mM Tris and 1mM EDTA) used to prepare immobilization and hybridization solutions were purchased from IDT. The sequence composition used was:

Capture-probe (miRNA-206): 5'-/5 $HSMC_6$-D/ C-CAC- ACA-CUU- 3'

Target (Fully complementary): 3'- G-GUG-UGU-GAA-GGA-AUG-UAA-GGU- 5'

Target (4 base mismatch- miRNA-1): 3'-UAU GUA UGA AGA AAU GUA AGG U-5'

Screened human plasma samples from healthy donors and Alzheimer disease patients tested in this work were provided from CIBERNED and were collected with full ethical approval and patient consent. Virkon® solutions (purchased from VWR) were used to disinfect surfaces and was added to all plasma samples prior to disposal.

2.1.2 Instrumentation

Electrochemical measurements were performed using a conventional three-electrode cell consisting of a gold disc working electrode (diameter, Φ = 2 mm), a silver/silver chloride reference electrode (Ag/AgCl in 3 M KCl) and a platinum wire as a counter electrode. All the solutions were deoxygenated with nitrogen prior to use. Moreover, these measurements were performed using a CHI760D electrochemistry workstation at room temperature (22±2°C).

2.1.3 Procedures

2.1.3.1 Electrode Cleaning and surface preparation

Prior to surface modifications, the gold disc electrode was mechanically polished and electrochemically cleaned. For the mechanical cleaning, 0.3 and 0.05 μm of aqueous alumina paste was deposited on a polishing pad and polishing was carried out for 10 minutes. To eliminate remnants of alumina powder and other impurities, the electrode was washed and sonicated with milli-Q water for 10 minutes.

The electrochemical cleaning of the polished electrode was made by the immersion of the electrode in the three-electrode electrochemical cell with 0.5 M H_2SO_4. Cyclic voltammograms was performed between −0.2 V and 1.6 V at a scan rate of 0.1 V/s until a stable cyclic voltammogram was obtained. Then, the gold electrode was washed with milli-Q water and dried with nitrogen.

Studies of surface roughness were conducted as the final step of surface preparation. For that purpose, the integration of the gold reduction peak was obtained using cyclic voltammetry in 0.1 M H_2SO_4 with the potential sweeping between −0.3 V and 1.5 V at scan rate of 0.1 V/s. Equation 1 shows the relationship between the Au reduction peak and the reduction charge per microscopic unit area that has been experimentally determined by Trasatti *et al.* [7] as 390 ± 10 μC cm^{-2}. The surface roughness could, then, be calculated by correlating the geometric area (Equation 2) to the results obtained by Equation 1 , described here as equation (3).

$$A_M = \frac{Ip}{3.9\ x\ 10^{-4}\ C\ cm^{-2}} \qquad \text{Equation 2.1: Microscopic Area}$$

$$A_G = \pi r^2 \qquad \text{Equation 2.2: Geometric Area}$$

$$R.F.= \frac{A_M}{A_G}$$ Equation 2.3: Roughness factor

All electrodes used at this work had as prerequisite to maintain their surface roughness between 1.6 to 1.8 to enhance reproducibility between experiments.

2.1.3.2 Construction of the label-free sensor

Initially, a mixed monolayer of miRNA/MCH was prepared in a clean gold electrode by the incubation of the surface in an Eppendorf containing 10 μM solution of the 5'-thiolated oligo and 40 μM of 6- mercapto-1 hexanol. The Eppendorf was sealed with parafilm and placed in the oven at 37℃ for eighty minutes. Then, the electrode was rinsed with nuclease free water to remove any possible loosely bound strands.

Subsequently, the capture-probe modified gold electrode was incubated in different concentrations of miRNA target, between 1 aM and 1 μM, leading to the hybridization of the 3' end of this target to the capture-probe strand immobilized into the electrode surface. The optimum time for miRNA target hybridization was 20 min in an oven at 37℃. The electrode was washed with nuclease free water so that, afterwards, quantitative analyses on the electrode were possible.

It is worth noting that for the successful development of the miRNA assay, particular attention must be given for the following points: (1) preparation of the working solution and (2) reduction of the thiol bond tethered at the miRNA capture-probe. In the preparation of the working solutions, several aliquots from stock solutions of oligonucleotides (100 μM) were used to avoid freeze/thaw cycles. These solutions were always kept in the fridge prior to the measurements. From these samples, less concentrated standards were obtained by accurate dilution in the TE buffer (10 mM Tris and 1 mM EDTA).

Regarding the preparation of the immobilization buffer, TCEP (tris[2-carboxyethyl]phosphine) were added in 100x excess during 2h for reduction and release of the thiol bonds from the capture-probe oligo.

2.1.3.3 Electrochemical follow up of the modification steps

After the immobilization step, cyclic voltammetry (CV) curves were performed between -0.5 to 0.9 V over a range of scan rates, from 0.01 to 0.50 V s^{-1}. The gold modified electrode was placed in a three-electrode cell filled with 0.01 M of PBS solution and 1 mM of potassium ferro/ferricyanide.

Following hybridization of the miRNA capture-probe - target sequence, the CV curves were measured between -0.5 to 0.9 V at 50 mVs^{-1} scan rate over the same electrolyte (i.e. 1 mM potassium ferro/ferricyanide dissolved in 0.01 M PBS).

2.1.3.4 Calculation of capacitance from CV

To determine the differential capacitance using CV it was necessary to find a region in the i-E curve, where no faradaic reaction occurs (i.e. where no current related to a typical charge transfer process flows). Once in this potential region, the current (i_c) has capacitive nature and is directly proportional to scan rate. The slope of the CV plotting of i_c versus several scan rates (v) leads to the capacitance (*Cdl*) values.

$$2C_{dl} = \frac{\Delta ic}{Av}$$

2.1.3.5 Estimation of the heterogeneous electron transfer (k_0) and the diffusion coefficient (D) from CV

In terms of experimental determination of the standard heterogeneous electron transfer rate constant, k_0, the most popular method used in the literature is Cyclic Voltammetry. This approach became widely used in 1956, when the theory of electron transfer was reported by Marcus [8]. In this method, which was improved by Nicholson [9], a typical procedure for a quasi-reversible system is to investigate the peak- to- peak separation (ΔE) of a redox couple in solution as a function of scan rate.

Lavagnini *et al.* [10] simplified Nicholson's method by calculating the dimensionless parameter ψ using Equation 2.4 and correlating it, subsequently, to Equation 2.5 which shows the relationship between k_0 and ψ. Therefore, through this mathematical manipulation, k_0 can be obtained directly from the slope of the graph of ψ versus $\sqrt{\frac{RT}{\pi\, n\, F\, D}}\; v^{-1/2}$.

$$\psi = \frac{-0.6288+0.0021\,\Delta Ep}{1-0.017\,\Delta Ep} \quad \text{Equation 2.4}$$

$$\psi = \mathrm{k}_0 \sqrt{\frac{RT}{\pi\, n\, F\, D}}\, v^{-1/2} \quad \text{Equation 2.5}$$

It is also worth noting that this method only works for quasi-reversible systems. The diffusion coefficient was calculated using the equation Randles-Sevcik, described below.

$$i_p = 2.687\, x10^5\, n^{3/2}\, A\, C\, D^{1/2}\, v^{1/2} \quad \text{Equation 2.6}$$

In Equation 2.5 and 2.6, D is the diffusion coefficient of electroactive species ($cm^2\ s^{-1}$), n is the number of electrons transferred in the reaction, F is the Faraday constant ($C\ mol^{-1}$), R is the molar gas constant ($JK^{-1}mol^{-1}$), T is the absolute temperature (K), C is the concentration of the redox species in solution ($mol\ cm^{-3}$) and A is the area of the working electrode (cm^2). Therefore, the constant has units of $C\ mol^{-1}\ V^{-1}$.

2.1.3.6 Impedance analysis

The change in electron transfer, as well, the capacitive behaviour of the gold electrode surface was measured after each surface modification e.g. after immobilisation with miRNA capture-probe and hybridization with miRNA target. Electrochemical impedance spectroscopy was measured using a DC potential 0.231 V with an amplitude of 25 mV vs. Ag/AgCl in 0.01M of PBS electrolyte with 1mM of potassium ferrocyanide ($[Fe(CN)^{3-/4-}]$) over a frequency range from 0.1 Hz to 10^5 Hz.

The EIS parameters, such as: Electrolyte resistance (R_s) , Capacitance of the double layer (C_{dl}), charge transfer resistance (R_{ct}), heterogeneous electron transfer (k_0), and chi-square (χ^2), were obtained by modelling the AC data (obtained through the impedance experiments) to a standard Randles equivalent circuit using ZView software. Figure 2.2 illustrates this circuit, consisting of a parallel combination of a constant phase element (CPE) and a faradaic impedance (Z_f), which is a series combination of charge transfer resistance (R_{ct}) and the Warburg impedance (W_s or Z_w).

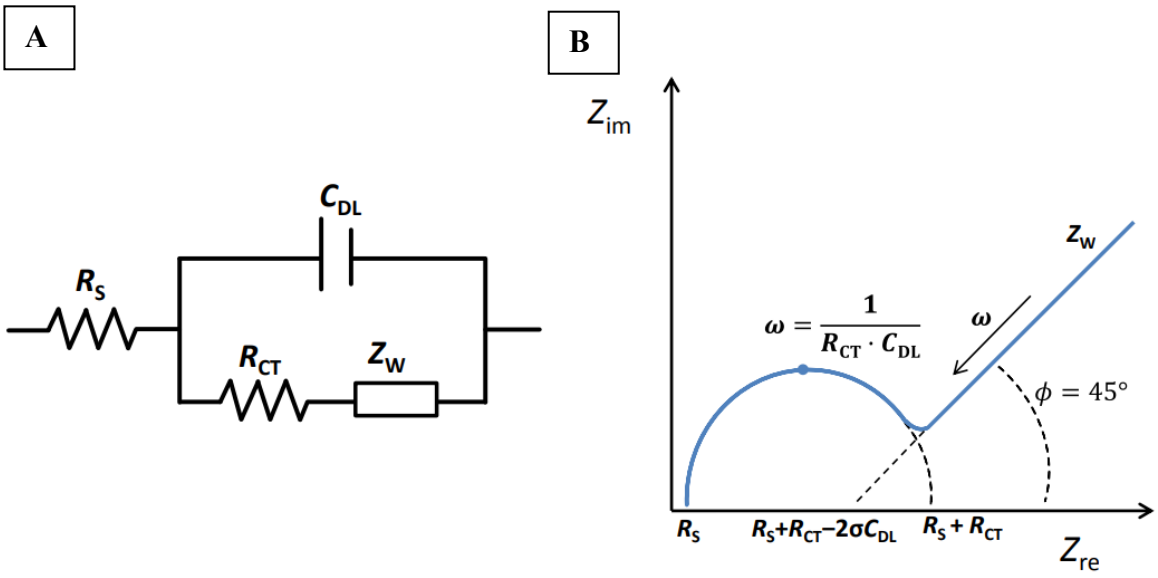


Figure 2.2. (A) Standard Randle's equivalent circuit model used to fit the electrochemical impedance spectroscopy data and (B) the corresponding Nyquist Diagram.

Using the values of R_{ct} obtained from the fitting of the impedance plot and the sum of the Equation 2.7 and 2.8, the heterogeneous electron transfer was calculated.

$$R_{ct} = \frac{R\,T}{n\,F}\,\frac{1}{I^o} \quad \text{Equation 2.7}$$

$$I^o = nFAk_0C \quad \text{Equation 2.8}$$

So,

$$k_0 = \frac{R\,T}{n^2\,F^2\,A\,C}\,\frac{1}{R_{ct}} \quad \text{Equation 2.9}$$

where R is the gas constant, T the temperature, F the Faraday's constant, n the number of electrons, I_0 the exchange current density, A the area of electrode, C the concentration of the redox couple, R_{ct} the charge transfer resistance.

2.1.3.7 Calculation of capacitance

The capacitance from a depressed semicircle model (a Constant Phase Element in parallel with a resistor) was first explained in the literature by the usage of the Cole-Cole circuit elements, also called by MacDonald [11] as ZARC element.

In MacDonald's work, the depressed semicircles were expressed through their direct modelling as a system with a distribution of time constants, as presented in Equation 2.10.

$$Z = \frac{R_0}{[\,1+(j\ x\ t\,)^n\,]} \quad \text{Equation 2.10}$$

Where R_0 is the low frequency real axis intercept, *t* is the mean time constant, and *n* is related to the depressed angle between the axis -Z" versus Z' in the Nyquist plot.

The use of this equation has a caveat. It considers that different points on an electrode surface presents different electrochemical activation energy (E^*), being the probability to find it described in Equation 2.11 [11].

$$P(E*) \cong e^{\frac{(1-n)\cdot E*}{k\cdot T}} \quad \text{Equation 2.11}$$

By analysing the time constant *(t)* as a function of activation energy, it can be expressed as illustrated by Equation 2.12

$$t(\,E*) = t°e^{[\,E*\,/\,k\cdot T\,]} \text{ Equation 2.12}$$

Therefore by applying the relation $t\,(E^*) = R(E^*) \cdot C$ at Equation 2.12, the faradaic resistance (resistance to the charge transfer) and the capacitance, presents its dependence to the activation energy.

However, the calculus of capacitance, nowadays, brings some modifications of the Equation 10, leading the focus in terms of distributions of capacitances instead of distributions of time constants. Derived from the work of Orazem *et al.* [12], Equation 2.13 demonstrate that the same Z could also be obtained from the parallel combination of resistor and CPE, yielding to the values of R_0 and Q_0 used by the majority of the commercially available EIS fitting programs.

$$Z = \frac{R_0}{[\,1+R_0\ x\ Q_0\ x\ (j\ x\ )^n\,]} \quad \text{Equation 2.13}$$

This equation could only be described, once it meets the condition elucidated below.

$$R_0 \, x \, Q_0 = t^n \qquad \text{Equation 2.14}$$

Deriving Equation 2.14 and considering **t = RC**, the real value of capacitance could be found by the mathematics shown in Equation 2.15.

$$C = \frac{(Q_0 \, x \, R_{ct})^{1/n}}{R_{ct}} \qquad \text{Equation 2.15}$$

In this work, the EIS fitting program used (Zview) yield values of R_0 (R_{ct}), CPE-P (n) and CPE-T (Q_0), which was directly applied at Equation 2.15 to obtain the capacitance of the system.

2.1.3.8 Calculation of the monolayer thickness

After obtaining the parameters of resistance to charge transfer between electrode-electrolyte and the capacitance values presented after different immobilization times of the miRNA monolayer at the gold surface, it was possible to calculate the monolayer thickness formed (d_i).

To estimate the monolayer thickness on the surface were made correlations of the capacitance of the double layer (C_{dl}), the permittivity of free space (ε_0), the dielectric constant of the layer (ε_i) and the electrode area (A), as suggested by Equation 2.16 [14].

$$d_{i=} \quad \frac{\varepsilon_0 \, \varepsilon_i \, A}{C_{dl}} \qquad \text{Equation 2.16}$$

For calculations, the dielectric constant of water was used as the ε_i value [15]. This approximation relies on several works found in the literature [15][16][17], where the relative humidity was pointed as the major contributor to tune the layer elasticity and thickness. So, once the elastic modulus is determined not by the forces between the structural atoms, but by the interaction with the "solvent", i.e. the water molecules, the calculations of thickness could be based on the water junctions.

However, it is important to keep in mind that surface density also plays an important role in the elasticity of miRNAs layers and, to use Equation 2.16, it is being considered a situation where the distance between the molecules maximizes the water mediated interactions between the strands. As this requisite is not satisfied for the whole range of the studied immobilizations

time, there is a degree of uncertainty over the thickness values, which needs to be confirmed by other surface analysis techniques (e.g. AFM, SEM).

2.1.3.9 Calculation of miRNA surface density

The miRNA surface density present in the gold electrode immobilized at different proportions of the mixed SAM, was quantified using the chronocoulometry technique (CC) as described by Zhang *et al.* [15]. In this methodology, the trivalent cation from the electroactive label $[Ru(NH_3)_6]^{3+}$ (RuHex) binds to the monovalent anionic phosphate from the miRNA strands (ratio 1:3), leading to the formation of a complex whose cumulative redox charge generates a direct signal, proportional to the amount of the capture-probe at the electrode surface [15]. As this technique permits the differentiation between the diffusional redox process and the surface-confined redox process (as double layer charge), it can reliably quantify the RuHex immobilized over the gold surface.

Therefore, initially, for the calculation of a double layer charge, the modified electrodes were submerged in 10 mM of Trizma-HCl buffer and a potential of -0.3V to -0.8 V for 500 ms was applied. Subsequently, to calculate the total charge of the cation ($[Ru(NH_3)_6]^{3+}$) adsorbed on the surface, 100 µM of hexaammineruthenium (III) chloride was added to the tris buffer solution and the measurement was repeated. Both solutions used in this experiment were purged thoroughly with nitrogen for 10 min.

After measuring these parameters, the Cottrell equation was used to relate the charges resulting from the reduction of the cation in surface and solution, in addition to the charge generated by the double layer, thus:

$$Q = \frac{2nFADo^{1/2}\,C}{\pi^{1/2}}\; t^{1/2} + Qdl + nFA\Gamma_0 \quad \text{Equation 2.17}$$

where, n is the number of electrons per molecule for reduction, F is the Faraday constant (C/mol), A is the electrode area (cm^2), D_o is the diffusion coefficient (cm^2/s), C is the bulk concentration of $[Ru(NH_3)_6]^{3+}$ (mol/cm^3), Q_{dl} is the double-layer charge (C) and $nFA\Gamma_0$ is the reduction charge of the surface adsorbed redox marker (mol/cm^2).

An Anson plot (Q versus t½) was also used in this work to assist in surface density calculations, since the extrapolation of the linear part through the least squares fit to the intercept at t = 0

corresponds to the sum of *Qdl* and $nFA\Gamma_0$. An example of this type of plot is illustrated in Figure 2.3.

In addition, as the double layer capacitance between the measurements with and without $[Ru(NH_3)_6]^{3+}$ varies by approximately 1%, this value was considered constant and $nFA\Gamma_0$was determined from the difference between intercepts. Therefore, the miRNA surface density was determined from the surface excess of $[Ru(NH_3)_6]^{3+}$ through the formula:

$$\Gamma_{miRNA} = \Gamma_0 \, (z/m) \;\; N_A \qquad \text{Equation 2.18}$$

where Γ_{miRNA} is the capture-probe surface density (molecules/cm^2), m is the number of miRNA bases, z the charge on the RuHex molecule and N_A is Avogadro's number.

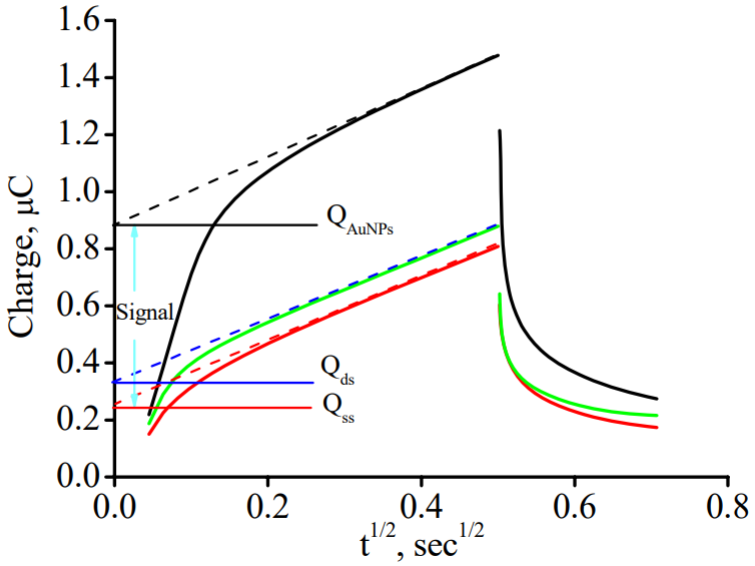


Figure 2.3. Representative experimental chronocoulometric curves for gold electrodes modified with ssDNA probes (red, Q_{ss}); electrodes after hybridization with 1 µM target DNA (green, Q_{ds}) and electrodes after hybridization with 10 pM target DNA and with the amplification of AuNPs (black, Q_{AuNPs}). Redox charges of RuHex bound to DNA are obtained from chronocoulometric intercepts at t=0. The signal is defined as the increment of the redox charge, i.e., signal = Qds-Qss, or signal = QAuNPS-Qss. Figure adapted from [18].

For the hybridization efficiency calculations, the density of the miRNA target hybridized to the capture-probe was determined using the same method described above. However, to use the same electrode through the quantification of miRNA immobilized and hybridized to the surface, it was necessary to remove the Ru $(NH_3)_6$ $^{3+}$ cation present in the electrode after

measuring its total charge adsorbed to the miRNAs immobilized on the surface. For that purpose, following what was reported by Su *et al.* [19] and Keighley *et al.* [6], the electrodes were immersed for 30 minutes in high ionic strength buffer, such as 50 mM of PBS + Na_2SO_4 + 10mM of EDTA, once $[Ru(NH_3)_6]^{3+}$ presents a high-dissociation rate in solutions with high concentrations of monovalent cations.

2.2 Results and Discussion

2.2.1 Electrochemical follow-up of the gold surface modifications

The surface coverage of miRNA on the gold electrode, as deposited from a solution containing 10 μM miRNA capture-probe under different times, was investigated by studying the changes in the electrochemical properties over time. To monitor the electron transfer properties, potassium ferro/ferricyanide was used as a redox probe in a phosphate-buffered saline electrolyte and cyclic voltammetry and EIS was used as the analytical tools.

Although cyclic voltammetry is known to be a less sensitive technique for detecting kinetic heterogeneity, when compared to the impedance technique, it was used in this work as a tool to assess not only the type of adsorptive process that occurs on the electrode surface, but also the integrity of the monolayer.

The cyclic voltammograms corresponding to the immobilization times: 0, 10, 30, 40, 80 min and 17 h were shown in Figure 2.4 and the variation in the reduction and oxidation potential of the redox probe during the different times was shown in Table 2.1.

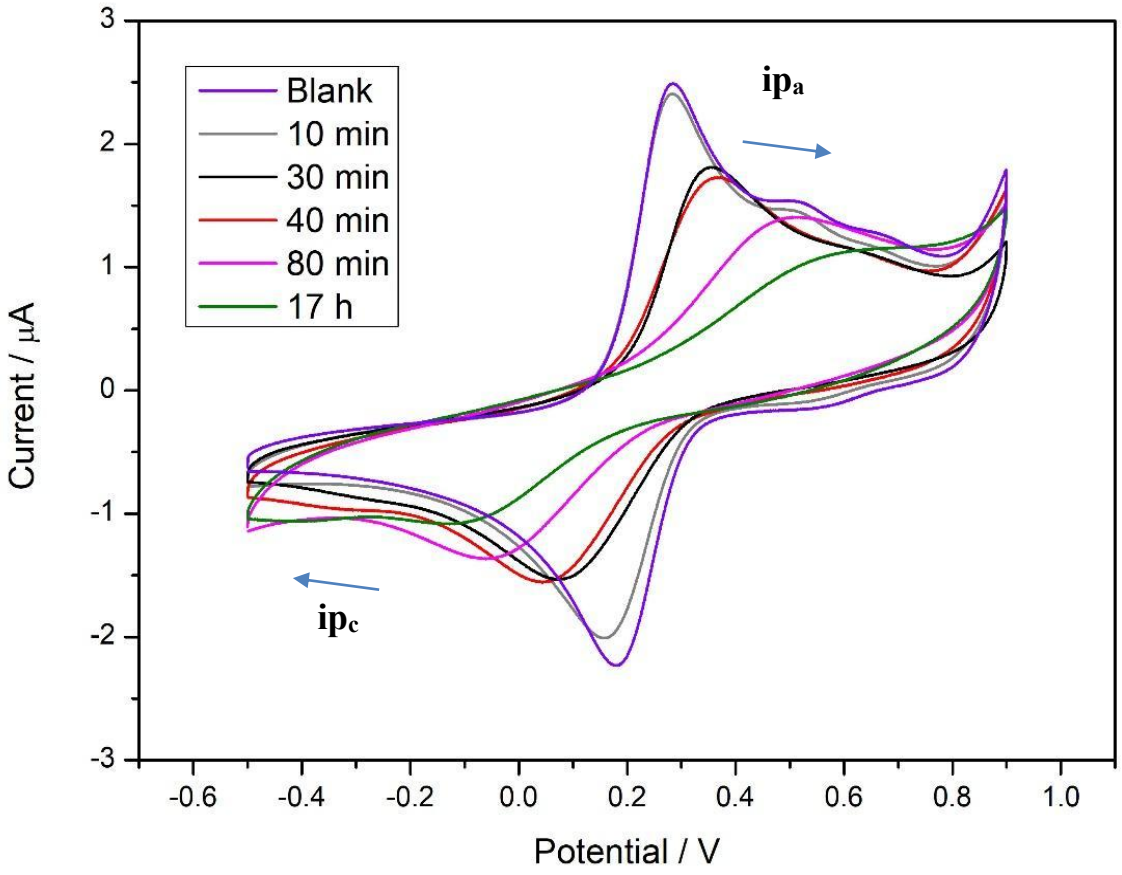


Figure 2.4. Representative cyclic voltammograms of the gold electrode modified with 10 µM solution of miRNA capture-probe at different immobilization times, such as: 0, 10, 30, 40, 80 min and 17 h. Electrochemical species: 1 mM $[Fe(CN)_6]^{3-/4-}$ with 0.01 M PBS. Scan rate: 500 mV/s. The analysis was performed in triplicate.

It was possible to notice that between the immobilization times 0 min, characterized only by the presence of the bare electrode (purple line), and 17h (green line), there were consecutive suppressions of the cathodic and anodic peaks caused by the increase of miRNA capture-probe immobilized on the gold surface. Consequently, at these times, an increase in the peak-to-peak separation can be observed, with cathodic peaks shifting to more negative values and anodic peaks to more positive values. It was also possible to observe that only after 80 min, the delta peak potential of the redox probe shifted significantly relative to the bare electrode.

Table 2.1. From the voltammogram in Figure 2.4 it is possible to extract the potentials of the anodic and cathodic peak. Also, the difference between them, ΔE, for each time of the immobilization. The average values and standard deviations are based on n=3.

Time (min)	*Epa (V)*	*Epc (V)*	*/ΔE (V)/*
0	0.231 ± 0.020	0.171 ± 0.010	0.060 ± 0.010
10	0.274 ± 0.009	0.157 ± 0.015	0.117 ± 0.024
30	0.350 ± 0.020	0.084 ± 0.022	0.266 ± 0.022
40	0.364 ± 0.010	0.052 ± 0.015	0.312 ± 0.016
80	0.514 ± 0.020	-0.049 ± 0.011	0.563± 0.022
1020	0.591 ± 0.022	-0.092 ± 0.032	0.683 ± 0.041

The decrease in the electron transfer rate between the ferro/ferricyanide and the gold surface (change in charge) is directly related to the barrier effect that the miRNA monolayer presents when adsorbed on the gold surface. Since miRNAs have a phosphate backbone, which is negatively charged, when present on the gold surface they can both physically block the surface of the electrode and also generate electrostatic repulsion due their interaction with the negative charge of the ferrocyanide ions, hindering the diffusion of the capture-probe to the electrode surface.

When correlating the increase in the coverage of the gold electrode by adsorption of miRNA capture-probe with the consequent decrease in the penetration of redox ions into the formed monolayer (as shown Figure 2.4), it was possible to formulate initial assumptions about the adsorption mechanism that occurs on the surface. Therefore, it is expected, in a fast-initial phase, miRNAs to be randomly adsorbed in the gold surface due to the strong affinity of sulphur to gold. At this low coverage rates, supposedly formed in this work in times less than 80 minutes, miRNAs are expected to be lying parallel to the surface [20][15], making it difficult for ferrocyanide ions to penetrate the defects present on the surface. In times between 80 min and 17h more molecules are adsorbed on the surface, and it is expected an increase in the lateral interactions between hydrocarbon chains present in the miRNA extension. These attached strands interacting with one another through Van der Waals force would generate the lateral movement of the bound species and explain the further stabilization of the structure.

To validate the model, calculations of redox ion diffusion, heterogeneous electron transfer rate (k_0) and interfacial capacitance (C_{dl}) were necessary. For that, the effects of scan rate (ν) on the peak current and on the potential in the cyclic voltammograms were initially investigated.

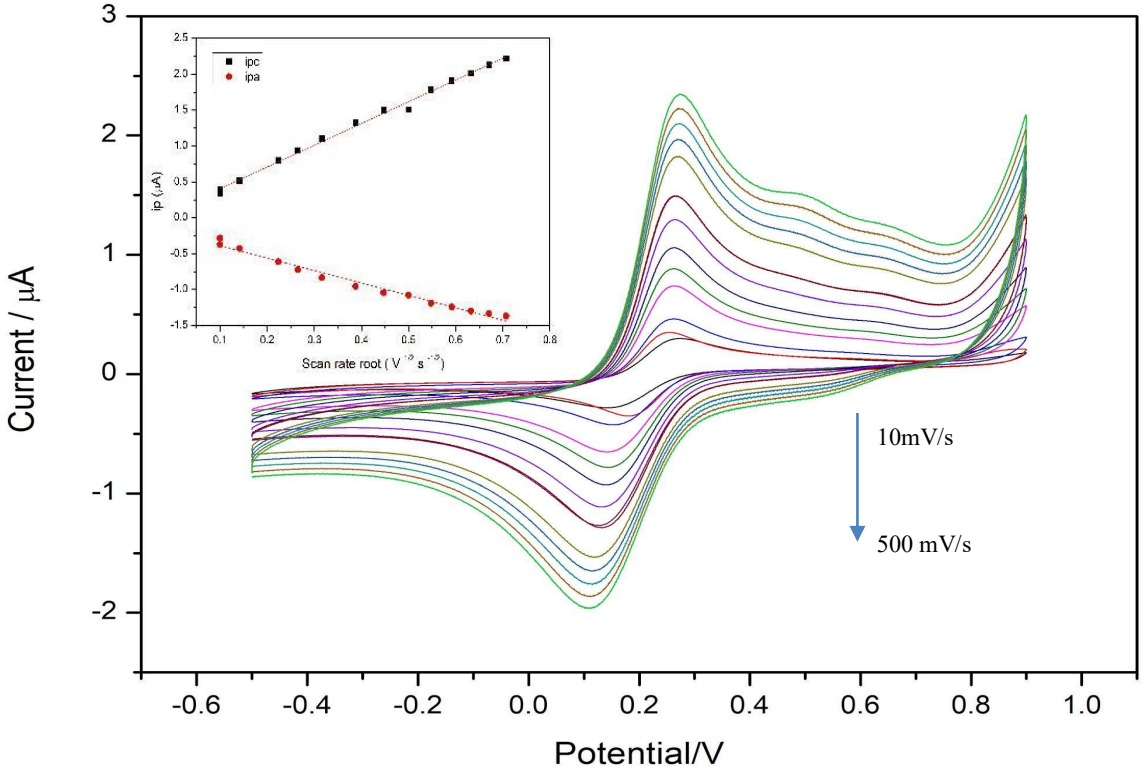


Figure 2.5. Cyclic voltammograms of the gold electrode modified with 10 µM of miRNA during 10 min at various scan rates (10, 20, 50, 70, 100, 150, 200, 250, 300, 350, 400, 450, 500 mV/s from outer to inner). Inset: Dependence of reduction and oxidation peak currents on the square root of scan rate ($\nu^{1/2}$). Electrochemical species: 1 mM $[Fe(CN)_6]^{3-/4-}$ with 0.01 M PBS. The analysis was performed in triplicate.

Figure 2.5 shows the cyclic voltammograms of the redox probe diffused at a gold electrode immobilized with miRNA capture-probe for 10 min and recorded at different scan rates (10 mVs^{-1} to 500 mVs^{-1}). The anodic peak at 0.255V at a scan rate of 0.01Vs^{-1} shifted towards more positive potential as scan rate increased reaching the potential of 0.274 V at 0.5 Vs^{-1} scan rate. On the other hand, cathodic peak at reverse scan appeared at 0.143 V and shifted toward more negative potential with increasing scan rate up to 0.5 Vs^{-1}.

Once the increase in the peaks separation is beyond 57/n (mV) but still depends linearly on the square root of the scan rate, this indicates a quasi-reversible electrode process (inset Fig. 2.5)

[21]. This plot (peak current versus $v^{1/2}$) also provides indications that the ion transport to and away from the electrode is under semi-infinite linear diffusion control.

After certifying the type of process that occurs on the electrode surface, the Randles-Sevcik equation was used to calculate the diffusion coefficients of the ferrocyanide ions on the electrodes immobilized with miRNAs capture-probe adsorbed at different times. In addition, as described in the experimental part of this work, k_0 and C_{dl} were calculated using the Lavagnini method and the currents in non-faradaic mode, respectively. Table 2.2 presents the data.

Table 2.2. Variations on the double-layer capacitance (C_{dl}) , heterogeneous charge transfer (k_0) and diffusion coefficients (D) values of a gold electrode immobilized with 10 µM of miRNA capture-probe at different times. The average values and standard deviation are calculated based on n=3.

Time (min)	C_{dl} (µFcm^{-2})	D_0 (cm^2 s^{-1})	k_0 ($cm\ s^{-1}$)
0	36.51± 1.01	6.20 x10^{-6}	(15.11 ± 0.03) x 10 $^{-3}$
10	29.20 ± 0.14	6.01 x10^{-6}	(8.30 ± 0.02) x 10 $^{-4}$
30	24.11 ± 0.21	6.01x10^{-6}	(7.32 ± 0.01) x 10 $^{-4}$
40	21.01 ± 0.20	-	(6.54 ± 0.05) x 10 $^{-4}$
80	18.23 ± 0.21	-	(3.70 ± 0.04) x 10 $^{-4}$
1020	18.01 ± 0.10	-	(3.63 ± 0.07) x 10 $^{-4}$

The diffusion value of the redox pair over bare gold electrode is 6.20 x10^{-6} cm^2 s^{-1}, which is in accordance with the values reported in the literature for this system [22]. Significantly, the diffusion coefficient does not measurably change as the miRNA capture-probe is immobilized confirming that diffusion through solution represents the controlling mass transport process.

Evaluating the values of heterogeneous charge transfer rate (k_0) and double layer capacitance (C_{dl}), it can be seen that both variables *decrease* when the exposure time of miRNA capture-probe to the surface increases. Furthermore, the slight increase in electron transfer and capacitance values between 80 min and 17h suggest that an optimum immobilization time of miRNA capture-probe on the surface can be obtained in 80 min.

The decreasing capacitance as the miRNA capture-probe deposits is consistent with displacement of water and ions from the electrode surface by the miRNA that has a lower dielectric constant (<80.4 at 20 °C) [23]. Hence, the decrease in capacitance over time is consistent with an increasing miRNA coverage over time. The final capacitance, approximately 18.01±0.10 μF cm^{-2}, is higher than that observed for alkane thiol monolayers (i.e. 5-10 μF cm^{-2}) which may suggest that the miRNA monolayer is not fully compact but may have some defects that act as channels for ionic exchange. Thus, for a more complete assessment of the monolayer, impedance studies following different deposition times (Figure 2.6) were made and the results modelled using modified equivalent Randles circuits.

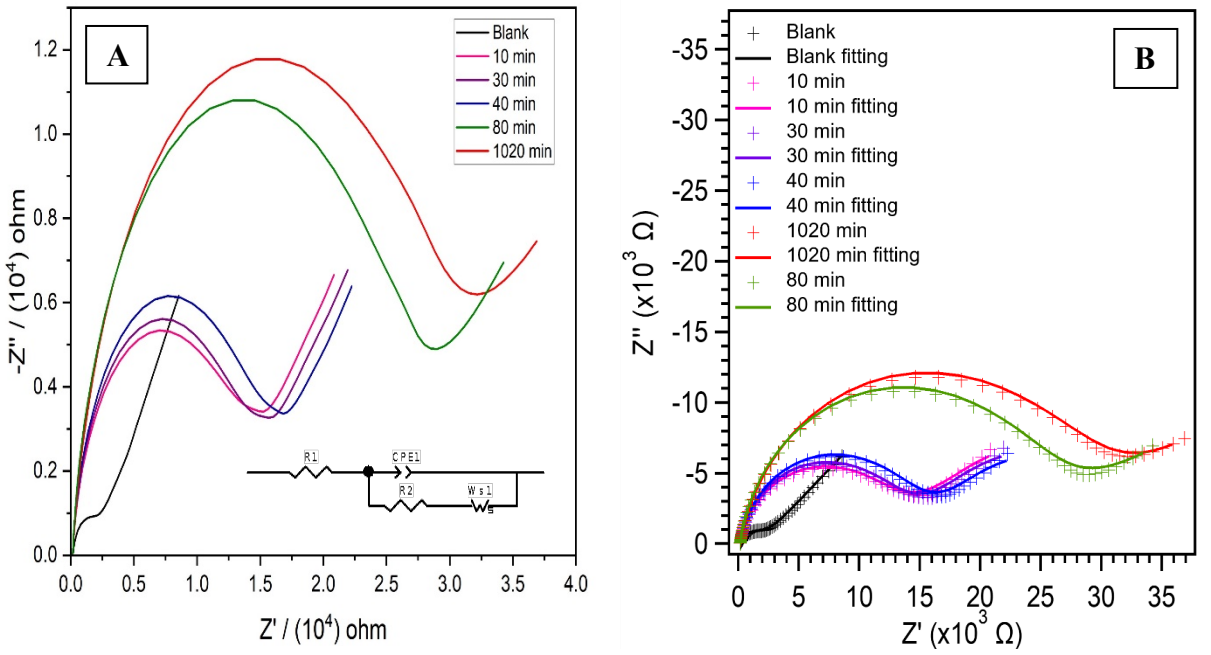


Figure 2.6. (A) Nyquist plot of the impedance spectra obtained by the gold electrode immobilized with 10 μM of miRNA capture-probe over different times. Inset: modified equivalent Randles circuit used to model impedance data, where R_1 is the electrolyte resistance; WS_1 is the Warburg impedance; R_2 is the charge-transfer resistance; and CPE_1 is the double-layer capacitance. Electrolyte used: 1mM [$Fe(CN)_6^{3-/4-}$] in 0.01 M PBS. Biasing potential: 0.231V. Amplitude: 25 mV. Frequency range: 0.1 Hz to 10^5 Hz. (B) Fitting of the Nyquist plots presented in (A) using the equivalent Randles circuit (inset) obtained through the ZView program. The analysis was performed in triplicate.

Initially, for the correlation of the results obtained by CV and EIS, a qualitative evaluation of the Nyquist plot was made after immobilization of miRNAs capture-probe over different times. Thus, it was possible to observe that the curve relative to the bare gold electrode has a long straight line in the low frequency region and a small semi-circular portion in the high frequency

region. This phenomenon, in agreement with that identified by cyclic voltammograms, characterizes a process in which mass transfer is controlled by diffusion. On the other hand, after immobilizations with miRNA capture-probe over different times, it was possible to observe a decrease in the straight line in the low frequency region with a subsequent increase in the semi-circular portion at high frequency. This phenomenon is indicative of the change in the system to a process that is strongly influenced by the rate of heterogeneous electron transfer [24]. Therefore, it is valid to conclude that by increasing the immobilization time of the miRNAs capture-probe on the surface, inhibits the dynamics of electron transfer.

It is known that an increasingly more efficient blocking of the surface will generate an increase in the charge transfer resistance (R_{ct}) and a lower corresponding heterogeneous electron transfer (k_0), as well as a decrease in the capacitance of the double layer (C_{dl}). Therefore, for a quantitative evaluation of these parameters, to generate data that reflect the reaction mechanism of this system, the Nyquist plot was modelled using the modified Randles circuit shown in the inset in Figure 2.6. Table 2.3 presents the measured EIS parameters.

Table 2.3. Summary of the impedance parameters obtained by fitting (with Randles circuit) the experimental results of a gold electrode immobilized with 10 µM of miRNA capture-probe at different times. Each value was reported with its standard deviation obtained from equivalent circuit modelling.

Time (min)	R_s (Ω)	C_{dl} (µFcm^{-2})	R_{ct} (KΩ)	k^0 (cm s^{-1})	d(nm)	χ^2
0	156.71 ± 0.03	37.30 ± 0.91	1.96 ± 0.03	(4.30± 0.05)x10 $^{-3}$	-	0.0005
10	146.02 ± 0.02	29.01± 0.11	11.76 ± 0.04	(7.21± 0.09) x10^{-4}	2.44 ± 0.10	0.0009
30	148.70 ±0.03	22.60 ± 0.45	12.33 ± 0.05	(7.03± 0.10) x10^{-4}	3.13 ± 0.15	0.0010
40	150.33 ±0.10	21.11± 0.20	13.69 ± 0.21	(6.20 ±0.30) x10^{-4}	3.37± 0.40	0.0010
80	151.42 ±0.13	18.44 ± 0.52	23.13 ± 0.50	(3.71± 0.30) x10^{-4}	3.83± 0.17	0.0010
1020	148.01 ±0.10	17.80 ± 0.13	26.77 ± 0.50	(3.20± 0.15) x10^{-4}	3.97± 0.33	0.0010

To confirm that the proposed equivalent Randles circuit are in good agreement with the experimental data, the chi-square values (χ^2) were evaluated. These values represent the error intrinsic to a specific circuit model when considering it as a representative of the reaction

mechanism between electrode-electrolyte. As the values presented here are less or equal to 0.001, it can be said that the model replicates the experimental behaviour accurately.

The electron transfer characteristics between the surface (where miRNA capture-probe is immobilized during different times) and the electrolyte, was investigated by the changes in the charge transfer resistance (*Rct*) and heterogeneous electron transfer rate constant (k_0) which, as stated in experimental section, are inversely proportional. By increasing the immobilization time from 0 min to 17h, an increase in *Rct* from 1.96± 0.03 KΩ to 26.77 ± 0.50 KΩ was observed, an approximately 13-fold increase. The resistance observed for the unmodified electrode is large because of the low concentration of electrolyte used. This has been chosen to ensure that the electrical double layer extends to the capture-probe -target binding region rather than collapsing close to the electrode surface as it would with a concentrated electrolyte.

The changes in resistance (from 0 min to 17h) correspond to a decrease in k^0 from 0.43 x10^{-2} cm s^{-1} to 3.20 x 10^{-4} cm s^{-1}, following capture-probe strand deposition. This data is consistent with the experiments analysed by cyclic voltammetry, which shows that increasing the miRNA immobilization time to 17h generates an increase in the blocking of the gold surface and consequently hinders the transfer of electrons between the electrode and the redox probe in solution.

The interfacial double-layer capacitance values decreased from 37.33 ± 0.91μF cm^{-2} for the bare gold electrode to 17.8 ± 0.13 μF cm^{-2} as the miRNA immobilization time increases, once more, in accordance with what was demonstrated by the studied cyclic voltammograms. This decrease can be justified if we consider that the immobilized oligonucleotides exhibit a behaviour that is similar to organic monolayers where, at very low frequencies, capacitance (*Cdl*) offers high impedance and slows the interfacial electron transfer rate compared to a bare working electrode [19]. In addition, after the 17h of the procedure, the resistance of the solution had a small variation (156.71 ± 0.03Ω to 148.1 ± 0.10 Ω) which, according to the literature, is expected for measurements under identical experimental conditions.

The thickness of the layer of oligonucleotides can be correlated with the heterogeneous electron transfer rate (k_0) and modulated by the concentration of the electrolyte, the potential applied to the system and the surface density of miRNA capture-probe. So, the monolayer thickness values (d_i) were used, in this work, as an asset to determine the optimal time to obtain the maximum miRNA adsorption on the surface and to hypothesize a mechanism of adsorption

[15]. Considering that the electrode is negatively charged by a potential of -0.231V and the concentration of the electrolyte is low (1 mM $[Fe(CN)_6]^{3-/4-}$ in 0.01M PBS), it will inefficiently screen the negative charge on the miRNA backbone, allowing a charge repulsion between electrode and causing the miRNA to adopt an extended configuration [25]. This phenomenon will increase the average electron transfer distances and decrease the rate of electron transfer. Therefore, the difference in the "apparent" thickness of the oligonucleotides, visualized in Figure 2.7, can be justified by its tilt and "concertinaing" when the density of miRNA plays a role (e.g. when the repulsion suffered by lateral interactions between adjacent miRNA strands adds to the described electrostatic interactions). Figure 2.7 illustrate the behaviour of the monolayer thickness as a function of immobilization time of the capture-probe strands, highlighting the correlation between the two measurements. Moreover, a deeper insight over the integrity of the monolayer (the association of surface coverage and electrostatic forces to the thickness) is explored in the next topic.

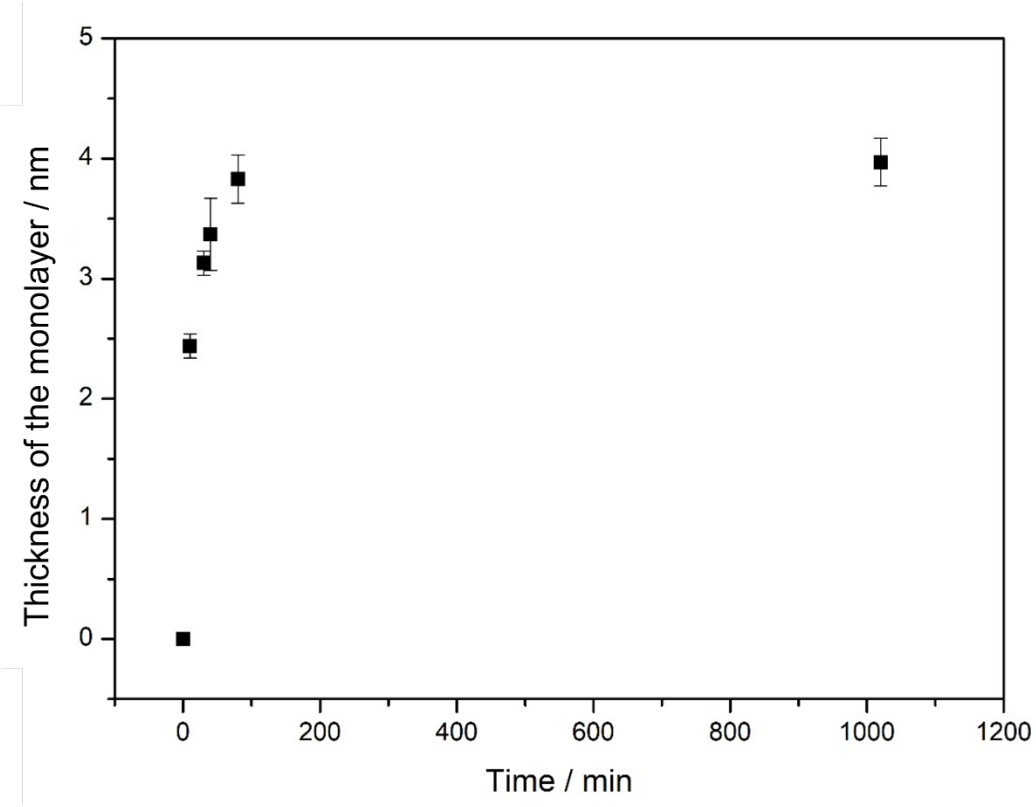


Figure 2.7. The monolayer thickness of the miRNA capture-probe immobilized onto the gold surface was estimated at multiple time points spanning from 0 to 1200 minutes. Error bars, indicative of the variability in results obtained from three independent measurements, are displayed on the graph. In cases where error bars are not discernible, they either reflect minimal variability or are comparable in size to the plotted symbols.

The monolayer thickness exhibited a progressive increase, rising from 2.4 to 4.0 nm as the immobilization time of miRNAs on the electrode surface was extended. This trend aligns remarkably well with the structural model for a 10-oligonucleotide miRNA sequence, which suggests a length of 4.7 nm. Impressively, within a mere 10 minutes of immobilization, approximately 60% of the maximum thickness had already formed, with subsequent measurements at 30 and 40 minutes showing only minor variations in coverage. Notably, a slight uptick in monolayer thickness was observed between the 80-minute mark and the 17-hour point, culminating in a mere 5% increase relative to the value recorded at 80 minutes. According to existing literature, the formation of a well-ordered monolayer typically requires an average of 12 hours. Consequently, the 17-hour duration employed in this study reflects the attainment of maximum surface coverage achievable under the described experimental conditions. Given the marginal change in monolayer thickness during the extended time period, it can be reasonably deduced that the optimal timeframe for establishing a well-ordered monolayer is approximately 80 minutes. However, to validate this assumption regarding monolayer integrity, further investigation is warranted, specifically through the correlation of the proposed Nyquist circuit with the pertinent physical variables outlined in Table 2.3. As such, the gap in data collection between 6 hours and 17 hours bears no significant impact, as it aligns seamlessly with the observed saturation of monolayer thickness and the established formation timeframe.

2.2.2 Insights on the integrity of the monolayer and validation of the proposed adsorption model

The equivalent Randles circuit presents the model proposed to a specific system. As such, the qualitative analysis of its parameters should bring insights into the electrical changes of the system and consequently on the quality of the barrier formed on the surface. Therefore, the fact that the model proposed in this work (insert Figure 2.6) presents a single resistance corresponding to the charge transfer rate (R_{ct}), and because it was not possible to obtain an adequate fitting of the Nyquist plot when adding an extra resistance to the system, generated evidence for the formulation of two initial hypotheses about the integrity of the monolayer.

The first model involves a reasonably homogeneous monolayer that was formed on the surface. The second model, on the other hand, leads to the idea that a heterogeneous layer was formed with small defects, which cause a kinetic dispersion considered insignificant in the overall

system. The qualitative analysis of the Nyquist plot as well as the analysis of the values of the circuit components described in Table 2.3, were used to try and discriminate between the two models.

The increase in the diameter of the Nyquist semicircle (R_{ct}) after 10 min of immobilization by approximately 44% of the maximum value, presumes that the initial adsorption step occurs quickly. However, the slight increase of the semicircles at higher frequency between the adsorption times 30 and 40 min and the reactively long Warburg line at lower frequencies are indications that the monolayer formed in this faster phase of adsorption are not compact, denoting the presence of holes in these layers [26]. On the other hand, the decrease of the Warburg contribution at 80 min and 17h further suggests that the increase of the miRNAs adsorption time reduces monolayer defects and leads to the formation of a denser monolayer.

In addition, the consecutive decrease in the k_0 value, between the bare electrode and after immobilization of miRNAs capture-probe over different times, also suggests the formation of a more compact and less defective monolayer. This is due to the following reasons. The apparent charge transfer resistance corresponds to the sum of the electron transfer resistances in pinholes, in collapsed sites and in non-defective domains. In sites where there is an insulating barrier preventing the heterogeneous charge transfer between the redox pairs and the electrode surface, electrons are transferred by tunnelling. However, increasing the thickness of the barrier exponentially minimizes this mechanism [27]. Therefore, the apparent resistance rate of charge transfer would only increase if the transfer of electrons in defects dominates the charge transfer process, which is not evidenced in this work.

From the evaluation of all the parameters described in this study, it can be said that the mechanism initially proposed through the analysis of CV is consistent with the AC impedance data. A well-ordered monolayer with relatively few defects/unmodified regions can be formed in 80 min. The results also suggest that formation of the monolayer occurs quickly, but that becoming organized and oriented occurs more slowly. The calculated monolayer thickness value of 4.0 nm is consistent with the expected length for a thiolated miRNA capture-probe formed by 10 oligonucleotides and suggest the presence of few defects and low orientation of the formed monolayer.

2.2.3 Optimization of the hybridization time between miRNA capture-probe and miRNA target

Studies on the optimal time capable to guarantee the maximum signal related to the hybridization event between miRNA capture-probe and target were carried out by evaluating the behaviour of cyclic voltammograms (Figure 2.8 (a)) and Nyquist plot (Figure 2.8 (b)) as the hybridization time is systematically varied. Reducing the capture probe-target hybridization time would also decrease the sample-to-answer time in a diagnostic device. The miRNA capture-probe strand was immobilized from a 10 μM solution onto the surface of the gold electrode for 80 min. Subsequently, a 10 μM solution of the complementary miRNA target was added and allowed to hybridise for 0, 5, 20, 40 and 60 min at 37 ℃. The parameters used in the CV and EIS analysis are described in the experimental section, and the electrolyte used was 0.01 M PBS with 1 mM of ferrocyanide as a redox probe.

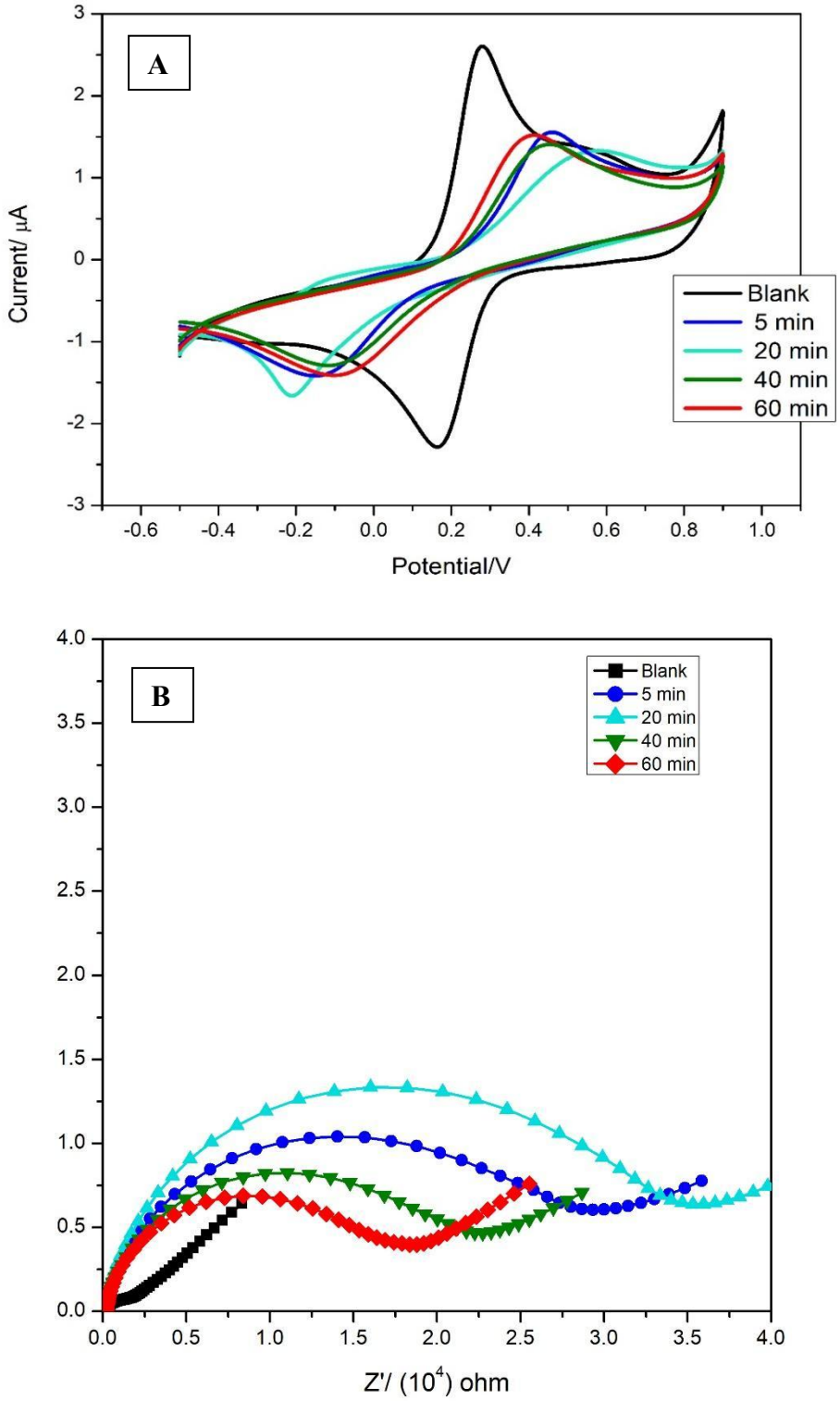


Figure 2.8. (A) Cyclic voltammograms and (B) Nyquist plots of impedance spectra obtained by the miRNA modified electrode after hybridization with 10 μM of miRNA target at times: 5, 20, 40 and 60 min. Electrochemical species: 1 mM $[Fe(CN)_6]^{3-/4-}$ with 0.01 M PBS. Scan rate: 50 mV/s. Potential: 0.231V. Amplitude: 25mV. Frequency range 0.1 Hz to 10^5 Hz. The analysis was performed in triplicate.

The Nyquist plots reveal a small increase in the values of resistance to charge transfer between electrodes and the redox ions (Z' or Rct) with the increase in the hybridization time of the capture-probe – target from 5 min to 20 min. It is possible to observe a decrease in current peaks with a consequent widening of the potential (anodic peaks shifted to more positive potential while cathodic peaks to more negative potential) described by the cyclic voltammograms in the 5 to 20 min. However, unlike the pattern predicted in miRNA capture-probe immobilization studies, increasing miRNA target hybridization times to values greater than 40 min generates a decrease in charge transfer resistance by approximately 43% of the maximum hybridization value achieved by this system. Likewise, cyclic voltammograms show an increase in current at 40 and 60 min, representing a decrease in the blocking properties of the gold surface and possibly in the hybridization efficiency.

The increase in resistance to charge transfer between the hybridization time of 5 to 20 min, is consistent with an increase in the negative charge added to the surface derived from the miRNA target available for hybridization. Therefore, a 20 min hybridization time results in a greater amount of negatively charged duplex forming, generating a greater electrostatic repulsion of the ferrocyanide ions in solution.

The decrease in the R_{ct} value by increasing the hybridization time to a time scale greater than 40 min could have two possible explanations. The first hypothesis is that although the monolayer formed by immobilizing the capture-probe for 80 min is compact, there is a high density of miRNA on the surface which, due to steric and electrostatic hindrance, will allow a large percentage of capture-probe not to be accessible to the target, thus reducing hybridization efficiency. The second explanation would be that the decrease in R_{ct} can be justified by the presence of non-specific bonds between the miRNA capture-probe and the surface of the gold electrode, e.g. presence of electrostatic interactions between the chemisorb miRNA chains and the gold electrode. This is better understood if one thinks that during the preparation of the SAM there was no use of spacers to prevent the formation of unspecified bonds. Therefore, it is possible that the hybridization event causes an orientation of the non-specifically adsorbed capture-probe molecules, making them stand up from the surface and generating low impedance channels which would facilitate the exchange charge transfer between electrode-electrolyte.

It is expected that the suppression of hybridization in times greater than 20 min will be affected by changes in the spacing between miRNA capture-probe and different surface densities, since

the steric effect, electrostatic repulsion and conformational restriction of the surface-tethered strands are highly influenced by these parameters. Therefore, the studies that follow show the correlation of different concentrations of spacer and miRNAs and their influences on surface density and hybridization efficiency.

2.2.4. Co-immobilization of miRNA capture-probe and MCH

To improve the organization of the monolayer, the 6 mercapto-1-hexanol (MCH) spacer was co-immobilized onto the electrode surface forming a mixed self-assembled monolayer (SAM). The reaction mechanism presented by this blocking agent occurs through the displacement of non-specific interactions between the capture-probe and gold by the alcohol functional group present in the MCH. Thus, these interactions stand up from the surface increasing the availability of capture-probe for hybridization. When adding a spacer, the intention is that the electron transfer occurs almost exclusively by tunnelling since the height of MCH oriented normal to the surface is 1.5 nm [28].

It is worth noting that although the MCH typically displaces weakly adsorbed strands, it can also displace specifically adsorbed capture-probe strands if added in excess since the bond strengths are comparable. Therefore, the conditions, e.g., mole ratio of MCH to capture-probe strand, must be carefully controlled to ensure a sufficient coverage of the capture-probe strand, which would cause a future problem for the detection limit of the sensor.

Adding a blocking agent is used to ensure that the capture-probe strands are sufficiently well separated to allow efficient capture -probe – target hybridization, thus avoiding issues related to low signal to background ratios and low sensitivity. The steric effect is still one of the biggest problems faced by most immobilization methods which needs to be solved for the next generation of highly sensitive miRNA sensors. As it is known that miRNA immobilized surface with sufficient distance between each miRNA capture-probe could ensure high hybridization yield [29], a study aiming to find the ideal ratio of [miRNA]: [MCH] and the standardization of these parameters can facilitate the reproducibility of sensors and ensure good surface design to maximize the sensitivity of the sensor.

The mole ratio of the constituents in the self-assembled monolayer, is known to depend on variables such as deposition time, temperature, thiols solubility and molar ratio in the

deposition solution [30]. However, as mentioned in the work of Xu *et al.* [31] the use of a higher temperature for hybridization between capture-probe and target, can reorganize possible defects present in a mixed self-assembled monolayer, generating a drift in the resistance response to the charge transfer. Therefore, in this work, the procedure used for the formation of a mixed monolayer was based on the one reported by Estrela *et al.*[6] with significant modifications, such as (1) the co-immobilization of MCH and miRNA capture-probe in a temperature of 37 ℃ and (2) the removal of the extra step of backfilling the electrode with MCH after complete formation of SAM (for the purpose of optimizing the overall experimental time).

The study of the formation of a mixed monolayer was evaluated with the amount of capture-probe density adsorbed to the surface to generate an environment capable of maximising hybridization of miRNAs and, consequently, greater electrochemical signals.

The density of miRNA capture-probe was investigated using the technique of chronocoulometry (CC) and EIS. The molar proportions studied here were based on the optimum quantities reported in the literature, such as: 0, 1: 2, 1: 4, 1:10, 1: 100 and 1 [miRNA] : [total thiol], so that a ratio of zero corresponds to a pure MCH monolayer and one corresponds to a pure miRNA capture-probe layer.

2.2.3.1 Determination of the surface coverage using Chronocoulometry

2.2.3.1.1 Calculation of surface coverage: general considerations

The coverage of miRNA immobilized at the gold electrode was evaluated using the technique of chronocoulometry using the parameters described in the section 2.1.3.9. Tris-HCl was used as an electrolyte in these analyses due to its low tendency to associate with other ions which favours the complete exchange between monovalent miRNA counterions and redox cation ($[Ru(NH_3)_6]^{3+}$) in a 1: 3 ratio. A potential of -800 mV was used to generate a current limited by diffusion and also the complete reduction of all ruthenium hexamine associated with the electrode surface.

In contrast to other reports [32] [33], in this work the surface coverage of miRNA was calculated considering the microscopic area instead of the geometric area. Since the electrodes

were mechanically polished with 0.3 μm alumina, this is expected to be the maximum size of roughness found on the surface. Once this value is greater than the 5.5 nm thickness presented by the miRNA/MCH layer, one can affirm that the studied immobilization protocol analysed represents the surface density of miRNA over the microscopic surface area instead of the geometric surface area. As different forms of gold electrode present different roughness factors, to compare this work with other studies of DNA density in the literature (that uses the geometric area in their calculation), these reported results should be divided by the typical roughness factor of the electrode used.

Table 2. 4 displays the microscopic area values of the gold electrodes studied here, which were determined from the integration of the reduction peak of the chemisorbed oxygen during the electrode cleaning process, as described in Section 2.1.3.1

Table 2.4. Summary of the microscopic area and roughness factor calculated from the integration of the reduction current of the chemisorbed oxygen during the electrode cleaning process. The standard deviations represent the spread of the results performed in triplicate.

Electrode	*Ip* (A)	*Microscopic Area* ($A/\mu C\ cm^2$)	*Roughness factor*
E1	$(1.92 \times 10^{-5}) \pm 0.06$	$(4.92 \times 10^{-2}) \pm 0.15$	1.57 ± 0.05
E2	$(2.29 \times 10^{-5}) \pm 0.03$	$(5.87 \times 10^{-2}) \pm 0.27$	1.87 ± 0.08
E3	$(2.16 \times 10^{-5}) \pm 0.10$	$(5.53 \times 10^{-2}) \pm 0.07$	1.76 ± 0.02

It is worth noting that since the roughness factor values vary from approximately 1.6 to 1.9, the use of the geometric area for surface density calculations would bring an error approaching two for all quantities involving the electrode area.

2.2.3.2 The effect of a low ion- pairing electrolyte on chronocoulometric curves

Figure 2.9. (a) illustrates a chronocoulometric curve obtained by varying the mole ratio between miRNA capture-probes and the total amount of thiols in the 1:2 proportion.

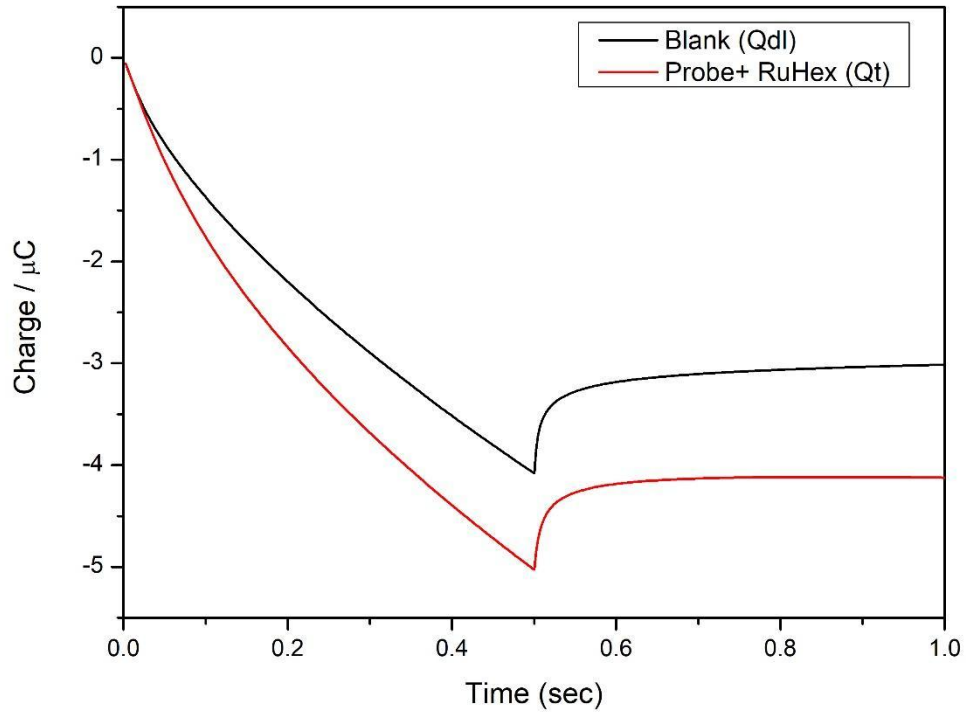


Figure 2.9. Chronocoulometric response curves for the miRNA: MCH functionalized at the gold electrode at 1[miRNA]:2[total thiol] molar ratio. Parameters: -0.3V to -0.8 V during 0.5 s. Sample interval: 0.0025 s and numbers of steps: 2.

Analysing Figure 2.9, one can notice the occurrence of a delay before any charge flows, and therefore, a delay for the reduction of ruthenium cations to occur. This non-ideal feature that are common to others results in the literature [34][35], can be explained by considering two major factors: (1) the use of an electrolyte with low tendency to associate with other ions (e.g., Tris-HCl) during measurements and (2) due to the rise time of the potentiostat.

Regarding the usage of a low ion- pairing electrolyte, although it was absolutely necessary to the development of the chronocoulometric measurement as it strongly favours the complete replacement of miRNA counterions by ruthenium cations, it generates a high uncompensated series solution resistance (Rs). This resistance makes charging the double layer capacitance and to establish the voltage at the working electrode take longer to occur. Thus, this relatively large time constant (R_s C_{dl}) present in the analysis could be corrected experimentally.

Reducing the spacing between the working and reference electrodes, by the exchange of the usual counter electrode to another one with a bigger area and the working electrode to another one with a smaller area, would leads to a reduction in the solution resistance (Rs) and the double

layer capacitance (C_{dl}), helping to minimize the time lag. However, as there was no interest in work with different types of electrodes through the development of the research, the time issue was partially corrected by a simple change in the experimental parameters. Therefore, shifting the applied potential to a more negative value (from – 600 mV to -800 mV) was the strategy used to minimize the time of reduction of the RuHex cations.

The rise time of the potentiostat should also be summed to the time lag visualized here, presenting as a total time period (t_i) where there was no reduction of the ruthenium cations at the diffusion limited rate. In this work, this time lag was identified as t_i= 0.50 s, which correspond to $t_i^{1/2}$= 0.7 $s^{1/2}$. For the further calculations, this delay could be compensated by subtracting the time lag time (t_i) from the time identified as the start of reduction of ruthenium (t_f). Therefore, a modified Anson plot can be generated with axes called Q versus $(t_f\text{-}t_i)^{1/2}$ instead of the usual $t^{1/2}$ vs. Q.

In this study, an estimation of the error generated by the usage of the conventional Anson plot (Q vs. $t^{1/2}$) that does not consider the correction of the time lag was investigated. The results presented an overestimation of the $nFA\Gamma_{miRNA}$ value in 3 nC. Considering a roughness factor of 1.8, this would have an increase in the 10-oligonucleotides capture-probe surface coverage of $5x10^{10}$ cm^{-2} for all the different ratios of surface density. Once this work examined higher miRNA densities, this value was considered irrelevant, and the need for correction was neglected.

2.2.3.2.1 miRNA surface Coverage

The miRNA surface coverage co-immobilized with MCH at the gold electrode was calculated using the technique of chronocoulometry in accordance with Section 2.1.3.9. In this technique, the cation ruthenium (III) hexamine is electroactive adsorbed with the monovalent anion from the phosphate group of miRNA capture-probe backbone ($K_{(RuHex)}$= 2 × 10^6 [36]) at 1:3 ratio. Further, the quantification of miRNA capture-probe coverage over the surface is determined by the event of desorption/reduction of the RuHex and the correlation of the cation to the binding capture-probe. The application of this methodology can be better understood by evaluation of the Anson plot present in Figure 2.10 in conjunction with the Cottrell equation, restated in the equation below.

$$Qt = \frac{2nFADo^{1/2}\,C}{\pi^{1/2}}\, t^{1/2} + Qdl + nFA\Gamma_0$$

Where, at t=0:

$$Qt - Q_{dl} = Q_{miRNA}$$

Considering that, $\Gamma_{miRNA} = \Gamma_0$ (z/m) N_A (Equation 2.18, experimental section 2.1.3.9

$$\Gamma_{miRNA} = (Q_{miRNA}\, N_A / nFA)\ (z/m)$$

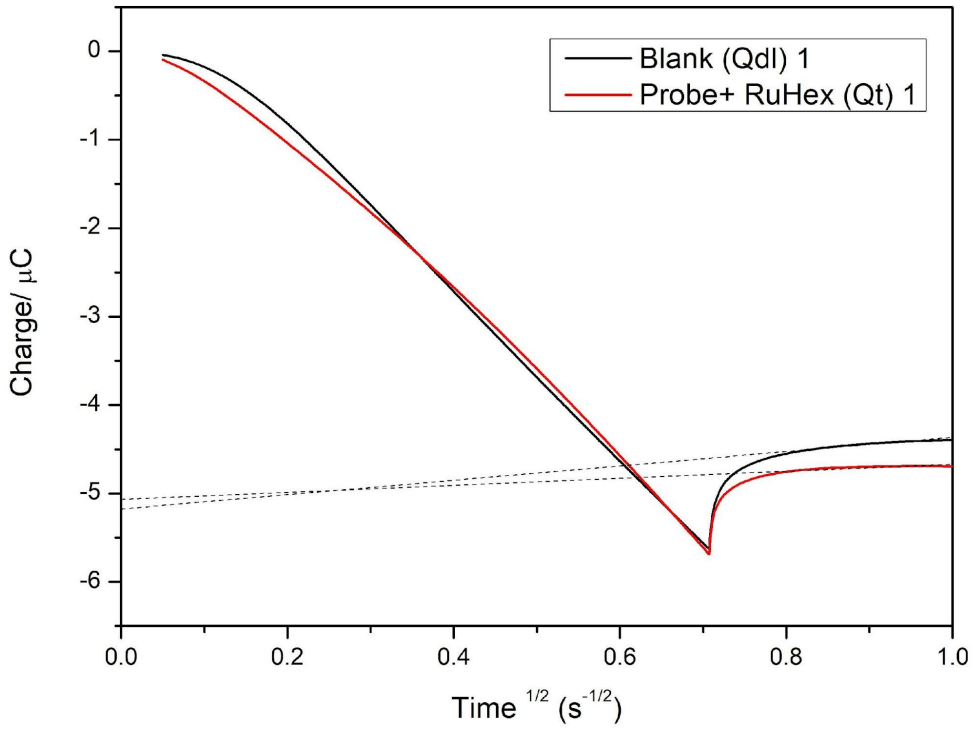


Figure 2.10. Chronocoulometric response curves for the miRNA: MCH functionalized at the gold electrode at 1[miRNA]:[total thiol] molar ratio. The dashed line represents the extrapolation of the linear part of the Anson plot by least square fit. Parameters: -0.3V to -0.8V during 0.5 s. Sample interval: 0.0025s and number of steps:2.

The chronocoulometric intercept at t=0 leads to the values of Q_{dl} = -5.176x 10^{-6} C and Q_t = -5.0679 x10^{-6} C. Considering n =1 e^- , z = +3, m = 10 and A = 0.0553 cm^2 (see Table 2.4, E_3) so, $\Gamma_{miRNA=}$ 3.67 x 10 ^{12} capture- probes/ cm^2 for the mole fraction of 1[miRNA]: [total thiol].

Using similar calculations as described above, the surface coverage of the molar fractions 1: 2, 1: 4, 1:10 and 1: 100 [miRNA]:[total thiol] was examined. The possibility of non-specific

adsorption of $[Ru(NH_3)_6]^{3+}$ at the gold surface was investigated by analysing the intercepts of the chronocoulometric curves obtained when electrodes were modified with MCH in the absence and presence of the redox marker. As the values of Q_{dl} and Q_t (intercepts of the curve, at t=0) are nearly identical in both conditions, it was concluded that there is negligible non-specific adsorption of RuHex when miRNA is not co-immobilized to the electrode.

The correlation between density of miRNA capture over different molar fractions is illustrated in Figure 2. 11.

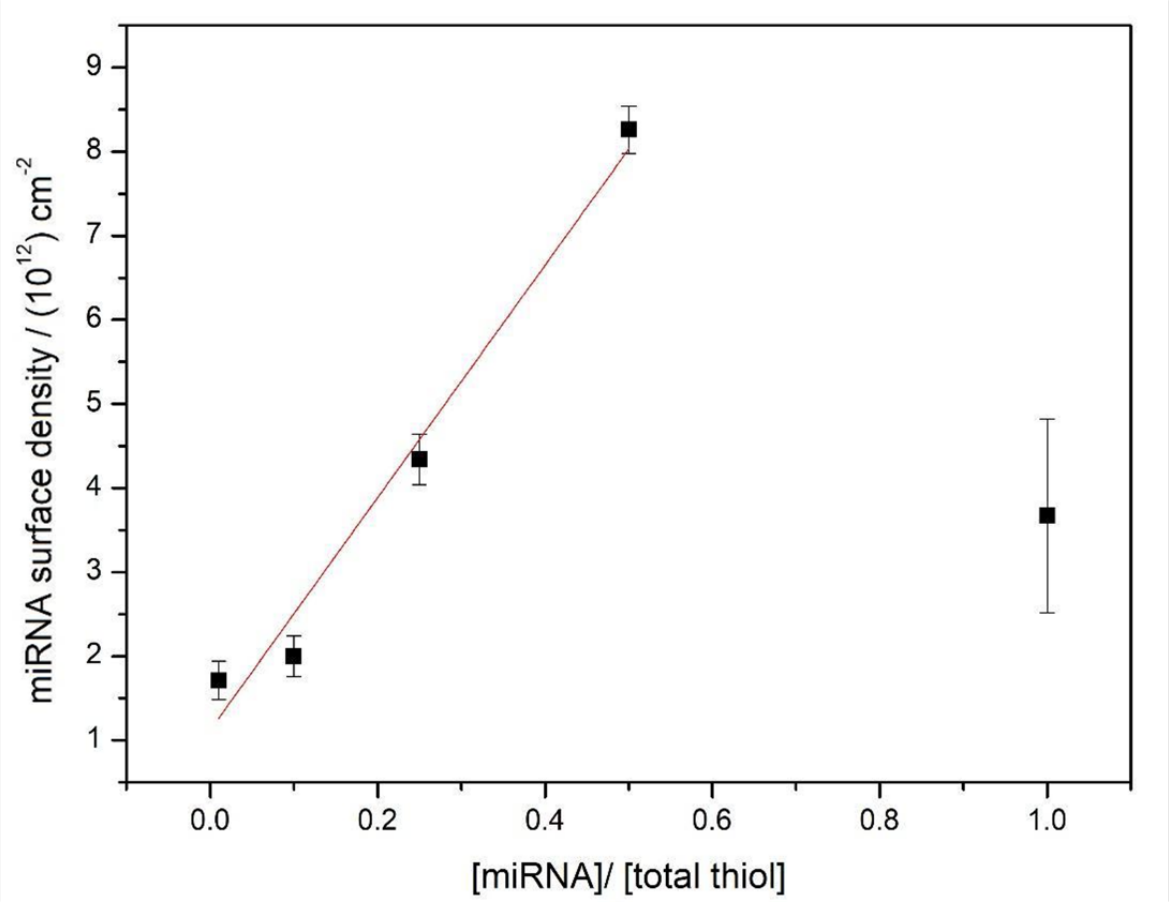


Figure 2.11. Relation between miRNA surface density and different molar ratios of miRNA: total thiol in the immobilization solution. The solid line is the least square fit where the [miRNA]/[Total thiol]=1 data point has been excluded. The error bars represent the spread of the results performed in triplicate.

These results suggest that the surface density of the capture-probe increases linearly (y=1.74 $x10^{13}$ [miRNA]/ [total thiol] + 4.16 $x10^{11}$) as the fraction of miRNA in solution increases for mole ratios less than 0.7. These values vary from 2.00 $x10^{12}$ molecules cm^{-2} when there is 10%

of miRNA: total thiol and reach a maximum coverage (Γ_{max}) of 8.26 x10^{12} molecules cm^{-2} at 50% of miRNA: total thiol. This coverage corresponds to an approximate area per molecule of 1190 $Å^2$ and is approximately an order of magnitude smaller than that typically observed for short chain nucleic acid monolayers. This result suggests that MCH apparently adsorbs preferentially (approximately 5-fold higher) relative to the miRNA capture-probe strand. Significantly, in the absence of MCH (mole ratio of 1), the miRNA surface coverage is approximately 50% lower than Γ_{max} suggesting that lateral electrostatic repulsions between the miRNA may be more influential on the coverage attained than stronger, or more rapid, binding of the MCH, which if present, simply "backfills" any vacancies on the gold surface.

It is worth nothing that, for lower molar fractions of miRNA such as 1: 100 and 1:10, there is little change in the surface coverage of the capture-probe strand. This pattern can be justified by the smaller fraction of capture-probes undergoing electrostatic repulsion and, consequently, a smaller probability of non-specific interactions affect the surface density. Therefore, it is notable that, although MCH can effectively assist in the orientation of miRNA capture-probe when present in its immobilization stage – as suggests the increase in surface density as the increase the MCH ratio- the control of its proportion is extremely important to moderate the rate between optimal concentration of surface miRNA, steric impediment and electrostatic repulsion of capture-probes.

2.2.3.3 Analysis of the binding properties of target in different molar fractions of miRNA: total thiol

The investigation of the optimal molar ratio between miRNA and total thiols co-absorbed on the gold electrode holds critical importance. This pertains not only to regulating surface density but also to enhancing the efficacy of hybridization. This efficacy is, to some extent, influenced by the orientation of miRNA relative to the gold surface. Achieving maximal miRNA hybridization involves positioning the miRNA capture-probe at an approximate 90-degree angle from the surface, connected primarily through its thiol groups.

Considering this, the impact of altering the [miRNA $_{capture\text{-}probe}$]:[total thiol] ratio gains significance. Such modifications could induce changes in the local microenvironment within which hybridization takes place. At lower ratios, the capture-probe strands are more likely to be encompassed by MCH (mercaptohexanol). This introduces a distinct charge distribution and

dielectric constant (Table A1, Appendix A) compared to higher ratios, where the capture-probe strands would be more densely packed and the interactions altered.

In terms of orientation, it is expected that in high molar miRNA fraction (e.g. 1: 2 miRNA / total thiol) there will not be enough MCH to compete effectively with non-specific miRNA interactions and, although the miRNA coverage is high, the poor oligonucleotide orientation to the gold surface will result in low rates of hybridization. However, as the concentration of MCH increases (decreasing the molar fraction of miRNA), MCH competes with non-specific interactions of oligonucleotides (electrostatic interaction between the chemisorb capture-probe strand and the gold surface) more effectively and the orientation of the miRNA on the surface is improved. Eventually, MCH begins to dominate the surface and the miRNA coverage decreases. It is this balance between the ratios (i.e. coverage) and the molecular environment (e.g., orientation of the miRNA) that allows the maximum amount of hybridization of the target.

Steel *et al.* [36] was one of the pioneers in the study relating the capture-probe density and target hybridization percentage. According to his research, the efficiency of hybridization increases up to 4×10^{12} capture-probe /cm^2 with subsequent decrease at higher values of surface density. Peterson *et al.* [37] reported that better hybridization values occur in the range below $3x10^{12}$ capture-probe /cm^2. Based on these values, it is expected that among the molar fractions of miRNA / total thiol studied here, those capable of producing the highest hybridization values are between 1: 4 , 1:10, 1: 100 and 1.

The agreement between the different densities of miRNA capture-probe generated in the aforementioned proportions and the signal relative to hybridization between miRNA capture-probe – target, was obtained from the analysis of the variation of the R_{ct} produced by this event during EIS studies in faradaic mode (Figure 2.12 (a) and (b)). For these analyses, the concentration of 1 μM target was used since it was described in the literature as ideal for complete hybridization of oligonucleotides [38]. Table 2.5 presents a summary of the fractional changes in R_{ct} upon hybridization as a function of molar fraction of miRNA to total thiol in immobilization solution.

Table 2.5. Rct values before and after hybridization according to the molar fraction of [miRNA]: [total thiol] in the immobilization solution. The average values and standard deviation represent are calculated based on n=3.

[miRNA]: [total thiol]	$Rct_{(capture\text{-}probe)}$ /Ω	$Rct_{(duplex)}$/ Ω	$\frac{Rct(duplex)}{Rct\ (capture-probe)}$
1:4	10.50 x 10^4	58.70 x10^4	5.62 ± 0.15
1:10	5.51 x 10^4	13.74 x10^4	2.53 ± 0.25
1:100	3.72 x 10^4	8.91 x10^4	2.31 ± 0.10
1	2.95 x 10^4	3.51x10^4	1.20 ± 0.35

According to these results, a 1: 4 molar fractions of miRNA / total thiol, which corresponds in a mean density of 4.74 x10^{12} capture-probe cm^{-2}, performed the maximum fraction change in R_{ct} achieving the value of 5.62 with a standard deviation of ± 0.15. In addition, it can be noted that the modulation of charge transfer does not occur very significantly between the surface densities corresponding to the 1:10 and 1: 100 molar fractions.

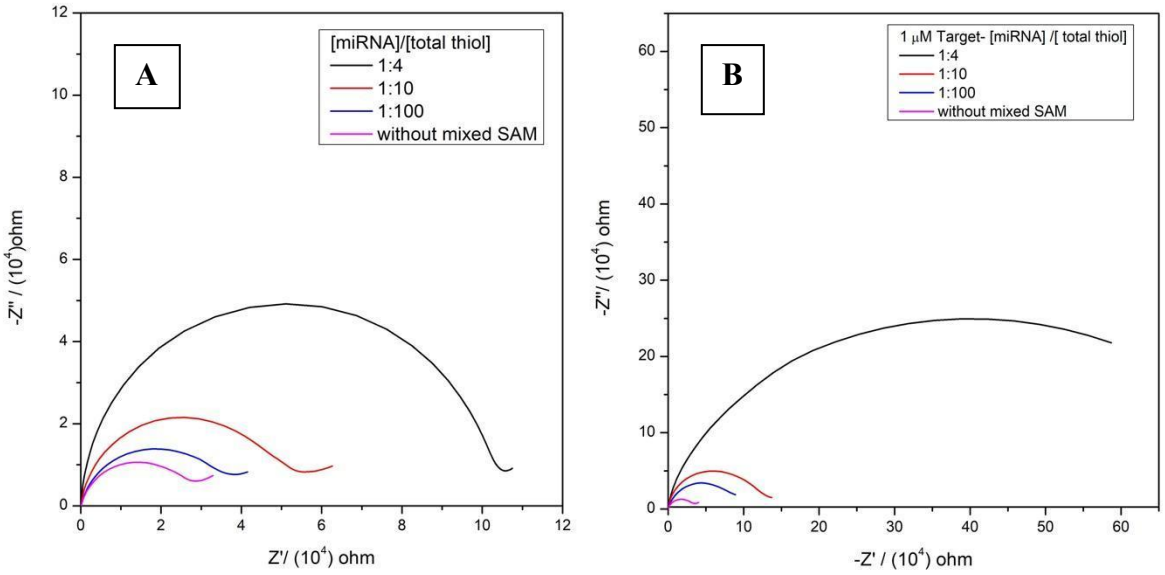


Figure 2.12. (A) Nyquist plots of the impedance spectra obtained by the gold electrode immobilized with different molar ratios of [miRNA]:[total thiol] and **(B)** Nyquist plot curve response upon the hybridization event of the gold electrode immobilized with different mixed SAM ratios and 1 μM of miRNA target. Electrolyte used: 1 mM [Fe $(CN)_6^{3-/4-}$] in 0.01 M PBS. Biasing potential: 0.231V. Amplitude: 25 mV. Frequency range: 0.1 Hz to 10^5Hz. The analysis was performed in triplicate.

Figure 2.12 (A) presents Nyquist plots for various capture-probe layer compositions, clearly demonstrating that the charge transfer resistance for the ferro/ferri couple is influenced by the interfacial composition. The Nyquist plots reveal an interesting trend: as the surface density increases, the charge transfer also increases. This phenomenon can be explained by the addition of potential barriers that arise due to the proximity of neighbouring oligonucleotides.

The increase in potential barriers significantly hampers the exchange current density, consequently impeding the efficient transfer of electrons between the redox probe and the electrode. This higher charge transfer resistance (R_{ct}) can be attributed to the approximate 4.7 nm length of the miRNA capture-probe, in contrast to the 1.5 nm length of the MCH. The predominance of miRNA capture-probe strands on the surface results in a higher average electron transfer distance.

However, it is worth noting that the resistance to charge transfer does not occur efficiently at low surface densities due to the effects explained by Manning's counterion condensation theory. According to Manning [39], if the polyelectrolyte axial charge spacing (spacing

between miRNA capture-probe) is greater than Debye screening length, the polyelectrolyte charge is compensated by counterions, reducing the capture-probe net charge and establishing nano-channels between capture-probe, through which, the mass transport of the redox probe will occur. Therefore, the change in R_{ct} will result as an interplay between reduced charge screening and decreasing hybridization efficiency with increase surface density [6].

2.2.3.4 Correlation of charge transfer resistance with hybridization efficiency at different surface densities

The efficiency of the capture-probe and target strand hybridization will depend on the balance between charge screening, electrostatic repulsions, surface homogeneity (SAM order and defects), the local dielectric constant and the free volume, all of which may depend on the surface coverage of the capture-probe e strands. To maximize the sensitivity of the label-free sensor under construction, an optimal hybridization efficiency between capture-probe -target must be balanced with the maximum variation on the resistance to charge transfer obtained by this event**.** Therefore, to correlate these variables, the effect of the target hybridization density by the capture-probe density immobilized on the surface (H_E) was initially examined.

For this analysis, 1 μM of miRNA target was hybridized at surface coverages prepared at different molar fraction of [miRNA]: [total thiol] in the immobilization solution. The substitution of the values of target hybridization density and capture-probe density- obtained by the chronocoulometric technique- to Equation 2.19, promoted the data over hybridization efficiency presented in Table 2.6.

$$H_E\,(\%) = \frac{HD}{\Gamma capture} \text{ x } 100 \quad \text{Equation 2.19}$$

Table 2.6. Variation of the target hybridization density and miRNA capture-probe surface density in accordance to the molar fraction of [miRNA]: [total thiol] in the immobilization solution. The standard deviation represent the spread of the results performed in triplicate.

[miRNA]: [total thiol]	Hybridization Density (H_D) / molecules cm^{-2}	Surface density ($\Gamma_{\text{capture-probe}}$) / molecules cm^{-2}	$H.E.$ (%)
1:100	$(1.48 \times 10^{12}) \pm 0.33$	$(1.72 \times 10^{12}) \pm 0.20$	86 ± 1
1:10	$(1.42 \times 10^{12}) \pm 0.20$	$(2.00 \times 10^{12}) \pm 0.24$	71 ± 4
1:4	$(1.71 \times 10^{12}) \pm 0.28$	$(4.74 \times 10^{12}) \pm 0.30$	36 ± 3
1:2	$(8.26 \times 10^{11}) \pm 0.20$	$(8.26 \times 10^{12}) \pm 0.28$	10 ± 1
1	$(1.30 \times 10^{12}) \pm 0.67$	$(3.26 \times 10^{12}) \pm 1.15$	40 ± 1

In addition, Figure 2.13 illustrate the variation in hybridization efficiency for 1 μM of miRNA target at different densities of miRNA capture-probe obtained from the molar concentrations: 1: 2; 1: 4; 1: 10; 1: 100 and 1 miRNA : total thiol.

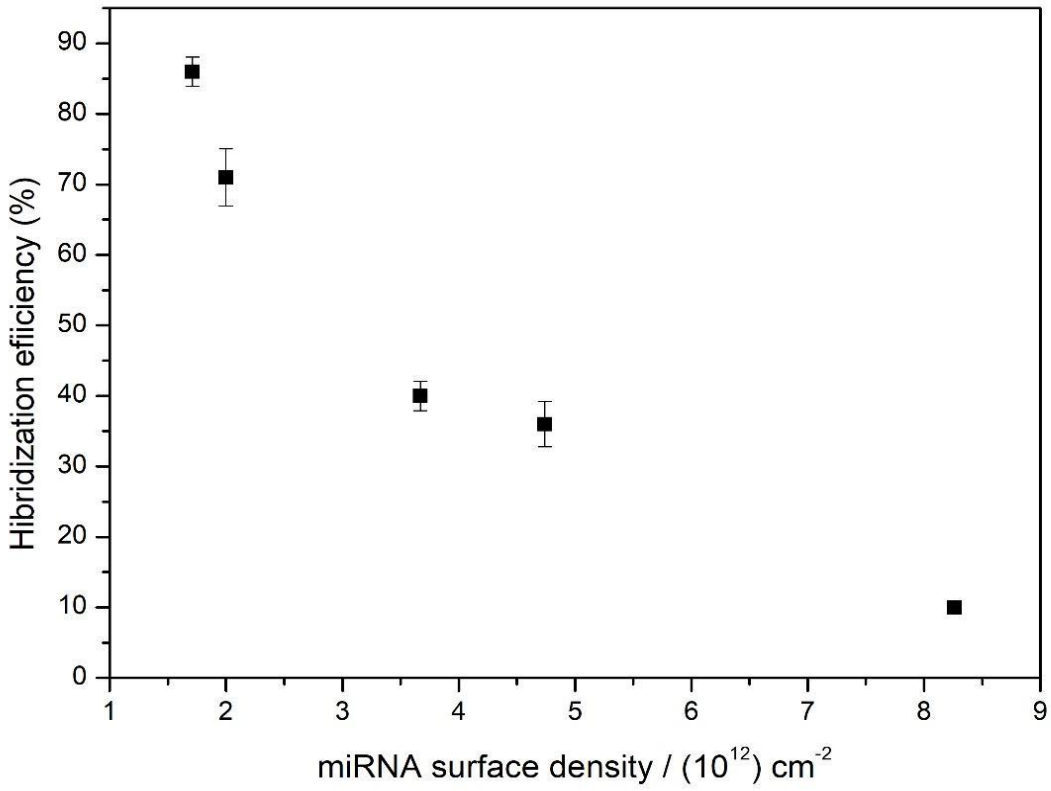


Figure 2.13. Correlation between the hybridization efficiency and the surface density of miRNA capture-probe. Hybridization event occurs using 1 μM of miRNA target during 20 min at 37°C. The error bars represent the spread of the results performed in triplicate.

Evaluating this study, as the density of miRNA increases on the surface, there is a significant drop in hybridization efficiency. Maximum hybridization efficiency is found at 86% for a density of 1.72 x10^{12} capture-probe cm^{-2} and decays to 10% at a density of 8.26 x10^{12} capture-probe $cm^{-2.}$ For the density of 4.74 x10^{12} capture-probe cm^{-2} hybridization is in the range of 36% and at 3.26 x10^{12} capture-probe cm^{-2} hybridization is in the range of 40%. The observation that the hybridization efficiency is highest for low surface coverage suggests that there are significant electrostatic repulsions that impede target binding when the capture-probe strands are closer together and that the capture-probe strands are dispersed across the electrode surface rather than forming islands of close-packed adsorbates.

If investigating these results separately, it can be thought that the best proportion for the electrode surface design would be the one related to the molar concentration ratio 1: 100 miRNA: total thiol, since this mixed SAM generates the highest hybridization efficiency. However, as already explained for the results of charge transfer, at this low capture-probe density, the increase in charge resulting from the hybridization process is screened and lateral

interactions between neighbours' miRNAs are insufficient to control the rate of heterogeneous electron transfer [25].

In addition, despite the mole fraction 1 miRNA: total thiol presented a hybridization efficiency of 40% which is greater than the 36% obtained at proportion 1 miRNA: 4 total thiol (under a close-packed surface density), at this fraction, the variation in the resistance of charge transfer is lower. This behaviour is evidence that the modulation of R_{ct} does not depend solely on the surface density and, once more, should account for the effects of capture-probe orientation and surface homogeneity (SAM order and defects). Therefore, the ideal molar proportion for obtaining an excellent analytical signal of charge transfer resistance and good hybridization efficiency would be 1 miRNA: 4 total thiols, corresponding to a hybridization of 36% and a variation of R_{ct} of 5.6-fold. The proposed surface design aiming to obtain a good analytical signal, considers the balance between charge screening, electrostatic repulsions, and sufficient capture-probe density.

2.2.4 Validation of the developed biosensor

2.2.5 Analytical performance of the impedimetric biosensor

To evaluate the analytical performance of the label-free biosensor towards the detection of miRNA-206, different concentrations of the miRNA target were added to clean buffer solutions and incubated under the optimized experimental conditions.

Figure 2.14 A illustrates the Nyquist plots for the biosensor as the concentration of miRNA is systematically varied. The results indicate that increasing the quantity of miRNA bound to the electrode surface increases the R_{ct} of the system. The reduction in the rate of interfacial electron transfer - appearing as an increase in the resistance - occurs because of two main events. The physical barrier generated by the bulky miRNA molecules and the repulsion of the redox probe caused by the increased negative charge of the self-assembled monolayer .

Additional assessment on the relation between the resistance to the charge transfer and the concentration of the target, is illustrated in Figure 2.14 B. For a more reliable quantification of miRNA, the plot was based on the average of ΔR_{ct}, which was described in this work as the ratio between the resistance generated by the duplex (miRNA capture-probe – target) over the

resistance of the capture-probe alone. The measurements were made for each biosensor in triplicate.

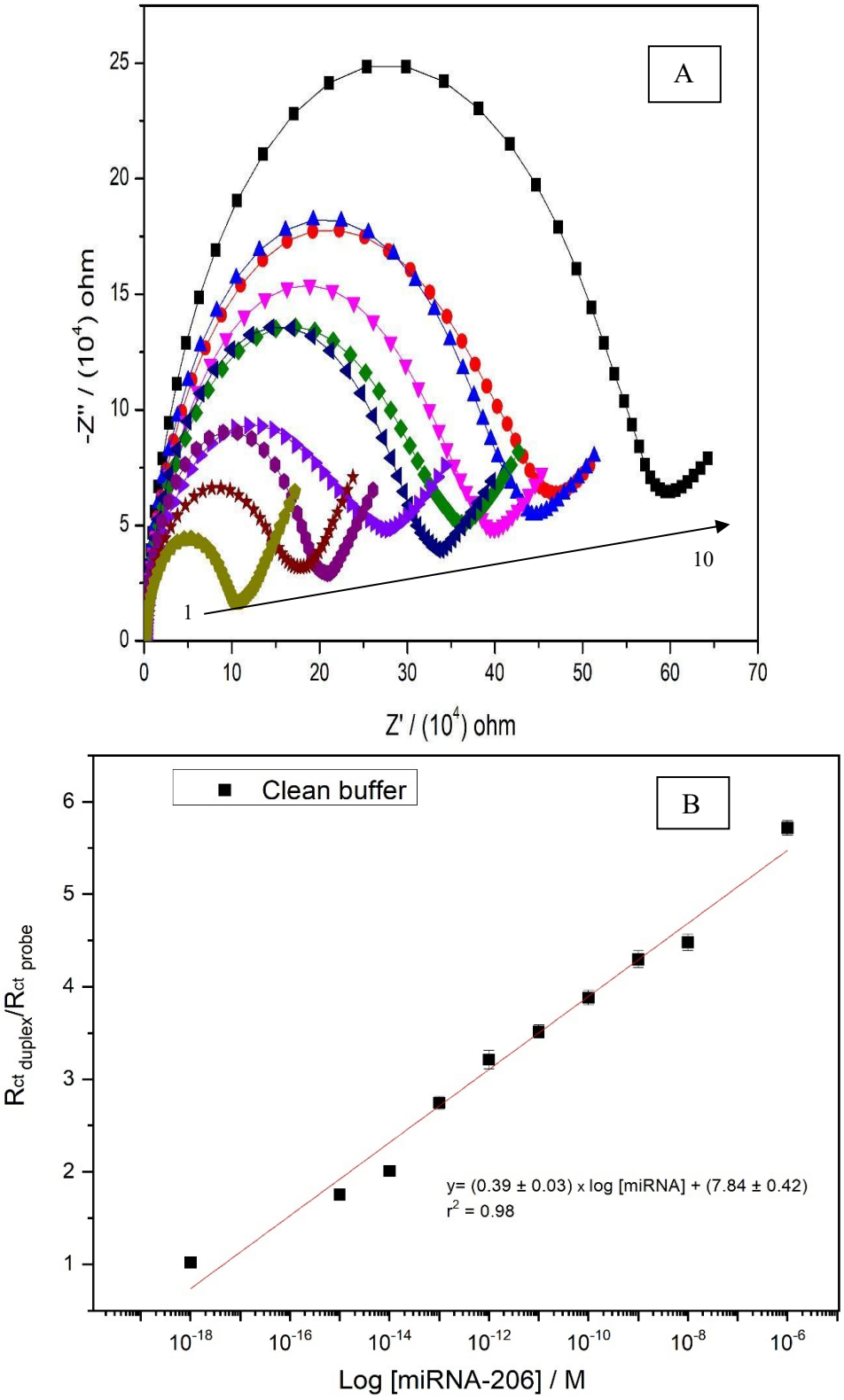


Figure 2.14. (A) Nyquist plots of impedance spectra obtained by the miRNA capture-probe electrode after hybridization with different concentrations of miRNA-206 during 20 min at 37°C and (B) the corresponding calibration curve based on the variation of charge transfer and log concentration of the

miRNA-206. The error bars were indicated on the curve (n = 3). Electrochemical species: 1 mM $[Fe(CN)_6]^{3-/4-}$ with 0.01 M PBS. Scan rate: 50 mV/s. Biasing potential: 0.231 V. Amplitude: 25 mV. Frequency range 0.1 Hz to 10^5 Hz. Numbers 1-10 correspond to 1aM to 1μM of miRNA-206.

The results indicated a logarithmic correlation between the concentration of miRNA target and the ΔR_{ct} presented by the system. The best-fit least-squares regression line equation determined was y = 0.39 log [miRNA] + 7.84, with a relative standard deviation between 1.80-2.20% (n = 3) for all concentrations. The assay has a wide dynamic range covering more than 10 orders of magnitude. Linear regression was observed within a concentration range from 10^{-6} to 10^{-18} M, with a regression coefficient of 0.98.

Limit of detection, which is characterized as the lowest analyte concentration likely to be reliably distinguished from the blank, was also determined in this study. As described in the experimental section of this chapter, the LOD was calculated considering the standard deviation of the blank and the slope of the calibration curve. The limit of detection obtained for the designed biosensor was 0.15 aM.

The concentration linear range and the detection limit obtained by the developed biosensor were also evaluated by comparison with relevant published studies on miRNA detection. Table 2.7 summarizes some sensitive label-free electrochemical biosensors. The obtained LOD of 0.15 aM shows to be superior to most of the LODs compared to this work. As the concentration of miRNA-206 in circulating human blood is considered to be at concentrations of fM (analysis at healthy patient) to μM (analysis at disease patient) [40], the fabricated biosensor provided a satisfactory LOD to detect the miRNA in human samples.

The improved LOD reported here reflects the careful optimization of the capture-probe layer surface coverage and the simultaneous optimization of the impedance change upon target binding and the hybridization efficiency. Understanding the effect of the miRNA capture-probe to MCH ratio and the addition of an optimal temperature in the hybridization and immobilization reactions, as well as reduced steric hinderance by controlling the separation/dispersion of the capture-probes all contribute to the wide dynamic range and low LOD.

The assay has a wide dynamic range covering 10 orders of magnitude suggesting relatively weak association of the target and capture-probe strands. In solution, the expected association constant is 3.04 $x10^8$, corresponding to a Gibbs free energy, ΔG, of -48.4 kJ mol^{-1}. Plotting the data shown in Figure 2.14 (B) according to a linearised Langmuir adsorption isotherm yields a high-quality fit (R^2 = 0.9997) and the slope gives an association constant of $1.38x10^6$, i.e., approximately 220-fold lower than that found in solution. This result most likely arise because the interfacial dielectric constant, 53.7±0.1 (Table A1, Appendix A) is significantly lower than that of water 81. The upper limit on the linear dynamic range is dictated by the availability of capture-probe strands on the electrode surface and a lower K_{assoc} means that less target will be bound relative to aqueous solution extending the linear range to higher concentrations. The lower limit of the dynamic range is dictated by the ability to generate a measurable signal in response to small amounts, ideally single binding events, of the target binding. Here, the hybridisation of the target increases the negative charge density of the interface (as reflected in the higher dielectric constants observed for higher target concentrations (Table A2, Appendix A)), which significantly decreases the interfacial concentration of the negatively charged ferrocyanide probe and decreases the rate of heterogeneous electron transfer allowing ultralow (aM) concentrations of the target to be detected.

Table 2.7. Comparison of the developed biosensor with different label-free electrochemical biosensors reporter in the literature for the detection of miRNAs. The current sensitive electrochemical biosensors selected here, performed the measurements under the same redox probe used at this work.

Electrode	Recognition element	Target	Signalling element	Technique	LOD	Linear range	Reference
Graphene/ PBSE	ssDNA	miRNA-21	$Fe(CN)_6^{3-/4-}$	EIS	3 fM	10 fM - 10 nM	[41]
Carbon black	ssDNA	miRNA-125	$Fe(CN)_6^{3-/4-}$	EIS	10 pM	1.0 nM – 1.98 µM	[42]
Naphthalene sulfonic acid	NH_2-ssDNA	miRNA-21	$Fe(CN)_6^{3-/4-}$	Coulometry	20 fM	10 fM – 10 nM	[43]
Biotinylated polythiophene/ streptavidin	Biotinylated-DNA	miRNA-221	$Fe(CN)_6^{3-/4-}$	EIS	0.70 pM	1.0 pM – 10 nM	[44]
Chit/NRGO	NH_2-ssDNA	miRNA-660	$Fe(CN)_6^{3-/4-}$	EIS	28 pM	82 pM- 0.1 nM	[45]
AuE	miRNA $_{\text{capture-probe}}$	miRNA-375	$Fe(CN)_6^{3-/4-}$	SWV	11.70 aM	10-30 fM	[46]
FTO/NFG/AgNP/ PANI	ss-DNA	miRNA-21	$Fe(CN)_6^{3-/4-}$	DPV	0.20 fM	10 fM – 10 µM	[47]
SPE/rGO-Au	ssDNA	miRNA-21	$Fe(CN)_6^{3-/4-}$	DPV	1 pM	1.0 pM – 1.0 µM	[48]
Laser induced graphene	N-doped-LIG	Has-miR-485-5p	$Fe(CN)_6^{3-/4-}$	DPV	10 fM	–	[49]
Au/SPE	Anti-miR-155	miRNA-155	$Fe(CN)_6^{3-/4-}$	EIS	0.54 fM	1 fM – 100 pM	[50]
AuE	miRNA $_{\text{capture-probe}}$	miRNA-206	$Fe(CN)_6^{3-/4-}$	EIS	0.15 aM	1aM – 1 µM	This work

2.2.5.1 Specificity of the miRNA detection

The selectivity of the proposed miRNA impedimetric biosensor was examined by two main studies. The first one evaluated the effect of bovine serum albumin, BSA, as a surrogate for the human serum albumin, HSA, that is commonly present in patient plasma samples. This protein has the ability of non-specifically bind to miRNA capture-probe thus competing with miRNA-206. To obtain more realistic data over the disruption generated by this protein, it was tested at a concentration that is close to its physiological levels e.g., 1mM. As shown in Figure 2.15, the interference was checked at varying concentrations (ranging from 1 μM to 1 aM) of the miRNA target and the results were compared to samples containing miRNA in the absence of BSA. Table 2.8 summarises the data.

Table 2.8. Comparison between the resistance to the charge transfer of a fully complementary nucleic acid strand in and without an environment of BSA.

Concentration of miRNA (M)	ΔRct target	ΔRct target with BSA	% Decrease
$1x10^{-6}$	5.72 ± 0.06	5.44 ± 0.05	4.89
$1x10^{-9}$	4.30 ± 0.03	4.07± 0.02	5.35
$1x10^{-12}$	3.21 ± 0.05	3.05 ± 0.02	4.98
$1x10^{-15}$	1.75 ± 0.02	1.64 ± 0.03	6.48
$1x10^{-18}$	1.02 ± 0.03	0.96± 0.03	5.88

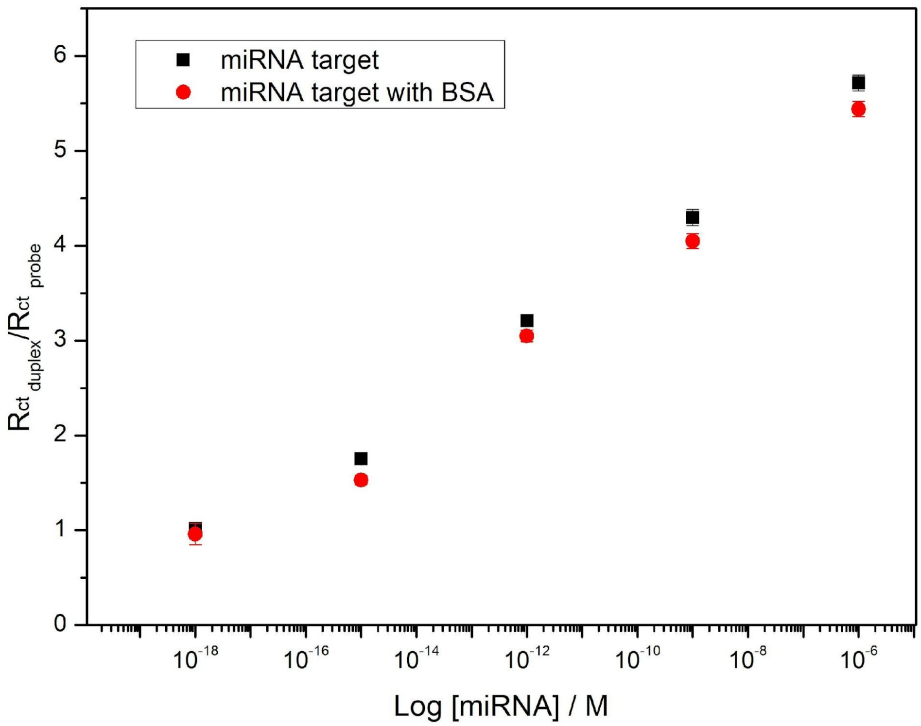


Figure 2.15. Calibration curves of a miRNA capture-probe hybridized with different concentrations of miRNA-206 (from µM to aM) without any interfering assay (black line) and in an environment where BSA is present (red line). The variations of charge transfer resistance were obtained from the response of the Nyquist plots at the different concentrations. The error bars were indicated on the curve (n = 3). The parameters used were scan rate: 50 mV/s, biasing potential: 0.231 V, amplitude: 25 mV and frequency range: 0.1Hz to 10^5 Hz. The analysis was performed at 0.01 M PBS containing 1 mM $[Fe(CN)_6]^{3-/4-}$ as a redox probe.

The result shows that this sensor has good resistance to non-specific binding of BSA across a wide range of target concentrations. The high level of discrimination against excess of undesirable proteins- presented here by a decrease of approximately 6.5% in the charge transfer resistance- points to a significant reduction of non-specific binding of protein on the transducer surface.

Additional studies to evaluate the sensor selectivity were performed using a non-complementary target, miRNA-1. This has a highly similar sequence to miRNA-206, differing in only 4 bases [51]. The biosensor was incubated with miRNAs in the range of nM and pM and the obtained results were illustrated in Figure 2.16.

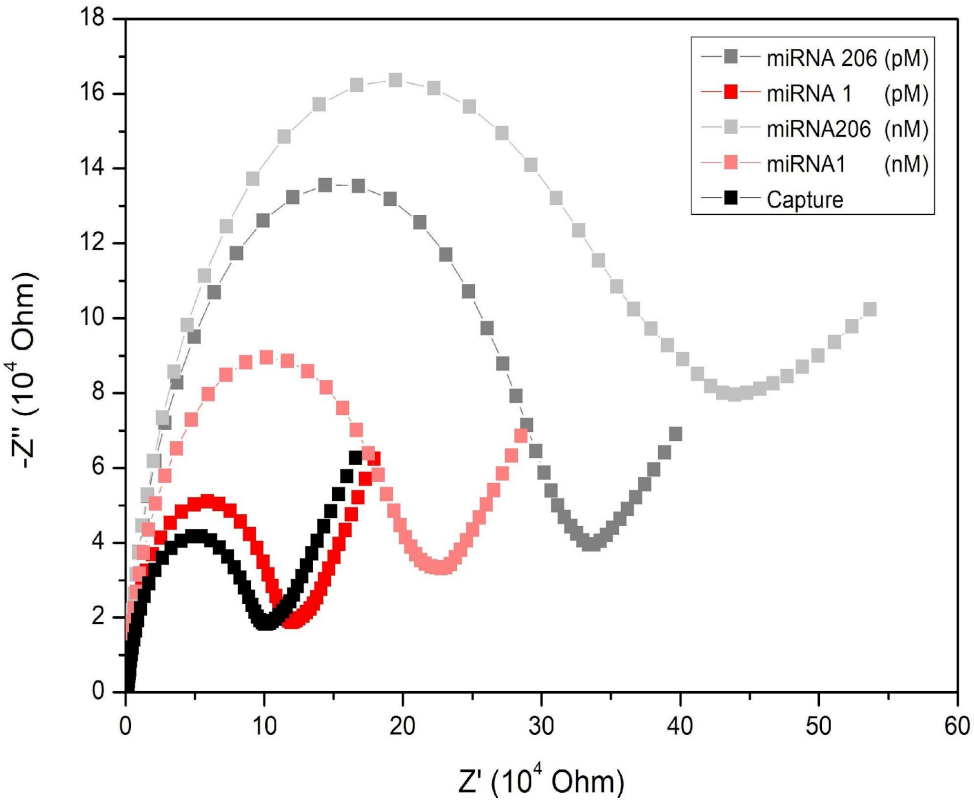


Figure 2.16. Impedimetric curves (Nyquist plots) showing the variation of the charge transfer resistance between miRNA capture-probe and a fully complementary target strand (black and grey line) and a 4-base mismatched strand (red and pink line). Electrochemical species: 1 mM $[Fe(CN)_6]^{3-/4-}$ with 0.01 M PBS. Scan rate: 50 mV/s. Potential applied: 0.231 V, amplitude: 25 mV and frequency range: 0.1Hz to 10^5Hz.

The Nyquist plot presents the degree of variation of the charge transfer resistance when in the presence of 4-base mismatches and a fully complementary sequence. Both miRNAs cause a shift in the charge transfer resistance. However, the shift caused by the fully complementary target is significantly larger reflecting its larger association constant and greater surface coverage of the capture probe –target duplex. Therefore, the difference/decrease in the R_{ct} generated by the hybridization with miRNA-1 to capture when comparing to the hybridization with miRNA-206 to capture is in the range of 51% for 1nM of target and 64% for 1 pM of target (see Table 2.9). These results indicate a good ability of the system to accurately hybridize with nucleotides that is highly compatible with its capture sequence.

Table 2.9. Comparison between the resistance to the charge transfer of a fully complementary nucleic acid strand and a 4-base mismatch. The average values and standard deviation are calculated based on n=3.

Concentration of miRNA (M)	R_{ct} (10^5 Ω) Fully Comp.	R_{ct} (10^5 Ω) Mismatch	% Decrease
$1x10^{-9}$	4.49 ± 0.03	2.27 ± 0.02	50.56
$1x10^{-12}$	3.36 ± 0.05	1.20 ± 0.02	64.28

As already explained in the scope of this chapter, the substantial increase in the charge transfer resistance is justified by the sequence-specific formation of the double helix between the miRNA capture-probe and its complementary sequence of target [52]. Therefore, a decrease in the R_{ct} values is an indication that the miRNA capture-probe cannot bind completely to the miRNA target sequence leading to a process of target differentiation by the system.

2.2.5.2 Stability and reproducibility of the fabricated biosensor

To assess the stability of the proposed biosensor, three identical assays were performed over independent electrodes with further storage in an immobilization buffer at 4 °C over a period of 14 days. The EIS analysis towards miRNA-206 was studied at two different concentrations (1 nM and 1 pM) to get an insight into the effect of storage on the calibration sensitivity. Measurements were made in intervals of 4-5 days. Figure 2.17 illustrates the response of the charge transfer resistance across different times.

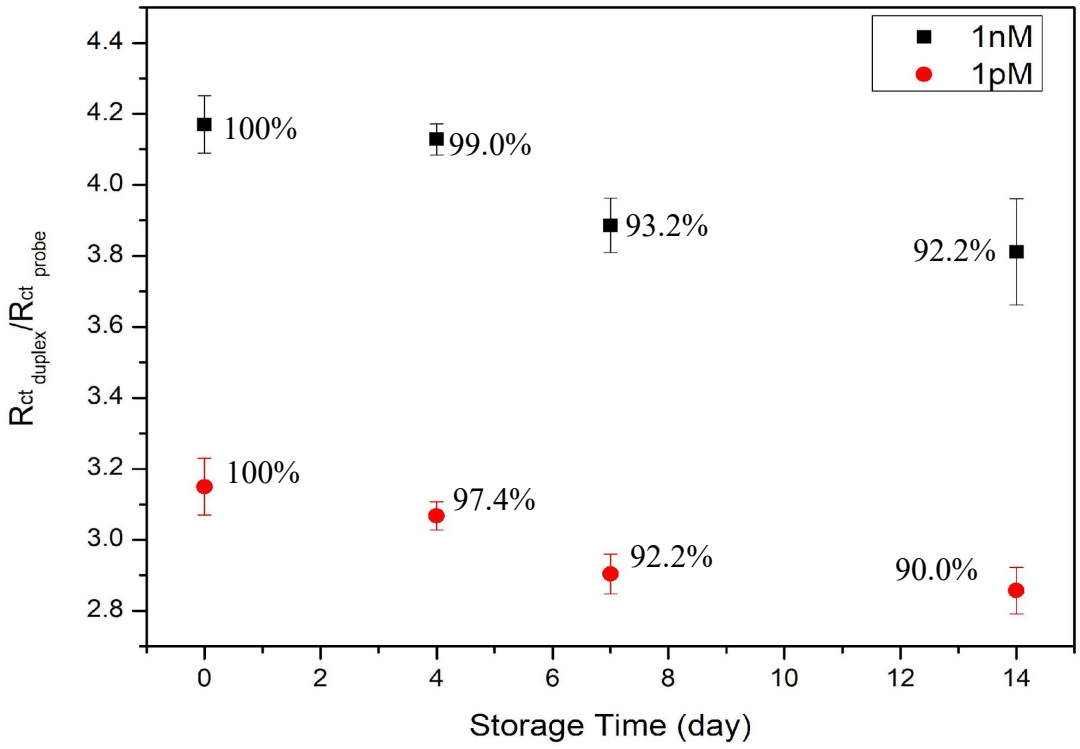


Figure 2.17. Impedimetric response of the biosensor toward miRNA-206 at different concentrations after storage in the immobilization buffer at 4 °C. The number next to each data point represents the average percent of response compared to the freshly prepared biosensors. The error bars were calculated based on standard deviation of the measurements performed in triplicate (n=3).

The response of the biosensor hybridized with 1 nM of miRNA-206 after 14 days of storage in a refrigerator presented at about 92.2% of of the value find when the sensors were fabricated and used directly with no storage. On the other hand, the response of the biosensor for 1pM of the miRNA target under the same conditions of time and temperature was restored up to 90.0% of the time zero response. These results suggested that the self-assembled monolayer formed by MCH and miRNA capture-probe at the gold electrode is stable for a period of at least 14 days, possessing a good activity for hybridization. The major cause of losses is likely to be exogenous ribonucleases (RNAse) that decompose the capture-probe strands on the electrode surface.

The reproducibility of the biosensor can be discussed by analysing the relative standard deviation (RSD) obtained by the response of three independent electrodes prepared in parallel under identical procedure. The results of this experiment can be visualized on the calibration

curve described by Figure 2.14. Additional assessment over which concentration correlates to RSD can be visualized in Table 2.8 (data available in section 2.2.5.1).
The concentration studied was in the range of 1 μM to aM and the RSD obtained presented between 2.10-5.80%. As in accordance with the literature, the limit for reliable measurements should be smaller or equal to 5% [53] which is achieved by the fabricated sensor, validating the procedure as a suitable methodology for developing a sensitive and reproductive platform of miRNA detection.

2.2.5.3 Quantitative detection of miRNA-206 in plasma samples

To validate the capability of the developed biosensor to accurately detect miRNA-206 in real samples, two complementary studies were performed i.e., standard additions to plasma samples and correlation of the sensor results with quantitative PCR, qPCR. In the first study, the feasibility of the detection was examined by measuring the absolute concentration of miRNA target present in human plasma samples. For that was used both, female and male samples, from sick patients, e.g. AD positive (miRNA-206 upregulated) and from healthy patients, e.g. AD negative (miRNA-206 normally regulated). The plasma samples were diluted 1000 times in a hybridization buffer and the variations in charge transfer resistance were used to quantify the amount of miRNA incubated on the surface of the biosensor.

To ensure a more reliable calculation of sample concentrations, calibration curves were constructed using healthy plasma samples (previously diluted 1000 times) as a control. Figures 2.18 A and B show the R_{ct} variations obtained in response to the different additions of standard miRNAs (from μM to aM range) to female and male healthy diluted samples.

In the standard addition investigation, specific concentrations of miRNA-206 at nM scale (100 nM and 1 nM) and pM scale (10 pM and 1pM) were spiked to AD positive and AD negative samples, respectively. The recovery values at each spiked concentration were, once more, calculated based on the correlation of the sensor response (variation of R_{ct}) to the equation obtained by the analysis of the calibration curve. Table 2.10 summarizes the recovery results of the different samples and the errors related to the above measurements.

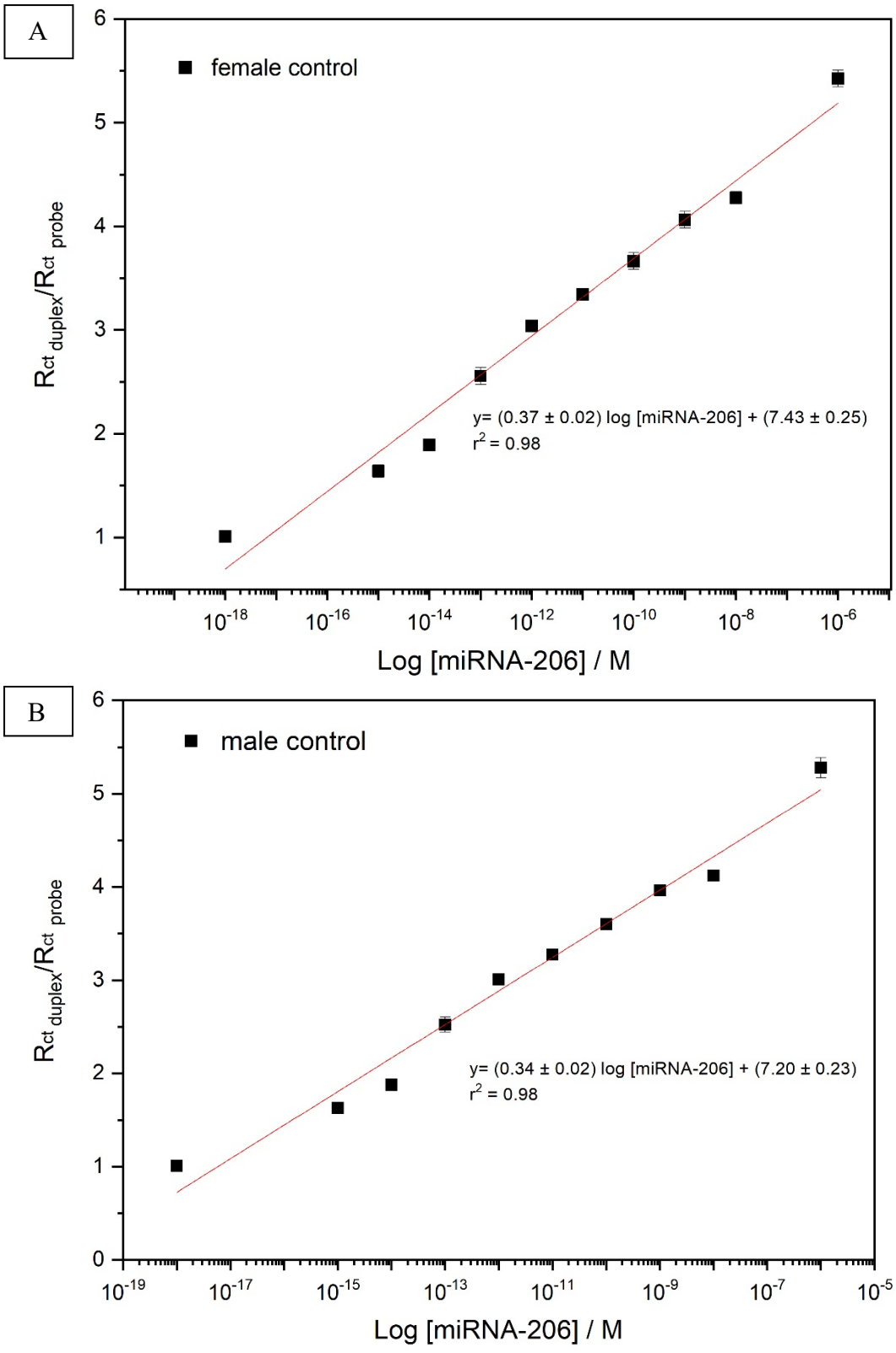


Figure 2.18. (A) Calibration curves of a miRNA capture-probe electrode hybridized with different concentrations of standard miRNA-206 (from µM to aM) in a healthy female control sample and (B) in a healthy male control sample. The variations of charge transfer resistance were obtained from the response of the Nyquist plots at the different concentrations. The error bars were indicated on the curve

and were calculated based on standard deviation of the measurements performed in triplicate (n = 3). The parameters used were: scan rate: 50 mV/s, biasing potential: 0.231 V, amplitude: 25 mV and frequency range: 0.1 Hz to 10^5 Hz. The analysis was performed at 0.01 M PBS containing 1 mM $[Fe(CN)_6]^{3-/4-}$ as a redox probe.

Table 2.10. Detection of miRNA-206 in healthy (control) and disease plasma (AD positive) samples (n = 3) by the developed biosensor.

Sample	Added [miRNA-206]	Detected [miRNA-206]	Recovery (%)	RSD%	qPCR/ A.U.
L059: AD positive Female plasma (82y)	0 100 nM 1 nM	23.70 nM 120.10 nM 24.80 nM	96.40 110.00	4.01 5.10 4.93	13.67
L076: AD positive Male plasma (83y)	0 100 nM 1 nM	14.20 nM 109.60 nM 15.26 nM	95.40 106.00	5.02 4.81 4.71	9.54
0003: Control Female plasma (75y)	0 10 pM 1 pM	2.67 pM 12.54 pM 3.74 pM	98.72 107.00	10.03 4.89 5.41	1.52
0048: Control Male plasma (76y)	0 10 pM 1 pM	2.37 pM 12.05 pM 3.43 pM	96.84 105.60	6.01 6.76 6.33	0.52

The recovery results obtained were in the range of 95.4-110% for AD positive samples and between 96.8-107% for AD negative samples. Considering that these values are within the clinically acceptable range, described in the literature as being between 80-120% [54], the biosensor is classified as satisfactory for accurate and precise detection of circulating blood biomarkers in clinical diagnostics. Moreover, the relative standard deviation of 4.7–5.1% for AD positive samples (n = 3) and 4.89 to 6.76% for AD negative analysis (n=3) indicates a very good reproducibility between the assays.

The average of miRNA concentration in the AD positive samples were found to be 23.70± 0.04 nM for female and 14.20± 0.05 nM for male samples. On the other hand, the average of target concentration in AD negative samples was found to be in the pM range, achieving 2.67±0.10 pM for female and 2.37±0.06 for male control. It is noteworthy that the variation found between the analyses of female and male genders for AD negative and AD positive samples were considered negligible.

The qPCR data shown in Table 2.10 are in arbitrary units but qualitatively correlate with the sensor data, i.e., the level in the controls is significantly lower than the AD patients and the relative levels in the patient samples correlate between the two techniques. There is also a strong quantitative correlation, i.e., when all patient and control data are included, the correlation coefficient (R^2) is 0.985.

On the work developed by Kenny *et al.* [40] where miRNA-206 concentrations were detected using a similar, but more complex, prototype electrochemical sandwich assay in unprocessed plasma, the concentrations detected for AD positive samples were in the range of nM to µM and AD negative samples were in the range of aM to pM. Therefore, comparing these results to the one found at this work, it is not only possible to validate the response of the developed sensor, but also to prove the success of the employed methodology. The developed platform proves to be highly sensitive and capable of quantifying miRNAs without the need to use signal amplifier particles, which makes the manufacture of this sensor cheaper and more feasible to produce.

2.3 Conclusion

In conclusion, an impedimetric biosensor for sensitive, selective, and label-free detection of a blood circulating miRNA related to Alzheimer disease, as miRNA-206, was developed. The principle was grounded in the effect of intramolecular forces generated between miRNAs and a redox probe. When a miRNA capture-probe binds to the target, an additional negative charge is induced through the surface which, in connection to an anionic redox active probe, leads to a repulsion between electrode-electrolyte. This effect enhances the change in the charge transfer resistance giving an excellent response in electrochemical EIS with a solution phase redox probe.

This enhanced performance has been achieved through a well-structured transducer platform. The experiments reported in this chapter lead to the formation of a compact well-ordered mixed monolayer that effectively inhibits non-specific adsorption issues that are common in bio-affinity assays. Specifically, the MCH co-immobilized to miRNA capture-probe in the 1:4 ratio (at 37°C) is an effective spacer of the capture-probe strands, assisting the orientation of the oligonucleotides and providing sufficient space for hybridization of the target. It also influences the electron transfer from the redox probe to the surface [55]. The usage of the optimal ratio between miRNA and MCH provides the ideal balance between R_{ct} modulation and hybridization efficiency.

The response of the constructed assay was investigated by examination of the LOD, linear range, selectivity, sensitivity, and stability. The analytical parameters of the biosensor were described over the analyses of a calibration curve constructed in a clean buffer. In addition, the selectivity of the assay was investigated using a 4-base mismatches miRNA (miRNA-1) and in a context of a competitive assay, where BSA were used as an interfering agent to the target. In parallel, stability was also studied by periodic analysis of the response of the biosensor stored at immobilization buffer for 14 days at 4°C. The wide linear range (from μM to aM), low limit of detection (found to be 0.15 aM), high sensitivity and stability (response of the signal maintained up to 90% of its original value) makes it attractive for the development of a point of care diagnostic device.

Validation of the method in real plasma samples was also performed to gain an insight into the effect of using real samples. A calibration curve was constructed using 1000X diluted healthy plasma samples, AD negative, and standard additions (μM to aM) of miRNA-206.Additional assessment of the disease samples was made by specifical spiking on nM and pM scale of standard miRNA-206. A possible interfering factor was also studied by comparing the response of the sensor at female and male AD positive and negative samples. Gender was not considered a confounding factor and recovery was found to be at a clinical acceptable range, achieving values of 95.4-110% to AD positive samples and 96.8-107% to AD negative samples.

A vision, looking forward, is to incorporate the impedimetric biosensor as a periodic monitoring system, e.g., at an annual medical exam. A first step was already achieved through

the reliable quantification of miRNAs at a pinprick volume (approximately 50 µL of plasma). The simple platform fabricated, which does not require additional amplification methods, also brought accessibility over the confection price of the sensor. Therefore, these results suggest that with some additional studies regarding the miniaturization of the platform to a portable device, it could be used as a detection system for mass screening of people suffering from Alzheimer disease.

2.4 References

[1] Zhu, C. S., Zhu, L., Tan, D. A., Qiu, X. Y., Liu, C. Y., Xie, S. S., & Zhu, L. Y. (2019). Avenues Toward microRNA Detection *In Vitro*: A Review of Technical Advances and Challenges. *Computational and structural biotechnology journal*, *17*, 904–916. https://doi.org/10.1016/j.csbj.2019.06.018

[2] Gillespie, P., Ladame, S., & O'Hare, D. (2018). Molecular methods in electrochemical microRNA detection. *The Analyst*, *144*(1), 114–129. https://doi.org/10.1039/c8an01572d

[3] Bardea, A., Patolsky, F., Dagan, A., & Willner, I. (1999). Sensing and amplification of oligonucleotide-DNA interactions by means of impedance spectroscopy: a route to a Tay-Sachs sensor. *Chemical Communications*, 21-22.

[4] Cederquist, K. B., & Keating, C. D. (2010). Hybridization efficiency of molecular beacons bound to gold nanowires: effect of surface coverage and target length. *Langmuir : the ACS journal of surfaces and colloids*, *26*(23), 18273–18280. https://doi.org/10.1021/la1031703

[5] Herne, T. M., & Tarlov, M. J. (1997). Characterization of DNA probes immobilized on gold surfaces. *Journal of the American Chemical Society*, 119(38), 8916–8920. https://doi.org/10.1021/ja9719586

[6] Keighley, S. D., Estrela, P., Li, P., & Migliorato, P. (2008). Optimization of label-free DNA detection with electrochemical impedance spectroscopy using PNA probes. *Biosensors & bioelectronics*, *24*(4), 912–917. https://doi.org/10.1016/j.bios.2008.07.041

[7] Trasatti, S., & Petrii, O. A. (1991). Real surface area measurements in electrochemistry. *Pure & Applied Chemistry, 63*, 711-734. https://doi.org/10.1351/pac199163050711

[8] Marcus, R. A. (1956). On the theory of oxidation-reduction reactions involving electron transfer I. *The Journal of Chemical Physics, 24*(5), 966-978. https://doi.org/10.1063/1.1742723

[9] Nicholson, R. S., & Shain, Irving. (1964). Theory of stationary electrode polarography. Single scan and cyclic methods applied to reversible, irreversible, and kinetic systems. *Analytical Chemistry, 36*(4), 706–723. https://doi.org/10.1021/ac60210a007

[10] Lavagnini, I., Antiochia, R., & Magno, F. (2004). An extended method for the practical evaluation of the standard rate constant from cyclic voltammetric data. *Electroanalysis, 16*(6), 505-506. https://doi.org/10.1002/elan.200302851

[11] Macdonald, J. R. (Ed.). (1987). Impedance Spectroscopy (Sections 2.1.2.3 and 2.2.3.4). John Wiley.

[12] Orazem, M. E., Shukla, P., & Membrino, M. A. (2002). Extension of the measurement model approach for deconvolution of underlying distributions for impedance measurements. *Electrochimica Acta, 47*(13-14), 2027-2034. https://doi.org/10.1016/S0013-4686(02)00065-8

[13] Janek, R. P., Fawcett, W. R., & Ulman, A. (1998). Impedance Spectroscopy of Self-Assembled Monolayers on Au(111): Sodium Ferrocyanide Charge Transfer at Modified Electrodes. *Langmuir, 14*(11), 3011-3018. https://doi.org/10.1021/la970980+

[15] Sánchez-Pomales, G., Santiago-Rodríguez, L., Rivera-Vélez, N., & Cabrera, C. (2007). Control of DNA self-assembled monolayers surface coverage by electrochemical desorption. *Journal of Electroanalytical Chemistry, 611*, 80-86. https://doi.org/10.1016/j.jelechem.2007.08.003

[16] Zhang, J., Song, S., Wang, L., Pan, D., & Fan, C. (2007). A gold nanoparticle-based chronocoulometric DNA sensor for amplified detection of DNA. *Nature protocols*, *2*(11), 2888–2895. https://doi.org/10.1038/nprot.2007.419

[17] Domínguez, C. M., Ramos, D., Mendieta-Moreno, J. I., Fierro, J. L. G., Mendieta, J., Tamayo, J., & Calleja, M. (2017). Effect of water-DNA interactions on elastic properties of DNA self-assembled monolayers. *Scientific reports*, *7*(1), 536. https://doi.org/10.1038/s41598-017-00605-x

[18] Zhang, J., Song, S., Zhang, L., Wang, L., Wu, H., Pan, D., & Fan, C. (2006). Sequence-specific detection of femtomolar DNA via a chronocoulometric DNA sensor (CDS): effects of nanoparticle-mediated amplification and nanoscale control of DNA assembly at electrodes. *Journal of the American Chemical Society*, *128*(26), 8575–8580. https://doi.org/10.1021/ja061521a

[19] Su, L., Sankar, C. G., Sen, D., & Yu, H. Z. (2004). Kinetics of ion-exchange binding of redox metal cations to thiolate-DNA monolayers on gold. *Analytical chemistry*, *76*(19), 5953–5959. https://doi.org/10.1021/ac0494331

[20] McEwen, G. D., Chen, F., & Zhou, A. (2009). Immobilization, hybridization, and oxidation of synthetic DNA on gold surface: electron transfer investigated by electrochemistry and scanning tunneling microscopy. *Analytica chimica acta*, *643*(1-2), 26–37. https://doi.org/10.1016/j.aca.2009.03.050

[21] Nicholson, R. S. (1965). Theory and application of cyclic voltammetry for measurement of electrode reaction kinetics. *Analytical Chemistry*, 37(11), 1351–1355.https://doi.org/10.1021/ac60230a016

[22] Hu, I.-F., Karweik, D. H., & Kuwana, T. (1985). Activation and deactivation of glassy carbon electrodes. *Journal of Electroanalytical Chemistry and Interfacial Electrochemistry, 188* (1-2), 59–72. https://doi.org/10.1016/S0022-0728(85)80050-4

[23] Li, Z., Niu, T., Zhang, Z., Chen, R., Feng, G., & Bi, S. (2011). Exploration of the specific structural characteristics of thiol-modified single-stranded DNA self-assembled monolayers on gold by a simple model. *Biosensors & bioelectronics*, *26*(11), 4564–4570. https://doi.org/10.1016/j.bios.2011.05.024

[24] Ganesh, V., Pal, S. K., Kumar, S., & Lakshminarayanan, V. (2006). Self-assembled monolayers (SAMs) of alkoxycyanobiphenyl thiols on gold--a study of electron transfer reaction using cyclic voltammetry and electrochemical impedance spectroscopy. *Journal of colloid and interface science*, *296*(1), 195–203. https://doi.org/10.1016/j.jcis.2005.08.051

[25] Magriñá, I., Ortiz, M., Simonova, A., Hocek, M., O' Sullivan, C. K., & Forster, R. J. (2021). Ferrocene-Containing DNA Monolayers: Influence of Electrostatics on the Electron Transfer Dynamics. *Langmuir : the ACS journal of surfaces and colloids*, *37*(11), 3359–3369. https://doi.org/10.1021/acs.langmuir.0c03485

[26] Bardea, A., Patolsky, F., Dagan, A., & Willner, I. (1999). Sensing and amplification of oligonucleotide-DNA interactions by means of impedance spectroscopy: a route to a Tay-Sachs sensor. *Chemical Communications*, 21-22. https://doi.org/10.1039/A808319C

[27] Cederquist, K. B., & Keating, C. D. (2010). Hybridization efficiency of molecular beacons bound to gold nanowires: effect of surface coverage and target length. *Langmuir : the ACS journal of surfaces and colloids*, *26*(23), 18273–18280. https://doi.org/10.1021/la1031703

[28] Herne, T. M., & Tarlov, M. J. (1997). Characterization of DNA probes immobilized on gold surfaces. *Journal of the American Chemical Society, 119*(38), 8916–8920. https://doi.org/10.1021/ja9719586

[29] Nogues, C., Cohen, S. R., Daube, S. S., & Naaman, R. (2004). Electrical properties of short DNA oligomers characterized by conducting atomic force microscopy. *Physical Chemistry Chemical Physics, 6*(18), 4459-4466. https://doi.org/10.1039/B410862K

[30] Ouyang, T., Liu, Z., Han, Z., & Ge, Q. (2019). MicroRNA Detection Specificity: Recent Advances and Future Perspective. *Analytical chemistry*, *91*(5), 3179–3186. https://doi.org/10.1021/acs.analchem.8b05909

[31] Xu, X., Makaraviciute, A., Kumar, S., Wen, C., Sjödin, M., Abdurakhmanov, E., Danielson, U. H., Nyholm, L., & Zhang, Z. (2019). Structural Changes of Mercaptohexanol Self-Assembled Monolayers on Gold and Their Influence on Impedimetric Aptamer Sensors. *Analytical chemistry*, *91*(22), 14697–14704. https://doi.org/10.1021/acs.analchem.9b03946

[32] Bain, C. D., Evall, J., & Whitesides, G. M. (1989). Formation of monolayers by the coadsorption of thiols on gold: variation in the head group, tail group, and solvent. *Journal of the American Chemical Society, 111*(18), 7155-7164. https://doi.org/10.1021/ja00200a039

[33] Poirier, G. E., Pylant, E. D., & White, J. M. (1996). Crystalline structures of pristine and hydrated mercaptohexanol self-assembled monolayers on Au (111). *Journal of Chemical Physics, 104*, 7325-7328. https://doi.org/10.1063/1.471399

[34] Zhang, J., Song, S., Zhang, L., Wang, L., Wu, H., Pan, D., & Fan, C. (2006). Sequence-specific detection of femtomolar DNA via a chronocoulometric DNA sensor (CDS): effects of nanoparticle-mediated amplification and nanoscale control of DNA assembly at electrodes. *Journal of the American Chemical Society*, *128*(26), 8575–8580. https://doi.org/10.1021/ja061521a

[35] Yao, B., Liu, Y., Tabata, M., Zhu, H., & Miyahara, Y. (2014). Sensitive detection of microRNA by chronocoulometry and rolling circle amplification on a gold electrode. *Chemical communications (Cambridge, England)*, *50*(68), 9704–9706. https://doi.org/10.1039/c4cc03330b

[36] Steel, A. B., Herne, T. M., & Tarlov, M. J. (1998). Electrochemical quantitation of DNA immobilized on gold. *Analytical chemistry*, *70*(22), 4670–4677. https://doi.org/10.1021/ac980037q

[37] Peterson, A. W., Heaton, R. J., & Georgiadis, R. M. (2001). The effect of surface probe density on DNA hybridization. *Nucleic acids research*, *29*(24), 5163–5168. https://doi.org/10.1093/nar/29.24.5163

[38] Bielec, K., Sozanski, K., Seynen, M., Dziekan, Z., Ten Wolde, P. R., & Holyst, R. (2019). Kinetics and equilibrium constants of oligonucleotides at low concentrations. Hybridization and melting study. *Physical chemistry chemical physics : PCCP*, *21*(20), 10798–10807. https://doi.org/10.1039/c9cp01295h

[39] Manning G. S. (1978). The molecular theory of polyelectrolyte solutions with applications to the electrostatic properties of polynucleotides. *Quarterly reviews of biophysics*, *11*(2), 179–246. https://doi.org/10.1017/s0033583500002031

[40] Kenny, A., McArdle, H., Calero, M., Rabano, A., Madden, S. F., Adamson, K., Forster, R., Spain, E., Prehn, J. H. M., Henshall, D. C., Medina, M., Jimenez-Mateos, E. M., & Engel, T. (2019). Elevated Plasma microRNA-206 Levels Predict Cognitive Decline and Progression to Dementia from Mild Cognitive Impairment. *Biomolecules*, *9*(11), 734. https://doi.org/10.3390/biom9110734

[41] Asadi, H., & Ramasamy, R. P. (2020). Graphene-Based Electrochemical Biosensor for Impedimetric Detection of miRNA as Potential Cancer Biomarker. *Journal of The Electrochemical Society, 167*. https://doi.org/10.1149/1945-7111/abd284

[42] Yammouri, G., Mandli, J., Mohammadi, H., & Amine, A. (2017). Development of an electrochemical label-free biosensor for microRNA-125a detection using pencil graphite electrode modified with different carbon nanomaterials. *Journal of Electroanalytical Chemistry, 806*, 75-78. https://doi.org/10.1016/j.jelechem.2017.10.012

[43] Smith, D. A., Newbury, L. J., Drago, G., Bowen, T., & Redman, J. E. (2017). Electrochemical detection of urinary microRNAs via sulfonamide-bound antisense hybridisation. *Sensors and actuators. B, Chemical*, *253*, 335–341. https://doi.org/10.1016/j.snb.2017.06.069

[44] Voccia, D., Sosnowska, M., Bettazzi, F., Roscigno, G., Fratini, E., De Franciscis, V., Condorelli, G., Chitta, R., D'Souza, F., Kutner, W., & Palchetti, I. (2017). Direct determination

of small RNAs using a biotinylated polythiophene impedimetric genosensor. *Biosensors & bioelectronics*, *87*, 1012–1019. https://doi.org/10.1016/j.bios.2016.09.058

[45] Krishnan, S. K., Singh, E., Singh, P., Meyyappan, M., & Nalwa, H. S. (2019). A review on graphene-based nanocomposites for electrochemical and fluorescent biosensors. *RSC advances*, *9*(16), 8778–8881. https://doi.org/10.1039/c8ra09577a

[46] Jeong, B., Kim, Y. J., & Jeong, J.-Y. (2019). Label-free electrochemical quantification of microRNA-375 in prostate cancer cells. *Journal of Electroanalytical Chemistry, 846*, 113127. https://doi.org/10.1016/j.jelechem.2019.05.009

[47] Salahandish, R., Ghaffarinejad, A., Omidinia, E., Zargartalebi, H., Majidzadeh-A, K., Naghib, S. M., & Sanati-Nezhad, A. (2018). Label-free ultrasensitive detection of breast cancer miRNA-21 biomarker employing electrochemical nano-genosensor based on sandwiched AgNPs in PANI and N-doped graphene. *Biosensors & bioelectronics*, *120*, 129–136. https://doi.org/10.1016/j.bios.2018.08.025

[48] Low, S. S., Pan, Y., Ji, D., Li, Y., Lu, Y., He, Y., Chen, Q., & Liu, Q. (2020). Smartphone-based portable electrochemical biosensing system for detection of circulating microRNA-21 in saliva as a proof-of-concept. *Sensors and Actuators B: Chemical, 308*, 127718. https://doi.org/10.1016/j.snb.2020.127718

[49] Wan, Z., Umer, M., Lobino, M., Thiel, D., Nguyen, N.-T., Trinchi, A., Shiddiky, M. J., Gao, Y., & Li, Q. (2020). Laser induced self-N-doped porous graphene as an electrochemical biosensor for femtomolar miRNA detection. *Carbon, 163*, 385–394. https://doi.org/10.1016/j.carbon.2020.03.043

[50] Cardoso, A. R., Moreira, F. T. C., Fernandes, R., & Sales, M. G. F. (2016). Novel and simple electrochemical biosensor monitoring attomolar levels of miRNA-155 in breast cancer. *Biosensors & bioelectronics*, *80*, 621–630. https://doi.org/10.1016/j.bios.2016.02.035

[51] Lin, C. Y., Lee, H. C., Fu, C. Y., Ding, Y. Y., Chen, J. S., Lee, M. H., Huang, W. J., & Tsai, H. J. (2013). MiR-1 and miR-206 target different genes to have opposing roles during angiogenesis in zebrafish embryos. *Nature communications*, *4*, 2829. https://doi.org/10.1038/ncomms3829

[52] Pilehvar, S., Dierckx, T., Blust, R., Breugelmans, T., & De Wael, K. (2014). An electrochemical impedimetric aptasensing platform for sensitive and selective detection of small molecules such as chloramphenicol. *Sensors (Basel, Switzerland)*, *14*(7), 12059–12069. https://doi.org/10.3390/s140712059

[53] Miller, J. N., & Miller, J. C. (2010). *Statistics and Chemometrics for Analytical Chemistry* (6th ed.). Pearson Education.

[54] Zhang, K., Wang, K., Zhu, X., Xu, F., & Xie, M. (2017). Sensitive detection of microRNA in complex biological samples by using two stages DSN-assisted target recycling signal amplification method. *Biosensors & bioelectronics*, *87*, 358–364. https://doi.org/10.1016/j.bios.2016.08.081

[55] Khan, R., Ben Aissa, S., Sherazi, T. A., Catanante, G., Hayat, A., & Marty, J. L. (2019). Development of an Impedimetric Aptasensor for Label Free Detection of Patulin in Apple Juice. *Molecules (Basel, Switzerland)*, *24*(6), 1017. https://doi.org/10.3390/molecules24061017

CHAPTER 3

Development of an electrochemical biosensor using amperometry and gold nanorod labels.

3 INTRODUCTION

MicroRNAs (miRNAs) play a crucial role in the regulation of gene expression and have been linked to various diseases, including neurological disorders. Among them, miRNA-206 has shown significant relevance as biomarker of Alzheimer disease (AD), playing a significant role in disease progression [1] making its detection a pressing challenge that requires highly sensitive biosensors. This chapter describes an investigation to address this unmet need by developing a novel approach in the development of an electrochemical biosensor using gold nanorods (AuNRDs) as labels to enhance the signal associated with miRNA target hybridization.

Previous studies [2-4] have predominantly focused on utilizing AuNRDs in optical sensors, leveraging their unique optical properties for detection purposes. However, the potential of AuNRDs as electrocatalytic labels in amperometric biosensors remains largely unexplored. This work diverges from the existing literature by investigating the application of AuNRDs as electrocatalytic labels, aiming to amplify the signal and improve the sensitivity of miRNA detection in an electrochemical setting.

The utilization of spherical gold nanoparticles in electrochemical biosensors has been extensively studied, benefiting from their ability to adsorb biomolecules, enhance mass transport, and provide a large surface area for electrocatalytic reductions [5-7]. However, the distinctive properties of AuNRDs, including their rod shape, high aspect ratio, and increased surface area, suggest the possibility of improved catalytic activity specific to their size and shape. Specifically, the rod shape of the nanoparticle leaves a high ratio of surface atoms with free valences compared to the number of total atoms [8]. Their high aspect ratio results in a larger surface area, relative to a sphere, and perhaps more rapid decomposition of hydrogen peroxide [9]. By exploring their potential in electrocatalytic reactions, this chapter seeks to uncover new opportunities for highly sensitive miRNA detection.

The development of an electrochemical biosensor with AuNRDs as labels offers several advantages over optical biosensors employing the same labels. Electrochemical biosensors provide higher sensitivity and exhibit lower background noise, resulting in enhanced signal-to-noise ratios [10]. Moreover, they offer cost-effectiveness, portability, and versatility, making

them suitable for a wide range of applications, including healthcare, environmental monitoring, and food safety [11].

In the context of neurological diseases, the detection of miRNA targets holds significant clinical relevance and has the potential to improve disease treatment outcomes [12]. However, the low concentrations of miRNA-206 in biological samples, particularly in circulating blood (i.e., nM to μM range in patients with AD and in aM-pM for controls) pose a considerable challenge for accurate detection [13]. The proposed electrochemical biosensor utilizing AuNRDs aims to overcome this challenge by amplifying the signal associated with miRNA target hybridization, enabling the detection of extremely low concentrations of miRNA-206 and facilitating early diagnosis and effective disease management.

Specifically, this chapter reports an in-depth exploration of an miRNA sandwich assay utilizing a conventional gold electrode and AuNRDs as electrocatalytic labels. Building upon previous research (Chapter 2), the transducer platform was optimised by employing a mixed self-assembled monolayer with a 1:4 mole ratio of capture-probe to mercaptohexanol (MCH). Utilizing AuNRDs as electrocatalytic labels enhances the signal for target hybridization, enabling the successful fabrication of an amperometric biosensor that detects miRNA targets through hydrogen peroxide reduction by the nanorods. Through various optimizations, including the conjugation methodology between the miRNA reporter-probe and AuNRDs, control of the miRNA deposition process (i.e., $[\text{miRNA}_{\text{reporter-probe}}]_I$ / [AuNRDs]), determination of the optimum potential for hydrogen peroxide reduction, and identification of the optimal hydrogen peroxide concentration for miRNA detection, the sensitivity and accuracy of miRNA target detection were significantly enhanced.

Overall, this chapter presents a novel approach in the development of biosensors for the detection of miRNA targets in neurological diseases. By harnessing the electrocatalytic properties of gold nanorods (AuNRDs) as labels, the aim is to improve the sensitivity of miRNA detection in electrochemical biosensors. The potential advantages of this approach, including enhanced sensitivity, cost-effectiveness, portability, and versatility, hold great promise for the advancement of highly sensitive biosensing platforms in neurological disease diagnosis and monitoring. This significant progress brings us closer to the realization of point-of-care biosensing devices that can deliver rapid and reliable results, enabling timely diagnosis and effective disease management.

3.1 Experimental Procedures

3.1.1 Materials and Chemicals

Conventional gold disc working electrodes (Φ = 2mm) were purchased from IJ Cambria, Wales, UK. Alpha alumina with a particle size of 0.3 μm and 0.05 μm was used to polish the working electrode and was obtained from Buehler, USA.

Phosphate buffer (PBS, pH 7.4), sulfuric acid (H_2SO_4, 95-98%), tris[2-carboxyethyl]phosphine (TCEP), 6-mercapto-1-hexanol (MCH), hydrogen peroxide solution (H_2O_2, 3%) were purchased from Sigma Aldrich and used as received.

Gold Nanorods (50 nm x 15 nm) were obtained by NanoComposix. They are citrate stabilised and suspended in water. Zeta potential is -52 mV. Particle concentration: 4.30 x 10^{11} particles/mL.

All the aqueous solutions described in this work, if it was not stated otherwise, were prepared using Milli-Q water (Millipore Core, 18 MΩ cm).

The oligonucleotides (purity ≥98%), RNase free water and TE buffer (10 mM Tris and 1mM EDTA) used to prepare immobilization and hybridization solutions were purchased from IDT. The base sequences used were:

Capture-probe (miRNA-206): 5'-/5 $HSMC_6$-D/ C-CAC- ACA-CUU- 3'

Target (Fully complementary): 3'- G-GUG-UGU-GAA-GGA-AUG-UAA-GGU- 5'

Target (4 base mismatch, miRNA-1): 3'-UAU GUA UGA AGA AAU GUA AGG U-5'

Target (1 base mismatch): 3'-UGU GUG UGA AGA AAU GUA AGG U-5'

Reporter-probe: 5'-CCU-UAC-AUU-CCA/3ThioMC3-D/- 3'

3.1.2 Instrumentation

3.1.2.1 Electrochemical instrumentation

Electrochemical measurements were carried out using a CHI760D electrochemistry workstation at room temperature (22±2 ℃). For the measurements using a conventional gold disc working electrode (diameter, Φ = 2 mm), a three-electrode cell was used. The silver/silver chloride electrode (Ag/AgCl in 3 M KCl) and a platinum wire acted as a reference and counter electrodes, respectively.

3.1.2.2 Spectroscopic Instrumentation: UV-vis

Using a Varian Cary 50 UV-Vis spectrometer with a pathlength of 1 cm and a spectral range spanning from 200-1000 nm, the samples containing miRNA reporter-probe functionalized with AuNRDs at different molar ratios (i.e., 640:1, 960:1, 1280:1, and 6400:1 [miRNA $_{\text{reporter-probe}}]_i$ / [AuNRDs] were recorded.

For each measurement, a quartz microcuvette was prepared by adding 1000 μL of miRNA reporter-probe functionalized with AuNRDs and 3000 μL of deionized water. The absorbance at 520 nm and 670 nm was then measured.

To ensure accurate measurements, the background was corrected for blank solvent absorbance prior to each measurement. All measurements were performed at room temperature.

3.1.3 Experimental Procedures

3.1.3.1 Labelling of miRNA reporter-probe with AuNRDs

Prior to functionalizing the AuNRDs with miRNA reporter-probes, 15 mL of the specific nanomaterial was concentrated 10 times, by centrifugation at 6000 rpm for 10 minutes. The supernatant (approximately 14.85 mL) was removed from the solution leaving the nanoparticles as a precipitate in the Eppendorf.

Subsequently, 150 μL of 6.8 μM of miRNA reporter-probe was added to 150 μL of (7.14 nmol/L) of gold nanorods to form a ratio of [miRNA $_{\text{reporter-probe}}]_I$ / [AuNRDs] =960:1. After 1h

of incubation, the gold nanorods functionalized miRNA reporter-probe required a salt aging step to improve the adsorption capability of the conjugate [miRNA $_{\text{reporter-probe}}$]/ AuNRDs. To implement this procedure, 1 M NaCl was added dropwise to the solution to reach a final concentration of 50 mM. The solution was allowed to stabilize for 1h. The process was repeated until the salt concentration achieved 300 mM, over a 6-hr period. A vortex was used to ensure thorough mixing.

The hybridisation of the functionalized miRNA reporter-probe to the fully complementary assay at gold electrodes surfaces is described in the following section.

It is worth mentioning that AuNRDs functionalized with the miRNA reporter-probe remained stable for up to one week when stored in a refrigerator at 4°C. . They should be brought to room temperature only when they are being used.

3.1.3.2 Development of miRNA assay at conventional gold electrodes

Prior to surface modifications, the gold disc electrode was mechanically polished and electrochemically cleaned as outlined in Section 2.1.3.1.

Subsequently, the process commenced by depositing a mixed monolayer consisting of miRNA capture-probe /MCH onto a conventional gold electrode. This was achieved by immersing the electrode in a solution containing a 10 μM solution of the 5'-thiolated oligo dissolved in TE buffer (10 mM Tris and 1 mM EDTA), along with 40 µM of 6-mercapto-1-hexanol. The sealed Eppendorf containing the electrode in solution was then placed in an oven at 37°C for eighty minutes to allow the thiolated capture-probe strands to bind to the gold surface.

Further, the modified gold electrode was incubated with varying concentrations of the miRNA target ranging from 1 aM to 1 μM. This step involved hybridizing the 3' end of the target to the capture-probe strand. The optimal hybridization time for the miRNA target was determined to be 20 minutes at 37°C.

In a final step, the overhang of the miRNA target at the 5' end was hybridized with a fully complementary miRNA reporter-probe that was functionalized with gold nanorods. This hybridization process occurred over a period of 5 hours at 37°C.

The miRNA capture-probe and reporter-probe, dissolved in TE buffer, were treated with TCEP (tris[2-carboxyethyl]phosphine) in a 100x excess for 2 hours. This step facilitated the reduction and release of any thiol bonds present in the oligos' structure. Additionally, prior to the subsequent drying process, following the immobilization, hybridization, and functionalization steps, all the electrodes underwent rinsing with nuclease-free water to remove any loosely bound strands.

3.1.3.3 Limit of Blank and Limit of detection

After the development calibration curves based on the chronoamperometric reduction of hydrogen peroxide by the functionalized fully complementary sandwich assay on the gold electrode (1 μM to 1 aM miRNA-206), the limit of blank and limit of detection was determined.

The Limit of Blank (LOB) can be described as the maximum expected concentration of an analyte that can be detected when multiple replicates of a sample without the analyte are tested [15].

This term is defined using the following formula:

$$LOB = Blank_{mean} + 1.645(\sigma_{blank}) \qquad \text{Equation 3.1}$$

Where, $Blank_{mean}$ refers to the average measurement result of replicated tests on the blank sample, and σblank refers to the standard deviation of the blank sample.

The Limit of Detection (LOD) is the lowest concentration of the analyte that can be reliably distinguished from the LOB, indicating the point at which detection is possible. LOD is determined by using the calculated LOB and the results obtained from testing replicates of samples with a known low concentration of the analyte [15].

The LOD can be calculated using the following equation:

$$LOD = LOB + 1.645(\sigma_{\text{lowest sample concentration}}) \qquad \text{Equation 3.2}$$

Where, σ lowest sample concentration represents the standard deviation of the lowest sample concentration.

3.1.4 Electrochemical Analysis

3.1.4.1 Amperometric detection of miRNA-206

Following assembly of the capture probe—target—nanoparticle labelled reporter-probe miRNA sequence, the gold modified electrode was placed in a three-electrode cell filled with 7.2 mL of 0.1M of PBS solution. The initial current was measured at -0.25V after stabilization of the signal for 5 minutes. Then, under stirring, 3.27 μL of hydrogen peroxide (3% w/v) was introduced into the PBS solution to achieve a final concentration of 400 μM. The current associated with hydrogen peroxide reduction by the nanorods was measured under quiescent conditions after 20 minutes where the complete stabilization of the current signal is achieved. The analytical response was calculated by the difference in current signal before and after (Δi) hydrogen peroxide addition.

3.2 Results and Discussion

3.2.1 Optimal mole ratio of oligo molecules to gold nanorods

The successful and ultrasensitive detection of miRNA targets in the developed biosensor relies on the creation of high-quality miRNA reporter-probe /AuNRDs conjugates. For that, achieving stabilization of the conjugates and optimizing the loading of miRNA reporter-probes onto the nanorod surface are crucial factors. Increased adsorption of the miRNA reporter-probe onto the gold nanorods could enhance the miRNA target signal by enhancing the association constant. However, due to the negative charges carried by both miRNA and AuNRDs, electrostatic repulsion hinders their binding, making it less favourable to occur. Additionally, AuNRDs have a high Hamaker constant, making them prone to aggregation [16].

Typically, citrate capping of AuNRDs promotes their stabilization in solution. However, as the commercially available citrate-capped AuNRDs are usually present in low salt buffer (e.g., with ∼10 mM or lower Na^+ concentration) [17], when in presence of miRNAs, it result in a long Debye screening length and a strong miRNA repulsion. Herein, to overcome this repulsion and maintain the colloidal stability of AuNRDs, a modified salt-aging procedure, based on a well-established method [18-20], was employed.

The salt aging procedure involves the gradual addition of salt over time to optimize the loading of miRNA adsorption on the surface of AuNRDs. This procedure encompasses three main events that contribute to its effectiveness. Firstly, it reduces the repulsion between the oligonucleotides and gold nanorods. Secondly, it decreases the repulsion between oligo strands on the particle. Lastly, it reduces the repulsion between nanoparticles, which can promote AuNRDs aggregation.

Specifically, when salt is slowly added to the pellet of miRNA-functionalized AuNRDs, several beneficial effects occur. Neighbouring miRNA strands are screened, and the Debye length is shortened, allowing the AuNRDs to approach each other more closely and facilitating faster adsorption kinetics. Additionally, the conformation of the oligonucleotide supposed to change from a parallel orientation to an upright arrangement [9] [19] [21], providing more effective steric stabilization and enabling a higher oligonucleotide loading. The presence of miRNA attached to the surface of AuNRDs serves as a protective layer, preventing coalescence and the formation of gold aggregates. However, for this protective effect to occur, the density of miRNA on the AuNRDs surface needs to be sufficiently high before the addition of salt.

During a typical salt aging step, where the reaction time is standardized to 7 hour at 25°C, statistical analysis reveals that only around 5% of the oligonucleotides introduced to a 50 nm metallic nanoparticles solution is successfully attached [20]. Hence, it is expected that over 90% of the oligo introduced in this experimental process is ultimately discarded when working with large AuNRDs.

Functionalizing larger AuNRDs (≥40 nm) with oligonucleotides poses greater challenges compared to smaller nanorods. The difficulty in functionalizing larger AuNRDs can be attributed to the fact that the van der Waals force increased linearly with the size of the AuNRDs, as explained in [16]. In the initial stages of functionalization, the primary attractive force acting between the AuNRDs and oligonucleotides is the long-range van der Waals force. Van der Waals forces are weak forces that arise from fluctuations in electron density. They operate over larger distances and are responsible for bringing the particles and oligo closer together. However, achieving an optimal density of oligo molecules on the nanorods is crucial for promoting an upright conformation of miRNA molecules. This becomes particularly problematic due to the lower concentrations at which nanorods are commercially produced (e.g., 50 nm nanorods are produced at approximately 0.714 nM by Nanocomposix and 0.75

nM by BBI) in comparison with the higher concentrations of oligonucleotides typically used (~1-6 μM). The lower concentration of the nanorods can limit the number of available binding sites for functionalization. Consequently, if the desired density of oligo molecules cannot be achieved, even small additions of NaCl may cause an undesirable approach of AuNRDs at a very short distance. As a result, the van der Waals force becomes dominant and leads to aggregation. This scenario is not ideal for miRNA functionalization. Hence, the overall goal is to achieve an effective balance between the concentrations of AuNRDs and miRNA to ensure successful functionalization.

As the adsorption of miRNA reporter-probe on AuNRDs is limited by the initial concentration of miRNA (referred as $[miRNA_{reporter\text{-}probe}]_I$) covalent bonded to the nanorods at first step of salt aging process [18] which, in turn, can supress or induce aggregation of AuNRDs. Two steps were implemented to produce high quality conjugates. Firstly, gold nanorods were concentrated, ensuring a relatively high adsorption of miRNA on the nanometallic surface at a lower miRNA concentration. Secondly, $[miRNA_{reporter\text{-}probe}]_I$ was carefully controlled in relation to the concentration of AuNRDs. This protocol was based on the procedure developed by Zhang *et al.* [21].

Initially, the concentration of AuNRDs was increased by a factor of 10 (from 0.714 nM to 7.14 nM) and, during the extension of the experiment, sonication was employed. It is worth noting that, in contrast to the approach followed by Zhang and colleagues [21], the attachment of miRNA to AuNRDs was achieved without an acidic pH adjustment step. To evaluate the effect of varying initial miRNA reporter-probe concentrations on the sensor's response and the stability of the conjugate, amperometric analysis and UV-vis spectra were utilized.

The concentration of gold nanorods remained constant at 7.14 nM, while adjustments were made to the initial miRNA reporter-probe concentration introduced in the nanorods solution, denoted as $[miRNA_{reporter\text{-}probe}]_I$ / [AuNRDs]. According to literature [22], each 50 nm diameter gold nanorod has a theoretical full capacity to adsorb ~640 thiolated DNA ($8.1x10^{12}$ DNA/cm^2) after undergoing high concentration salt aging. Based on the research conducted by Zhang *et al.* [21], which examined the theoretical capacity at different mole ratios of DNA to AuNRDs, the optimal ratios tested were as follows: 640:1 (fully theoretical capacity), 960:1 (~1.5x

theoretical capacity), 1280:1 (~ 2x theoretical capacity), and 6400:1 (~ 10x theoretical capacity). The deposition time for these experiments was standardized to 7 hours.

Figure 3.1 displays representative curves illustrating the impact of the initial concentration of miRNA reporter-probe ($[miRNA_{reporter\text{-}probe}]_i$) on the amperometric current response of a functionalized fully complementary miRNA sandwich assay. Additionally, Table 3.1 provides a summary of the initial miRNA reporter-probe concentrations used for quantitative adsorption onto AuNRDs, taking into account the nanorod concentration and loading capacity.

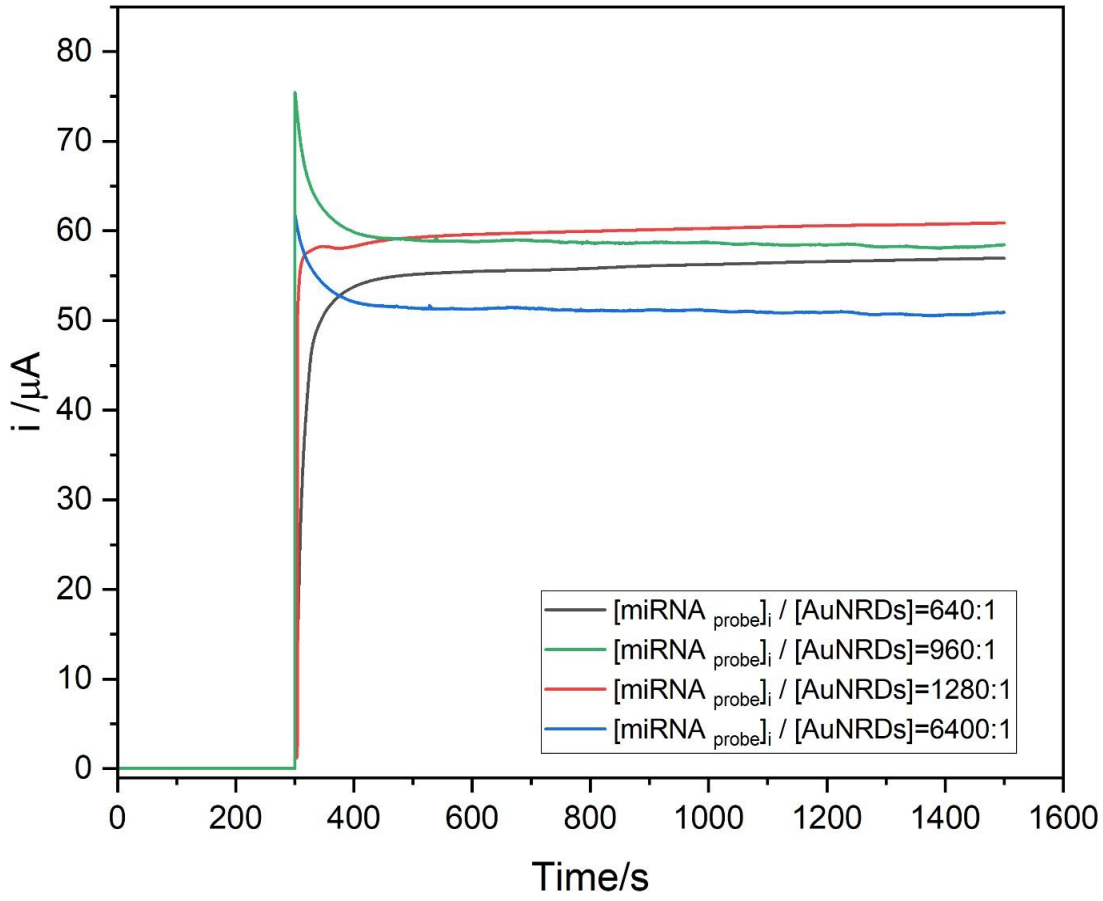


Figure 3.1. Amperometric i-t curves for gold electrode functionalized with 10 μM miRNA capture-probe, 1μM of miRNA target strands and different ratios of the conjugate $[miRNA_{reporter\text{-}probe}]_I$/[AuNRDs], such as 640:1 (black line), 960:1 (pink line), 1280:1 (red line) and 6400: 1 (blue line). Potential applied is -0.25 V in 0.1M PBS. The difference in current before and after the addition of 400 μM of hydrogen peroxide is displayed.

Table 3.1. Overview of the initial miRNA reporter-probe concentration used for quantitative adsorption onto AuNRDS based on its loading capacity. The effects of the different [$miRNA_{reporter\text{-}probe}$] $_I$ / [AuNRDs] ratios in the amperometric signal response are also displayed at this table.

[$miRNA_{reporter\text{-}probe}$]$_I$ /[AuNRDs]	[$miRNA_{reporter\text{-}probe}$] $_I$ /M	[AuNRDs]/M	Theorical capacity	$\Delta i / \mu$ A
640:1	4.60 x10^{-6}	7.14x10^{-9}	Full capacity	55.00±1.06
960:1	6.80 x10^{-6}	7.14x10^{-9}	1.5x	56.84±1.77
1280:1	9.20 x10^{-6}	7.14x10^{-9}	2.0x	59.27±1.55
6400:1	46.00 x10^{-6}	7.14x10^{-9}	10x	49.28 ±1.81

At an [$miRNA_{reporter\text{-}probe}$] $_i$ / AuNRDs ratio of 1280:1, a small but statistically significant enhancement of the current response is observed. Specifically, the [$miRNA_{reporter\text{-}probe}$]$_I$ /AuNRDs from 640:1 to 1280:1 leads to a 7.8% increase in the amperometric signal response observed. However, an additional increase of 6400:1 in the [$miRNA_{reporter\text{-}probe}$]$_I$ /AuNRDs ratios leads to a response that is 16.9% lower than the maximum value observed. Given that the deposition time is fixed and the miRNA density on the AuNRDs is expected to be higher for the higher mole ratio, this result suggests that there is an optimum miRNA density that maximises binding while allowing sufficient access to the gold surface by the hydrogen peroxide.

The stability of the conjugates was assessed by observing the colour change of the samples from red to grey following the salt aging process. It was observed that stable conjugates were formed when the immobilization of [$miRNA_{reporter\text{-}probe}$] $_I$ to AuNRDs reached its full capacity (640:1) and at 1.5 times its theoretical value (960:1). However, when the conjugates were formed with a 2-fold excess of the theoretical capacity ([$miRNA_{reporter\text{-}probe}$] $_I$/ AuNRDs = 1280:1), flocculation occurred, indicating reversible aggregation. This issue was resolved by using sonication to redisperse the particles. On the other hand, when the total moles of [$miRNA_{reporter\text{-}probe}$]$_I$ was increased to 10 times its theoretical fully capacity (6400:1), the formation of aggregates was observed.

Additional assessment of the AuNRDs stability was made through the evaluation of the UV-vis spectra at different ratios of the conjugate [$miRNA_{reporter\text{-}probe}$] $_I$/[AuNRDs] (Figure 3.2). It

is important to note that bare gold nanorods typically exhibit two distinct plasmon modes in their UV-vis spectra. The first mode is known as the single particle plasmon peak, which is observed at 520 nm. This peak corresponds to the collective oscillation of electrons perpendicular to the long axis of the nanorods, known as the transverse plasmon mode. The second mode is the plasmon-plasmon interaction peak, observed at 670 nm, arising from the collective oscillation of electrons along the long axis of the nanorods, referred to as the longitudinal plasmon mode [9]. When the miRNA reporter-probe is conjugated to AuNRDs, a decrease in the plasmon resonance intensity at 670 nm is observed, as expected. This decrease can be attributed to changes in the local refractive index and interparticle distance [16]. However, as the ratios were enhanced up to 6400:1 [miRNA $_{\text{reporter-probe}}]_{\text{I}}$ /[AuNRDs] an interesting phenomenon occurs. An increase in absorbance and a red-shift of both the plasmon-plasmon peak at 670 nm and the single particle peak at 520 nm were observed in the UV-vis spectra. This red-shift indicates a shift of the plasmon resonance towards longer wavelengths, which suggests an increased interparticle coupling [23].

Although, the relationship between the UV-Vis spectrum and the state of aggregation is complex and depends on various factors such as, size distribution of the nanoparticles, and type of aggregate structure [23], this data (red-shift) in conjunction to qualitative analysis (change in colour) of the samples containing the different ratios of [miRNA$_{\text{reporter-probe}}]_{\text{I}}$ /[AuNRDs] suggest the formation of aggregates only at the ratio 6400:1.

To verify the aggregation of nanoparticles in solution, several methods can be employed, depending on the level of detail required. DLS and zeta potential measurements are often the first-line techniques for assessing nanoparticle aggregation due to their ease of use and sensitivity to changes in particle size and surface charge. TEM, SEM, and AUC provide more detailed structural information but may require more time and specialized equipment. Ultimately, a combination of methods is often the most robust approach for verifying nanoparticle aggregation, allowing for cross-validation of results.

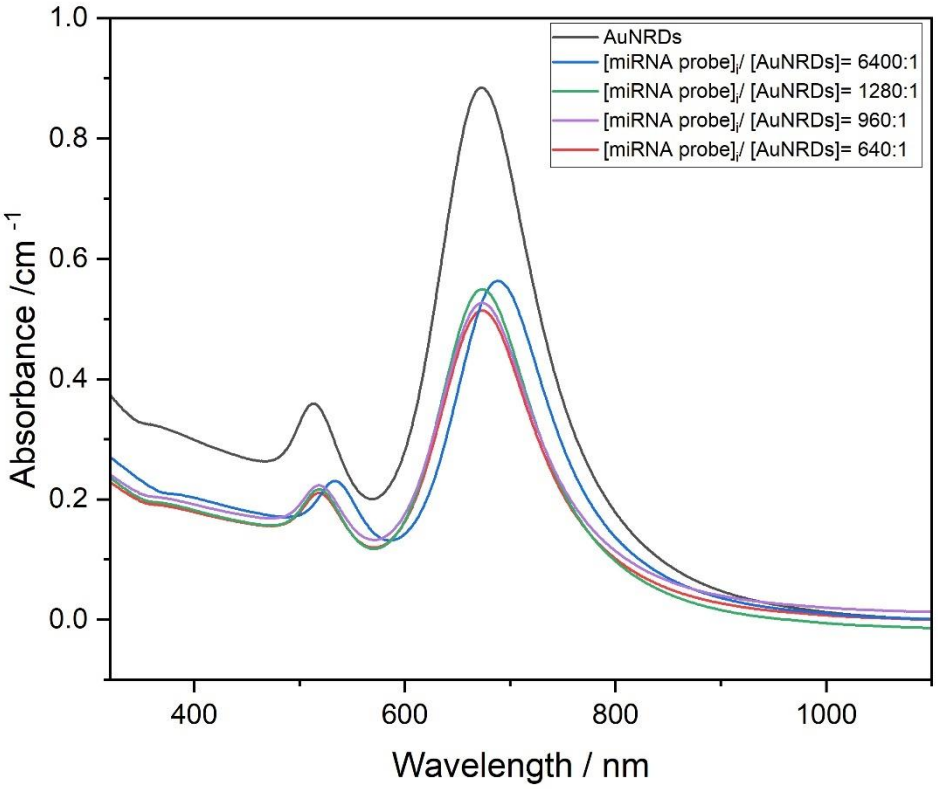


Figure 3.2. UV-vis absorption spectrum of 50 nm AuNRDs modified at different [$miRNA_{reporter\text{-}probe}$]$_I$ /[AuNRDs] ratios.

In conclusion, the successful detection of miRNA targets in the developed biosensor relies on the creation of high-quality miRNA reporter-probe/AuNRDs conjugates. The salt aging procedure, coupled with careful control of the initial miRNA probe concentration, plays a crucial role in achieving stabilization of the conjugate, optimum loading of oligonucleotides, and preventing aggregation of AuNRDs. The experimental results demonstrate that ratios of 960:1 (~1.5x theoretical capacity of oligo at each AuNRDs) or 1280:1 ([$miRNA_{reporter\text{-}probe}$]$_I$/[AuNRDs], ~2x theoretical capacity) effectively prevent AuNRDs aggregation and lead to high amperometric current responses in the biosensor. These results are consistent with the literature [16][24][25], where a high initial concentration of miRNA is necessary to achieve optimal adsorption to prevent nanorods aggregation.

Increasing the initial miRNA concentration beyond 1.5 to 2 times the theoretical capacity of AuNRDs has a negligible impact on the overall miRNA adsorbed onto the nanorod surface, as indicated by the minimal difference in Δi values between the surfaces. However, it significantly affects the stability of AuNRDs. Therefore, the optimal ratio of [$miRNA_{reporter\text{-}probe}$]$_I$

/[AuNRDs] for successful conjugation and enhanced stability is determined to be 960:1. Stable conjugates were observed at this ratio, and the use of sonication effectively resolved reversible aggregation at higher concentrations. UV-vis spectra analysis indicate the formation of aggregates at a ratio of 6400:1. These findings provide valuable insights for the development of ultrasensitive biosensors and highlight the importance of carefully controlling the miRNA reporter-probe density on AuNRDs for optimal performance, e.g., association constant and kinetics as well as reduction of peroxide, and stability of the conjugates.

3.2.2 Optimum hybridisation time between miRNA reporter-probe and target

After appropriately engineering the transducer platform and optimising the binding of AuNRDs onto the reporter-probe, it was necessary to optimise the last step of the assay, i.e., the binding between the miRNA reporter-probe and target. A saturation of the miRNA target overhang with reporter-probe was imperative to generate the maximum current response and to ensure reproducible results.

The assay was prepared as described in Section 3.1.3. However, the hybridisation of the miRNA reporter-probe to the target was performed at two distinct target concentrations, 1 nM and 1 pM. The time frame studied was 30 min, 1 h, 2 h, 5 h and 17 h. Figure 3.3 presents the current response of (A) 1 nM and (B) 1 pM of miRNA target at the varying hybridisation times. Table 3.2 presents the average variation in current signal (Δi) as a function of hybridisation time, considering three independent electrodes (n=3).

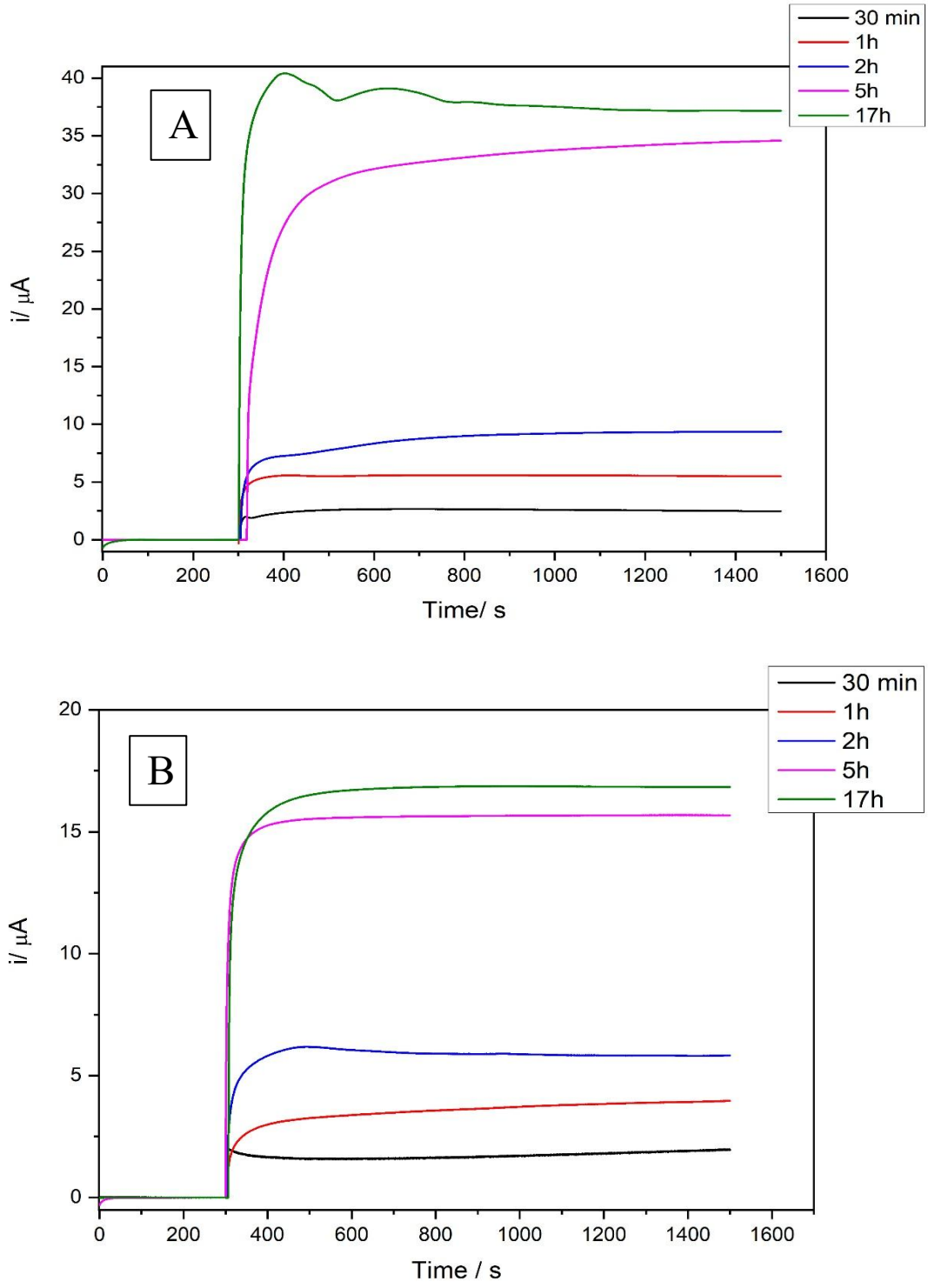


Figure 3.3. Amperometric i-t curves for gold electrodes functionalized with 10 µM miRNA capture-probe strands, (A) 1 nM and (B) 1 pM of miRNA target strands and 6.8 µM miRNA reporter-probe strands labelled with gold nanorods. The hybridization between the target and reporter-probe strands was allowed to occur for various durations, ranging from 30 minutes to 17 hours. Potential applied is -0.25 V in 0.1 M PBS. The difference in current before and after the addition of 400 μM of hydrogen peroxide is displayed.

Table 3.2. Variation in current signal (Δi) in a functionalized fully complementary sandwich assay as a over hybridisation time, considering three independent electrodes. The concentration of miRNA targets studied was nM and pM. Average values and standard deviation were calculated based on triplicate measurements (n=3).

Time/ min	Average Δi /μ A [$miRNA_{target}$] = 10^{-9}M	Average Δi /μ A [$miRNA_{target}$] = 10^{-12} M
30 (0.5 h)	2.45 ± 0.11	1.95 ± 0.10
60 (1 h)	5.43 ± 0.12	3.98 ± 0.17
120 (2 h)	9.19 ± 0.18	5.91 ± 0.19
300 (5 h)	36.04 ± 1.29	15.40 ± 1.05
1020 (17 h)	38.60 ± 1.64	16.70 ± 1.02

Analysing Figure 3.3, it can be seen that increasing hybridisation time of miRNA target — reporter-probe from 30 min to 5 h leads to a drastic increase in the current response of the biosensor. However, after 5 h, the increase in hybridisation time only generates a slight change in signal (Δi). Specifically, in 17 h the maximum current achieved was 38.60 ±1.64 μA vs. 36.04 ±1.29 μA produced at 5 h. An enhancement of only 7% in current signal for an additional 12 h of analysis. The stabilization of the current indicates that when the hybridization time exceeds 5 h, all potential binding sites for the miRNA target have been occupied by miRNA reporter-probe strands.

Similarly, to the pattern observed in the aforementioned results, when 1 pM of miRNA target is bonded to reporter-probe at varying hybridisation times, the current dramatically increases with time until 5h of analysis is achieved. At 17 h of analysis the maximum current produced is 16.70 ±1.02 μA while 5 h of measurements leads to 15.40 ±1.05 μA. An 8% increase in current signal occurs with an additional 12 hours of hybridisation. This relatively constant current produced implies that 5 h is the optimal hybridization time required for miRNA target— reporter-probe hybridization.

3.2.3 Influence of the hydrogen peroxide concentration on the electrocatalysis of miRNA assay

One of the major features of the amperometric current response of the functionalized miRNA assay towards hydrogen peroxide is the possibility of radial diffusion of the peroxide to the gold nanorods. During the electrocatalysis of hydrogen peroxide at nanorod surface, a layer of diminished peroxide concentration is formed around the nanorod surface. When there is a depletion of the hydrogen peroxide in this region a steady state current can be achieved due to radial diffusion. Even in a system saturated with AuNRDs the peroxide concentration will significantly affect the maximum reduction achieved by the system. Therefore, this slow amperometric process is diffusion controlled ($\sim D = 10^{-5}$ cm^2/s [26]) and concentration dependent on hydrogen peroxide.

The miRNA layer may be sufficiently porous to allow the hydrogen peroxide to access the gold electrode surface which would give rise to an unwanted background current. Therefore, the effect of concentration of hydrogen peroxide on the background current must be analysed. Figure 3.4 depicts the amperometric i-t curve of a fully complementary miRNA sandwich assay at 9 sequential additions of hydrogen peroxide at concentration of 200 μM, 400 μM, 500 μM, 600 μM, 700 μM, 800 μM, 1 mM, 2 mM and 10 mM. The electrolyte used was 0.1M PBS.

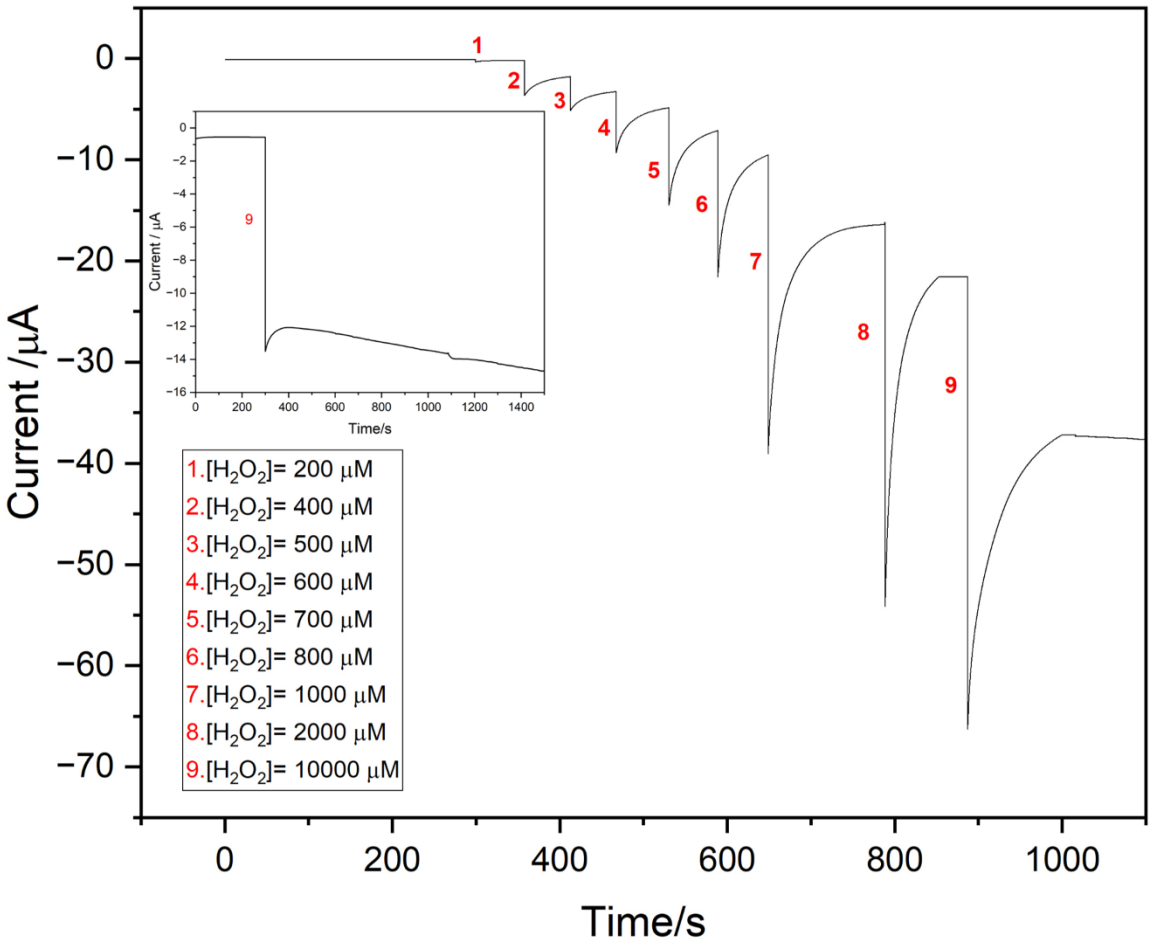


Figure 3.4. Representative chronoamperometric curves of a non-functionalized fully complementary miRNA sandwich assay ([miRNAtarget = 1nM) at sequential additions of hydrogen peroxide to form a final concentration ranging from 200 μM to 10000 μM. The electrolyte used was 0.1 M PBS. Inset depicts the chronoamperometric behaviour of the same assay at longer reaction times and at hydrogen peroxide concentration of 10 mM. Measurements were conducted in triplicate.

A flat baseline, completely independent of the hydrogen peroxide concentration is the ideal response. However, as the hydrogen peroxide concentration increases up to 10 mM, the background current becomes significantly larger. As the purpose of the biosensor is to analyze ultralow concentrations of miRNAs in circular blood, present in fM or lower, the background of the assay needs to be as low as possible, while still can differentiate between initial and final current (Δi). Through this analysis, it is expected that an optimum concentration of hydrogen peroxide to be used is between 400 μM to 800 μM.

Table 3.3. Change in the current before and after the addition of different concentrations of hydrogen peroxide in a non-functionalized miRNA sandwich assay. The average values and standard deviation are calculated based on n=3.

	[Hydrogen peroxide]/ μM	Average /i_{final} / /μ A	Average /$i_{initial}$/ /μ A	/$\Delta i_{background}$ / /μ A
1	200	0.20 ± 0.11	0.11 ± 0.01	0.09± 0.10
2	400	1.81 ± 0.22	0.20 ± 0.11	1.61± 0.11
3	500	3.39 ± 0.88	1.81 ± 0.22	1.58± 0.66
4	600	4.88 ± 1.01	3.39 ± 0.88	1.59± 0.12
5	700	7.00 ± 0.86	4.88 ± 1.01	2.12± 0.14
6	800	9.59± 0.76	7.00± 0.86	2.59± 0.10
7	1000	16.41± 1.56	9.59± 0.76	6.82± 0.80
8	2000	22.57± 2.13	16.41± 1.56	6.16± 0.56
9	10000	----	22.57± 1.12	---

In an additional assessment, the electrochemical response of a functionalized fully complementary miRNA assay was evaluated. Figure 3.5 illustrates amperometric i-t curves of AuNRDS functionalized miRNA assay at hydrogen peroxide concentration of 400 μM, 600 µM, 800 µM, 1 mM and 2 mM. The electrolyte used was 0.1M PBS.

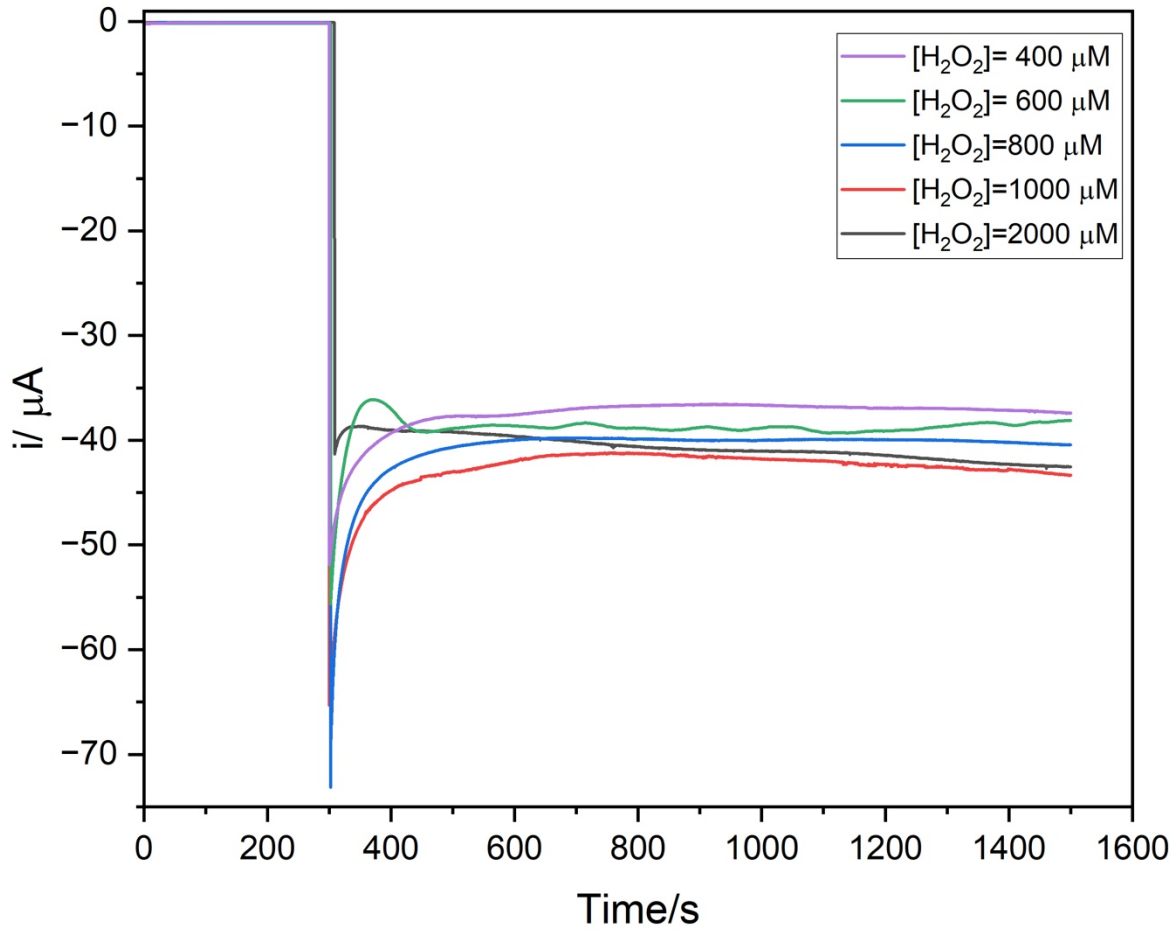


Figure 3.5. Chronoamperometric curves of a functionalized fully complementary miRNA sandwich assay ([miRNA target= 1nM) at different hydrogen peroxide concentrations, such as 400 µM (purple curve), 600 µM (green curve), 800 µM (blue curve), 1000 µM (red curve) and 2000 µM (black curve). Potential applied is -0.25V in 0.1 M PBS. Measurements were conducted in triplicate.

As illustrated in Figure 3.4, the background currents (Δi) produced when 400 μM, 600 μM and 800 μM of hydrogen peroxide is added to system with the non-functionalized assay, are almost identical. Following a similar pattern, Figure 3.5 shows that the effect of these hydrogen peroxide concentrations to the final current of a functionalized miRNA assay is minimal, with a maximum current enhancement of 5% observed for an additional 400 μM of hydrogen peroxide. However, when the concentration is raised from 1 mM to 2 mM, a decrease in overall current (Δi,) is observed (see Table 3.4). This phenomenon can be attributed to both, the elevated background current generated when the concentration of hydrogen peroxide is increased, and the limit imposed by the rate of peroxide reduction at the AuNRDs. As the nanoparticles contribution to the current become dominant in the 400 μM-800 μM range, and

the 3 concentrations leads to similar current results, 400 μM is defined as the optimum concentration of hydrogen peroxide to maximize the redout response.

Table 3.4. Summary of average current response of the system in accordance with different concentrations of hydrogen peroxide. The variation in current is given by Δi assay (variation in current of functionalized assay)- Δi background (variation in current of blank, non-functionalized assay).

[Hydrogen peroxide]/ μM	Average $/i_{\text{assay}}/\!/\mu$ A	Average $/\Delta i_{\text{background}}/\,/\mu$ A	$/\Delta i/\,/\mu$ A
400	37.40 ± 1.31	1.61± 0.11	35.80 ± 1.20
600	38.10 ± 1.18	1.59 ± 0.12	36.52 ± 1.06
800	40.43 ± 1.22	2.59± 0.10	37.84 ± 1.12
1000	43.33 ± 1.35	6.82± 0.80	36.50± 0.56
2000	42.52 ± 1.35	6.16 ± 0.56	36.36 ± 0.80

It is noteworthy that if the hydrogen peroxide concentration falls below 400 μM, the generated current response from the assay prevents the accurate determination of miRNA targets. Additionally, at 10 mM, the current response of the functionalized assay is not considered optimal since, unlike other concentrations that follow a response time pattern of 100s to reach 95% of maximum current, there was no current stabilization within 30 minutes of analysis. Since the fast stabilisation of the electrocatalytic reduction of hydrogen peroxide is vital for the ultimate objective of the project, point-of-care sensors, this concentration was not considered suitable for this analysis.

3.2.4 Amperometric response of the biosensor

To evaluate the analytical response of the optimised biosensor towards miRNA-206, the gold nanorods functionalized reporter-probe was hybridised to a full range of miRNA target concentration, from 1 µM to 1 aM. In this system, miRNA target is hybridised to a complementary sequence of miRNA capture-probe, which, in turn, is used to form a mixed self-assembled monolayer with MCH at the gold electrode surface. PBS is used as an electrolyte and measurements were performed at -0.25V. The current was allowed to stabilise

for 5 min, with subsequent addition of 400 μM of hydrogen peroxide. Amperometry is used as the detection technique and the response of the sensor is given through the difference in the current before and after (Δi) the addition of the hydrogen peroxide.

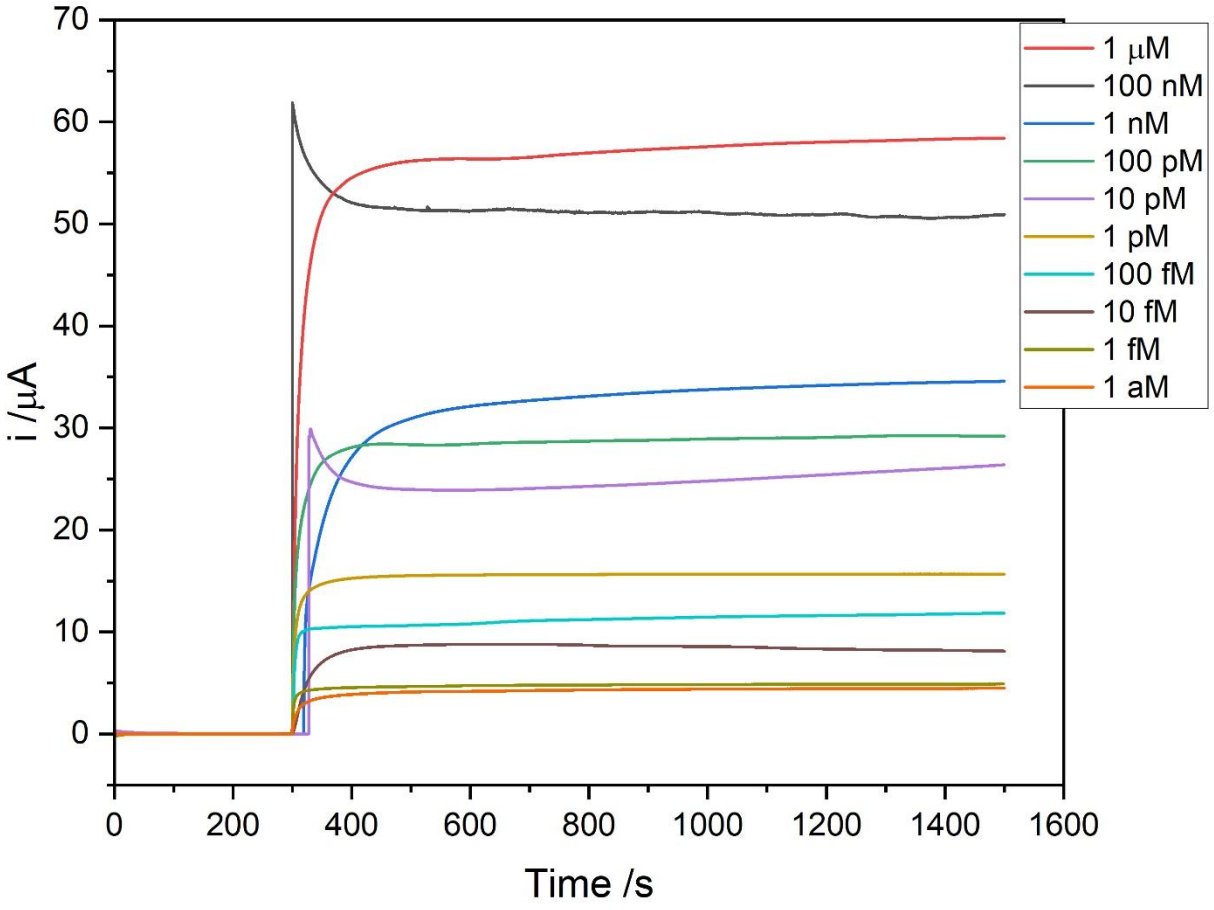


Figure 3.6.Amperometric i-t curves for gold electrodes functionalized with 10 µM miRNA capture-probe strands, varying concentrations of miRNA target stands (as shown in subtitle) and 6.8µM miRNA reporter-probe strands labelled with gold nanorods. Potential applied is -25V in 0.1M PBS. The difference in current before and after the addition of 400µM is displayed.

Figure 3.6 shows the variation of the signal as the concentration of target increases. The amperometric signal relies on the fully complementary hybridisation between the functionalized reporter-probe and miRNA target as it is due this 1: 1 bounding that gold nanorods are brought to the gold transducer surface. If a higher concentration of miRNA target is available for the binding, more probe conjugated to gold nanorods is available for the reduction of hydrogen peroxide and, therefore, a higher current will be generated. So, as

expected, the magnitude of the current presented to be influenced by the loading of the conjugate [miRNA $_{\text{reporter-probe}}]_I$ /[AuNRDs] which is directly proportional to the concentration of miRNA target.

The background current of the gold electrode is stable and close to zero (approximately 0.1098 μA) after 5 min of applied potential. After addition of 400 μM of hydrogen peroxide, there is a rapid response of the sensor achieving a high current loading with subsequent formation of a plateau. A steady state current was obtained within a time frame of 300 to 1500 seconds depending on the miRNA target concentration.

The shape of the transient state observed in the electrochemical system is a result of limited diffusion of hydrogen peroxide towards the gold nanoparticles, rather than being solely governed by the rate of heterogeneous electron transfer, e.g., as described by Butler-Volmer kinetics. Radial diffusion, with a diffusion coefficient of approximately 10^{-5} cm^2/s, leads to the transient reaching a plateau. Radial diffusion is desirable since the current would continue to decay over time if it was under semi-infinite linear diffusion control.

While Butler-Volmer kinetics describe the electron transfer rates in electrochemical processes, including the reduction of hydrogen peroxide [27], it is important to note that the transient behaviour in this system is primarily dictated by diffusion. The overpotential, i.e., the driving force, influences the reaction rate. In this case, a highly negative overpotential would increase the reaction rate; however, the rate-limiting step is the diffusion of hydrogen peroxide, not the electron transfer at the electrode surface. This diffusion-limited behaviour ensures that the rate is primarily controlled by the availability of hydrogen peroxide and allows for a distinct differentiation in current levels before and after the addition of peroxide.

At higher concentrations of target, longer times were needed for the current to plateau. This can be explained by the highest probability that a concentrate of miRNA target has to generate a cluster of nanoparticles over the surface. If nanoparticles are too close to one another, their diffusion zones will overlap [28]. This size polydispersity phenomenon causes the diffusion of hydrogen peroxide to the nanoparticle and its electrocatalysis to be less efficient.

Table 3.5 illustrates the current response before and after the injection of hydrogen peroxide on a varying concentration of miRNA target hybridized to a fully complementary nucleic acid

strand labelled with AuNRDs. Analysing this data, one can have a better understanding on the trade-off between the number of nanoparticles over the transducer surface and nanoparticle electrocatalytic activity. Despite the higher probability of experiencing agglomeration effects during detection, micromolar concentrations still result in a greater change in reduction current compared to attomolar concentrations. However, even though the current is directly proportional to the target concentration, its increase is not proportional to the rise in target concentration due to the impact of agglomeration effects and its impact on the nature of peroxide diffusion.

Table 3.5. Average variation of the current response before and after the injection of hydrogen peroxide (Δi) on a functionalized fully complementary miRNA assay.

Concentration of miRNA-206 (M)	Log [miRNA]	ΔI (μA) ± STDV Fully complementary Assay
$1x10^{-6}$	**-6**	57.01 ± 1.83
$1x10^{-7}$	**-7**	51.33 ± 1.30
$1x10^{-9}$	**-9**	36.04 ± 1.27
$1x10^{-10}$	**-10**	30.10 ± 1.29
$1x10^{-11}$	**-11**	24.50 ± 1.02
$1x10^{-12}$	**-12**	18.40 ± 0.91
$1x10^{-13}$	**-13**	14.10 ± 0.75
$1x10^{-14}$	**-14**	7.96 ± 0.81
$1x10^{-15}$	**-15**	3.82 ± 0.86
$1x10^{-18}$	**-18**	3.18 ± 0.61

Figure 3.7 depicts a calibration curve that was constructed based on the data generated by Table 3.5. The results indicate a logarithmic correlation between the concentration of miRNA target and the Δi presented by the system. As the magnitude of the current increases with log [miRNA] instead of [miRNA] there is a confirmation that the current response is indeed limited by both the diffusion of hydrogen peroxide and miRNA concentration.

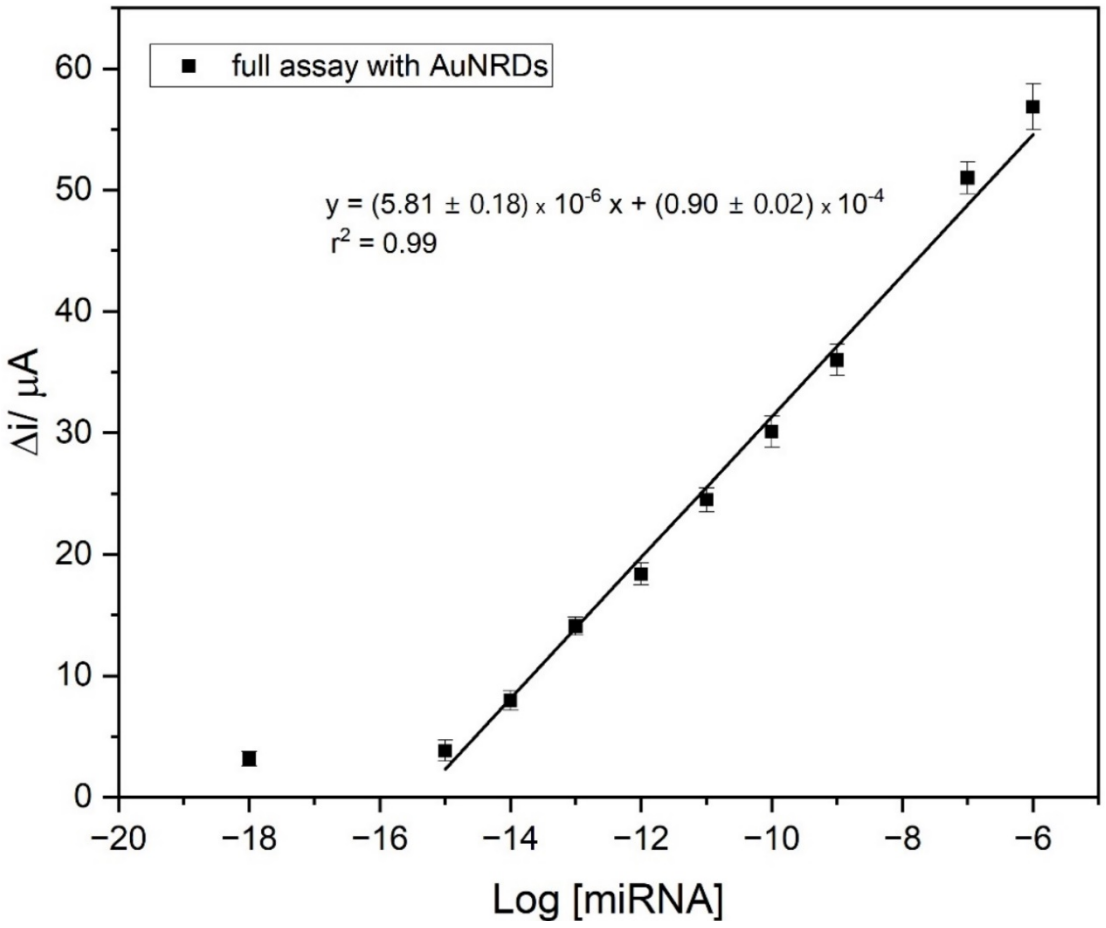


Figure 3.7. Chronoamperometric current response of a functionalized fully complementary sandwich assay as a function of target concentrations. The Y-axis is the difference in current before and after the addition of 400 μM hydrogen peroxide. The applied potential is -0.25V in 0.1M PBS. Measurements were conducted in triplicate, and therefore, error bars depicts the data spread (n=3). Where error bars are not visible, it means they are either very small or about the same size as the symbols used.

The best-fit least-squares regression line equation determined by the AuNRDs labelled electrode was $y = 5.81 \times 10^{-6} \log [miRNA] + 0.90 \times 10^{-4}$ A. The excellent reproducibility of the sensor was determined by the low standard deviation achieved at all concentrations (n=3). The assay presented a wide dynamic range covering 9 orders of magnitude. A linear correlation was observed within a concentration range from 10^{-6} to 10^{-15} M, with a correlation coefficient of 0.99.

The lowest concentration of the analyte that can be accurately distinguished from a blank sample, i.e., LOD was also measured. Despite the different methods used in the literature to

calculate LOD, was calculated from the limit of blank (LOB), as explained in the experimental section of this chapter. The biosensor developed at this study was found to have a limit of detection of 0.46 fM.

3.2.5 Comparison between label-free and labelled amperometric biosensor

A comparison between the catalytic current responses of a fully complementary miRNA assay labelled with AuNRDs, at varying concentrations of miRNA target, and of an assay with the same design but without signal amplification (i.e., without the use of gold nanorods as labels) is presented in the calibration curves at Figure 3.8. All the assays were developed at optimum conditions. Current signal was measured before and after (Δi) addition of 400 μM of hydrogen peroxide.

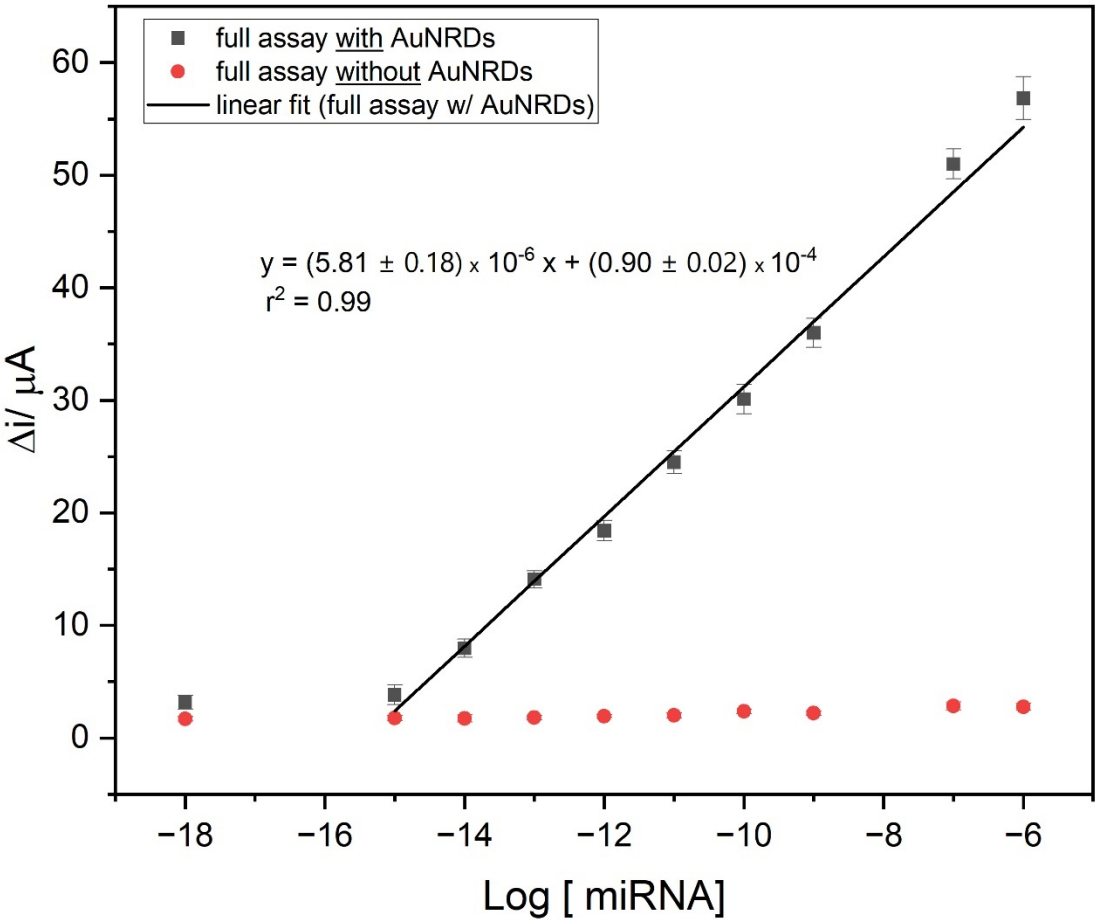


Figure 3.8. Comparison of the current response of miRNA-206 at different concentrations (aM- μM) in a full sandwich assay functionalized with AuNDRs (black line) and without AuNRDs (red line). The Y-axis is the difference in current before and after the addition of 400 μM of hydrogen peroxide. The applied potential is -0.25 V in 0.1M PBS. Measurements were conducted in triplicate, and therefore,

error bars depicts the data spread (n=3). Where error bars are not visible, it means they are either very small or about the same size as the symbols used.

The AuNRDs labelled assays presented a more sensitive and rapid response towards the reduction of hydrogen peroxide when compared with assays without the nanorods labels. A dynamic linear range of the AuNRDs modified assay is presented to be from 10^{-6} to 10^{-15} M with a correlation coefficient of 0.99.

Although the label-free assay presented an apparent stretch in linearity, in this environment, the change in current between different concentrations is not as significant. A variation of 1.70 $\pm$ 0.05 μA vs. 2.76 $\pm$ 0.13 μA is achieved at the lowest and highest concentration, respectively. Despite the low standard deviations, the closeness of the values generates a gain in linearity at resolution cost. A better understanding of this effect can be obtained by analysis of Table 3.6.

Table 3.6. Comparison of the current response before and after the injection of hydrogen peroxide (Δi) on a functionalized fully complementary assay and a label-free functionalized sandwich assay. Average values and standard deviations were calculated from triplicate measurements (n=3).

Concentration **of miRNA target (M)**	Log [miRNA]	Average Δi (μA) Fully Assay with AuNRDs	Average Δi (μA) Full Assay without AuNRDs	**Decrease in current (%)**
$1x10^{-6}$	-6	57.01 ± 1.83	2.76 ± 0.13	95.15
$1x10^{-7}$	-7	51.33 ± 1.30	2.83 ± 0.16	94.48
$1x10^{-9}$	-9	36.04 ± 1.27	2.20 ± 0.11	93.90
$1x10^{-10}$	-10	30.10 ± 1.29	2.35 ± 0.11	92.19
$1x10^{-11}$	-11	24.50 ± 1.02	2.06 ± 0.15	91.59
$1x10^{-12}$	-12	18.40 ± 0.91	1.93 ± 0.10	89.51
$1x10^{-13}$	-13	14.10 ± 0.75	1.81 ± 0.07	87.16
$1x10^{-14}$	-14	7.96 ± 0.81	1.73 ± 0.03	78.26
$1x10^{-15}$	-15	3.82 ± 0.86	1.77 ± 0.02	53.66
$1x10^{-18}$	-16	3.18 ± 0.61	1.70 ± 0.05	46.54

Table 3.6 compares the current before and after the injection of hydrogen peroxide on a fully complementary nucleic acid assay with and without AuNRDs. Throughout the label-free calibration curve, even at the lowest miRNA concentration, the response of the sensor (Δi) presented to be small yet significant. This may arise because of pores or defects in the mixed self-assembled monolayer, through which the hydrogen peroxide diffuses, and becomes reduced at the underlying gold electrode. However, when the reporter-probe strand are unlabelled, its binding to the target strand not only impacts the magnitude of the current but also is responsible for its small fluctuations at different concentrations. This is because the amount of target present on the electrode surface has no effect on the catalytic activity when the reporter-probe strand lacks labelling. Higher concentrations of target will only create additional barriers for hydrogen peroxide diffusion towards the gold transducer surface.

Overall, the current signal (Δi) obtained from a label-free assay was found to be 95.15% (μM) to 46.54% (aM) lower than that of an assay functionalized with AuNRDs. These results suggest that gold nanorods play a critical role in catalysing peroxide, being essential for both signal amplification and generation of accurate results.

3.2.6 Control Studies

The current associated with reduction of hydrogen peroxide was measured after each immobilisation and hybridisation step. This analysis was undertaken to quantify the impact of all stages on the background signal.

Figure 3.9 displays amperometric i-t curves for various stages of the hybridization process, including a bare gold electrode, following immobilization of the capture-probe and MCH, after hybridization of miRNA target, as well as a gold electrode functionalized with a full assay (10 μM capture-probe, 1 nM target, and 6.8 μM reporter-probe labelled with AuNRDs). The potential applied was -0.25 V in 0.1M PBS, and the graph shows the difference in current before and after the addition of 400 μM hydrogen peroxide. To assist comprehension, Table 3.7 summarizes the average change in current before and after the injection of hydrogen peroxide for the different steps of the hybridization process.

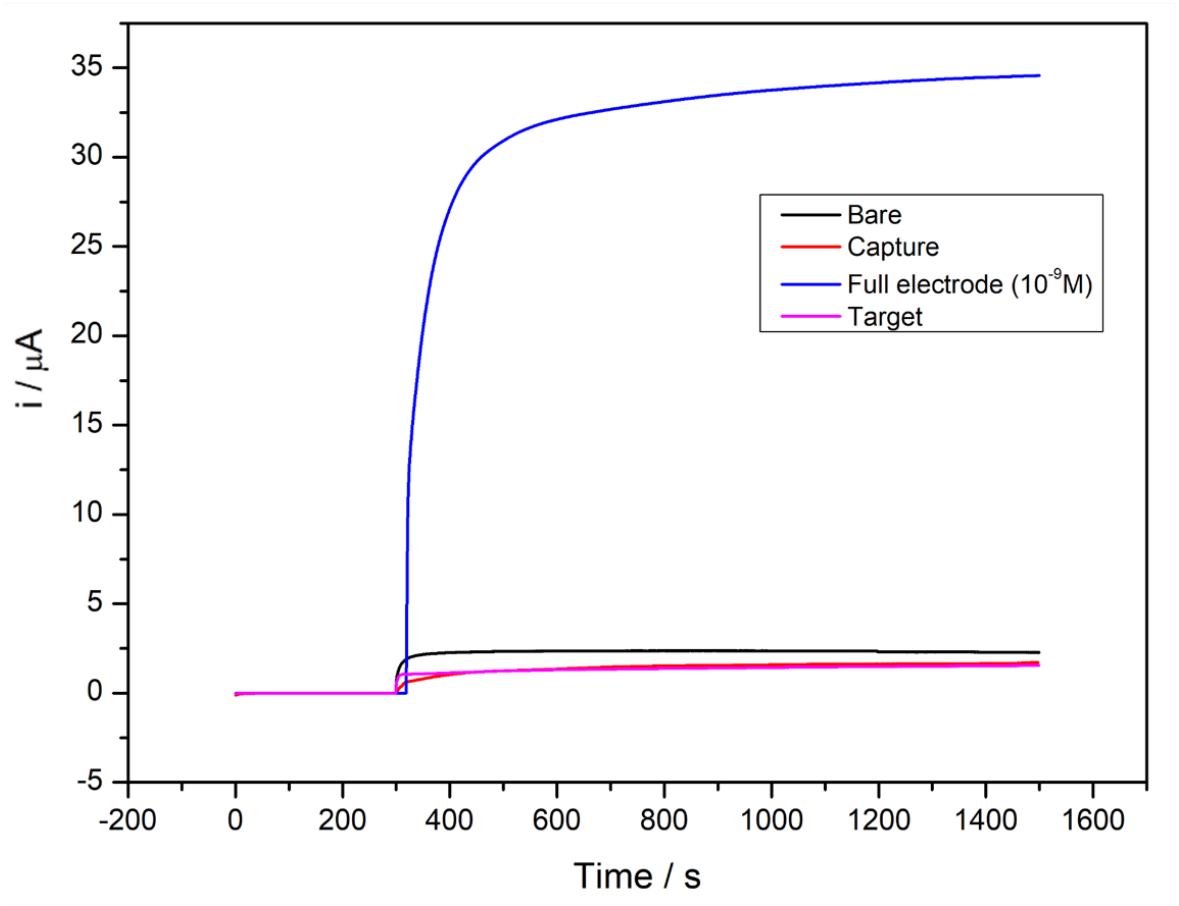


Figure 3.9. Amperometric i-t curves for a bare gold electrode (black line), a gold electrode functionalized with 10 µM capture-probe miRNA/40 µM MCH (red line), a gold electrode functionalized with capture-probe and hybridised to 1 nM target miRNA (pink line), and a gold electrode functionalized with full sandwich assay (blue line). Potential applied is -0.25 V in 0.1M PBS. The difference in current before and after the addition of 400 μM of hydrogen peroxide is displayed. Measurements were performed in triplicate.

Table 3.7. Change in the current before and after the injection of hydrogen peroxide for varying stages of the hybridisation process. Average values and standard deviations were calculated from triplicate measurements (n=3).

Type of modification	Δi /μ A	Standard Deviation
Bare	2.27	0.33
Mixed Sam (miRNA capture-probe + MCH)	1.71	0.20
miRNA target	1.64	0.22
Functionalized assay (1 nM miRNA target)	34.60	1.14

Upon analysing the data presented in Figure 3.9 and Table 3.7, it was expected that the current generated by an assay without labels would originate from the underlying gold. This was confirmed by comparing the current of a bare electrode to that observed after modification with a mixed SAM (miRNA capture-probe /MCH) and after hybridisation of the miRNA capture-probe /MCH-target. As more material is bound to the surface, there is a decrease in the current, from 2.27 $\pm$ 0.33 µA (bare electrode) to 1.64 $\pm$ 0.22 µA (mixed SAM—target). This agrees with the theory highlighted in topic 3.2.5, where a greater barrier of miRNA will hinder the diffusion of hydrogen peroxide.

The hybridisation of miRNA target to the mixed self-assembled monolayer (SAM) results in a small change in current (from 1.71 µA to 1.64 µA). This indicates that the miRNA target does not form a densely packed layer but rather creates a porous structure that does not significantly impede the access of peroxide to the electrode surface. However, as the background current is kept low, it accounts for only a small portion of the overall current. This low background current is highly desirable in ultrasensitive detection as it enables a higher signal-to-noise ratio, which is essential for accurate detection. The limited contribution of the electrode to the total current underscores the importance of minimizing background noise and maximizing the signal from the specific analyte of interest.

3.2.7 Selectivity studies

To evaluate the specificity of the biosensor towards miRNA-206, the response of the functionalized fully complementary sandwich assay was compared to the response generated by an assay where miRNA target is bonded through a different number of mismatches.

1-base mismatch

An initial assessment was made using a miRNA target that contained a single base mismatch. Here, the sequence of target strands used was 3'-UGU GUG UGA AGA AAU GUA AGG U-5'. The base U in red is the one mismatch, non-complementary to the miRNA reporter-probe. Figure 3.10 depicts a comparison plot of the fully complementary calibration curve to a one-base mismatch calibration curve. Table 3.8 presents the average current values obtained by the assays, considering n=3.

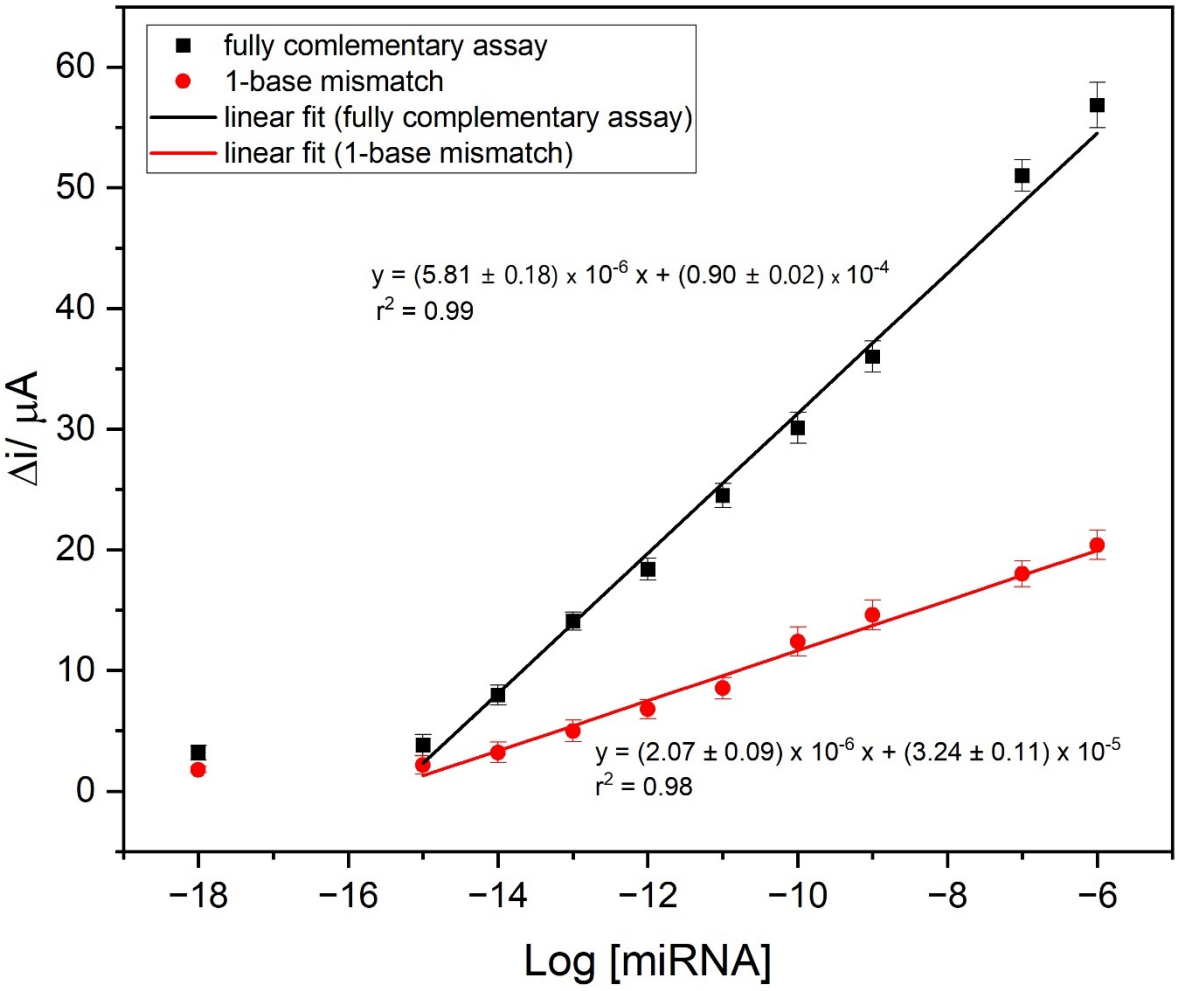


Figure 3.10. Comparison of the chronoamperometric current response of a functionalized fully complementary sandwich assay (miRNA-206, black line) to a non-complementary, 1 base mismatch assay (red line) as a function of target concentrations. The Y-axis is the difference in current before and after the addition of 400 μM hydrogen peroxide. The applied potential is -0.25 V in 0.1M. Measurements were conducted in triplicate, and therefore, error bars depicts the data spread (n=3).

Table 3.8. Comparison of the current response before and after the injection of hydrogen peroxide (Δi) on a functionalized fully complementary nucleic acid strand (miRNA-206) to functionalized, non-complementary sandwich assay (1-base mismatch). Average values and standard deviations were calculated based on n=3.

Concentration **of miRNA target (M)**	Log [miRNA]	Average Δi (μA) Fully complementary Assay	Average Δi (μA) 1 base mismatch Assay
$1x10^{-6}$	-6	57.01 ± 1.83	20.44 ± 1.22
$1x10^{-7}$	-7	51.33 ± 1.30	18.03 ± 1.07
$1x10^{-9}$	-9	36.04 ± 1.27	14.60 ± 1.21
$1x10^{-10}$	-10	30.10 ± 1.29	12.45 ± 1.20
$1x10^{-11}$	-11	24.50 ± 1.02	8.52 ± 0.90
$1x10^{-12}$	-12	18.40 ± 0.91	6.80 ± 0.80
$1x10^{-13}$	-13	14.10 ± 0.75	4.99 ± 0.89
$1x10^{-14}$	-14	7.96 ± 0.81	3.21 ± 0.87
$1x10^{-15}$	-15	3.82 ± 0.86	2.16 ± 0.75
$1x10^{-18}$	-18	3.18 ± 0.61	1.77 ± 0.26

The response of a functionalized assay with a 1-base mismatch was found to be linear across a concentration range of 1 fM to 1 μM, with a regression coefficient of 0.98. This coefficient indicates reasonably good linearity and is only marginally lower than that of the assay with a fully complementary miRNA. Despite similar linearities, the slope of the calibration curves are easily distinguished. As expected, the calibration curve for the fully complementary assay is steeper, indicating a larger change in signal per unit change in analyte concentration, compared to the 1-base mismatch assay. From the theorical calculation of association constant* (K_a) of a fully complementary assay (K_a= 4.2 x10^9) to the 1-base mismatch (K_a=2.1 x10^9) a decrease of 50% in the sensitivity of the assay was expected. Exceeding expectations, the assay presented

a reduction in sensitivity of approximately 64%. This means that the fully complementary assay would be better able to distinguish between small differences in target concentration.

The magnitude of the current generated in the presence of 1-base mismatch was 2.9-fold lower than the highest current produced by the fully complementary electrode (i.e., at [target]=1 μM). This suggests that the current formed by the assay is sufficiently sensitive to differentiate between a miRNA strand that is fully complementary and one that contains a single mismatched base.

*Details on the calculations of association constants and the expected decrease in sensitivity between fully complementary and mismatches strains are shown in the Appendix B.

4-base mismatches

The functionalized fully complementary assay was then compared to the same designed assay differentiating by the usage of miRNA target strand with four base mismatches. The sequence of target strands used was 3'-UAU GUA UGA AGA AAU GUA AGG U-5', being represented in red the mismatches. The miRNA-1 sequence used here was explored because it shares an identical seed sequence to miRNA-206. As a result, any given bioinformatics search predicts a possibility of targeting the same genes [29]. While the actual targeting and regulation of Alzheimer disease (AD) genes is uncertain and only miRNA-206 is recognized as a biomarker of AD, both miRNAs are speculated to be present in the samples of AD patients.

Figure 3.11 shows the calibration curves of a functionalized assay with a fully complementary sequence of target (miRNA-206) versus the calibration curve for sequences with a four-base mismatch (miRNA-1). Table 3.9 presents the average current values obtained by the assays, considering n=3.

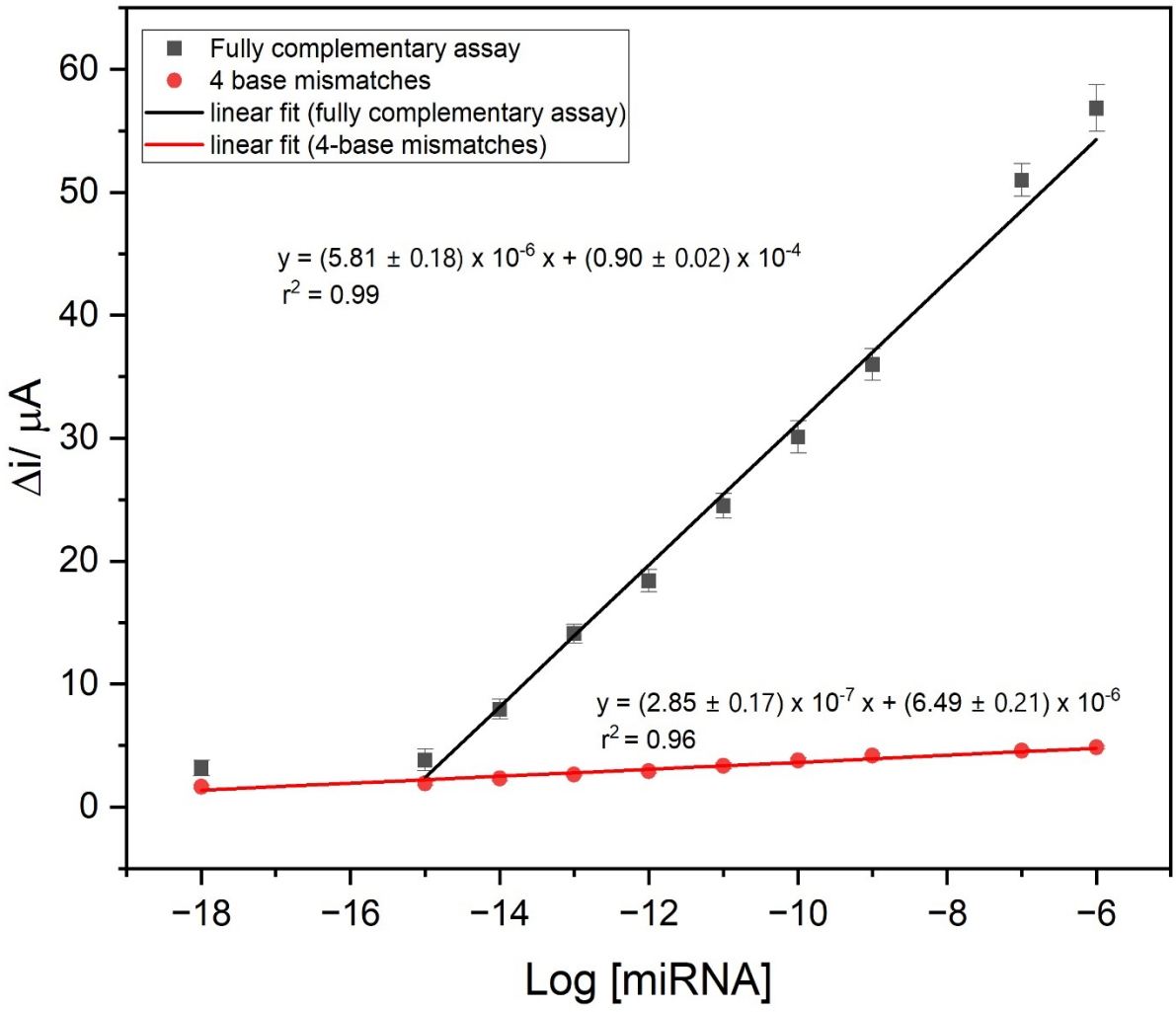


Figure 3.11. Comparison of the chronoamperometric current response of a functionalized fully complementary sandwich assay (miRNA-206, black line) to a non-complementary, 4-base mismatched assay (miRNA-1, red line) as a function of target concentrations. The Y-axis is the difference in current before and after the addition of 400 μM of hydrogen peroxide. The applied potential is -0.25 V in 0.1 M. Measurements were conducted in triplicate, and therefore, error bars depicts the data spread (n=3). Where error bars are not visible, it means they are either smaller or comparable to the same size of the symbols used.

Table 3.9. Comparison of the current response before and after the addition of hydrogen peroxide (Δi) on a functionalized fully complementary nucleic acid strand (miRNA-206) to functionalized, non-complementary sandwich assay (4 base mismatch, miRNA-1). Average values and standard deviations were calculated from triplicate measurements (n=3).

Concentration **of miRNA target (M)**	Log [miRNA]	Average Δi (μA) Fully complementary Assay	Average Δi (μA) 4-base mismatches Assay
$1x10^{-6}$	-6	57.01 ± 1.83	4.85 ± 0.13
$1x10^{-7}$	-7	51.33 ± 1.30	4.56 ± 0.14
$1x10^{-9}$	-9	36.04 ± 1.27	4.17 ± 0.18
$1x10^{-10}$	-10	30.10 ± 1.29	3.80 ± 0.17
$1x10^{-11}$	-11	24.50 ± 1.02	3.36 ± 0.23
$1x10^{-12}$	-12	18.40 ± 0.91	2.91 ± 0.14
$1x10^{-13}$	-13	14.10 ± 0.75	2.65 ± 0.10
$1x10^{-14}$	-14	7.96 ± 0.81	2.32 ± 0.19
$1x10^{-15}$	-15	3.82 ± 0.86	1.93 ± 0.15
$1x10^{-18}$	-16	3.18 ± 0.61	1.64 ± 0.11

The electrochemical response of the assay with 4 base mismatched sequence is linear over a wider range of concentrations (1 μM to 1 aM) compared to a fully complementary assay that is linear from 1 μM to 1 fM. In a similar phenomenon that was explained in Section 3.2.5, this stretch in linearity occurs due to the magnitude of the current generated at different concentrations being too close to one another. A variation of 2.96 μA occurs over 13 orders of magnitude. This generates resolution issues, which is confirmed by the decrease in regression coefficient from 0.99 at fully complementary sequences to 0.96 at 4 base mismatches.

It was expected on the basis of calculated binding energies/association constants that the sensitivity of the assay with the mismatches to decrease approximately 96.8% in comparison with a fully complementary miRNA target. This value was calculated considering a K_a for the

fully complementary assay of 4.2 x10^9 and a K_a for the 4-base mismatch of 1.05 x10^8 . Details on the calculations are shown in the Appendix B. In agreement with the calculated value, the decrease in sensitivity present to be 95.1%.

The outcomes are very encouraging as they suggest that the number of target strands with four distinct bases, which attach to the capture-probe strand, is minimal. Moreover, the excellent discrimination between fully complementary and mismatched assays that contain the same seed structure on its sequence is impressive. Despite the complexity of the miRNA binding process, the seed region is considered the primary factor for determining miRNA-target specificity, as it typically contains the "seed match" for the target mRNA. The seed match is essential to ensure that the miRNA specifically binds to its intended targets and not to non-target mRNAs with partially complementary sequences [30].

Overall, the greater decrease in sensitivity when in presence of mismatches and highly specificity against miRNA-206 can be justified not only by the optimised engineering of the platform which guarantees saturation of miRNAs strands at each step of the assay and same level of fully complementary binding between miRNA reporter-probe and target, but also due to well structuring and alignment of the mixed SAM.

3.3 Conclusion

In conclusion, this work represents a significant advancement in the development of electrochemical biosensors for the detection of miRNA targets associated with neurological diseases. By using gold nanorods (AuNRDs, 50 nm x 15 nm) as labels for the miRNA sandwich assay, the study has demonstrated the potential of using specific size and shape of gold nanostructures to enhance the electrocatalytic activity of the biosensor. The optimization of the biosensor platform, including the mixed self-assembled monolayer, the concentration ratios of miRNA reporter-probe to AuNRDs, hybridization and immobilisation steps, and hydrogen peroxide concentration for electrocatalysis, was crucial for achieving high sensitivity and stability of the biosensor. Hence, the optimal loading of miRNA reporter-probe to AuNRDs occurred at a mole ratio of 960:1 [miRNA $_{\text{reporter- probe}}]_I$ /AuNRDs in solution. The optimal hybridization time between miRNA reporter-probe and target were determined as 5 hours, and an optimal concentration of hydrogen peroxide of 400 μM was identified for the electrocatalysis of gold nanorods.

The engineered platform was tested against 4 bases mismatches (miRNA-1) and 1 base mismatch, presenting a decrease in current signal of 95% and 64% in comparison with a fully complementary miRNA target, respectively. As the number of target strands with distinct bases that attach to the capture-probe strand is minimal, the biosensor was classified as highly specific to miRNA-206. Also, the biosensor developed in this study demonstrated a limit of detection of 0.46 fM and a wide dynamic range covering nine orders of magnitude.

Finally, the biosensor showed promising results in terms of its ability to provide quick and accurate results, which is crucial for point-of-care devices. The amperometric response of the biosensor was found to be directly proportional to the logarithm of miRNA target concentration, with a steady-state current achieved within a time frame of 300 to 1500 seconds depending on the miRNA target concentration. Overall, these findings can contribute to the development of biosensors with improved sensitivity and specificity, which can ultimately lead to earlier diagnosis and better treatment outcomes for patients with neurological diseases.

3.4 References

[1] Shabaninejad, Z., Yousefi, F., Movahedpour, A., Ghasemi, Y., Dokanehiifard, S., Rezaei, S., Aryan, R., Savardashtaki, A., & Mirzaei, H. (2019). Electrochemical-based biosensors for microRNA detection: Nanotechnology comes into view. *Analytical biochemistry*, *581*, 113349. https://doi.org/10.1016/j.ab.2019.113349

[2] Ma, H., Tian, L., Wang, T., & Wang, C. (2010). Optical DNA detection based on gold nanorods aggregation. *Analytica Chimica Acta*, *673*(2), 179-184. https://doi.org/10.1016/j.aca.2010.05.036

[3] Parab, H. J., Jung, C., Lee, J.-H., & Park, H. G. (2010). A gold nanorod-based optical DNA biosensor for the diagnosis of pathogens. *Biosensors and Bioelectronics*, *26*(2), 667-673. https://doi.org/10.1016/j.bios.2010.06.067

[4] Lu, X., Dong, X., Zhang, K., Han, X., Fang, X., & Zhang, Y. (2013). A gold nanorods-based fluorescent biosensor for the detection of hepatitis B virus DNA based on fluorescence resonance energy transfer. *The Analyst*, *138*(2), 642–650. https://doi.org/10.1039/c2an36099c

[5] Zanoli, L. M., D'Agata, R., & Spoto, G. (2012). Functionalized gold nanoparticles for ultrasensitive DNA detection. *Analytical and bioanalytical chemistry*, *402*(5), 1759–1771. https://doi.org/10.1007/s00216-011-5318-3

[6] Saha, K., Agasti, S. S., Kim, C., Li, X., & Rotello, V. M. (2012). Gold nanoparticles in chemical and biological sensing. *Chemical reviews*, 112(5), 2739–2779. https://doi.org/10.1021/cr2001178

[7] Cao, X., Ye, Y., & Liu, S. (2011). Gold nanoparticle-based signal amplification for biosensing. *Analytical biochemistry, 417*(1), 1–16. https://doi.org/10.1016/j.ab.2011.05.027

[8] Chen, W.; Cai, S.; Ren, Q-Q.; Wen, W., Zhao, Y. D. (2012). Recent advances in electrochemical sensing for hydrogen peroxide: A review. *Analyst, 137*(1), 49-58 . https://doi.org/10.1039/C1AN15738H

[9] Vigderman, L., Khanal, B. P., & Zubarev, E. R. (2012). Functional Gold Nanorods: Synthesis, Self-Assembly, and Sensing Applications. *Advanced Materials, 24*(36), 4811-4841. https://doi.org/10.1002/adma.201201690

[10] Naresh, V., & Lee, N. (2021). A Review on Biosensors and Recent Development of Nanostructured Materials-Enabled Biosensors. *Sensors (Basel, Switzerland), 21*(4), 1109. https://doi.org/10.3390/s21041109

[11] Sołoducho, J., & Cabaj, J. (2015). Electrochemical and Optical Biosensors in Medical Applications. In Biosensors - Micro and Nanoscale Applications. InTech. https://doi.org/10.5772/60967

[12] Xia, N., & Zhang, L. (2014). Nanomaterials-Based Sensing Strategies for Electrochemical Detection of MicroRNAs. *Materials, 7* (7), 5366–5384. https://doi.org/10.3390/ma7075366

[13] Kenny, A., McArdle, H., Calero, M., Rabano, A., Madden, S., Adamson, K., Forster, R., et al. (2019). Elevated Plasma microRNA-206 Levels Predict Cognitive Decline and Progression to Dementia from Mild Cognitive Impairment. *Biomolecules, 9*(11), 734. http://dx.doi.org/10.3390/biom9110734

[14] Trasatti, S., & Petrii, O. A. (1991). Real surface area measurements in electrochemistry. *Pure & Applied Chemistry, 63*, 711-734. https://doi.org/10.1351/pac199163050711

[15] Armbruster, D. A., & Pry, T. (2008). Limit of blank, limit of detection and limit of quantitation. *The Clinical biochemist. Reviews*, *29 Suppl 1*(Suppl 1), S49–S52.

[16] Bishop, K. J., Wilmer, C. E., Soh, S., & Grzybowski, B. A. (2009). Nanoscale forces and their uses in self-assembly. *Small (Weinheim an der Bergstrasse, Germany)*, *5*(14), 1600–1630. https://doi.org/10.1002/smll.200900358

[17]Liu, B., & Liu, J. (2017). Methods for preparing DNA-functionalized gold nanoparticles, a key reagent of bioanalytical chemistry. *Analytical Methods, 9*, 2633. https://doi.org/10.1039/c7ay00368d

[18] Storhoff, J. J., Elghanian, R., Mucic, R. C., Mirkin, C. A., & Letsinger, R. L. (1998). One-Pot Colorimetric Differentiation of Polynucleotides with Single Base Imperfections Using Gold Nanoparticle Probes. *Journal of the American Chemical Society, 120*(9), 1959-1964. https://doi.org/10.1021/ja972332i

[19] Cutler, J. I., Auyeung, E., & Mirkin, C. A. (2012). Spherical Nucleic Acids. *Journal of the American Chemical Society, 134*(3), 1376-1391. https://doi.org/10.1021/ja209351u

[20] Hurst, S. J., Lytton-Jean, A. K. R., & Mirkin, C. A. (2006). Maximizing DNA Loading on a Range of Gold Nanoparticle Sizes. *Analytical Chemistry*, *78*(23), 8313-8318. https://doi.org/10.1021/ac0613582

[21] Zhang, X., Gouriye, T., Göeken, K., Servos, M. R., Gill, R., & Liu, J. (2013). Toward Fast and Quantitative Modification of Large Gold Nanoparticles by Thiolated DNA: Scaling of Nanoscale Forces, Kinetics, and the Need for Thiol Reduction. *Journal of Physical Chemistry C, 117*(30), 15677-15684. https://doi.org/10.1021/jp403946x

[22] Hill, H. D., Millstone, J. E., Banholzer, M. J., & Mirkin, C. A. (2009). The Role Radius of Curvature Plays in Thiolated Oligonucleotide Loading on Gold Nanoparticles. *ACS Nano*, *3*(2), 418-424. https://doi.org/10.1021/nn800726e

[23]Lang, N. J., Liu, B., Zhang, X., & Liu, J. (2013). Dissecting Colloidal Stabilization Factors in Crowded Polymer Solutions by Forming Self-Assembled Monolayers on Gold Nanoparticles. *Langmuir, 29*(20), 6018-6024. https://doi.org/10.1021/la3051093

[24] Zhang, X., Servos, M. R., & Liu, J. (2012). Ultrahigh nanoparticle stability against salt, pH, and solvent with retained surface accessibility via depletion stabilization. *Journal of the American Chemical Soci*ety, 134(23), 9910-9913. https://doi.org/10.1021/ja303787e

[25] Zu, Y., & Gao, Z. (2009). Facile and controllable loading of single-stranded DNA on gold nanoparticles. *Analytical chemistry, 81*(20), 8523-8528. https://doi.org/10.1021/ac901459v

[26] Laidler, K. J., & Meiser, J. H. (1982). Physical Chemistry (3rd ed.). Benjamin/Cummings Publishing Company.

[27] Bard, A. J., & Faulkner, L. R. (2000). Electrochemical methods: fundamentals and applications (2nd ed.). John Wiley & Sons.

[28]Gao, Z., & Yang, Z. (2006). Detection of microRNAs using electrocatalytic nanoparticle tags. *Analytical Chemistry, 78*(5), 1470-1477. https://doi.org/10.1021/ac051726m

[29] Lin, C.-Y., Lee, H.-C., Fu, C.-Y., Ding, Y.-Y., Chen, J.-S., Lee, M.-H., Huang, W.-J., & Tsai, H.-J. (2013). miR-1 and miR-206 target different genes to have opposing roles during angiogenesis in zebrafish embryos. *Nature Communications, 4,* 2829. https://doi.org/10.1038/ncomms3829

[30] Alvarez-Garcia, I., & Miska, E. A. (2005). MicroRNA functions in animal development and human disease. *Development, 132*(21), 4653-4662. https://doi.org/10.1242/dev.02073

CHAPTER 4

Development of labelled amperometric biosensors based on screen printed electrodes that contain different gold microstructures within the carbon ink.

4 INTRODUCTION

As discussed in previous chapters, neurological diseases are debilitating conditions that affect the central and peripheral nervous systems, leading to severe disability and reduced quality of life [1]. Early detection of these diseases is critical for a higher possibility in management of the disease, as well as, to improve the patient outcomes to treatment. The need for early detection of these diseases has driven the development of novel detection methods that are highly sensitive, rapid, and specific.

MicroRNAs (miRNAs) are small non-coding RNA molecules that regulate gene expression and play a critical role in various biological processes, including neuronal development and function [2]. Aberrant expression of miRNAs has been linked to several neurological disorders, including Alzheimer's disease and epilepsy. Therefore, the early detection of miRNAs associated with neurological diseases has significant clinical implications.

Electrochemical techniques have become widely used in the detection of miRNAs due to their ease of operation, portability, low cost, and rapid results [3]. Screen-printed electrodes (SPEs) have emerged as a popular platform for electrochemical sensing, e.g., for glucose monitoring in diabetic patients, due to their low cost, disposability, and ease of fabrication [4]. Traditional SPEs are based on carbon containing inks but it may be possible to improve the biosensor's performance by incorporating gold microstructures directly into the ink used for screen printing the working electrodes. This approach allows for easy modification, e.g., using thiol chemistry, of the SPE with functional biomolecules without additional surface modification steps. The integration of gold nanostructures directly into the ink could also lead to an increase in the electrochemical signal and sensitivity of the biosensor [5]. Moreover, metal nanoparticles have unique optical, electronic, and catalytic properties that make them suitable candidates for electrochemical sensing [6].

In the present work, the electrochemical behaviour and the analytical performance of the in-house developed screen-printed electrodes with different compositions of gold nanoparticles mixed into a carbon-based ink was evaluated. The goal was to compare different screen-printed electrodes and nanoparticle labels to create an optimal miRNA biosensor platform for detecting biomarkers of neurological disease, such as miRNA-206. The response of the sensor was

obtained through amperometry, and by analysing the reduction of hydrogen peroxide by the nanoparticles confined to the gold surface via complementary hybridization between the functionalized reporter-probe and the capture-probe –target.

The electrocatalytic properties of metal nanoparticles for the reduction of hydrogen peroxide are highly dependent on their size and shape. AuNRDs have shown improved electrocatalytic activity due to their high aspect ratio, which results in a larger surface area capable to facilitate the reduction of hydrogen peroxide [7]. Palladium nanocubes (PdNCBs) exhibit excellent electrocatalytic activity due to their well-defined facets and edges, which create more active sites for the reduction of hydrogen peroxide[8]. Similarly, platinum nanoparticles (PtNPs) with a high surface area and a size close to the double layer thickness have demonstrated superior electrocatalytic activity for the reduction of hydrogen peroxide [9]. The optimal size for metal nanoparticles in electrocatalytic reduction of hydrogen peroxide is around 50 nm [10]. Therefore, by controlling the size and shape of metal nanoparticles one can optimize their electrocatalytic activity for hydrogen peroxide reduction, which is vital for various applications, including biosensors and fuel cells.

Thus, the use of screen-printed carbon electrodes with integrated gold particles for the detection of miRNAs associated with neurological diseases could offer an excellent platform for early detection of neurological disorders. Moreover, they could simplify the fabrication process, by reducing the overall fabrication time, improve the reproducibility and scalability of the biosensor manufacturing process, and offer a greater potential for tailoring the incorporated gold structures to specific sizes and shapes optimized for the detection of various biomolecules and different applications.

4.1 Experimental Procedures

4.1.1 Materials and Chemicals

Ferrocenemethanol (FcMcOH), phosphate buffer (PBS, pH 7.4), Ethyl Cellulose, dipropylene glycol monomethyl ether, alpha-terpineol, sulfuric acid (H_2SO_4, 95-98%), tris[2-carboxyethyl]phosphine (TCEP), hydrogen peroxide solution (H_2O_2, 3%), nafion® 117 solution (5%), palladium (II) chloride ($PdCl_2$), hydrochloric acid (HCl),

cetyltrimethylammonium bromide (CTAB) and ascorbic acid (AA) were purchased from Sigma Aldrich and used as received.

Conductive Carbon Black (Ensaco) and Graphite (Timrex) were purchased from Imerys Graphite & Carbon (Bironico, Switzerland). Au microparticles (Gold powder, spherical or flakes, APS 1.5 - 3.0 micron) were obtained by Alfa Aesar (Lancashire, UK).

Nanoparticles used as labels in this study were obtained from nanoComposix. Specifically, gold nanorods measuring 50 nm x 15 nm in size with a zeta potential of -52 mV and a particle concentration of 4.30 x 10^{11} parts/ mL, as well as platinum nanoparticles measuring 50 nm ± 4 nm in size with a zeta potential of -40 mV and a particle concentration of 9.6 x 10^{11} particles/mL, were used. All nanoparticles were citrate-stabilized and suspended in water.

A third and final label used in this work was palladium nanocubes which was fabricated in-house. These nanocubes had an edge length of 50 nm and zeta potential of 38.6 ± 5.0 mV.

All the aqueous solutions described in this work, if it was not stated otherwise, were prepared using Milli-Q water (Millipore Core, 18 MΩ cm^{-1}).

The oligonucleotides (purity ≥ 98%), RNase free water and TE buffer (10 mM Tris and 1mM EDTA) used to prepare immobilization and hybridization solutions were purchased from IDT. The base sequences used was:

Capture-probe (miRNA-206): 5'-/5 $HSMC_6$-D/ C-CAC- ACA-CUU- 3'

Target (Fully complementary): 3'- G-GUG-UGU-GAA-GGA-AUG-UAA-GGU- 5'

Reporter-probe: 5'-CCU-UAC-AUU-CCA/3ThioMC3-D/- 3'

4.1.2 Synthesis of PdNCBs (50 nm in size)

The synthesis of palladium nanocubes was based on the approach described by Niu *et al.* [11] and was initiated by preparing a solution of 10 mM H_2PdCl_4. For this purpose, 0.1775 g of $PdCl_2$ was added to a 10 mL volumetric flask that had been filled with 0.2 M HCl. Subsequently, the resulting solution was diluted to 100 mL of distilled water to achieve a final concentration of 10 mM.

In the next step, a beaker containing 200 mL of 12.5 mM CTAB was prepared, and 12.5 mL of 10 mM H_2PdCl_4 solution was added to it. The beaker was heated to 95 ℃ and kept under constant stirring. After a duration of 14 minutes, 2.5 mL of freshly prepared 100 mM ascorbic acid solution was introduced into the beaker. The reaction was allowed to proceed for an additional 30 minutes.

To separate the desired palladium nanocubes, the solution was subjected to centrifugation at 6000 rpm for 1 hour. The supernatant was carefully removed, leaving the solid residue, which was subsequently washed with DI water. This centrifugation and washing procedure was repeated two more times.

4.1.3 Labelling of miRNA reporter-probes with PdNCBs and PtNPs

To prepare the PdNCBs and PtNPs for functionalization with miRNA reporter-probes, 1 mL of the specific nanomaterial was centrifuged with 1 mL of nuclease-free water at 6000 rpm for 10 minutes. After centrifugation, the excess water was carefully removed, leaving the nanoparticles as an aggregate in the Eppendorf tube.

To achieve an optimal* nucleic acid density on the platinum spheric surface, 3140 µL of 1 µM miRNA reporter-probe (complementary to the target let-7b) was combined with 88 µL of 1.59 nM platinum nanoparticles. Similarly, for optimal nucleic acid coverage of the palladium cubic surface, 2409 µL of 1 µM miRNA reporter-probe (complementary to the target miRNA-135a) was mixed with 150 µL of palladium nanocubes (4.72 nM). The immobilization of the labels to the specific miRNA reporter-probe was carried out at 37℃ for 3 hours.

Following the described procedure, 150 µL of the functionalized miRNA reporter-probe was added to an Eppendorf for subsequently hybridization with the complementary sandwich assay developed at screen-printed electrode (20% AuS SPCE). Detailed information regarding the development of the assay will be outlined in the subsequent section.

*The volumes needed to functionalize ~40% of surface of the nanoparticles and nanocubes surfaces were calculated in accordance with their shape and size.

4.1.4 Labelling of miRNA reporter-probe with AuNRDs

Prior to functionalizing AuNRDs with miRNA reporter-probes, 15 mL of the specific nanomaterial was concentrated 10 times, by centrifugation at 6000 rpm for 10 minutes. The supernatant (approximately 14.85 mL) was removed from the solution leaving the nanoparticles as a precipitate in the Eppendorf. Subsequently, 150 μL of 4.6 μM of miRNA reporter-probe was added to 150 μL of (7.14 nmol/L) of gold nanorods to form a ratio of $[miRNA_{reporter\text{-}probe}]_I$ / [AuNRDs] = 640:1. After 1h of incubation, the gold nanorods functionalized miRNA reporter-probe required a salt aging step* to improve the adsorption capability of the conjugate miRNA reporter-probe to AuNRDs. Therefore, 1M NaCl was added dropwise to the solution to reach a final concentration of 50 mM. The solution was allowed to stabilize for 1h. The process was repeated until the salt concentration achieved 300 mM, over a 6-hr period. A vortex was used to fully mix the solutions following each addition.

Following the described procedure, the hybridization of the miRNA reporter-probe with the complementary sandwich assay on a screen-printed carbon electrode (SPCE) occurred. The specific details of the assay development are outlined in the subsequent section.

*It is important to note that the salt aging process utilized in this work follows the methodology described by [10] while the optimum molar ratio of the initial concentration of miRNA reporter-probe to AuNRDs ($[miRNA_{reporter\text{-}probe}]_I$ / [AuNRDs]) follow the studies performed in Chapter 3.

4.1.5 Development of miRNA assay at screen printed electrodes

In this investigation, the setup incorporated the working electrode (WE), reference electrode (RE), and counter electrode (CE) printed together as a single unit. However, to prevent the unintended binding of miRNAs at the CE and RE during the immobilization and subsequent hybridization phases, it became imperative to physically separate the CE and RE electrodes.

To commence the development of the miRNA assay, we initially applied a monolayer of miRNA capture-probe onto the screen-printed electrode, which featured diverse combinations* of gold microstructures within the carbon ink. This process involved immersing the surface of the working electrode in an Eppendorf tube containing a 10 μM solution of the 5'-thiolated

oligo. The sealed Eppendorf tube was then incubated in an oven at 37°C for 80 minutes. Afterward, the electrode was thoroughly rinsed with nuclease-free water to eliminate any loosely attached or physiosorbed strands.

Subsequently, the capture-probe-modified screen-printed electrode was exposed to different concentrations of the miRNA target (1 M when the electrode was functionalized with PdNCBs or PtNPs and 100 nM when functionalized with AuNRDs). This step facilitated the hybridization of the miRNA target's 3' end with the capture-probe strand, a process carried out for 20 minutes in an oven at 37°C. Once again, the electrode underwent a thorough washing with nuclease-free water.

Finally, the free 5' end of the miRNA target was allowed to hybridize with its complementary sequence found in the miRNA reporter-probe functionalized with metal nanoparticles. This hybridization of the labeled miRNA reporter-probe to its complementary sequence transpired over a 5-hour duration at 37°C.

Two crucial aspects require careful attention for the successful development of the miRNA assay. Firstly, the preparation of the working solution necessitates thorough consideration. To circumvent the adverse effects of freeze/thaw cycles, we drew multiple aliquots from stock solutions of oligonucleotides (100 μM) and stored them in the refrigerator until needed. Additionally, to obtain less concentrated standards, precise dilution in the TE buffer (comprising 10 mM Tris and 1 mM EDTA) was meticulously carried out.

Secondly, the preparation of the immobilization buffer (miRNA capture-probe and reporter-probe) entails specific steps. We introduced TCEP (Tris [2-carboxyethyl] phosphine) in a 100-fold excess and allowed it to react for 2 hours. This crucial step ensures the reduction and liberation of thiol bonds from the capture-probe and reporter-probe oligos, thereby facilitating efficient immobilization on the metallic surfaces.

*In this study, various compositions of gold microstructures were blended with the screen-printed carbon ink of the SPCE to create electroactive adsorption sites, which were pivotal for the development of the fully complementary assay mentioned earlier. These compositions included 10% (w/w) and 20% (w/w) gold microspheres (2 μm) mixed with the screen-printed carbon ink, as well as 10% (w/w) and 20% (w/w) gold microflakes (2 μm).

4.1.6 Drop-casting of metal nanoparticles

In order to get an insight into the electrocatalytic properties of the nanoparticles developed to act as labels, they were drop cast onto the electrode surface. The PdNCBs, AuNRDs and PtNPs were drop cast on a screen-printed electrode that contained 20% (w/w) of gold microspheres mixed to the carbon ink (referred as 20% AuS SPCE) following a washing step. Hence, 1 mL of the nanoparticles were centrifuged with 1 mL of nuclease free water at 6000 rpm for 10 minutes. The excess water was removed from the solution leaving the nanomaterials in the bottom of the Eppendorf. Then, the Eppendorf was oven dried at 80^{o}C for 15 minutes. Finally, 50 µL of Nafion was added to the nanoparticles and 5 µL of this solution was drop-casted on to the 20% AuS SPCE surface. Electrochemical measurements were carried out after complete evaporation of the solvent present at the SPCE.

4.1.7 Electrochemical Analysis

4.1.7.1 Voltametric Analysis

Scan rate studies of a conventional gold electrode and SPCEs with different gold nanoparticles shapes within the carbon ink such as, 10% (w/w) gold microspheres (referred as 10% AuS SPCE) and 10% (w/w) microflakes (referred as 10% AuF SPCE), were performed. Cyclic voltammetry (CV) curves were obtained between -0.5 to +0.9 V over a range of scan rates, from 0.05 to 0.50 V s^{-1}. The electrodes were placed in a three-electrode cell filled with 0.01 M of PBS solution and 1 mM of ferrocene methanol (FcMeOH). All electrochemical measurements were performed in triplicate. The solutions were vigorously deoxygenated with nitrogen to remove oxygen prior to analysis.

4.1.7.2 Amperometric detection of miRNA-206

After functionalizing the screen printed carbon electrode surface with the capture-probe — target — labelled reporter-probe assay, the working electrode, reference electrode, and counter electrode were assembled together and immersed in a small cell filled with 7.2 mL of 0.01M PBS solution. Amperometry was employed as the detection method to identify the presence of the metal nanoparticles and hence the target concentration.

Initially, the current was measured at the identified specific potentials for each type of nanoparticle: -0.375V for PdNCBs, -0.25V for AuNRDs, and -0.5V for PtNPs. The current was allowed to stabilize for 5 min. Following that, 3.27 µL of hydrogen peroxide (3% w/v) was introduced into the PBS solution to achieve a final concentration of 400 µM. Stirring was employed for 1 min, upon addition of hydrogen peroxide.

Subsequently, the current associated with the reduction of hydrogen peroxide by the nanoparticles was measured after 20 minutes. The analytical response was determined by calculating the difference in current (Δi) observed before and after the addition of hydrogen peroxide.

4.1.8 Instrumentation

Electrochemical measurements were carried out using a CHI760D electrochemistry workstation at room temperature (22±2 °C). For the measurements using a conventional gold disc working electrode (diameter, Φ = 2 mm) a three-electrode cell was used. The silver/silver chloride electrode (Ag/AgCl in 3 M KCl) and a platinum wire acted as a reference and counter electrode, respectively.

A screen-printed carbon/graphite/ gold nanoparticles* working electrodes (diameter, Φ = 3 mm) were fabricated in-house with appropriate stencil designs using a DEK Horizon APiX screen-printing machine (Maxem, IE) by Dr Loanda Cumba, DCU. For the electrochemical measurements applying SPCEs, a screen-printed Ag/AgCl was used as a pseudo-reference and carbon/graphite as a counter electrode.

*Specifically, the composition of the 10% Au SPCE was ethyl cellulose (5.85%), dipropylene glycol monomethyl ether (30.60%), alpha-terpineol (26.10%), carbon black (8.55%), graphite (18.90%) and gold microparticles (spheres or flakes,10%).

The 20% AuS SPCE contained: ethyl cellulose (5.20%), dipropylene glycol monomethyl ether (27.20%); alpha-terpineol (23.20%), carbon black (7.60%), graphite (16.80%) and Au microspheres (spheres, 20%).

4.1.9 Microscopic measurements

4.1.9.1 TEM and SEM

The formation and shapes of AuNRDs was observed by high-resolution transmission electron microscopy (HRTEM, JEM-2200FS, JEOL, Japan). Scanning electron microscopy (SEM) was performed using a Hitachi S-3400N scanning electron microscope. It was used to evaluate the structure of SPCE with different gold microparticles mixed to the carbon ink, as well as the formation of synthesized palladium nanocubes.

4.1.10 Spectroscopic measurements

4.1.10.1 DLS and Zeta potential

Dynamic Light Scattering (DLS) and zeta potential was performed at 25℃ on a Nanosizer NanoZS (Malvern Instruments, Malvern U.K.) using a detection angle of 90 degrees.

4.1.11 Estimation of the heterogeneous electron transfer (k_0) and the diffusion coefficient (D) from CV:

In this work, the determination of the standard heterogeneous electron transfer rate constant, k_0, was experimentally obtained using cyclic voltammetry. The method, improved by Nicholson [12], involves investigating the peak-to-peak separation (ΔE) of a redox couple in solution as a function of scan rate.

To simplify Nicholson's method, Lavagnini *et al.* [13] introduced the dimensionless parameter ψ, calculated using Equation 4.1. This parameter was subsequently correlated with Equation 4.2, which describes the relationship between k_0 and ψ. By manipulating these equations mathematically, the value of k0 can be directly obtained from the slope of the ψ versus $\sqrt{\frac{RT}{\pi\, n\, F\, D}}\, v^{-1/2}$ graph.

$$\psi = \frac{-0.6288 + 0.0021\, \Delta Ep}{1 - 0.017\, \Delta Ep} \qquad \text{Equation 4.1}$$

$$\psi = k_0 \sqrt{\frac{RT}{\pi\, n\, F\, D}}\, v^{-1/2} \qquad \text{Equation 4.2}$$

It is important to note that this method specifically applies to reversible or quasi-reversible systems. The diffusion coefficient (D) was determined using the Randles-Sevcik equation, described below.

$$i_p = 2.687\ x10^5\ n^{3/2}\ A\ C\ D^{1/2}\ v^{1/2} \quad \text{Equation 4.3}$$

Where, D is the diffusion coefficient of electroactive species ($cm^2\ s^{-1}$) , n is the number of electrons transferred in the reaction, F is the Faraday constant ($C\ mol^{-1}$), R is the molar gas constant ($JK^{-1}mol^{-1}$), T is the absolute temperature (K), C is the concentration of the redox species in solution ($mol\ cm^{-3}$) and A is the area of the working electrode (cm^2). As a result, the constant has units of $C\ mol^{-1}\ V^{-1}$.

4.2 Results and Discussion

4.2.1 Evaluation of the Electrochemical Behaviour of SPCE with different gold structures mixed to the carbon ink

Two distinct screen printed carbon electrodes (SPCE) were fabricated, each incorporating different gold particle structures within the carbon ink. Both electrodes comprised 10% (w/w) gold microstructures (2 μm) blended into the carbon-based ink. $SPCE_1$ utilized gold microspheres (AuS) alongside graphite as a conductive pathway (denoted 10% AuS SPCE). On the other hand, $SPCE_2$ deviated from $SPCE_1$ by incorporating gold microflakes in place of gold microspheres within the screen-printed carbon ink (10% AuF SPCE). Despite this difference, both $SPCE_1$ and $SPCE_2$ shared a common feature—a precisely formulated ink with an optimized composition, maintaining an identical proportion of base materials (carbon/graphite).

Metallic functionalization of the transducer platform was used with the purpose of creating an electroactive surface area available for capture-probe strand immobilisation. If the sensing phase have more sites available to bind with the full miRNA assay, higher is it sensitivity, leading to an overall improvement of the analytical performance of the sensor.

Additional features as enhancement of electron transfer properties and decreasing of the resistance of the surface, provided by the gold particles, was assessed through scan rate studies of the 10% AuS SPCE and 10% AuF SPCE platform. Each electrode was immersed in a

solution of 1 mM ferrocene methanol in 0.01M PBS. The electrochemical behaviour of the benchmark redox species was recorded by cyclic voltammetry applying scans from -0.5 V to +0.9 V at rates from 0.005 V/s to 0.5 V/s.

Figure 4.2 compares the scan rate studies of (A) a conventional gold electrode, (C) 10% AuF SPCE and (E) 10% AuS SPCE. Table 4.1 presents the analysis of the cyclic voltammograms in regards of peak-to peak potential (ΔE_p). The peak current densities of the oxidation and reduction processes and the diffusion behaviour of the redox species was also evaluated through its corresponding graphs of peak current vs. square root of scan rates.

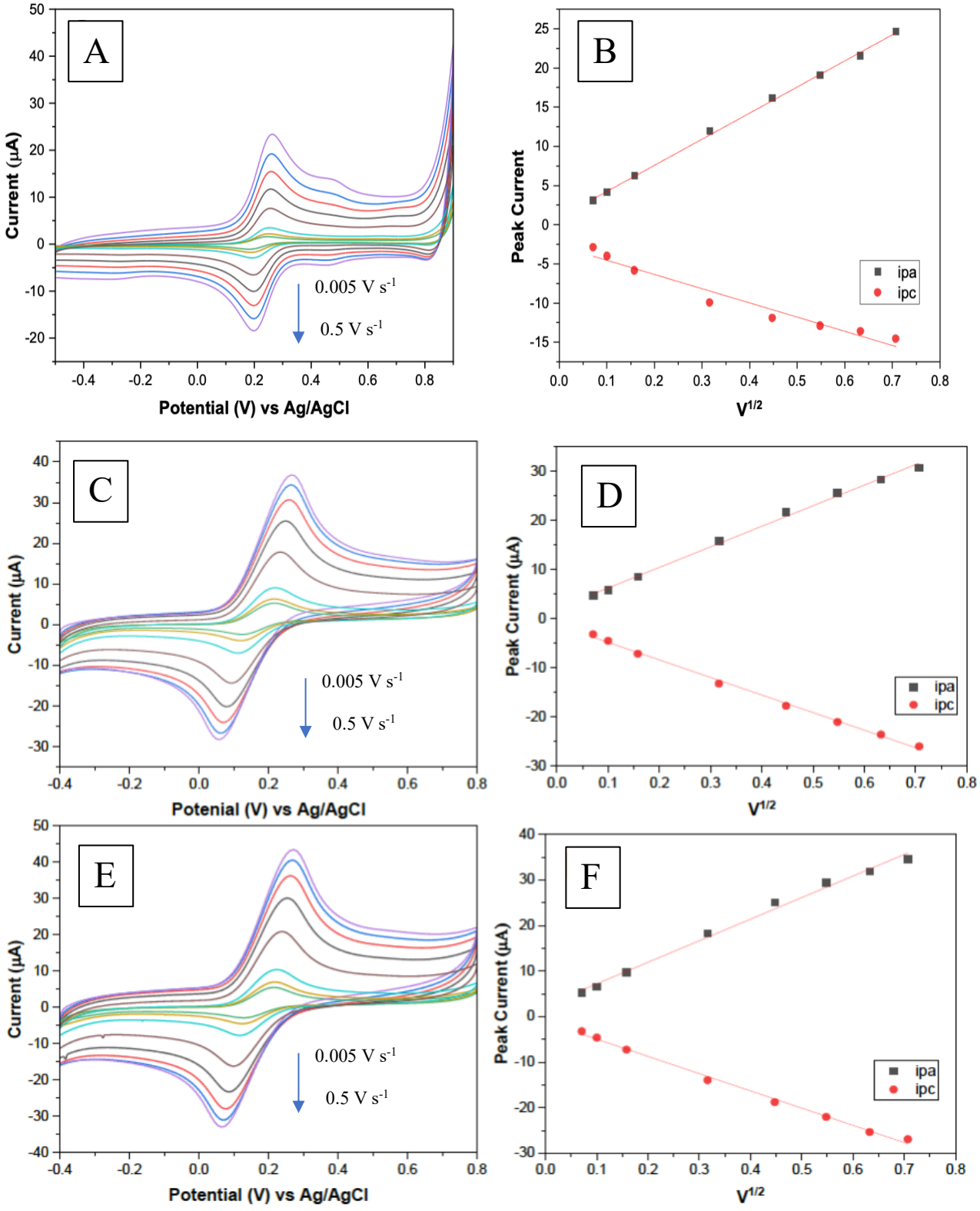


Figure 4.1. Cyclic voltammograms of (A) a conventional gold disk electrode, (C) 10% AuF SPCE and (E) 10% AuS SPCE in 0.01 M PBS with 1mM FcMeOH at scan rates from 0.005 V/s to 0.5 V/s. Graphs of peak current vs. square root of scan rate are depicted in (B), (D) and (F). Error bars were estimated as triple of the standard deviation.

Table 4.1. Average of the peak-to-peak potentials obtained from scan rate studies of conventional gold electrode, 10% AuF SPCE and 10% AuS SPCE in FcMeOH and 0.01 M PBS.

Scan Rate (V/s)	ΔEp (mV) Gold Electrode	ΔEp (mV) 10% AuF SPCE	ΔEp (mV) 10% AuS SPCE
0.005	82.0 ± 0.5	98.0 ± 1.0	96.0 ± 0.7
0.010	113.1 ± 22.5	98.0 ± 1.1	97.0 ± 0.6
0.025	66.2 ± 16.0	100.1 ± 6.0	107.1 ± 4.1
0.100	78.0 ± 32.5	13.2 ± 7.8	145.0 ± 3.0
0.200	156.1 ± 56.5	156.0 ± 3.0	165.2 ± 5.2
0.300	157.2 ± 63.0	213.0 ± 7.3	195.0 ± 2.2
0.400	196.0 ± 5.5	213.0 ± 2.9	208 .0 ± 1.8
0.500	190.1 ± 9.5	245.2 ± 2.9	218.0 ± 2.4

A conventional gold electrode was selected as an exemplary representation of ideal electron transfer properties sought after in the sensing phase. Consequently, when ferrocene methanol was introduced to this system, a quasi-reversible reaction was observed. It is important to discuss the factors that contribute to the lack of full reversibility in this context. In a truly reversible system, the ΔEp (peak separation) would ideally remain constant or display minimal variation with increasing scan rate. However, in this case, the ΔEp exhibited an increase from 82 mV to 190 mV ($\Delta E_p \geq 57/n$ (mV)) as the scan rate escalated from 0.005 V/s to 0.5 V/s. The quasi-reversible nature of the reaction can be attributed to a combination of factors such as surface heterogeneity, kinetic limitations, or other influences that hinder the complete reversibility of the electrochemical process [14]. Additionally, the plot demonstrating the linear relationship between ip (peak current) versus $v^{1/2}$ (square root of the scan rate) signifies that the transport of ions to and from the electrode is predominantly governed by diffusion, as expected in a quasi-reversible system.

Each of the in-house developed SPCEs exhibited distinct electron transfer properties when exposed to ferrocene methanol, with the SPCE containing 10% AuS SPCE demonstrating the most reversible behaviour. The greater reversibility and reduced ΔEp (98 mV to 245 mV for 10% AuF SPCE versus 96 mV to 218 mV for 10% AuS SPCE) suggest that the platform incorporating 10% (w/w) gold microspheres possesses higher electronic transfer kinetics. It is important to consider the role of the iR drop in this context.

The iR drop, which accounts for the resistance associated with the electrode-electrolyte interface, can influence the observed electrochemical behaviour. A larger ΔEp indicates a higher iR drop, which can impede the electron transfer process and result in slower kinetics. Consequently, the SPCE with 10% (w/w) gold microflakes experienced a higher ΔEp, suggesting a larger iR drop and consequently slower electron transfer kinetics compared to the 10% AuS SPCE.

Moreover, the 10% AuS SPCE demonstrated the highest i_p values (peak current) and the lowest overvoltage among the in-house electrodes. These characteristics further support the superior electronic transfer properties of the 10% AuS SPCE, indicating its enhanced ability to facilitate efficient electron transfer with minimal overpotential.

The heterogeneous electron transfer (k_0) values were calculated as described in the experimental section of this work (4.1.11) and are given in Table 4.2. Differently from ordinary Nernstian one electron reaction, ΔEp for SPCEs are expected to be greater than 57 mV and k_0 to be lower than conventional gold electrodes [15]. 10% AuS SPCE and 10% AuF SPCE presented values 220-fold and 300-fold lower than the obtained for conventional gold, respectively. The decrease in reactivity of the surfaces its due the composition of the ink being only partially made of conductive carbon particle and smaller percentage of gold.

Table 4.2. Average heterogeneous electrons transfer rate (k_0) for conventional gold electrode, 10% AuS SPCE and 10% AuF SPCE. Average values and standard deviations were calculated from triplicate measurements (n=3).

Electrode	k_0 (cm s^{-1})
Conventional Gold Electrode	$(3.64 \pm 0.05) \times 10^{-2}$
10% AuS SPE	$(1.65 \pm 0.06) \times 10^{-4}$
10% AuF SPE	$(1.21 \pm 0.04) \times 10^{-4}$

Considering that the resistance to charge transfer (Rct) is inversely proportional to the heterogeneous electron transfer rate (k_0), it can be inferred that the 10% AuS SPCE exhibits lower resistance compared to the 10% AuS SPCE. This disparity in resistance can be attributed to a specific effect observed during the electrode drying process. It is proposed that the ink used in the 10% AuF SPCE partially floods and covers the flat gold microflakes, which in turn

hinders their electrochemical activity. Conversely, this phenomenon does not significantly affect the SPEs with gold microspheres. This is due to the fact that the gold microspheres are partially embedded within the ink while remaining exposed on the SPCE surface, resulting in a distinct distribution. Consequently, the 10% AuS SPEs exhibit a larger electrochemical surface area compared to the 10% AuF SPEs. This expanded surface area enables increased interaction with the analyte and promotes more efficient electron transfer during electrochemical reactions.

The validity of this theory is supported by the SEM image presented in Figure 4.3, which clearly demonstrates that gold nanoparticles with a flake structure possess a reduced extent of exposure for their electroactive surface area. The presence of a discernible "halo" in Figure 4.3 B, where SEM secondary electrons are emitted at a higher voltage, penetrating deeper into the surface, provides evidence that the carbon from the ink partially covers the flat gold microflakes. This phenomenon may contribute to variations in the electroactive surface area, potentially affecting the electron transfer process.

In contrast, such a phenomenon is not observed with the 10% AuS SPCE, as depicted in Figure 4.4. In this case, the distribution of the gold microspheres is characterized by approximately half of each sphere being embedded within the ink, while the remaining half is exposed on the SPCE surface. When comparing the different SPCE platforms, the superior reversibility of the redox probe, enhanced electron transfer, and higher current density observed in the 10% AuS SPCE can be attributed to the lower resistance encountered in its conducting path.

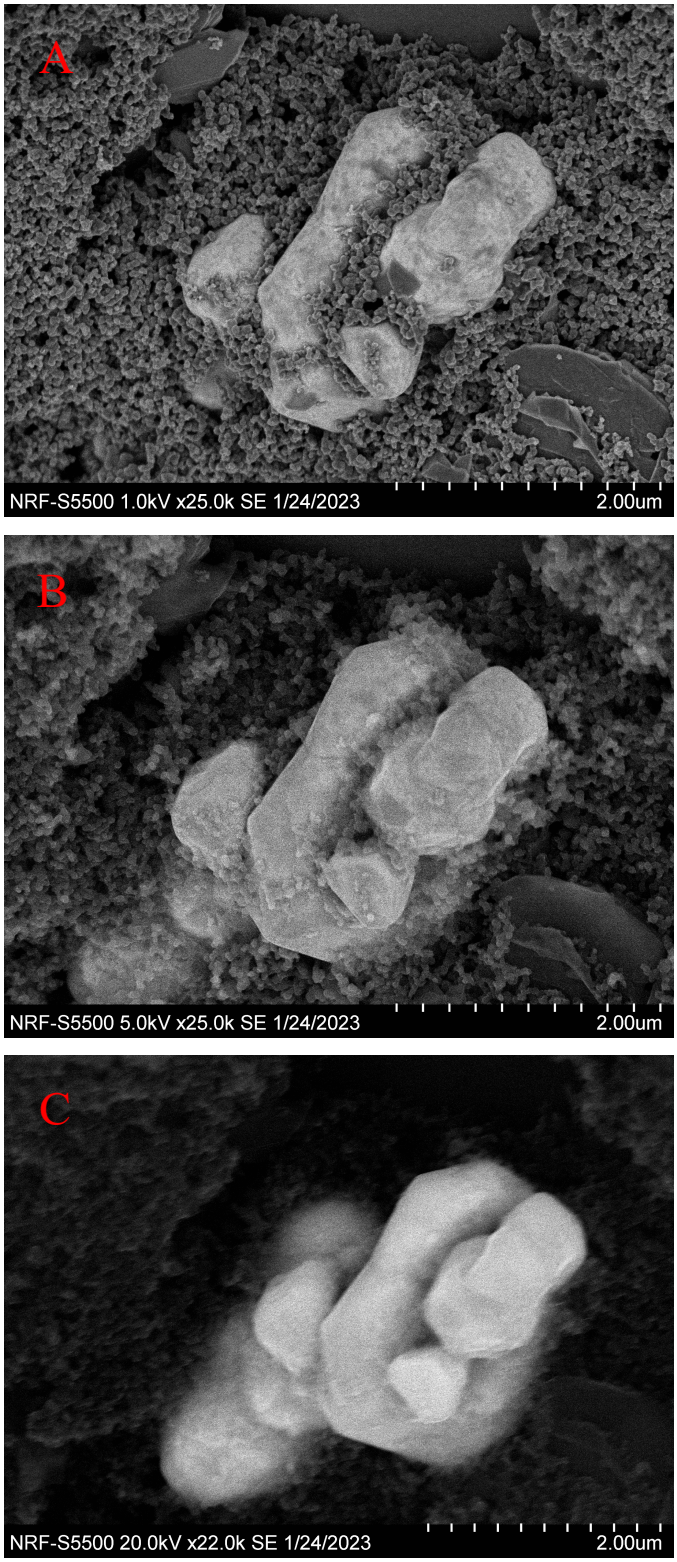


Figure 4.2. SEM images of a 10% AuF SPCE surface made with secondary electrons. Magnification and accelerating voltage used was of (a) 25 k, 1 kV (b), 25 k, 5 kV and (b) 22 k, 20 kV.

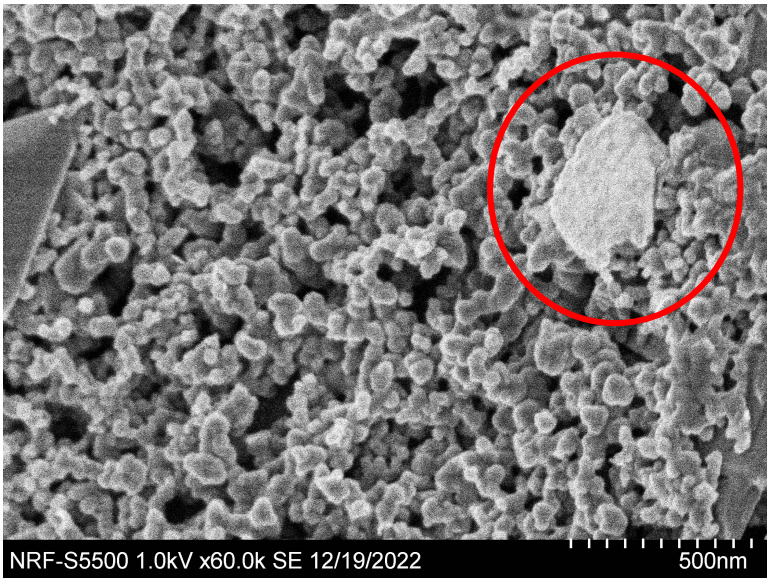


Figure 4.3. SEM image of a 10% AuS SPCE surface generated by secondary electrons. Magnification and accelerating voltage used was of (a) 60 k, 1 kV.The gold nanoparticle were highlighted for clarity.

SEM images were also utilized to assess the size and dispersion of particles on the surfaces of both 10% AuS SPCE and 10% AuF SPCE (Figure 4.5A and C, respectively). These images revealed a homogeneous distribution of gold nanoparticles on both surfaces, indicating a uniform arrangement. It is important to avoid agglomeration of microparticles since it leads to their transformation into larger particles, resulting in a reduction of the available surface area. Consequently, maintaining a good dispersion of the metal microparticles becomes essential.

In this regard, the proper dispersion of gold microparticles plays a significant role in enhancing the overall chemical activity and responsiveness of the gold sphere substrate. Specifically, when considering electrochemical reactions occurring at the surface of the gold microspheres, such as electron transfer processes or interactions with analytes, achieving a good dispersion becomes crucial. This ensures the efficient utilization of the entire surface area of the gold microspheres, promoting increased contact and interaction with reactants or species involved in the electrochemical reactions. As a result, this improved dispersion contributes to enhancing the efficiency and effectiveness of the electrochemical processes taking place on the gold sphere substrate.

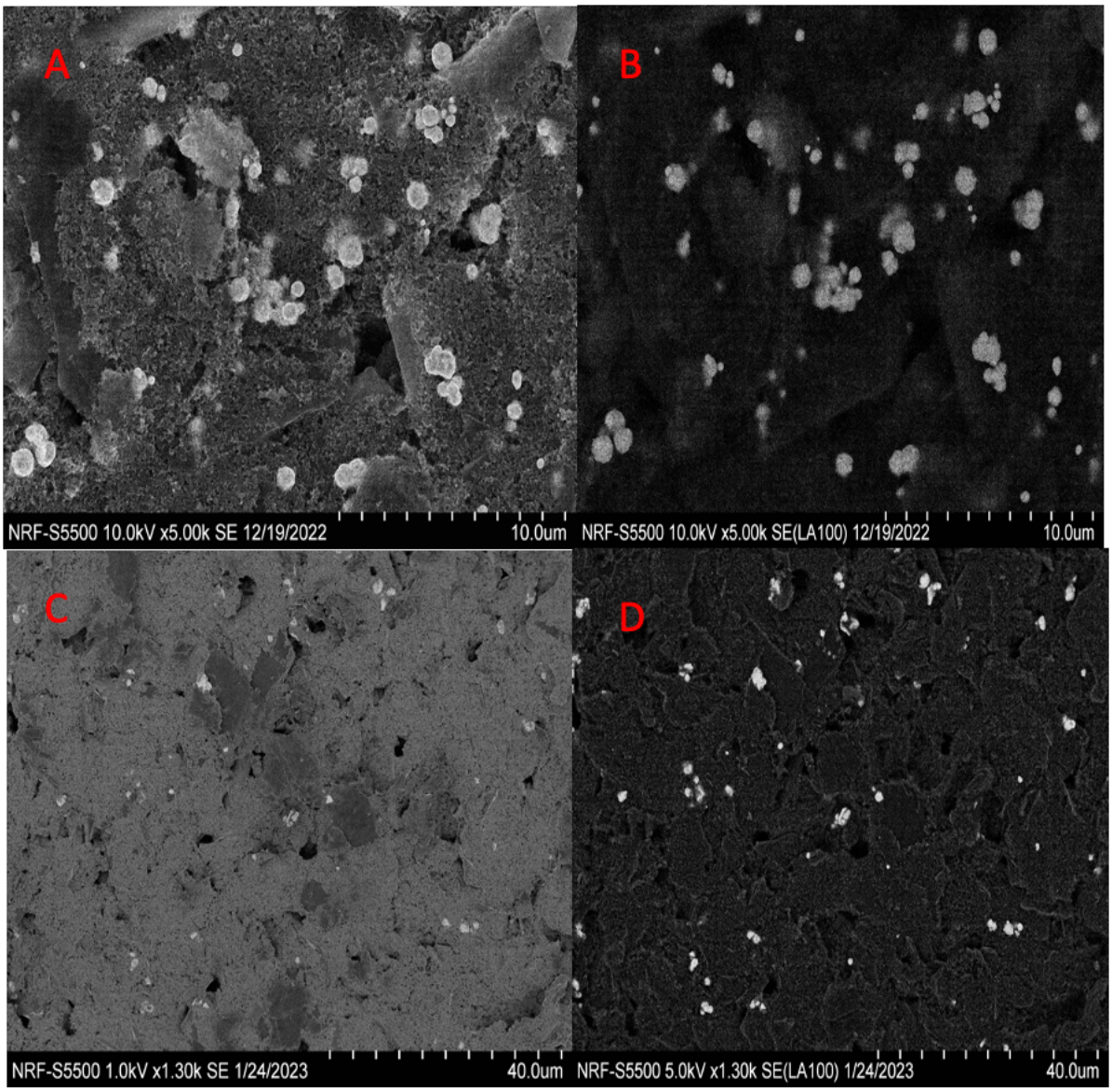


Figure 4.4. SEM images of 10% AuS SPCE surface made with magnification and accelerating voltage of 5 k and 10 kV using (A) secondary electrons (B) secondary electrons (LA1000) and SEM images of 10% AuF SPCE surface made with magnification and accelerating voltage used of (C)1.3 K, 1 kV using secondary electrons and (D) 1.3 k, 5 kV using SE (LA100).

4.2.2 Analytical Performance of the 10% AuS SPCE and 10% AuF SPCE

The analytical performance of the SPCEs with different shapes of gold nanostructures within its carbon ink were investigated to elucidate how the different nanostructured platforms affect the sensitivity of the biosensor.

The magnitude of the signal difference (Δi) between bare SPCEs and SPCEs functionalized with a fully complementary miRNA assay, utilizing either palladium nanocubes (PdNCBs) or

gold nanorods (AuNRDs) as labels, was rigorously assessed. This evaluation involved measuring the reduction behaviour of the platforms before and after the addition of 400 μM hydrogen peroxide in a 0.01 M PBS solution. For the electrodes labelled with PdNCBs, a potential of -0.375 V was applied, while a potential of -0.250 V was applied to the electrodes with AuNRDs labels.

The metallic labels were used to amplify the signal of the target miRNAs . As the concentration of miRNA target increases, the number of nanoparticle functionalised miRNA reporter-probe increases and a proportional increase of the reduction current of hydrogen peroxide is expected to occur.

Figure 4.6 shows the comparison of the current responses (Δi) of 10% AuS SPCE and 10% AuF SPCE functionalized electrode where the reporter-probe label is (A) palladium nanocubes and (B) gold nanorods. A fixed potential was used for the specific particles and the final analytical signal was evaluated after hydrogen peroxide injections.

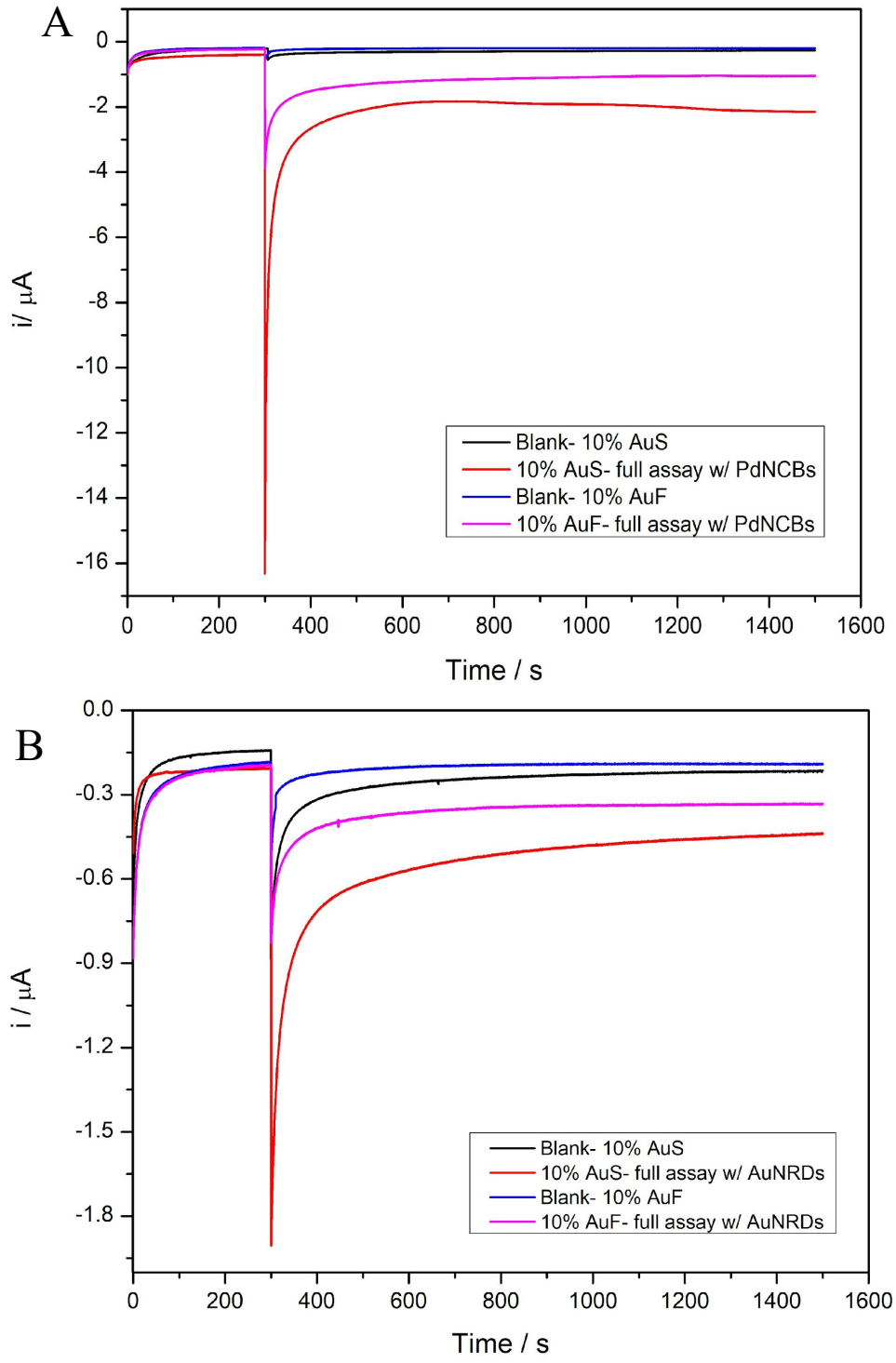


Figure 4.5. Amperometric i-t curves for 10% AuF and AuS SPCEs functionalised with (A) 10 µM miRNA capture-probe strands, 1 µM of miRNA target stands, and 1 µM miRNA reporter-probe strands labelled with palladium nanocubes at an applied potential of -0.375 V in 0.01 M PBS and (B) 10 µM miRNA capture-probe strands, 100 nM of miRNA target strands and 4.6 μM miRNA reporter-probe strands labelled with AuNRDs at an applied potential of -0.250 V in 0.01 M PBS. The difference in current before and after the addition of 400 µM hydrogen peroxide is displayed in the graphs. Measurements were conducted in triplicate.

Table 4.3. Changes in the current before and after the injection of 400 µM hydrogen peroxide in **10% AuS SPCE** and **10% AuF SPCE** functionalised with a full sandwich assay and **PdNCBs**. Average values and standard deviations were calculated from triplicate measurements (n=3).

10% AuF SPCE	i / A Full Assay w/ PdNCBs	i / A Bare SPCE	Δi/ A (final – initial)	10% AuS SPCE	i / A Full Assay w/ PdNCBs	i / A Bare SPCE	Δi/ A (final – initial)
SPE 1	-8.23×10^{-7}	-6.56×10^{-8}	-7.57×10^{-7}	SPE 4	-1.76×10^{-6}	-7.56×10^{-8}	-1.68×10^{-6}
SPE 2	-8.92×10^{-7}	-5.95×10^{-8}	-8.33×10^{-7}	SPE 5	-1.52×10^{-6}	-7.47×10^{-8}	-1.45×10^{-6}
SPE 3	-8.76×10^{-7}	-5.67×10^{-8}	-8.19×10^{-7}	SPE 6	-1.40×10^{-6}	-7.91×10^{-8}	-1.32×10^{-6}
Mean	-8.64×10^{-7}	-6.06×10^{-8}	-8.03×10^{-7}	Mean	-1.56×10^{-6}	-7.65×10^{-8}	-1.48×10^{-6}
STDV	0.36	0.45	0.40	STDV	0.18	0.23	0.18

Table 4.4. Changes in the current before and after the injection of 400 µM hydrogen peroxide in **10% AuS SPCE** and **10% AuF SPCE** functionalised with a full sandwich assay and **AuNRDs.** Average values and standard deviations were calculated from triplicate measurements (n=3).

10% AuF SPCE	i / A Full Assay w/ AuNRDs	i / A Bare SPCE	Δi/ A (final – initial)	10% AuS SPCE	i / A Full Assay w/ AuNRDs	i / A Bare SPCE	Δi/ A (final – initial)
SPE 7	-1.29×10^{-7}	-6.63×10^{-8}	-6.27×10^{-8}	SPE10	-2.33×10^{-7}	-7.60×10^{-8}	-1.57×10^{-7}
SPE 8	-1.17×10^{-7}	-6.24×10^{-8}	-4.96×10^{-8}	SPE11	-1.98×10^{-7}	-8.05×10^{-8}	-1.18×10^{-7}
SPE 9	-1.12×10^{-7}	-6.16×10^{-8}	-5.04×10^{-8}	SPE12	-2.12×10^{-7}	-7.86×10^{-8}	-1.33×10^{-7}
Mean	-1.19×10^{-7}	-6.34×10^{-8}	-5.59×10^{-8}	Mean	-2.14×10^{-7}	-7.84×10^{-8}	-1.36×10^{-7}
STDV	0.09	0.25	0.06	STDV	0.18	0.23	0.20

The electrocatalytic properties of nanoparticles can be finely tuned by the changes in surface atoms and/or surface structures [16]. Hence, the different type and shapes of the labels were also explored at this work to enhance the performance of the sensor. It was observed that the

analytical signal of 10% AuS SPCE platform hybridised with full miRNA assay labelled with PdNCBs was 10-fold higher than that found the same platform where the label was AuNRD. For 10% AuF SPCE, the full assay labelled with PdNCBs presented an enhancement of signal of approximately14-fold when compared to the same platform labelled with AuNRDs. Overall, 10% AuS SPCE platform presented the highest sensitivity in terms of current density while 10% AuF SPCE exhibited the lowest values. The 10% AuS also showed a greater signal to noise (S/N) ratio. This result correlates with the voltammetric behaviour.

It is expected that palladium nanocubes would be more electrocatalytic than gold nanorods as they have major (1 0 0) exposed facets which can make them more reactive [17]. This phenomenon occurs as a result of the high index surface structure. So, in summary, the excellent response of the 10% AuS SPCE platforms functionalised with PdNCBs is attributed to the synergetic effects of increased surface area for biomolecules adsorption (effect generated by particles onto the platform) and enhancement of metal catalytic activity.

Regarding the background signal of 10% AuS SPCE and 10% AuF SPCE, the current intensities are around 8 x 10^{-8}A which is not a significant value in comparison with the analytical signals obtained. Thus, the optimised ink recipe forms a surface capable of distinguishing between the signal of miRNA target and bare gold SPCE electrodes.

4.2.3 Enhancement of the analytical performance of AuS SPCEs

The in-house 10% AuS SPCE developed has the best charge transfer properties towards ferrocene methanol when compared with 10% AuF SPCE platform. However, its behaviour (i.e., k_0, R_{ct}) are far from the ideal. Two parameters can be optimised in order to enhance this exchange of electrons, the conducting path and the carbon composition. As graphite has already excellent conductivity properties, a higher percentage of gold microspheres (20% in weight/weight) mixed to the WE ink was studied.

Figure 4.7 shows the comparison of the chronoamperometric response of 10% AuS SPCEs and 20% AuS SPCEs functionalised with full miRNA assay labelled with (A) PdNCBs and (B) AuNRDs before and after the addition of 400 µM hydrogen peroxide. Table 4.5 and 4.6 shows the difference in current density data obtained from Figure 4.7.

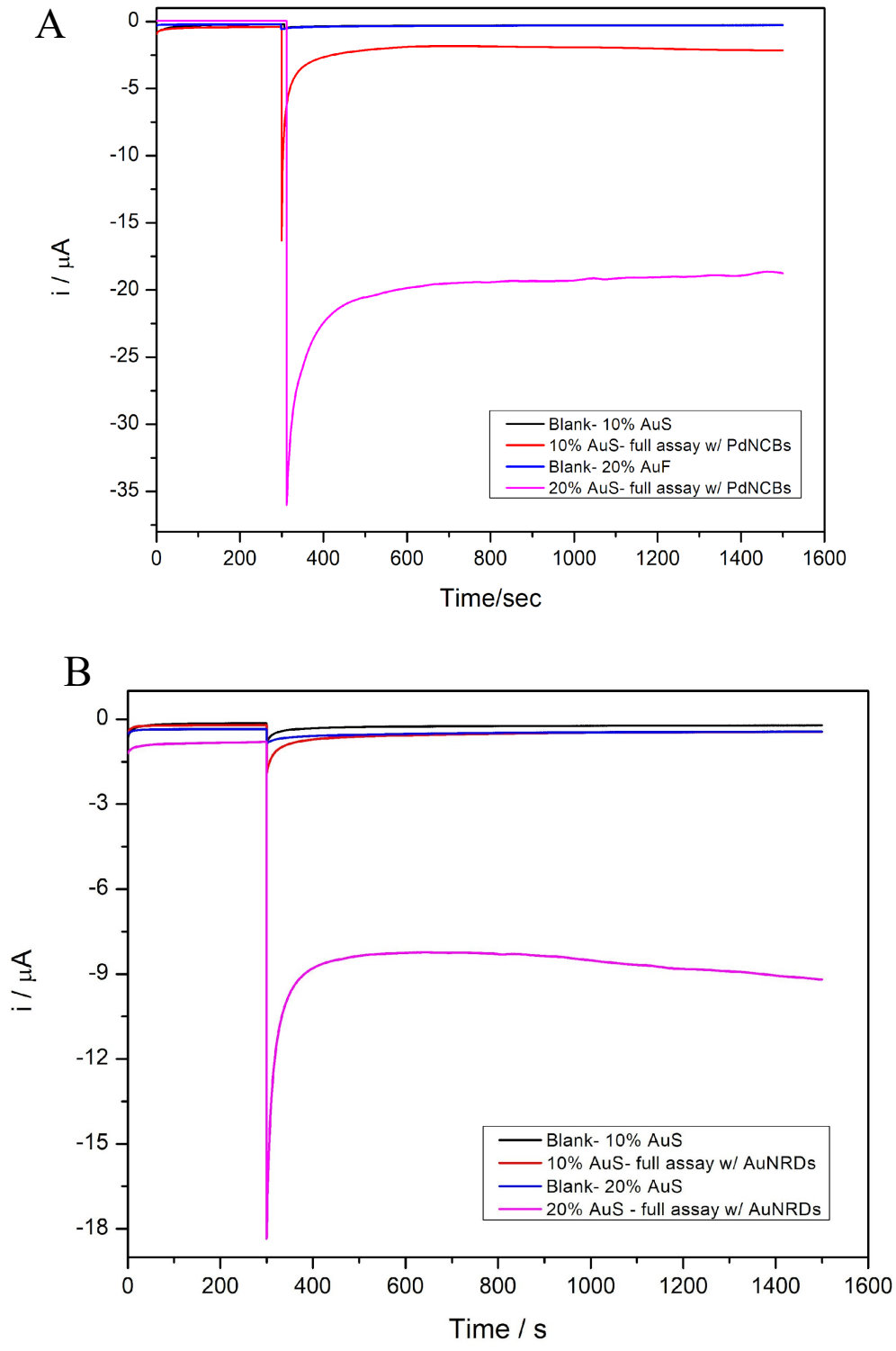


Figure 4.6. Representative amperometric i-t curves for 10% AuS and 20% AuS SPCEs functionalised with (A)10 µM miRNA capture-probe strands, 1 µM of miRNA target strands, and 1 µM miRNA reporter-probe strands labelled with PdNCBs at -0.375 V in 1 mM PBS and (B) 10 µM miRNA capture-probe strands, 100 nM of miRNA target strands and 4.6 µM miRNA reporter-probe strands labelled

with gold nanorods at -0.25 V in 0.01M PBS. The difference in current before and after the addition of 400 μM hydrogen peroxide is displayed. Measurements were conducted in triplicate.

Table 4.5. Changes in the current before and after the injection of hydrogen peroxide of **10% AuS SPCE** and **20% AuS SPCE** with full sandwich assay functionalised with **PdNCBs**. Average values and standard deviations were calculated from triplicate measurements.

10% AuS SPCE	i / A Full Assay w/ PdNCBs	i / A Bare SPCE	Δi/ A (final – initial)	20% AuS SPCE	i / A Full Assay w/ PdNCBs	i / A Bare SPCE	Δi/ A (final – initial)
SPE13	-1.76×10^{-6}	-6.56×10^{-8}	-1.69×10^{-6}	SPE16	-18.21×10^{-6}	-9.93×10^{-8}	-18.21×10^{-6}
SPE14	-1.52×10^{-6}	-5.95×10^{-8}	-1.46×10^{-6}	SPE17	-18.33×10^{-6}	-1.12×10^{-7}	-18.22×10^{-6}
SPE15	-1.40×10^{-6}	-5.67×10^{-8}	-1.34×10^{-6}	SPE18	-18.80×10^{-6}	-9.89×10^{-8}	-18.70×10^{-6}
Mean	-1.56×10^{-6}	-6.06×10^{-8}	-1.50×10^{-6}	Mean	-18.40×10^{-6}	-1.03×10^{-7}	-18.37×10^{-6}
STDV	0.18	0.45	0.18	STDV	0.31	0.07	0.28

Table 4.6. Changes in the current before and after the injection of hydrogen peroxide of **10% AuS SPCE** and **20% AuS SPCE** with full sandwich assay functionalised with **AuNRDs**. Average values and standard deviations were calculated from triplicate measurements.

10% AuS SPCE	i / A Full Assay w/ AuNRDs	i / A Bare SPCE	Δi/ A (final – initial)	20% AuS SPCE	i / A Full Assay w/ AuNRDs	i / A Bare SPCE	Δi / A (final – initial)
SPE 19	-2.33×10^{-7}	-7.33×10^{-8}	-1.60×10^{-7}	SPE22	-8.17×10^{-6}	-1.10×10^{-7}	-8.06×10^{-6}
SPE 20	-1.98×10^{-7}	-6.74×10^{-8}	-1.31×10^{-7}	SPE23	-7.95×10^{-6}	-9.96×10^{-8}	-7.85×10^{-6}
SPE 21	-2.12×10^{-7}	-6.96×10^{-8}	-1.42×10^{-7}	SPE24	-8.39×10^{-6}	-9.89×10^{-8}	-8.29×10^{-6}
Mean	-2.14×10^{-7}	-7.01×10^{-8}	-1.44×10^{-7}	Mean	-8.17×10^{-6}	-1.03×10^{-7}	-8.06×10^{-6}
STDV	0.18	0.30	0.15	STDV	0.22	0.06	0.20

The response of the biosensor was produced by the reduction of hydrogen peroxide by the nanoparticles confined in the electrode surface via hybridization process with miRNA target. The measurements conducted on 10% AuS SPCEs resulted in a delta current density (Δi) of -0.144 ± 0.015 μA when labelled with AuNRDs, whereas it was -1.50 x ± 0.18 μA when labelled with PdNCBs. For 20% AuS SPCEs labelled with AuNRDs, the delta current density (Δi) was found to be -8.08 ± 0.21 μA, whereas it was -18 ± 0.03 μA when the platform was functionalized with PdNCBs.

As expected, the 20% AuS SPCE platform outperformed the 10% AuS SPCE, providing significant signal amplification with a 56-fold enhancement for the full assay when AuNRDs labels are used and a 12-fold enhancement for the sandwich assay using PdNCBs. The remarkable difference in sensitivity can be attributed to the substantial electrocatalytic surface-to-volume ratio achieved by incorporating gold nanoparticles onto the SPCE surface, summed to the catalytic effects of the different nanoparticles. This successful combination led to a satisfactory signal enhancement when an extra 10% of material was added to the SPE matrix.

To ensure the reliability of the findings, all experiments were repeated in triplicate, and the obtained reduction currents (specific to each system) consistently displayed minimal deviations, within ≤ 5%. These results demonstrate the high reproducibility of the platforms, instilling confidence in their potential for practical use in biosensing applications.

Considering that the ultimate goal is to create a point-of-care, close to the patient device, it becomes essential to strike a balance between development costs and sensitivity. These results show promise that a multiplexed electrochemical biosensor for detecting miRNAs associated with neurological diseases could be successfully fabricated using the 20% AuS SPCE.

4.2.4 Optimisation of the studied conditions

4.2.4.1 Studies of the optimal potential for hydrogen peroxide reduction

To create point of care biosensors with a greater degree of accuracy it is imperative to design a platform capable of detecting multi-analytes. As specified in the previous sections, the amplification of miRNA target signal occurs through the reduction of hydrogen peroxide by the different nanoparticles. Considering that each nanoparticle label is linked to a miRNA

target, the differentiation between biomarkers relies on the ability of the nanoparticle to electrocatalyse the reduction of hydrogen peroxide at distinct potentials if the multianalyte assay was to be implemented on a *single* sensor surface, i.e., the different capture-probe miRNA deposited on a single sensor. The need for different reduction potentials for peroxide would not be needed if the sensors for each miRNA type were physically separated within a microfluidic device.

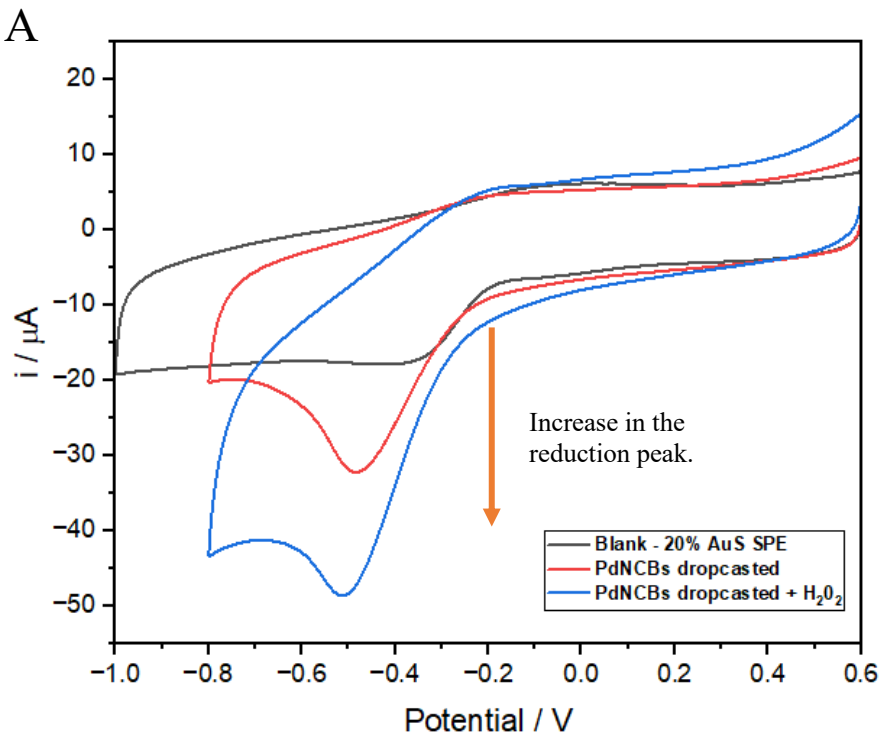
An optimum potential for hydrogen peroxide reduction was investigated using two techniques, cyclic voltammetry and amperometry. The surface of 20% AuS SPCEs was saturated with either PdNCBs, AuNRDs or PtNPs through drop-casting, as detailed in Section 4.1.6. CVs were obtained before and after the injection of 400 μM hydrogen peroxide in 0.01 M degassed PBS solution.

Through evaluation of the label's redox peak shapes in a blank PBS solution, one can see a well-developed cathodic voltammetric peak, suggesting that the mechanism of the hydrogen peroxide reduction reaction process (HPRR) is likely initiated through the reduction of oxygen traces adsorbed on the surface of the nanoparticles [18]. Specifically, the assessment of the PdNCBs peaks at the SPCE surface (Figure 4.8A), presented a composition of two overlapping peaks positioned at about −0.200 V and −0.375 V. Overlapping of two distinct peaks also occurs when AuNRDs and PtNPs were analysed, suggesting that the reduction of oxygen at the nanoparticles' surface may proceed as a two-step process of adsorbed species. The proposed mechanism begins with adsorbed oxygen (O_2 (ads)) and a subsequent electrochemical formation of adsorbed hydrogen peroxide which will be reduced to adsorbed hydroxide ions [19][20].

While these observations provide valuable evidence for the proposed reaction mechanism, it is important to acknowledge that electrochemical reactions can be complex, and other factors may also influence the observed behaviour. To gain a more comprehensive understanding of the adsorbed species and their involvement in the reduction process, it is strongly advised to conduct further investigations using complementary techniques, such as *in situ* spectroscopy or surface analysis. These advanced techniques can offer deeper insights into the interactions occurring at the nanoparticles' surface and shed light on any intermediate species involved in the reaction. Moreover, exploring different experimental conditions, such as varying pH levels or electrolyte compositions, will be instrumental in unravelling the intricacies of the reaction.

By systematically varying these parameters, we can uncover how the reaction kinetics, electron transfer rates, and adsorption processes are influenced, ultimately contributing to a more comprehensive understanding of the overall mechanism.

Figure 4.8 shows the reduction of hydrogen peroxide by the three studied labels. The reduction of the hydrogen peroxide by the PdNCBs started at -0.12V and achieved a maximum value at -0.5V. The reduction of hydrogen peroxide by AuNRDs started at -0.25V and presented a maximum current at an E_p value of -0.45 V. Finally, the reduction of the hydrogen peroxide by PtNPs presented a starting point at -0.15 V and a maximum reduction current at -0.57 V.



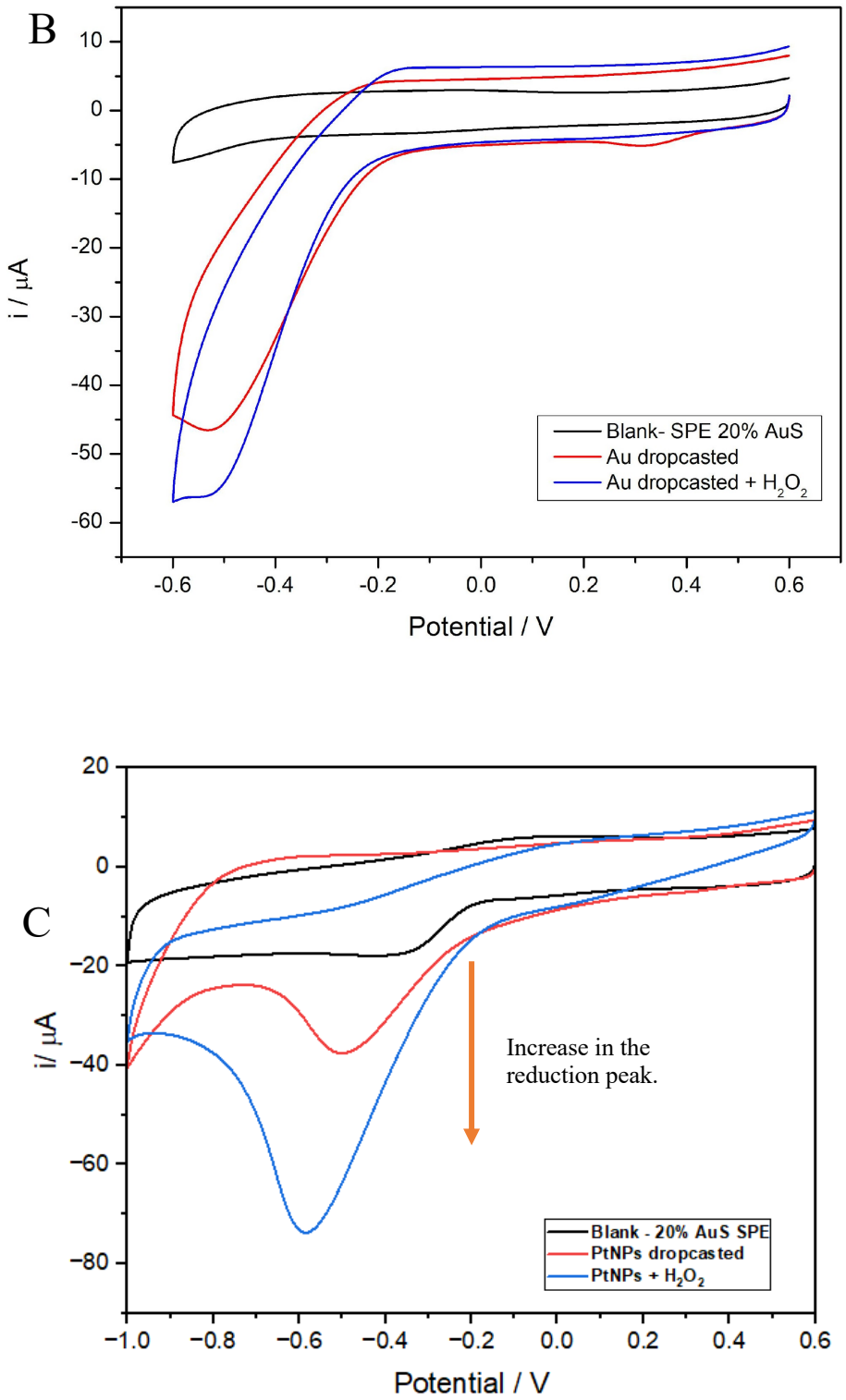
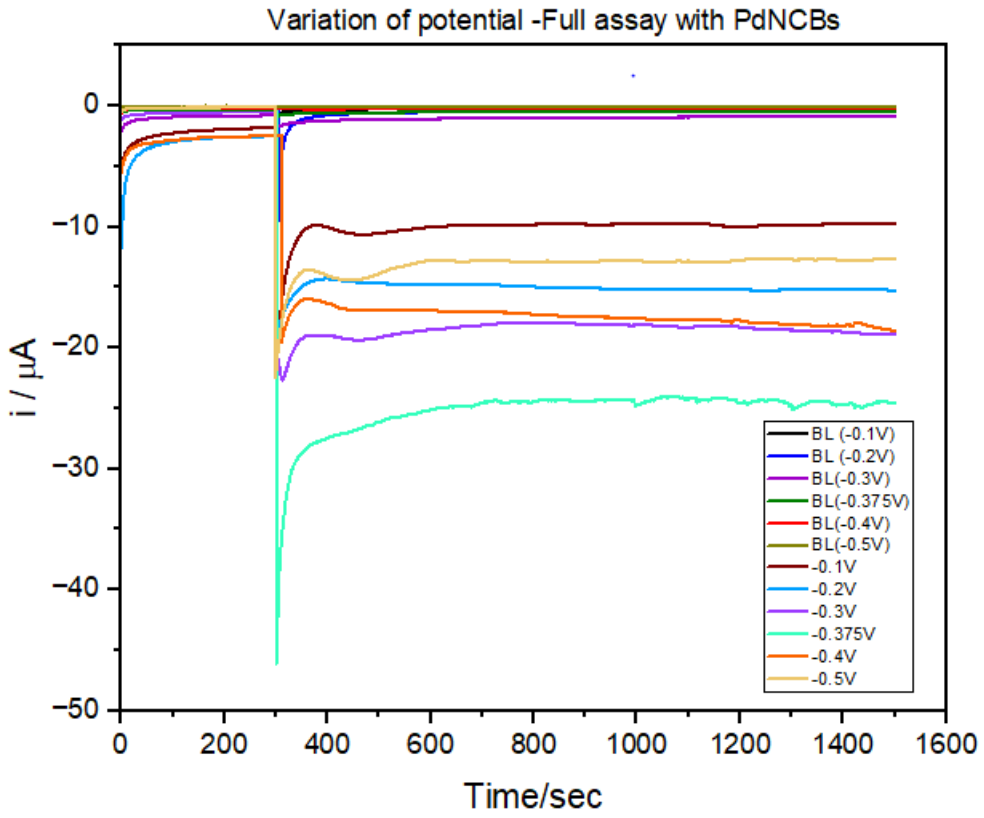


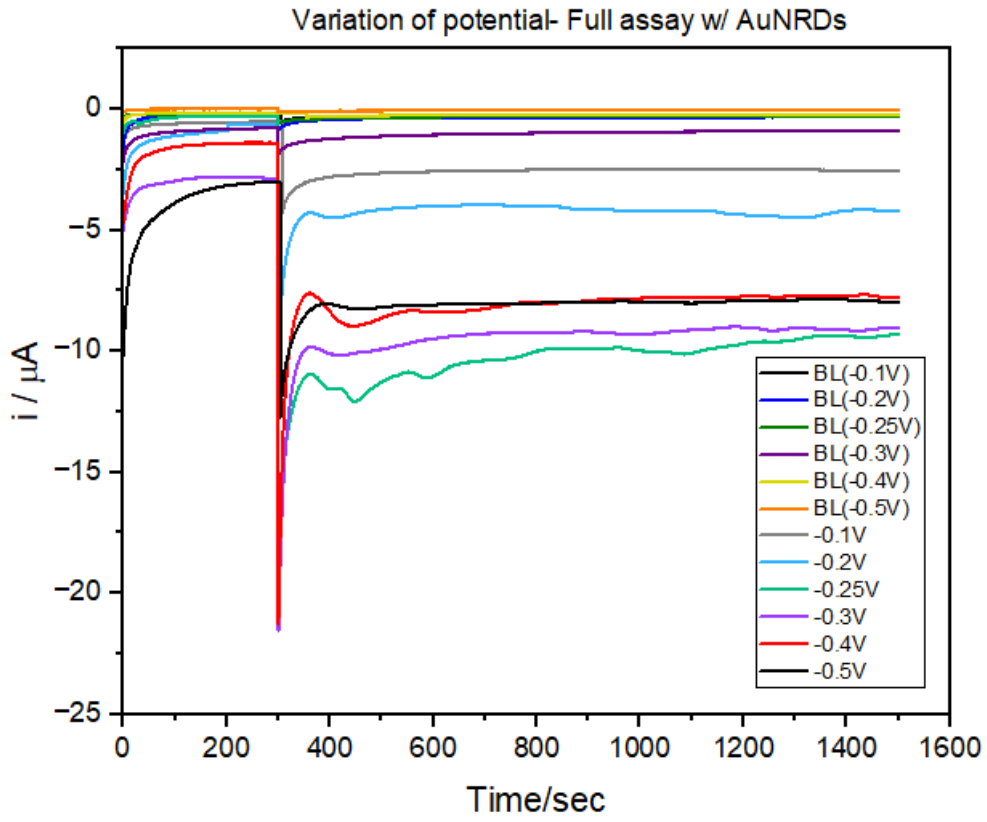
Figure 4.7. Cyclic voltammograms of a 20% AuS SPCE without any modification over the surface (black curve). Cyclic voltammograms of a 20% AuS SPCE with 2 µL of (a) palladium nanocubes, (b) gold nanorods and (c) platinum nanoparticles drop-casted on its surface. Electrolyte: 0.01 M of PBS with 400 μM of hydrogen peroxide. Scan rate: 0.05 V/s. Measurements were conducted in triplicate.

Numerous definitions for what is considered the onset of a reduction potential can be found in the literature. Some authors indicate that the reduction occurs when the current density is bigger than 10 μA/cm^2, others indicate that the current itself should be 10 μA. However, the applied experimental conditions will produce variations to this value. To analyse the window of potentials previously defined by CVs , i.e. from -0.1 to -0.5, SPCEs functionalised with the full miRNA assay and the nanoparticle labels were placed in a 3-electrode cell. Measurements using a technique with greater sensitivity, as amperometric i-t curves, was produced before and after addition of 400 μM hydrogen peroxide in 0.01 M PBS.

A



B



C

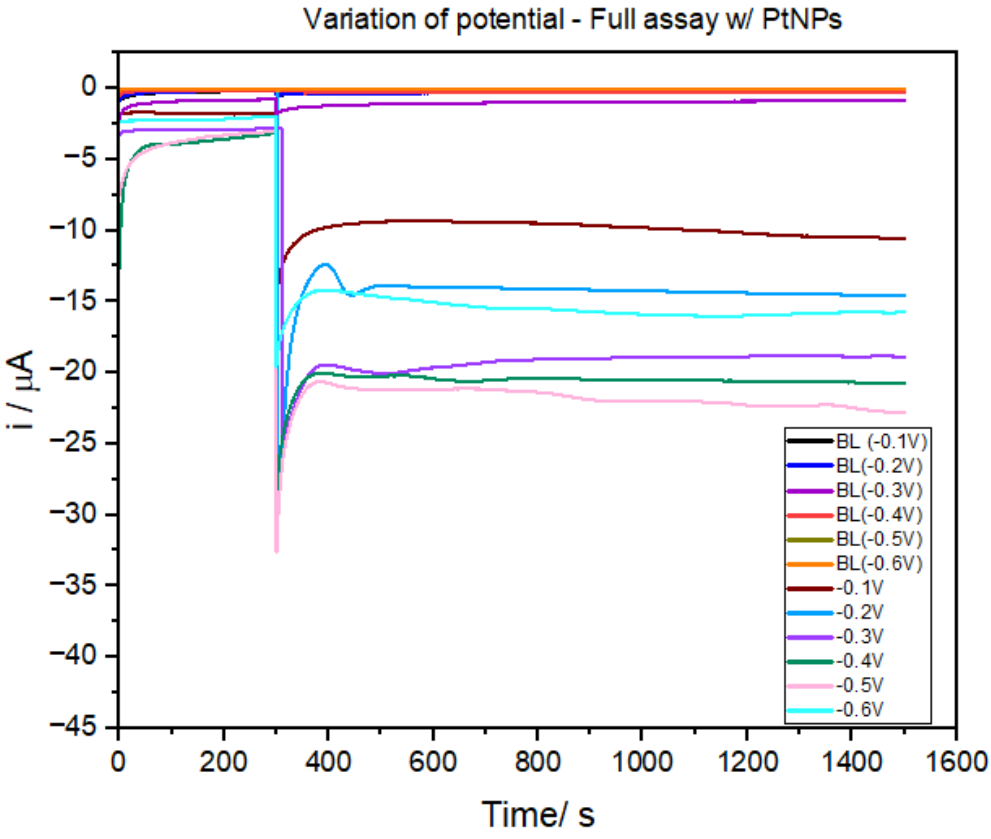


Figure 4.8. Amperometric i-t curves of 20% AuS SPCEs functionalised with (A) 10 µM miRNA capture-probe strands, 1 µM of miRNA target stands and 1 µM miRNA reporter-probe strands labelled with PdNCBs ; (B) 10 µM miRNA capture-probe strands, 100 nM of miRNA target strands, and 4.6

µM miRNA reporter-probe strands labelled with AuNRDs and (C) 10 µM miRNA capture-probe strands, 1 µM of miRNA target stands and 1 µM miRNA reporter-probe strands labelled with PtNPs (n=3). The studied potential window ranged from -0.1 to -0.5 V in 0.01 M PBS. The difference in current before and after the addition of 400 µM hydrogen peroxide is displayed in the graphs.

Table 4.7. Summary of the changes in the current before and after the injection of hydrogen peroxide in a blank 20% AuS SPCE and in 20% AuS SPCE functionalised with a full sandwich assay and PdNCBs; AuNRDs or PtNPs at different applied potentials. Average and standard deviations were calculated from triplicate measurements.

E/V	Δi / µA Full Assay w/ PdNCBs	Δi / µA Full Assay w/ AuNRDs	Δi /µ A Full Assay w/ PtNPs	Δi /µ A Bare 20% AuS SPCE	Δi / µA (full assay w/ Pd– blank)	Δi / µA (full assay w/ Au – blank)	Δi / µA (full assay w/ Pt – blank)
-0.10	-7.95±0.15	-2.03 ± 0.18	-8.82 ± 0.34	-0.07 ± 0.01	-7.87 ± 0.13	-1.94 ± 0.22	-8.75 ± 0.46
-0.20	-15.30±0.47	-3.16 ± 0.23	-14.43± 0.23	-0.10 ± 0.01	-15.23± 0.65	-3.07 ± 0.18	-14.32 ± 0.27
-0.25	---	-8.39 ± 0.22	---	-0.09 ± 0.001	---	-8.29 ± 0.30	---
-0.30	-18.31±0.42	-6.42 ± 0.31	-16.22± 0.19	-0.08 ± 0.01	-18.22± 0.58	-6.99 ± 0.33	-16.12 ± 0.26
-0.37	-24.52±0.25	---	---	-0.06 ± 0.03	-24.44± 0.34	---	---
-0.40	-16.22±0.46	-6.18 ± 0.25	-17.90± 0.28	-0.06 ± 0.03	-16.21± 0.57	-5.73 ± 0.26	-17.82 ± 0.38
-0.50	-12.54±0.55	-4.96± 0.21	-19.51± 0.11	-0.04 ± 0.02	-12.40± 0.77	-4.88 ± 0.29	-19.42 ± 0.15
-0.60	---	---	-13.80± 0.33	-0.04 ± 0.01	---	---	-13.72 ± 0.46

Figure 4.9 shows that the efficiency of the electrocatalytic current increases as the applied potential is made more negative (shifted in the anodic direction) with a slightly decrease after achieving a maximum, specific potential (E_p). Hence, the E_p when AuNRDs, PdNCBs and PtNPs was used as labels was -0.25 V, -0.375V and -0.5V, respectively.

It is valid to note that, in this measurement (i.e. amperometric i-t curves), nanoparticles are brought to the SPCE surface via miRNA reporter-probe functionalization instead of being deposited onto SPCE surface (i.e. CV measurements). Direct deposition might lead to a different distribution and packing of the nanoparticles on the electrode surface compared to the

functionalization process used in the assay. The specific arrangement of the labels can influence the electrochemical reaction kinetics [21] which may result in slight shift in the observed onset potential between the two techniques.

4.2.5 Characterization of Metal nanomaterials

The electrocatalytic activity of noble nanoparticles towards the reduction of hydrogen peroxide can be enhanced through the modulation of their specific sizes and shapes. According to the literature, gold nanoparticles with approximately 50 nm in length and rod shapes acts not only as a satisfactory electrocatalyst agent for peroxides but also have optical properties that can be explored throughout other techniques, such as ECL [22]. The optical properties, tuneable surface chemistry, and compatibility with biomolecules (DNA, miRNA) give greater designs possibilities for the development of multiplexed sensing technologies.

It is worth mentioning that the gold nanoparticles (AuNRDs) were procured from nanoComposix. The morphological validation the nanoparticles was thoroughly investigated using various characterization techniques, including Transmission Electron Microscopy (TEM), Dynamic Light Scattering (DLS), and zeta potential measurements. These rigorous assessments ensured that the nanoparticles possessed the desired size, shape, and stability required for their successful implementation in the electrochemical sensing platform.

4.2.5.1 Morphology of AuNRDs: Correlation between TEM, DLS and zeta potential

Figure 4.10 (A) displays a Bright-field Scanning Transmission Electron Microscopy (TEM) image of the gold nanorod labels. This TEM image reveals clear lattice fringes, confirming the single crystalline nature of the nanorods. In the Bright-field TEM mode, the image formation relies on transmitted electrons, which interact differently with regions of varying electron densities in the crystal lattice, resulting in distinguishable brighter or darker areas. Consequently, this mode allowed for the identification of distinct lattice fringes in the gold nanorods. The presence of regular and repeating atomic arrangements (lattice fringes) in the image is a characteristic feature of crystalline materials. Therefore, as anticipated, the analysed nanoparticles displayed a uniform rod-like shape, with an average size of approximately 50 nm, corroborating their single crystalline nature [23].

The population analysis for the nanorods, i.e., DLS measurements was also performed. A single, monodisperse population of 46.6 ± 2.6 nm was observed, confirming TEM size analyses and indicating no significant aggregation. The charge of the particles was also measured by zeta potential and presented a value of -55.5 ± 3.0 mV. All parameters were in agreement with the certificate of analysis provide by nanoComposix.

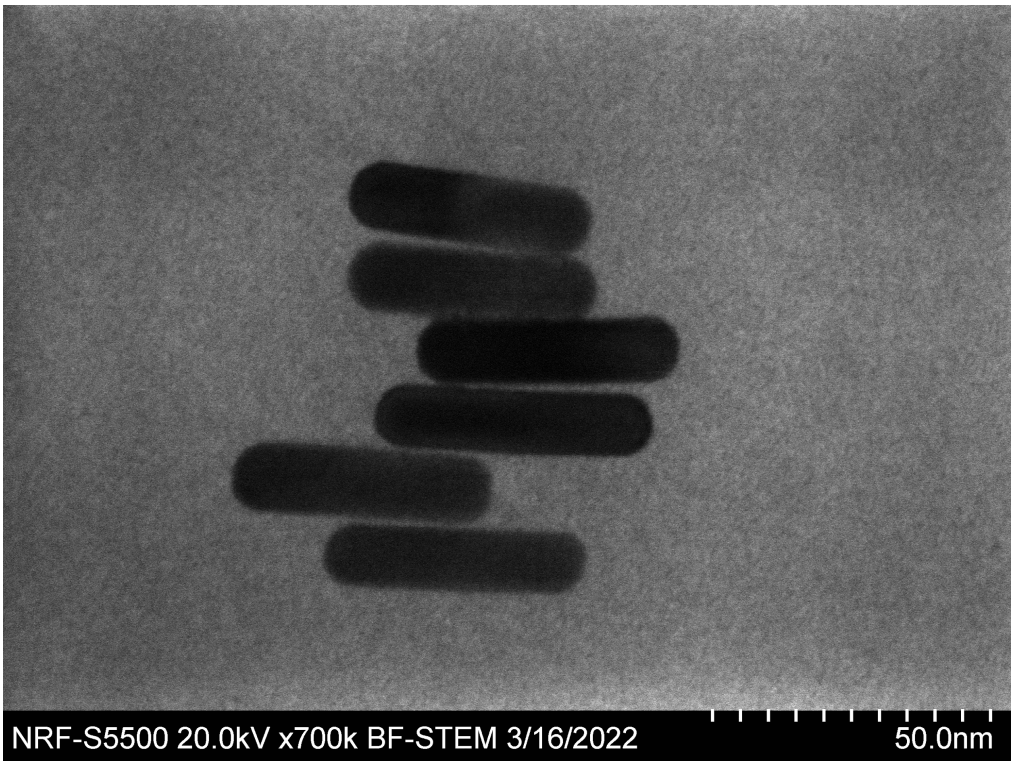


Figure 4.9. TEM image of AuNRDs in citrate. Magnification and accelerating voltage used was 700k and 20kV, respectively.

4.2.6 Fabrication and Characterization of Pd Nanocubes labels

The methodology used to synthetise palladium nanocubes is similar to the one reported by Niu *et al.* [11]. As detailed in section 4.1.2., through one step reduction, 22 nm palladium nanocubes were formed. Cetyltrimethylammonium bromide (CTAB), dihydrogentetrachloropalladate(II) (H_2PdCl_4), and ascorbic acid (AA) was further used as growth solutions. However, the biggest difference encountered at this procedure relies in the usage of a higher reaction temperature (95 °C) and a different growing time. Variations in these parameters are expected to generate an optimum (electrocatalytic) size for palladium particles, such as 50 nm, besides the specific cubic shapes. Size distribution is another parameter tuned by the modulation of these reaction conditions.

4.2.6.1 SEM of PdNCBs

The morphology of the as-synthesized PdNCBs were assessed through scanning electron microscopy (SEM). Figure 4.11 demonstrates the successful formation of cubic palladium nanocrystals. Through the secondary electron emissions, the structure of the surface could be easily evaluated. The PdNCBs presented approximately 50 nm in size and a uniform surface distribution with no signs of aggregation. In addition, the particles presented sharp edges and corners and well-defined and smooth faces. This result agrees with previous reports for palladium nanocubes [24] [25].

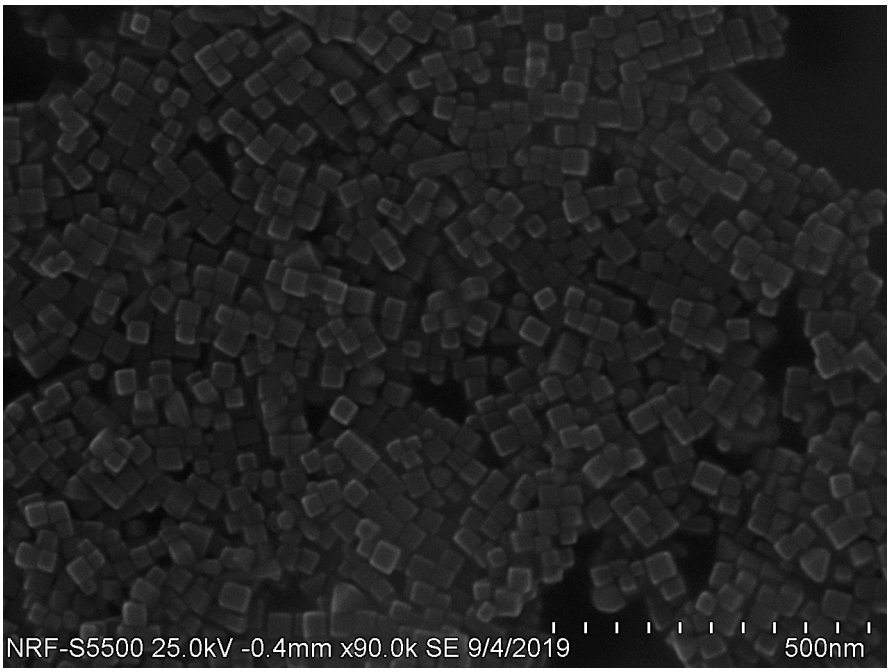


Figure 4.10. SEM image made with secondary electrons. Magnification of 90 k was used. Accelerating voltage of 25 kV.

The edge length of the PdNCBs was confirmed using a Malvern Zetasizer Nano Zs and the DLS response received was 44.0 ± 4.0 nm. The charge of the particles was also measured with zeta potential given a value of 38.6 ± 5.0 mV.

The observed results align with the Ostwald ripening theory [26] and previous experimental investigations [27][28]. By controlling the reaction time and increasing the reaction temperature, it was expected that the particle size would increase while leading to a narrower size distribution. The obtained SEM and DLS data provided substantial evidence supporting this theory, confirming the successful control of particle size and distribution.

4.2.6.2 XRD of Palladium nanocubes

The structure of the as-obtained Pd nanocubes was also characterized by X-ray diffraction (XRD). Figure 4.12 illustrate the XRD pattern for the 50 nm Pd nanocubes. The diffraction peaks can be observed at angles of 40.0, 46.5, and 67.9 assigned to the (111), (200) and (220) planes of Pd, respectively. In accordance with the JCPDS card (File No. 46-1043) these peaks represent a face-centred cubic structure (fcc) of bulk Pd. An average diameter was calculated from the line broadening of (111) reflection and the Sherrer's formula. Nanoparticle size of approximately 48.9 nm was obtained, which is consistent with the SEM and DLS results.

The intensity ratio of (111) to (200) peak was evaluated and compared to the standard value calculated from JCPDS data. A negligible decrease from 2.38 to 2.05 was achieved, which indicates that reflection of (100) planes dominate in Pd nanocubes [29].

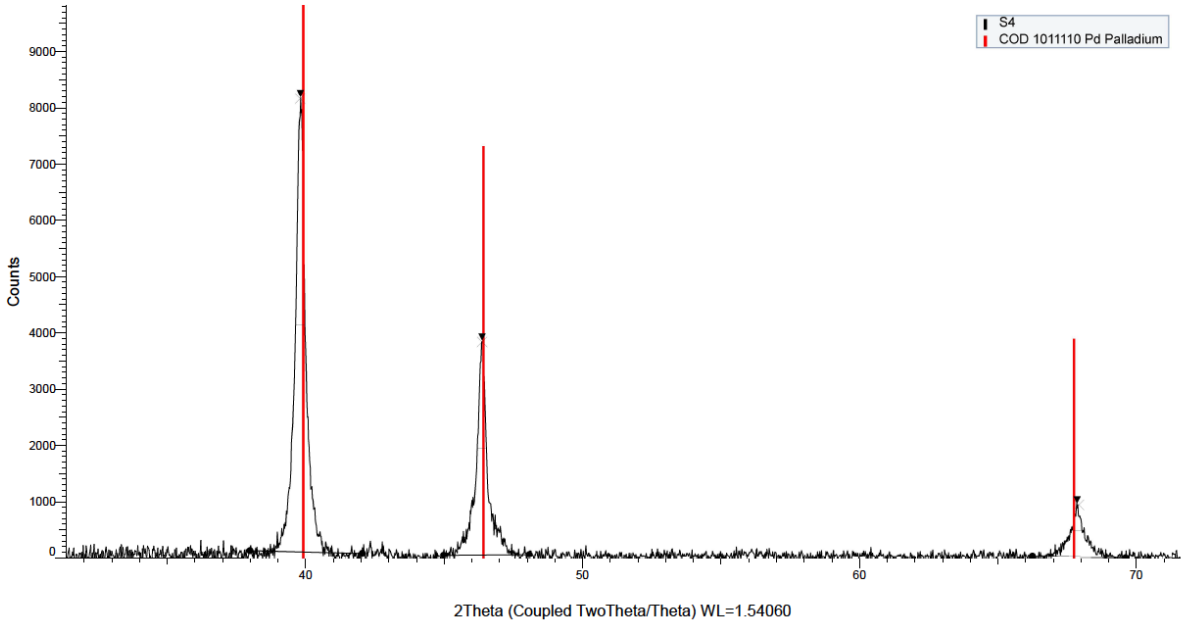


Figure 4.11. XRD pattern of Pd nanocubes with average size of 48.9 nm.

The formation of palladium nanostructures with (100) facets is justified by the usage of CTAB as surfactant in the synthesis. Previous reports [30][31][11] demonstrate that bromide anions (Br^-) acts as an effective etchant, adsorbing on the surface of the palladium seeds, controlling the growth of Pd nanocubes and altering the order of surface free energies to $\gamma(110) <$

$\gamma(111) < \gamma(100)$. Therefore, the anisotropic growth of Pd nanocrystals leads to the formation of thermodynamically favoured (100) facets.

Others synthesis conditions as the usage of high temperature (95 ℃) and relatively high ascorbic acid (AA) concentrations are also responsible to promote preferential reduction of palladium salts to palladium atoms on the (111) facets. The disappearance of (111) facets lead to the formation of cubic nanocrystals enclosed completely by the (100) facets [11].

4.2.7 Characterisation of PdNCBs— reporter probe conjugates on 20% AuS SPCE

Figure 4.13 presented the SEM of a (A) 20% AuS SPCE surface before (bare) and (B) after its functionalisation with a full miRNA assay and palladium nanocubes as labels. miRNA target and reporter-probe concentration used was 1 μM. The images are highly sensitive to differences in the atomic number. The higher the atomic number, the brighter the material appears in the image. A higher energy electron is obtained from the higher contrast material. Hence, the bright spots clearly represent gold particles on the surface.

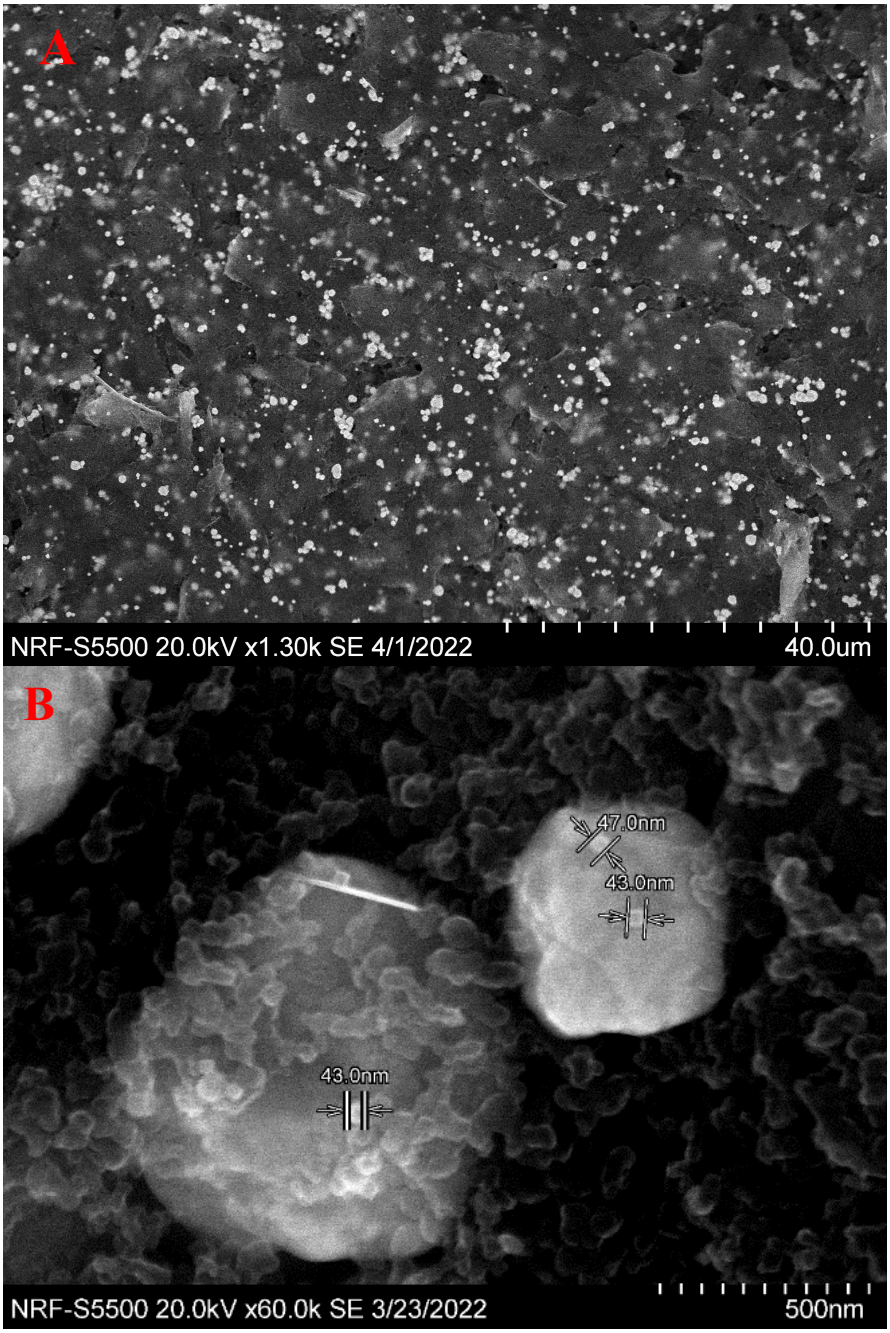


Figure 4.12.SEM images of (A) 20% AuS SPCE without modification of the surface and (B) 20% AuS SPCE functionalised with full miRNA assay and PdNCBs labels. Magnification and accelerating voltage used is described in the respective images.

Through the analysis of the bare gold surface one can see that by enhancing in 10% the number of gold microspheres mixed to the ink, there is a substantial increase in the density of gold microspheres present on the surface (Fig. 4.5 (A) vs. Fig. 4.13 (A)). A uniform, homogeneous distributed gold particles was also observed in the SEM analysis and validated by DLS experiments (DLS data not shown).

The discernible differences in the morphology of the SPEs observed in Figure 4.13 (B) indicate the successful binding between the miRNA sandwich assay and labels confined in the gold surface. The size of PdNCBs presented as approximately 43-47 nm. As expected, the as-synthetised palladium nanocubes retained their size and shape throughout the hybridisation process.

4.2.8 Characterisation of 20% AuS SPCE

4.2.8.1 Thickness of the electrode surface

Studies of the thickness of the 20% AuS SPCEs (i.e. the printed layer thickness) was performed using a Bruker DektaKXT Stylus profilometer. The electrode presented a value of 50 ± 5 µm. A Ossila Four-Point Probe instrument was also used to assess additional physical and electrochemical parameters of the sensor surface. The results are displayed in Table 4.8.

The small standard deviation generated by the good reproducibility between electrodes can be associated to the consistency of the viscosity of the inks used to produce the SPEs. If the viscosity of the inks differed, after a single print, the physical and electrochemical properties would also differs [32], causing undesirable variations in the surface's electron transfer properties, i.e., changes in charge transfer effects.

Table 4.8. Four-point probe analysis results of bare 20% AuS SPCE. Average values and standard deviations were calculated from triplicate measurements.

Sheet resistance	4.67 ± 0.12 Ω/square
Resistivity	235.80 ± 50.02 µΩ·m
Conductivity	4.26 ± 0.80 kS/m

4.3 Conclusion

At this work, three studies were performed to evaluate the electrochemical behaviour and the analytical performance of the in-house developed screen-printed carbon electrodes (SPCEs) with different compositions of gold microparticles within its carbon-based ink. Hence, the first study evaluated SPCEs with 10% (w/w) gold microspheres (referred as 10% AuS SPCE) and SPCE with 10% (w/w) microflakes particles (referred as 10% AuF SPCE) mixed to the carbon ink. The results showed that the 10% AuS SPCE generated the most reversible behaviour, highest I_p values, and lowest overvoltage of the in-house electrodes, suggesting that this platform has higher electronic transfer kinetics. The 10% AuS SPCE also presented the lowest resistance due to the geometry of the gold particles, resulting in its homogeneous distribution over the surface which enhances the reactivity of the substrate. These findings indicate that the use of gold microspheres mixed to the ink could significantly improve the analytical performance of the sensor, making it a promising approach for developing new electrochemical sensors.

The second study investigates how the different nanostructured gold SPCE (10% AuS SPCE and 10% AuF SPCE) affect the sensitivity of a biosensor functionalised to a fully complementary miRNA sandwich assay. The performance of the platforms were compared using two different labels (PdNCBs and AuNRDs) . The analytical signal of 10% AuS SPCE with PdNCBs was 10 times better than that obtained with AuNRDs, while 10% AuF SPCE with PdNCBs showed a 5-fold increase in signal. Additionally, the 10% AuS SPCE platform had the highest sensitivity and signal-to-noise ratio compared to the 10% AuF platform. The excellent response of this platform was attributed to the synergetic effects of increased surface area for biomolecules adsorption and enhancement of metal catalytic activity. The optimised ink recipe resulted in a surface capable of perfectly distinguishing between the signal of miRNA target and bare gold SPCE electrodes.

The third study presented an optimization of the conducting path of the SPCE to enhance the number of electroactive adsorption sites. The study then evaluated the performance of 10% (w/w) and 20% (w/w) AuS SPCEs functionalized with miRNA assay labelled with PdNCBs and AuNRDs. The 20% AuS SPCEs showed the greatest performance with a 56-fold signal amplification when the full assay was labelled with AuNRDs. Other optimisations, such as the

study of potentials for enhancing the electrocatalysis of nanoparticles for the reduction of hydrogen peroxide was also performed. The morphology of gold nanorods, and palladium nanocubes was confirmed through TEM or SEM, DLS, and zeta potential. The results suggest that the efficiency of electroreduction reaction of hydrogen peroxide can be enhanced through the modulation of the metal nanoparticles' favourable characteristics associated with specific sizes and shapes. These findings have implications for the development of multiplexer sensing technologies with greater design possibilities and accuracy in point-of-care biosensors.

Overall, this study provides useful insights into designing and optimising SPCE for improved analytical performance. The newly developed platforms were found to be effective and reproducible, indicating high potential for use in biosensing. The studies suggest that a multiplexed electrochemical biosensor for the detection of miRNAs associated with neurological diseases could be fabricated using the 20% AuS SPCE.

4.4 References

[1] Thakur, K. T., Albanese, E., Giannakopoulos, P., Jette, N., Linde, M., Prince, M. J., Steiner, T. J., & Dua, T. (2016). Neurological Disorders. In V. Patel (Eds.) et. al., *Mental, Neurological, and Substance Use Disorders: Disease Control Priorities, Third Edition (Volume 4)*. The International Bank for Reconstruction and Development / The World Bank. https://doi.org/10.1596/978-1-4648-0426-7_ch5

[2] Kosik K. S. (2006). The neuronal microRNA system. *Nature reviews. Neuroscience*, *7*(12), 911–920. https://doi.org/10.1038/nrn2037

[3] Hasan, M. R., Ahommed, M. S., Daizy, M., Bacchu, M. S., Ali, M. R., Al-Mamun, M. R., Saad Aly, M. A., Khan, M. Z. H., & Hossain, S. I. (2021). Recent development in electrochemical biosensors for cancer biomarkers detection. *Biosensors and Bioelectronics:* X, *8*, 100075. https://doi.org/10.1016/j.biosx.2021.100075.

[4] Silva, R. M., da Silva, A. D., Camargo, J. R., de Castro, B. S., Meireles, L. M., Silva, P. S., Janegitz, B. C., & Silva, T. A. (2023). Carbon Nanomaterials-Based Screen-Printed Electrodes for Sensing Applications. *Biosensors*, *13*(4), 453. https://doi.org/10.3390/bios13040453

[5] Antuña-Jiménez, D., González-García, M. B., Hernández-Santos, D., & Fanjul-Bolado, P. (2020). Screen-Printed Electrodes Modified with Metal Nanoparticles for Small Molecule Sensing. *Biosensors*, *10* (2), 9. https://doi.org/10.3390/bios10020009

[6] Chen, A., & Chatterjee, S. (2013). Nanomaterials based electrochemical sensors for biomedical applications. *Chemical Society reviews*, *42*(12), 5425–5438. https://doi.org/10.1039/c3cs35518g

[7] Vigderman, L., Khanal, B. P., & Zubarev, E. R. (2012). Functional Gold Nanorods: Synthesis, Self-Assembly, and Sensing Applications. *Advanced Materials*, 24(36), 4811-4841. https://doi.org/10.1002/adma.201201690

[8] Nie, G., Lu, X., Lei, J., Yang, L., Bian, X., Tong, Y., & Wang, C. (2013). Sacrificial template-assisted fabrication of palladium hollow nanocubes and their application in electrochemical detection toward hydrogen peroxide. *Electrochimica Acta*, 99, 145-151. https://doi.org/10.1016/j.electacta.2013.03.066.

[9] López-Ortega, A., Rojas-Chavez, H., & Vázquez-Durán, A. (2012). Electrocatalytic reduction of H_2O_2 by Pt nanoparticles covalently bonded to thiolated carbon nanostructures. *Electrochimica Acta*, 65, 288-293. https://doi.org/10.1016/j.electacta.2012.01.070

[10] Kleijn, S. E. F., Lai, S. C. S., Koper, M. T. M., & Unwin, P. R. (2014). Electrochemistry of Nanoparticles. *Angewandte Chemie International Edition*, 53(12), 3558-3586. https://doi.org/10.1002/anie.201306828

[11] Niu, W., Zhang, L., Xu, G. (2010). Shape-Controlled Synthesis of Single-Crystalline Palladium Nanocrystals. *ACS Nano, 4* (4),1987-1996. https://doi.org/10.1021/nn100093y.

[12] Nicholson, R. S., & Shain, Irving. (1964). Theory of stationary electrode polarography. Single scan and cyclic methods applied to reversible, irreversible, and kinetic systems. *Analytical Chemistry, 36*(4), 706–723. https://doi.org/10.1021/ac60210a007

[13] Lavagnini, I., Antiochia, R., & Magno, F. (2004). An extended method for the practical evaluation of the standard rate constant from cyclic voltammetric data. *Electroanalysis, 16*(6), 505-506. https://doi.org/10.1002/elan.200302851

[14] Nicholson, R. S. (1965). Theory and application of cyclic voltammetry for measurement of electrode reaction kinetics. *Analytical Chemistry*, 37(11), 1351–1355. https://doi.org/10.1021/ac60230a016

[15] Morrin, A., Killard, A.J. and Smyth, M.R. (2003) Electrochemical Characterization of Commercial and Home-Made Screen-Printed Carbon Electrodes. *Analytical Letters*, 9, 2021-2039. https://doi.org/10.1081/AL-120023627

[16] Xu, Y., Xu, R., Cui, J., Liu, Y., & Zhang, B. (2012). One-step synthesis of three-dimensional Pd polyhedron networks with enhanced electrocatalytic performance. *Chemical communications (Cambridge, England)*, *48*(32), 3881–3883. https://doi.org/10.1039/c2cc00154c

[17] Peng, X., Cui, Z., Bai, X., & Lv, H. (2018). Bio-synthesis of palladium nanocubes and their electrocatalytic properties. *IET nanobiotechnology*, *12*(8), 1031–1036. https://doi.org/10.1049/iet-nbt.2018.5159

[18] Čović,J., Mirceski,V, Zarubica, A., Enke, D., Carstens, S., Bojić,A, Ranđelović, M. (2022). Palladium-graphene hybrid as an electrocatalyst for hydrogen peroxide reduction. *Applied Surface Science, 574*,151633. https://doi.org/10.1016/j.apsusc.2021.151633

[19] Amirfakhri, S.J., Meunier, Jean-Luc , Berk, Dimitrios. (2014). Electrocatalytic activity of $LaNiO_3$ toward H_2O_2 reduction reaction: Minimization of oxygen evolution. *Journal of Power Sources*, *272*, 248-258. https://doi.org/10.1016/j.jpowsour.2014.08.068.

[20] Chen, W.,Cai, S., Ren, Q.-Q., Wen, W., Zhao, Y.-D. (2012). Recent advances in electrochemical sensing for hydrogen peroxide: a review. *Analyst*, *137* (1) 49-58. https://doi.org/10.1039/C1AN15738H

[21] Kitte, S.A, Assresahegn, B. D., Soreta, T. (2013). Electrochemical Determination of Hydrogen Peroxide at Glassy Carbon Electrode Modified with Palladium Nanoparticles. *Journal of the Serbian Chemical Society , 78* (5), 701-711. https://doi.org/10.2298/JSC120619122K.

[22] Mayer, K. M., Lee, S., Liao, H., Rostro, B. C., Fuentes, A., Scully, P. T., Nehl, C. L., & Hafner, J. H. (2008). A label-free immunoassay based upon localized surface plasmon resonance of gold nanorods. *ACS nano*, *2*(4), 687–692. https://doi.org/10.1021/nn7003734

[23] Parab, H. J., Jung, C., Lee, J. H., & Park, H. G. (2010). A gold nanorod-based optical DNA biosensor for the diagnosis of pathogens. *Biosensors & bioelectronics*, *26*(2), 667–673. https://doi.org/10.1016/j.bios.2010.06.067

[24] Niu, W., Li, Z.-Y., Shi, L., Liu, X., Li, H., Han, S., Chen, J., & Xu, G. (2008). Seed-Mediated Growth of Nearly Monodisperse Palladium Nanocubes with Controllable Sizes. *Crystal Growth & Design, 8*, 4440–4444.https://doi.org/10.1021/cg8002433

[25] Berhault, G., Bausach, M., Bisson, L., Becerra, L., Thomazeau, C., & Uzio, D. (2007). Seed-Mediated Synthesis of Pd Nanocrystals: Factors Influencing a Kinetic- or Thermodynamic-Controlled Growth Regime. *Journal of Physical Chemistry C, 111*, 5915–5925. https://doi.org/10.1021/jp0702752

[26] Ostwald, W. (1901). Blocking of Ostwald Ripening Allowing Long-Term Stabilization. *Physikalische Chemie, 37*, 385.

[27] Voorhees, P. W. (1985). The theory of Ostwald ripening. *Journal of Statistical Physics* **,** *38*, 231-252 . https://doi.org/10.1007/BF01017860

[28] Ganesan, M., Freemantle, R. G., & Obare, S. O. (2007). Monodisperse Thioether-Stabilized Palladium Nanoparticles: Synthesis, Characterization, and Reactivity. *Chemistry of Materials, 19*(14), 3464-3471.https://doi.org/10.1021/cm062655q

[29] Ding, H., Xue-Zhao, S., Cheng-Min, S., Chao, H., Zhi-Chuan, X., Chen, L., Yuan, T., Deng-Ke, W., & Hong-Jun, G. (2010). Synthesis of monodisperse palladium nanocubes and their catalytic activity for methanol electrooxidation. *Chinese Physics B, 19*(10), 106104. https://doi.org/10.1088/1674-1056/19/10/106104.

[30] Chang, G., Oyata, M., & Hirao, K. (2007). Facile Synthesis of Monodisperse Palladium Nanocubes and the Characteristics of Self-Assembly. *Acta Materialia, 55*(10), 3453–3456. https://doi.org/10.1016/j.actamat.2007.01.042

[31] Fan, F.-R., Attia, A., Sur, U. K., Chen, J.-B., Xie, Z.-X., Li, J.-F., Ren, B., & Tian, Z.-Q. (2009). An Effective Strategy for Room-Temperature Synthesis of Single-Crystalline Palladium Nanocubes and Nanodendrites in Aqueous Solution. *Crystal Growth & Design, 9*(5), 2335–2340. https://doi.org/10.1021/cg801231p

[32] Gonzalez-Macia, L., Morrin, A., Smyth, M.R., Killard, A.J. (2010). Advanced printing and deposition methodologies for the fabrication of biosensors and biodevices. *Analyst***,** *135* (5), 845-867. https://doi.org/10.1039/B916888E.

[33] Trasatti, S., & Petrii, O. A. (1991). Real Surface Area Measurements in Electrochemistry. *Pure & Applied Chemistry, 63*(5), 711-734. http://dx.doi.org/10.1351/pac199163050711.

CHAPTER 5

A sandwich electrochemical biosensor for miRNA-206, miRNA-135a and let-7b detection based on metal nanoparticles labelled SPEs.

5 INTRODUCTION

Neurological diseases pose significant challenges in terms of accurate diagnosis and monitoring due to their complex nature and diverse manifestations. The absence of definitive diagnostic tests, the overlap between different disorders, and the variability in disease progression further complicate the diagnostic process [1]. However, microRNAs (miRNAs) hold promise as biomarkers for addressing these challenges. miRNAs, small non-coding RNA molecules, have been found to be associated with various neurological disorders and play a crucial role in gene regulation [2]. Detecting miRNAs could enable early diagnosis, accurate monitoring, and effective treatment of neurological diseases.

The development of point-of-care devices for miRNA detection in neurological diseases is of paramount importance in healthcare. These devices could enable early and accurate diagnosis, facilitating timely interventions and personalized treatment plans. Key features of such devices include portability, user-friendliness, high sensitivity and specificity, quick results, and cost-effectiveness [3]. Point-of-care devices incorporating these features can revolutionize patient care through the promotion of prognosis, improving outcomes, and enhanced quality of life.

In recent years, screen-printed carbon electrochemical biosensors (SPCEs) have gained attention in clinical settings due to their low cost, ease of use, low volume requirements, possibility to mass produce and portability [4]. Although the conductivity and electron transfer properties may be lower than traditional electrodes, their surfaces can still be tailored to meet specific analytical needs and their low cost enables testing at scale. The incorporation of nanomaterials, such as gold microspheres (AuS), into SPCEs can increase the surface area, act as catalytic sites and improve biocompatibility. Nanomaterials offer advantages such as signal amplification, improved sensitivity, and versatile sensing platforms [5]. Ever since the initial reports of an electrochemical miRNA biosensor in 2006, extensive endeavours have been dedicated to improving the detection sensitivity. In part, this has been accomplished by harnessing the distinctive chemical and physical characteristics of nanostructures [6].

This work presents a proof-of-concept study on an innovative electrochemical platform that utilizes screen-printed working electrodes. These electrodes consist of 20% (w/w) gold microspheres with a diameter of 2 μm mixed with carbon ink, referred to as 20% AuS SPCE. By limiting the theorical fraction of gold surface to ~20% of the SPCE, interference from

products formed at the counter electrode that could react at the gold surface is minimized, resulting in improved reproducibility.

Furthermore, the optimized percentage of gold-to-carbon enhances the performance of the electrode (in comparison to conventional SPCE) by increasing its electroactive binding area. This, in turn, boosts the efficiency of miRNA capture-probe binding at the electrode surface and facilitates the attachment of a higher number of nanoparticle labels in a complementary sandwich miRNA assay. Various shaped nanoparticles, including gold nanorods (AuNRDs), platinum nanoparticles (PtNPs), and palladium nanocubes (PdNCBs), have been employed as labels to amplify the signal of the miRNA target and enhance charge collection. These nanoparticles act as catalysts, promoting the reduction of hydrogen peroxide and thereby increasing the detection efficiency.

SPCEs that incorporate metal nanoparticles provides advantages over traditional approaches. With their high conductivity and tailored structure, these SPCEs can improve analytical sensitivity and expand the range of applications for biosensors [7]. The sensitive, selective, and fast detection of targets make them suitable for point-of-care devices in healthcare, enabling quick and accurate diagnosis of diseases. The miniaturization potential of electrochemical biosensors based on SPCEs further opens up opportunities for the development of compact and efficient lab-on-a-chip systems, capable of real-time monitoring of biomarkers and even environmental contaminants [8]. These advancements hold the promise of revolutionizing real-time detection, enhancing efficiency and accuracy in healthcare and environmental monitoring scenarios.

The biosensor platform developed in this work utilizes an enhanced transducer component (i.e., 20% (w/w) gold microspheres mixed in the carbon ink). These microparticles act as anchor points for the thiolated capture-probe strands that bind the target. Once the target binds to an electrocatalytic nanoparticle labelled reporter-probe strand, there is a conversion of miRNA binding events into detectable signals. The detection process involves amperometry, where the current generated by the electrocatalytic reduction of hydrogen peroxide by differently shaped nanoparticles in a fully complementary sandwich assay is measured. The sensor can detect a variety of miRNA targets at different potentials without significant cross-reactivity giving the possibility that it can be developed as a multiplexed sensor system.

The novel AuS screen-printed carbon electrode (20% w/w AuS SPCE) used as the platform for a sandwich assay, utilizing metal nanoparticles as labels, exhibits selectivity towards base mismatches, low non-specific binding of BSA, and sensitive detection at distinct potentials for miRNA-206, miRNA-135a, and let-7b. Thus, this platform has the potential to improve the accuracy of neurological disease diagnosis and monitoring.

5.1 Experimental Procedures

5.1.1 Materials and Chemicals

Ethyl Cellulose, dipropylene glycol monomethyl ether, alpha-terpineol, potassium ferricyanide ($K_3Fe(CN)_6$; $K_4Fe(CN)_6$), potassium chloride (KCl), phosphate buffer (PBS, pH 7.4), tris[2-carboxyethyl]phosphine (TCEP), hydrogen peroxide solution (H_2O_2, 3%), BSA (Bovine Serum Albumin), palladium (II) chloride ($PdCl_2$), hydrochloric acid (HCl), cetyltrimethylammonium bromide (CTAB) and ascorbic acid (AA) were purchased from Sigma Aldrich and used as received.

Conductive Carbon Black (Ensaco) and Graphite (Timrex) were purchased from Imerys Graphite & Carbon (Bironico, Switzerland). Au microparticles (Gold powder, spherical or flakes, APS 1.5-3.0 micron) were obtained by Alfa Aesar (Lancashire, UK).

Nanoparticles used as labels in this study were obtained from nanoComposix. Specifically, gold nanorods measuring 50 nm long with a diameter of 15 nm were used. Their zeta potential was -52 mV and had a particle concentration of 4.30 x 10^{11} parts/mL. A second label, platinum nanoparticles with a diameter of 50 nm ± 4 nm, a zeta potential of -40 mV and a particle concentration of 9.6 x 10^{11} particles/mL, were used. All nanoparticles were citrate-stabilized and suspended in water.

A third and final label used in this work was palladium nanocubes which was fabricated in-house. These nanocubes had an edge length of 50 nm and zeta potential of 38.6 ± 5.0 mV.

All the aqueous solutions described in this work, if it was not stated otherwise, were prepared using Milli-Q water (Millipore Core, 18 MΩ cm).

The oligonucleotides (purity ≥98%), RNase free water and TE buffer (10mM Tris and 1mM EDTA) used to prepare immobilization and hybridization solutions were purchased from IDT. The base sequences used was:

miRNA-206

Capture- probe: SH-C6- 5'-CCA CAC ACU U-3'
Target (miRNA-206): 3'- GGU GUG UGA A GGA-AUG-UAA-GGU- 5'
Target (miRNA-1- 4 bases mismatches): 3'-UAU GUA UGA A GAA AUG UAA GGU-5'
Target (miRNA-206' -1 base mismatch): 3'- UGU GUG UGA A GGA AUG UAA GGU- 5'
Reporter-probe: 5'-CCU-UAC-AUU-CCA/3ThioMC3-D/- 3'

Let-7b

Capture- probe: SH-C6- 5'-AACC AGA CAA-3'
Target (Let-7b): 3'-UUGG UCU GUU GGA UGA UGG AGU-5'
Target (Let- 7f - 2 base mismatches) : 3'-UUGA UUU GUU GGA UGA UGG AGU-5'
Target (Let-7g - 1 base mismatch: 3'-UUGG UUU GUU GGA UGA UGG AGU-5'
Reporter-probe: 5'-CCU-ACU ACC UCA /3ThioMC3-D/- 3'

miRNA-135a

Capture-probe: SH-C6- 5'-UCACA UAG GA-3'
Target (miRNA-135a): 3'-AGUGU AUC CUU AUU UUU CGG UAU-5'
Target (miRNA-135b- 1 base mismatch): 3'-AGUGU AUC CUA ACU UUU CGG UAU-5'
Reporter-probe: 5'-UAA AAA GCC AUA /3ThioMC3-D/- 3'

5.1.2 Development of functionalized miRNA assay at 20% (w/w) AuS SPCE

In this study, the working electrode (WE), reference electrode (RE), and counter electrode (CE) were printed together as part of the experimental setup. However, to prevent the binding of miRNAs at the CE and RE during the immobilization and subsequent hybridization steps, it was necessary to physically separate the CE and RE electrodes. Figure 5.1 presents a schematic diagram of the assembly of the labelled miRNA biosensor.

To initiate the development of the miRNA assay, the 5'-thiolated miRNA capture-probe was deposited onto gold microspheres (2 μm) that were incorporated within the carbon ink of the screen printed electrode (denoted as 20% AuS SCPE).For this, the surface of the working electrode was incubated in an Eppendorf tube containing a 10 μM solution of the 5'-thiolated oligo. The Eppendorf tube was sealed with parafilm and placed in an oven at 37°C for 80 minutes. The electrode was rinsed with nuclease-free water to remove any loosely bound strands.

Subsequently, the capture-probe modified screen printed electrode was incubated with different concentrations of the miRNA target ranging from 1 aM to 1μM . This step led to the hybridization of the miRNA target's 3' end to the capture-probe strand. The hybridization time between the miRNA target and surface immobilized capture-probe strands was 20 minutes in an oven at 37°C. The electrode was then washed with nuclease free water.

Finally, the free 5' end of the miRNA target was hybridized with its complementary sequence present in the miRNA reporter-probe functionalized with metal nanoparticles*. The hybridization of the labelled miRNA reporter-probe to its complementary sequence occurred over a 5-hour period at 37°C.

The preparation of the immobilization buffer (miRNA capture-probe and reporter-probe) requires specific steps. TCEP (Tris [2-carboxyethyl] phosphine) was added in 100-fold excess and allowed to react for 2 hours. This step ensures the activation of the thiols bonds from the capture-probe and reporter-probe oligo, facilitating efficient immobilization with the metallic surfaces.

*The functionalization of palladium nanocubes (PdNCBs), platinum nanoparticles (PtNPs) and gold nanorods (AuNRDs) with miRNA reporter-probes occurred as described in section 4.1.3 and 4.1.4, respectively.

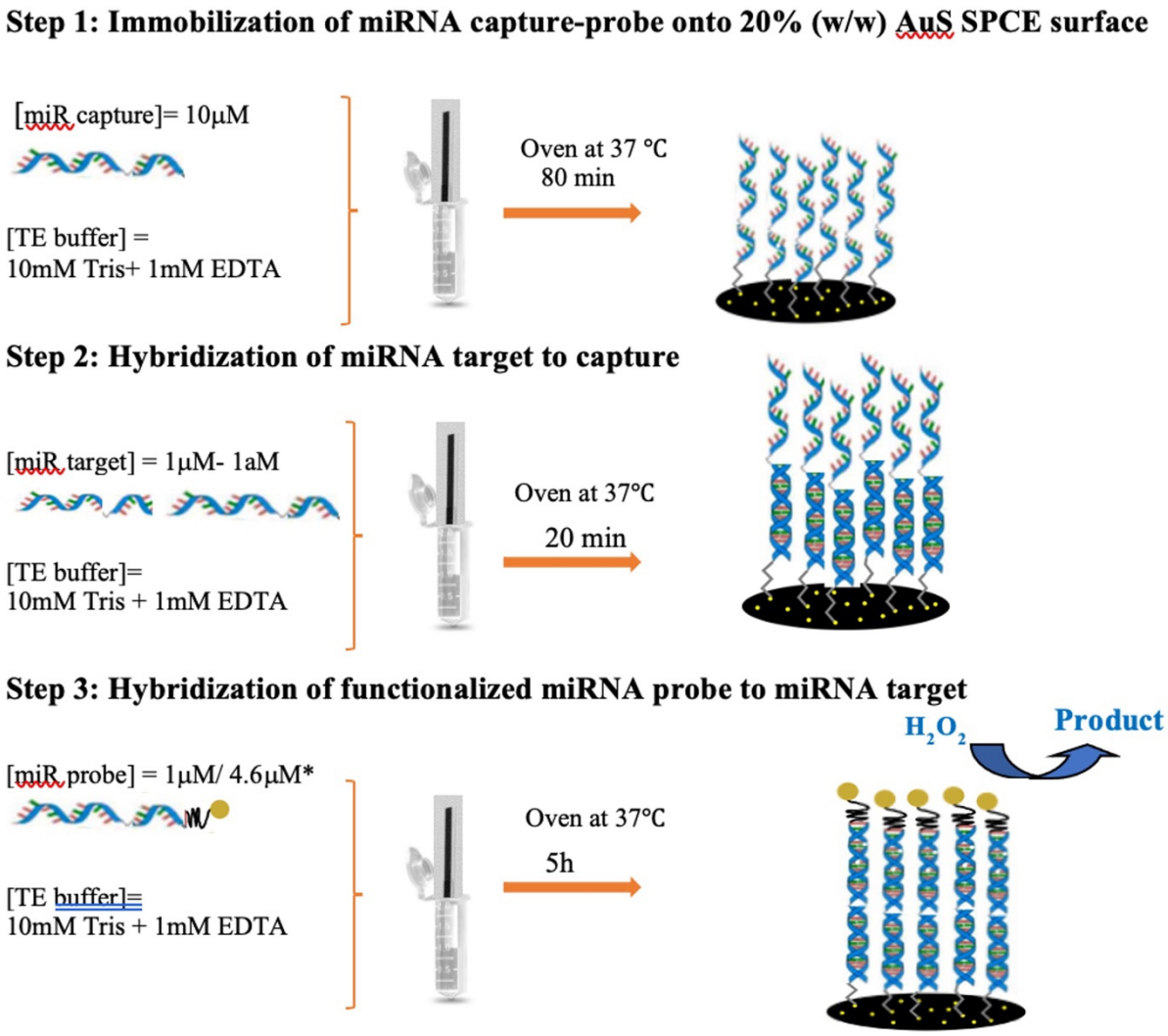


Figure 5.1. Assembly of the Labelled miRNA Biosensor: Schematic Diagram and Specific Parameters. For the functionalization of the electrode to AuNRDs, 4.6 μM reporter-probe solution were utilized. Alternatively, when functionalized with PtNPs and PdNCBs, a 1 μM miRNA reporter-probe solution were employed.

5.1.3 Electrochemical Analysis

5.1.3.1 Amperometric detection of miRNAs target

After the miRNA sandwich assay is completed, the working electrode, reference electrode, and counter electrode were assembled together. These electrodes were then immersed in a small cell filled with 7.2 mL of 0.01 M PBS solution. Amperometry was employed as the detection method to identify the presence of the metal nanoparticles and hence the target concentration.

Initially, the current was measured at a potential that is specific for each type of nanoparticle: -0.375V for PdNCBs, -0.25V for AuNRDs, and -0.5V for PtNPs. The current was allowed to stabilize for 5 min. Following that, 3.27 μL of hydrogen peroxide (3% w/v) was introduced into the PBS solution to achieve a final concentration of 400 μM. Stirring was employed for 1 min, upon addition of H_2O_2.

Subsequently, the current associated with the reduction of hydrogen peroxide by the nanoparticles was measured after 20 minutes. The analytical response was determined by calculating the difference in current (Δi) observed before and after the addition of hydrogen peroxide.

5.1.4 Instrumentation

The electrochemical measurements were conducted at room temperature (22 ± 2 ℃) using a CHI760D electrochemistry workstation. Dr. Loanda Cumba from DCU fabricated the working electrodes in-house by employing a DEK Horizon APiX screen-printing machine (Maxem, IE) and using appropriate stencil designs.

The working electrodes (Φ = 3 mm) were made of 20% AuS SPCE (i.e., ethyl cellulose (5.20%), dipropylene glycol monomethyl ether (27.20%); alpha-terpineol (23.20%), carbon black (7.60%), graphite (16.80%) and Au microspheres (20%). For all the electrochemical measurements, a screen-printed Ag/AgCl was utilized as pseudo-reference electrode, while a carbon/graphite screen-printed electrode served as the counter electrode.

5.2 Results and Discussion

5.2.1 Principle of the proposed electrochemical biosensor

In a proof-of-concept study, three independent screen-printed working electrodes with a 20% (w/w) mixture of gold microspheres in the carbon ink (referred to as 20% AuS SPCE), designed and optimized in Chapter 4, was used to develop labelled biosensors for the detection of biomarkers of neurological diseases such as, miRNA-206, miRNA-135a and let-7b. Labels in the form of gold nanorods (AuNRDs), platinum nanoparticles (PtNPs), and palladium nanocubes (PdNCBs) were selected due to their distinct reduction potential.

The direct incorporation of gold microspheres into the carbon ink of the SPE provided several advantages over traditional SPCE platforms. Firstly, it defines the region where the capture-probe strands bind and the microsphere loading can be changed to control their separation, e.g., to achieve local radial diffusion, improves kinetic reactions across the surface, including heterogeneous electron transfer. Secondly, it increases the rate of miRNA capture-probe strand adsorption on the electrode surface. If the sensing phase have more active sites available to bind with the labelled fully complementary miRNA assay, higher number of nanoparticles is brought to the electrode surface leading to an overall improvement of the analytical performance of the sensor.

Through fine-tuning the size and shape of the labelled nanoparticles, there was a notable enhancement in the charge collection capability of the platform. This improvement is facilitated by the faster electron transfer during the reduction reaction of H_2O_2. In other words, the nanoparticles acted as catalysts, promoting the reduction of H_2O_2 and thereby improving the signal, while minimising the background noise (the kinetics of peroxide reduction at the carbon matrix of the SPE are very slow) during the detection phase.

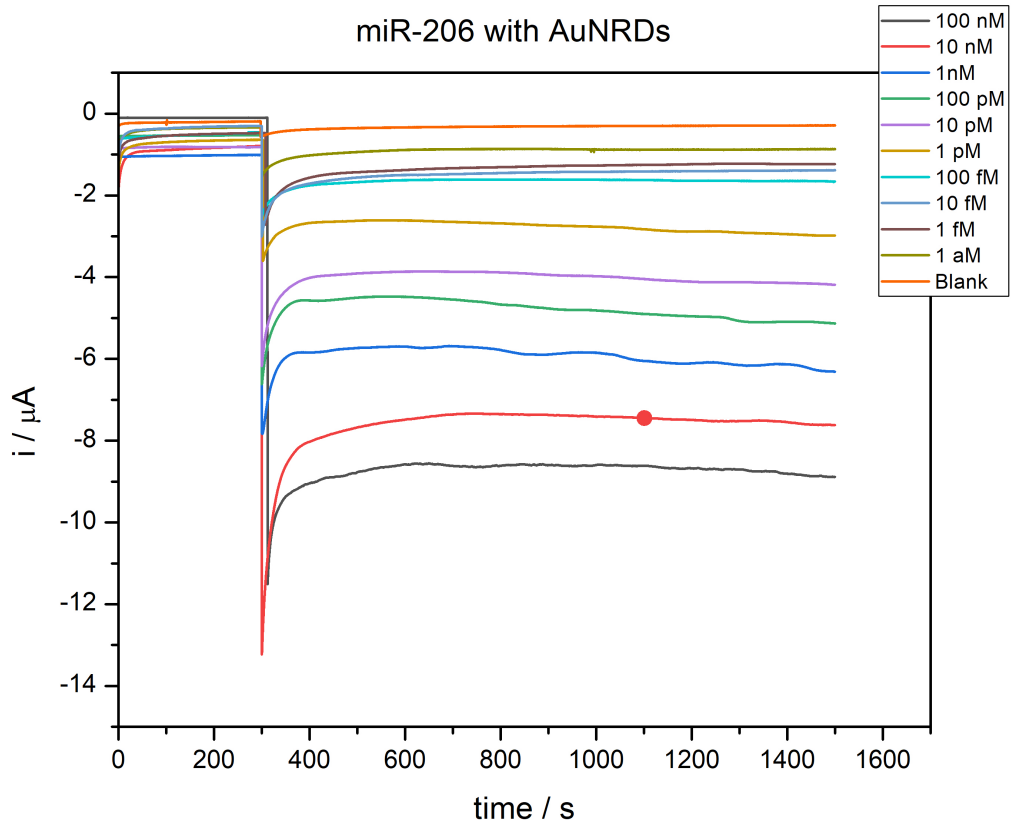
As a consequence of this enhanced charge collection, the signal from the targeted miRNA was amplified. Additionally, the binding event between the labelled miRNA reporter-probe and the target miRNA resulted in each biomarker possessing a distinct reduction potential. This distinct potential generated independent current signals, further contributing to the sensitivity and specificity of the biosensing system.

5.2.2 Analytical performance of the biosensor

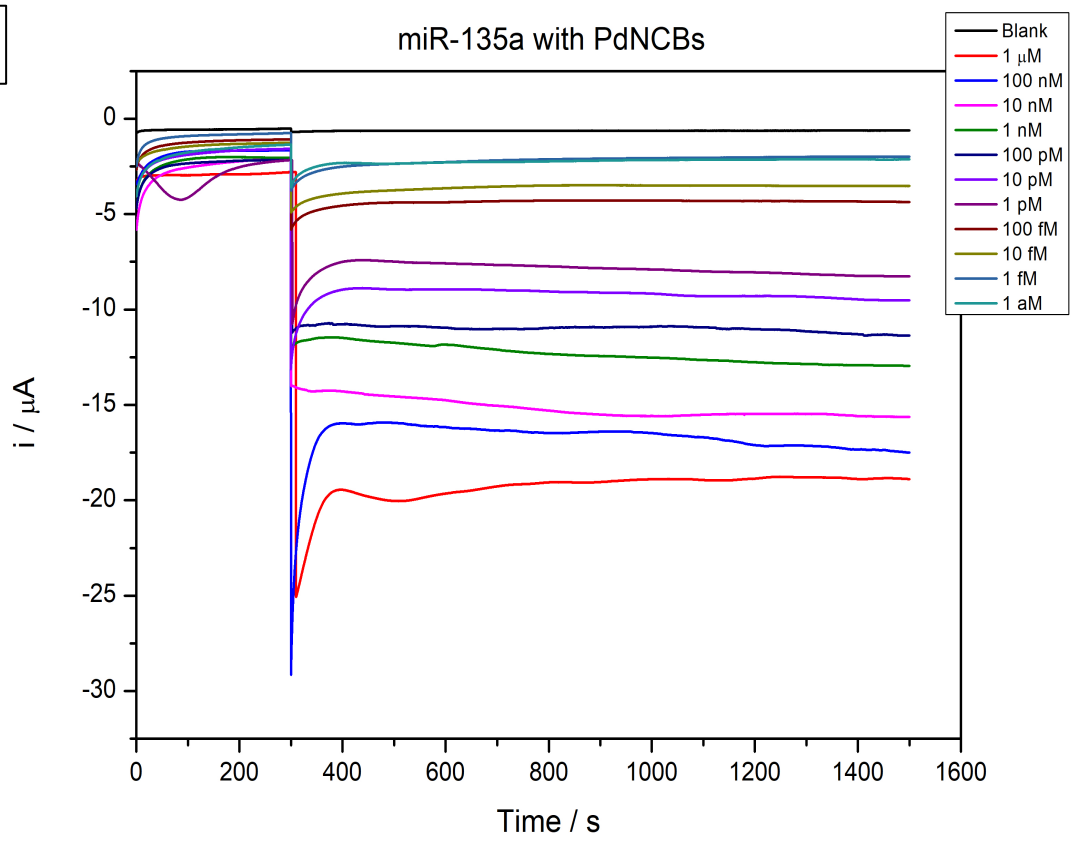
To validate the degree of signal amplification achieved by each nanoparticle label and the feasibility of the platform for the detection of biomarkers present in blood at ultralow concentrations, a calibration curve was developed. Standard miRNA targets was diluted to generate a sequential range of concentrations from 1 μM to 1 aM. Subsequently, on ***independent*** 20% AuS SPCE platforms, sandwich assays were constructed using capture-probe – target – reporter-probe labelled nanoparticles (AuNRDs, PtNPs, or PdNCBs) with specific targets (miR-206, let-7b, and miR-135a, respectively). These assays utilized the previously prepared target concentrations ranging from 1 μM to 1 aM. The gold nanorods were subjected to an potential of -0.25V, while the detection potentials for palladium nanocubes and platinum nanoparticles were -0.375V and -0.5V, respectively. The baseline current was measured after 5 minutes. After that, hydrogen peroxide was added to the system to give a final concentration of 400 μM and the current measured after 20 minutes. The signal was taken as the difference in the current before and after (Δi) the addition of the hydrogen peroxide.

Figure 5.2 depicts representatives amperometric i-t curves for the fully complementary miRNA assay for the detection of (A) miRNA-206, (B) miRNA-135a, (C) let-7b. In each case, the concentration of the reporter-probe labelled nanoparticles was high, to ensure that all capture-probe – target hybrids are labelled. Using a high concentration is important since the reporter-probe coverage may vary as the identity of the metal in the nanoparticle label is changed which will alter the binding kinetics and perhaps the association constant.

A


miR-206 with AuNRDs
100 nM
10 nM
1nM
100 pM
10 pM
1 pM
100 fM
10 fM
1 fM
1 aM
Blank
i / μA
time / s

B


miR-135a with PdNCBs
Blank
1 μM
100 nM
10 nM
1 nM
100 pM
10 pM
1 pM
100 fM
10 fM
1 fM
1 aM
i / μA
Time / s

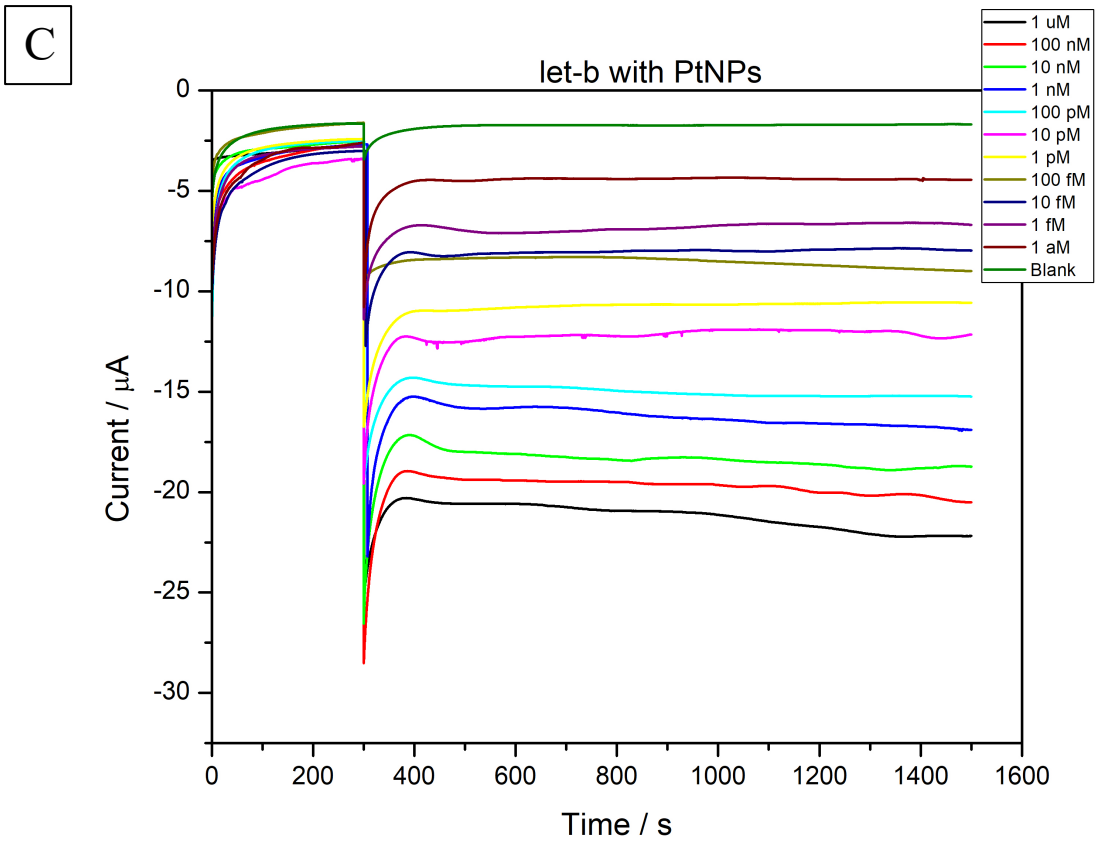


Figure 5.2. Amperometric i-t curves for 20% AuS SPEs functionalized with 10 µM miRNA capture-probe strands following hybridisation with the indicated concentration of the target. The concentration of the reporter-probe labelled nanoparticles is 1 µM. The reporter-probe labelled nanoparticles are (A) gold nanorods, (B) palladium nanocubes, and (C) platinum nanoparticles. The applied potentials were (A) - 0.25V, (B) - 0.375V, and (C) - 0.5 V. The electrolyte was 0.01 M PBS and hydrogen peroxide was added at 300 s to give a final concentration of 400 µM. Measurements were conducted in triplicate,

The background current for all the functionalized fully complementary assay at 20% AuS SPCEs remains stable and close to zero after applying the particle specific potential for 5 minutes. When 400 µM of hydrogen peroxide is introduced to the system, the sensor quickly responds, resulting in a high current and the subsequent formation of a plateau. The time frame needed to transition between temporary current to plateau, was between 300 to 1500 seconds depending on the concentration of the miRNA target.

The shift from a transient current to a plateau relies on the radial diffusion of H_2O_2 towards nanoparticles, such as AuNRDs, PtNPS, and PdNCBs. This diffusion phenomenon follows Fick's second law of diffusion, where it is directly proportional by factors such as the availability of surface area for diffusion, diffusion coefficient, and concentration, while being inversely proportional by the distance of diffusion

[12].As hydrogen peroxide is reduced at the surface of the nanoparticles, it forms a depleted peroxide layer, which reduces the concentration gradient and slows down the diffusion of hydrogen peroxide from the bulk solution to the nanoparticle surface. Since the diffusion rate between the bulk hydrogen peroxide solution and the nanoparticles is slow (approximately 10^{-5} cm^2/s), the current becomes limited, thereby contributing to the observed transient behaviour. This restricted diffusion rate explains the noticeable difference in current before and after the addition of peroxidase, making it easy to distinguish the two states.

It is worth nothing that the diffusion limitations cause the transient (i.e., the change in current over time) to level off. While the Cottrell equation can describe the initial part of the transient, where the current decreases with the square root of time in a diffusion-controlled process, it does not account for the plateau observed which arise due to radial diffusion of peroxide to the nanoparticle labels.

The concentration of the miRNA target directly affects the magnitude of the current signal (Δi) as depicted in Fig. 5.2. A higher density of miRNA targets on the surface increases the likelihood of binding to the labelled reporter-probe. This binding allows for a greater number of active sites present on the nanoparticle surface to be accessible for the reduction of hydrogen peroxide, resulting in an increased current. Essentially, the current is proportional to the loading of the functionalized reporter-probe, which is determined by the concentration of the miRNA target.

Higher concentrations of the miRNA target require more time to reach equilibrium due to two interconnected factors. Firstly, an increased quantity of nanoparticles becomes bonded through miRNA target— reporter-probe hybridization. Secondly, the presence of a high number of miRNA probes creates a physical barrier for the reduction of hydrogen peroxide on the nanoparticle surface. As a result, not only is the diffusion of hydrogen peroxide difficulted/limited at elevated miRNA target concentrations, but the likelihood of cluster formation also increases due to the abundance of nanoparticles on the electrode surface. Consequently, the nanoparticles exhibit behaviour similar to that of microelectrodes in terms of their size, leading to the close proximity of labelled miRNA probes. This proximity causes the diffusion zones of the nanoparticles to overlap, reducing the surface-to-volume ratio and hindering the efficient diffusion of hydrogen peroxide. Consequently, the electrocatalytic efficiency of the nanoparticles is diminished [13].

The magnitude of the current signal is also dependent on the electrocatalytic activity of the metal nanoparticles towards the reduction of hydrogen peroxide. This activity varies based on the nanoparticles' intrinsic properties, shape, and size. Among the used nanoparticles, platinum nanoparticles exhibited the highest electrocatalytic activity, followed by palladium nanocubes and gold nanorods (PtNPs > PdNCBs > AuNRDs). This difference was observed through consistently higher currents for a given target concentration of miRNA-206, miRNA-135a, and let-7b labelled with these nanoparticles. Signal to noise ratios for the highest target concentration of miRNA-206, miRNA-135a and let-7b labelled with AuNRDs, PdNCBs and PtNPs were found to be 88; 164 and 177, respectively.

The superior electrocatalytic activity of platinum nanoparticles can be ascribed to their heightened capacity to bind with peroxide, coupled with their electronic characteristics that induce polarization in H-O-O-H bonds [14]. This polarization facilitates the easier cleavage of hydrogen peroxide into water and oxygen during the electrocatalytic process. By fostering an increased number of interactions between hydrogen peroxide molecules and the platinum nanoparticles, a greater potential for effective collisions emerges, thereby amplifying the catalytic performance.

Similarly to platinum nanoparticles, palladium nanocubes have an irregular shape, which contributes to their enhanced electrocatalytic activity. Irregular shaped particles have a more complex surface structure with more exposed surface atoms [15]. Hence, a higher surface-to-volume ratio is formed, generating more active sites, and reducing the energy required for the reaction to occur.

Although gold nanorods have a high aspect ratio and a large surface area, their elongated surface structure is relatively uniform and less complex compared to palladium nanocubes or platinum nanoparticles. The arrangement of surface atoms in regular-shaped particles is more ordered and symmetrical, leading to a reduction in the number of exposed surface atoms [15] available for catalytic reactions. Additionally, gold nanorods are more prone to aggregation due to their higher Hamaker constant [16]. Aggregation reduces the effective surface area available for catalytic reactions because the active sites on the surfaces of the individual nanorods become less accessible. This decreased surface area limits the interaction between

the catalyst (AuNRDs) and the reactant (H_2O_2), resulting in a reduction in electrocatalytic activity.

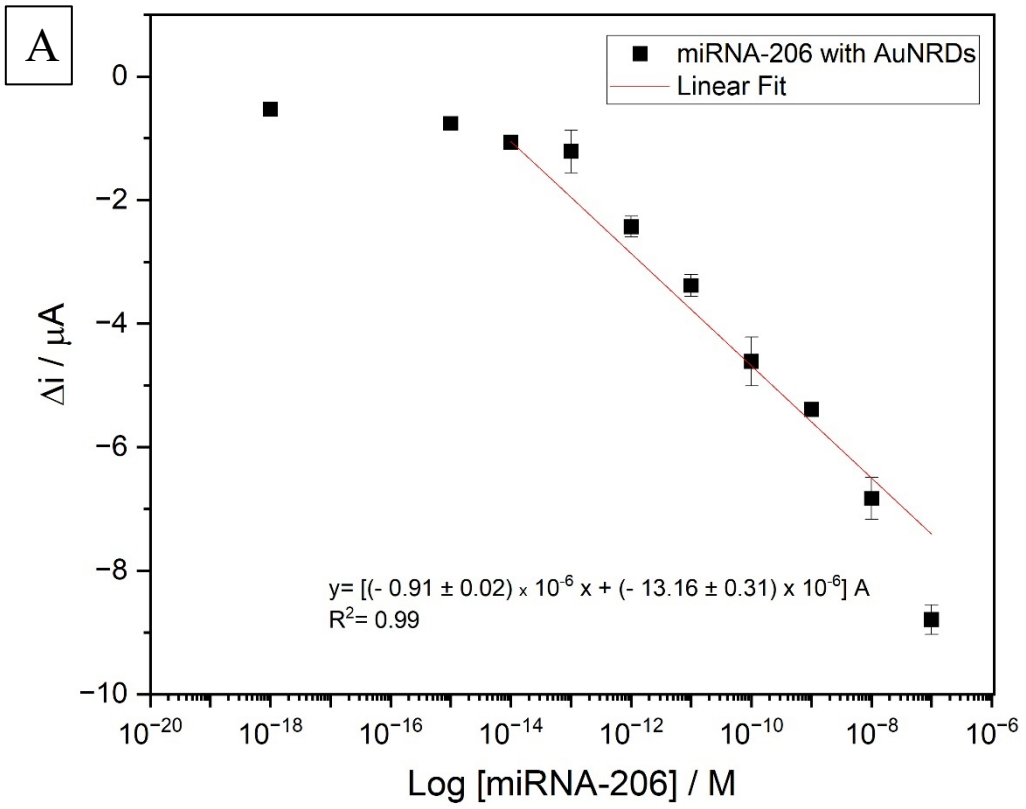
The selection of which nanoparticle would be bonded to the miRNA reporter-probe was determined based on the absolute concentration of its complementary target. In the context of studying miRNA-135a and let-7b expression levels in the brain of epileptic subjects, it has been observed that miRNA-135a-5p is significantly increased in children with temporal lobe epilepsy (TLE) and in animal models [17][18]. Similarly, let-7b has shown deregulation during epileptogenesis, being upregulated in TLE [19][20]. However, when it comes to measuring the concentrations of these miRNAs in circulating blood, reported values can vary due to differences in study design, patient population, and measurement techniques.

For instance, miRNA-135a was detected at a concentration of $2.2 \times 10^{-4} \pm 0.03$ ng/mL (~3.14×10^{-14} mol/L) for healthy controls and $3.40 \times 10^{-2} \pm 0.04$ ng/mL (~4.86×10^{-12} mol/L) for patients with epilepsy [21]. Let-7b was found at a concentration of $1.6 \times 10^{-4} \pm 0.02$ ng/mL (~2.67×10^{-14} mol/L) for healthy controls and $2.4 \times 10^{-2} \pm 0.03$ ng/mL (~4.0×10^{-12} mol/L) in patients with epilepsy [22] . Since miRNAs are theoretically present in the femtomolar (fM) range, it is essential to take account of this clinically relevant range. Therefore, the decision was made to functionalize these sequences with the nanoparticles that presented greater catalytic properties, i.e., PtNPs and PdNCBs.

The reason behind this sequential choice of nanoparticles is to address the issue of different absolute concentrations in a multi-analyte device. When the sensitivity of detection varies greatly among targets, it can pose a significant challenge. In this particular case, gold nanorods was implemented with miRNA-206 as its sensitivity is much higher (pM to nM range) compared to miRNA-135a and let-7b. Therefore, by employing different types of nanoparticles, such as platinum and palladium, it becomes possible to shift the measured signal so that all three miRNAs exhibit similar current magnitudes over their different clinically relevant concentration ranges.

By doing so, even if let-7b has a lower concentration than miRNA-206, the choice of nanoparticles allows their analytical sensitivities to be adjusted thus achieving comparable detection levels. This approach minimises sample preparation, e.g., dilution with buffer, and helps mitigate the problem caused by varying absolute concentrations, enabling a more accurate and reliable analysis of the miRNAs of interest.

Figure 5.3 presents the calibration curves of the current response (Δi), i.e., the difference in current before and after addition of hydrogen peroxide, obtained from the biosensors after exposure to a range of concentrations of (A) miRNA-206, (B) miRNA-135a and (C) let-7b. As the concentration of the miRNA target rises, the absolute current signal increases. The calibration curves indicated a good linear relationship between current and logarithm of the analytes concentration, which ranges from 10^{-8} M to 10^{-14} M for miRNA-206 and 10^{-6} M to 10^{-15} M for miRNA-135a and let-7b. The best-fit least-squares regression line equation determined for miRNA-206, miRNA-135a and let-7b were I = - 0.91 x 10^{-6} log [miRNA-206] - 14.01 x 10^{-6}; I = - 1.72 x 10^{-6} log [miRNA-135a] – 26.53 x 10^{-6} and I= -1.77 x 10^{-6} log [let-7b] - 29.68 x 10^{-6}, with a regression coefficient of 0.99.



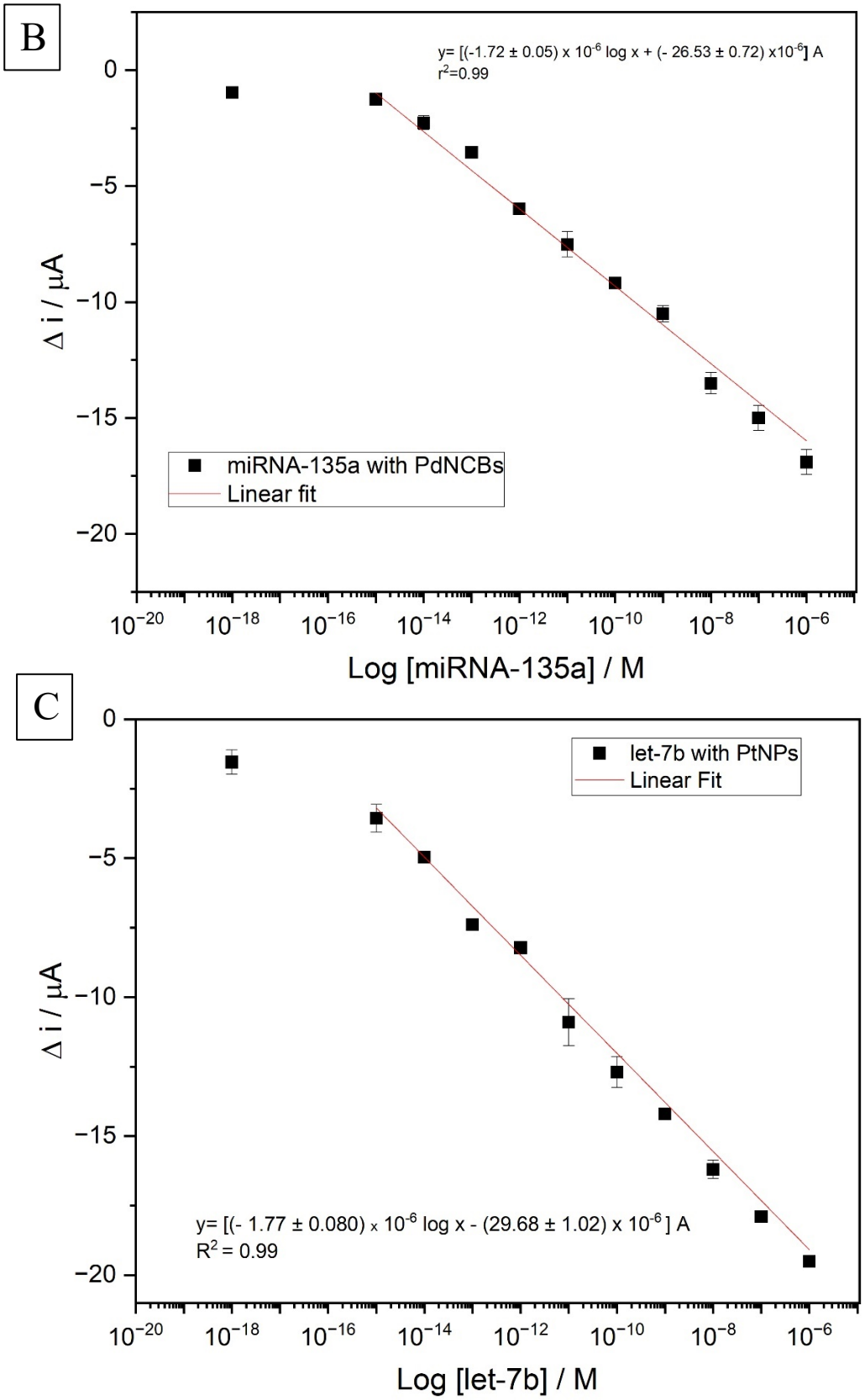


Figure 5.3. Calibration curves of the functionalized fully sandwich assay based on the amperometric variation of current and log concentration of the (A) miRNA-206, (B) miRNA-135a and (C) let-7b. Error bars were estimated as triple of the standard deviation (n = 3).

The limit of detection (LOD) was calculated from the limit of blank (LOB), as described in the experimental section of this chapter. Hence, the lowest concentration of the miRNA-206, miRNA-135a and let 7b that proved to be reliably distinguished from the background noise level were 0.6 fM, 0.42 fM, 1.17 fM, respectively.

The proposed biosensors were compared to relevant published studies on miRNA detection based in SPCEs. Table 5.1 provides an overview of several electrochemical biosensors known for their sensitivity in detecting miRNAs. The results showed a wider linear dynamic range, lower detection limit, and a higher sensitivity. The biosensor also presents the possibility to detect simultaneously up to three miRNAs. The multi-targeting ability of the sensor is desirable as it would improve accuracy of the detection. Further discussion about how to implement a multiplex platform at the developed platform is discussed in Chapter 6.

Table 5.1. Performances of the proposed electrochemical biosensor for miRNA detection compared with those of previous studies.

Platform	Target	Technique	LOD	Linear Range	Reference
SPCE	miRNA-21 miRNA-205	Amperometry	2.4 pM	8.2 - 250 pM	[23]
SPCE/MoS_2-$CuFe_2O_4$/ P2ABA	miRNA-205	SWV	0.48 pM	1 pM - 1.5 nM	[24]
GSPEs/rGO/ OMCNTs	miRNA-29b-1 miRNA-141	SWV	10 fM	10 fM - 1 nM	[25]
SPCE	miRNA-21	Amperometry	0.4 pM	1 - 100 pM	[26]
SPCE	miRNA-21	Amperometry	0.04 nM	0.14 - 10 nM	[27]
SPCE/rGO/ P2ABA/ AuNPs	miRNA-16 miRNA-21 miRNA-155	DPV	0.25 fM 3.58 fM 0.98 fM	1 fM - 10 nM 10 fM - 10 nM 1 fM - 10 nM	[28]
SPCE/PEG/ AuNPs	miRNA-155	SWV	3.57 fM	10 fM – 100 nM	[29]
SPCE	miRNA-21 miRNA-155	SWV	1.5 fM 1.8 fM	5 fM- 2 nM	[30]
20% AuS SPCE	miRNA- 206 miRNA-135a let-7b	Amperometry	0.6 fM 0.42 fM 1.17 fM	10 nM – 10 fM 1 fM – 1 μM 1 fM – 1 μM	This work

GSPE, gold screen-printed electrode; screen-printed carbon electrode (SPCE); SWV: square wave voltammetry; MoS_2, molybdenum disulfide; OMCNTs, oxidized multi-walled carbon nanotube; P2ABA, poly(2-amino-benzylamine); rGO, reduced graphene oxide; PEG, polyethylene glycol.

The reproducibility of the biosensor was assessed by analysing the relative standard deviation (RSD) of the current response (Δi) from three independent fully complementary assays. These

assays were prepared simultaneously using the same procedure. The biosensor's response was evaluated across a concentration range from 1 µM to aM. Table 5.2 shows the correlation of RSD values at different concentrations.

Table 5.2. Average variation of the current response before and after the injection of H2O2 (Δi) on functionalized fully complementary miRNA assays. These data were obtained from the calibration curves depicted in Figure 5.2 A-C. Average values and standard deviations were calculated based in the measurements performed in triplicate.

Concentration	$/\Delta i\ (\mu A)/$ miRNA-206	$/\Delta i\ (\mu A)/$ miRNA-135a	$\Delta i\ (\mu A)$ Let-7b
10^{-6} M	---	16.90 ± 0.05	19.50 ± 0.01
10^{-7} M	8.79 ± 0.02	15.02 ± 0.05	17.90± 0.03
10^{-8} M	6.83 ± 0.03	13.51 ± 0.05	16.20± 0.03
10^{-9} M	5.39 ± 0.01	10.50 ± 0.03	14.20 ± 0.01
10^{-10} M	4.61 ± 0.04	9.18 ± 0.02	12.70± 0.06
10^{-11} M	3.38± 0.02	7.51± 0.05	10.91± 0.08
10^{-12} M	2.43± 0.02	5.98 ± 0.01	8.22± 0.04
10^{-13} M	1.21± 0.03	3.54 ± 0.02	7.39± 0.08
10^{-14} M	1.06 ± 0.02	2.27 ± 0.03	4.96± 0.04
10^{-15} M	0.76 ± 0.02	1.25 ± 0.02	3.56 ± 0.05
10^{-18} M	0.52 ± 0.02	0.74 ± 0.08	1.54 ± 0.04

Across the entire concentration range, the RSD ranged from 1.95% to 3.95% for miRNA-206, 1.01% to 5.42% for miRNA-135a, and 1.07% to 5.80% for let-7b. These values fall within the acceptable limit of reliable measurements, which is described in the literature as ≤ 5% [31]. These results classify the platform as suitable for sensitive and reproducible detection of the target molecules.

Poor reproducibility of biosensors is a recurring issue in the literature and can be associated with the instability of the reference and counter electrodes. In the case of multiplex platforms, the significant difference in size between the multiple working electrodes and the counter electrode also poses challenges [32]. In this study, the sensor's good reproducibility is achieved through studies confirming the stability of the counter and reference electrodes, as well as the novel structure of the screen-printed carbon electrode (SPCE) working electrode.

To evaluate the stability of the counter and reference electrodes, cyclic voltammetry measurements were conducted on the designed 20% AuS SPEs, which included the counter and reference electrodes. These measurements involved 50 cycles in a solution containing 5 mM $[Fe(CN)_6]^{3-/4-}$ and 0.1 M KCl (data not shown). The counter and reference electrodes on the SPEs demonstrated good stability, which can have a significant impact on the current response and contribute to the sensor's reproducibility.

Furthermore, unlike other studies that deposited thick, complete layers of gold on the working electrode surface, these systems utilized only a 20% coverage of gold on the SPE surface (checked by acid voltammetry).This limited gold coverage ensures that the substantially larger surface area of the platinum counter, relative to the working electrode, prevents any interference in the current response.

5.2.3 Selectivity of the biosensor

miRNA-206

To evaluate the selectivity of the developed biosensor for miRNA-206, the response of the functionalized fully complementary assay was compared to assays with one-base mismatch 3’-UGU GUG UGA AGA AAU GUA AGG U-5’) and four-base mismatches (3'-UAU GUA

UGA AGA AAU GUA AGG U-5') in the miRNA target. The mismatched bases (U, A) in red do not complement the miRNA reporter-probe. This comparison of current (Δi) was conducted at two specific concentrations of targets, nM and pM, which not only lie in the middle of the calibration curve but also represent the range in which the target is detected in healthy control (pM) and Alzheimer's disease (AD) samples (nM).

Figure 5.4 illustrates the contrast in amperometric i-t curves between the fully complementary assay and assays containing one-base mismatch. Table 5.3 presents the average current values obtained from these assays, with n=3 measurements considered for each.

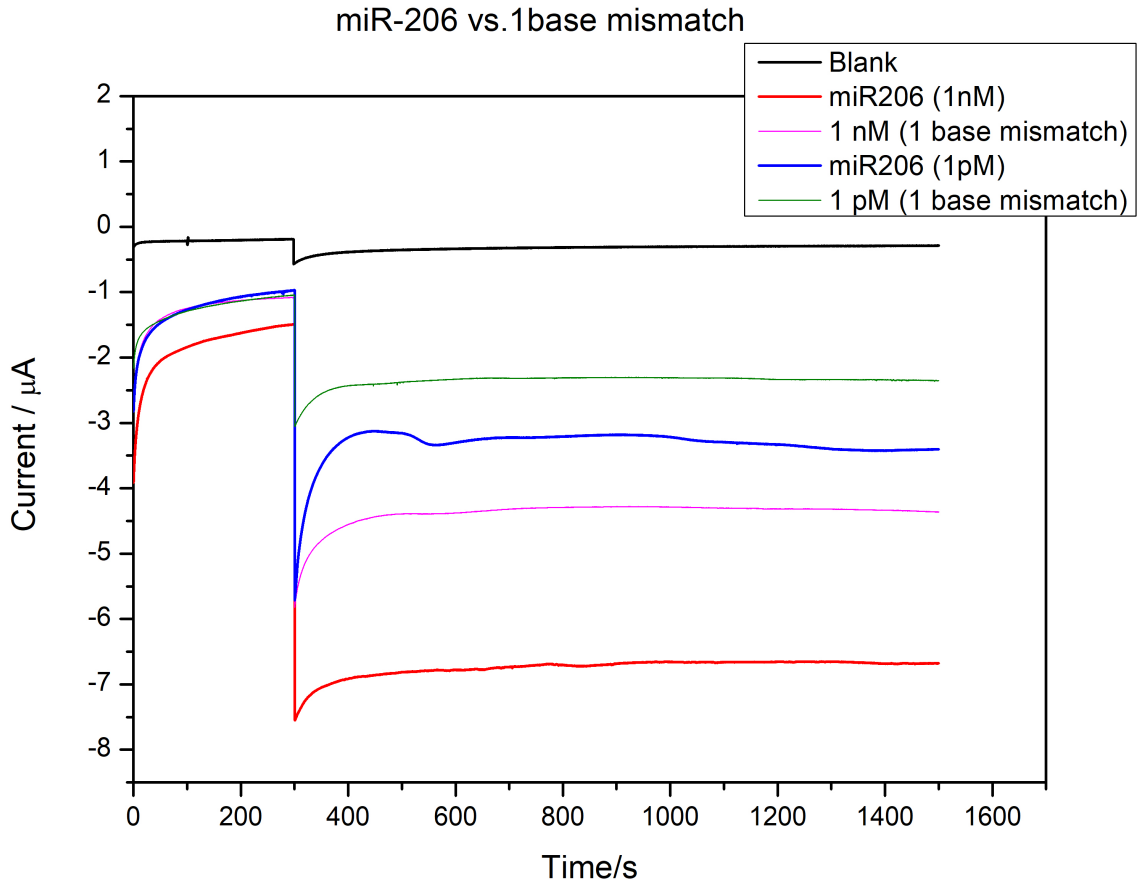


Figure 5.4. Chronoamperometric curves show the current difference between a fully complementary strand at nM and pM (red and blue line, respectively) and a 1-base mismatch strand (pink and green line) at the same concentrations. The fully complementary assay was labelled with gold nanorods. Potential applied is -0.25 V in 0.01 M PBS. The difference in current before and after the addition of 400 μM H_2O_2 is displayed. Measurements were performed in triplicate.

Table 5.3. Comparison between the current of a fully complementary nucleic acid strand and 1-base mismatch. Average values and standard deviations were calculated by measurements performed in triplicate.

Concentration	$/\Delta i\ (\mu A)/$ Fully complementary (miRNA-206)	$/\Delta i\ (\mu A)/$ 1 base mismatches (miRNA-206')	% decrease
1 pM	2.43± 0.02	1.34 ± 0.02	44.86%
1 nM	5.39 ± 0.09	2.92 ± 0.01	45.82%

The fully complementary assays exhibited a higher current signal (Δi) at both target concentrations compared to the one-base mismatch assays within the same concentration range. The current magnitude observed in the presence of a one-base mismatch was approximately 50% of the current generated by the fully complementary electrode (at the specified concentrations). The theoretical association constant (K_a) calculated for the fully complementary assay is 4.2 x 10^9 while for the one-base mismatch, it is 2.1 x 10^9. Consequently, a 50% decrease in assay response is reasonable for both nM and pM concentrations. Correspondingly, the biosensor response in the presence of the mismatch was approximately 45% for pM. These results indicate that the assay could differentiate between a fully complementary miRNA strand and one that has a single mismatched base if their concentrations are equal. However, real clinical samples are not likely to contain such closely related miRNAs.

Figure 5.5 depicts a comparison between the functionalized fully complementary assay to an assay that presents 4 base mismatches at miRNA target. Table 5.4 displays the average biosensor response at nM and pM scales for both scenarios. Based on the calculated K_a values (1.05 x10^8 for 4 base mismatches and 4.2 x10^9 for fully complementary assay), a decrease in sensitivity of approximately 97% was expected. However, when the assay was bonded to the mismatches, a decrease of only 63% for nM and 57% for pM concentrations were observed.

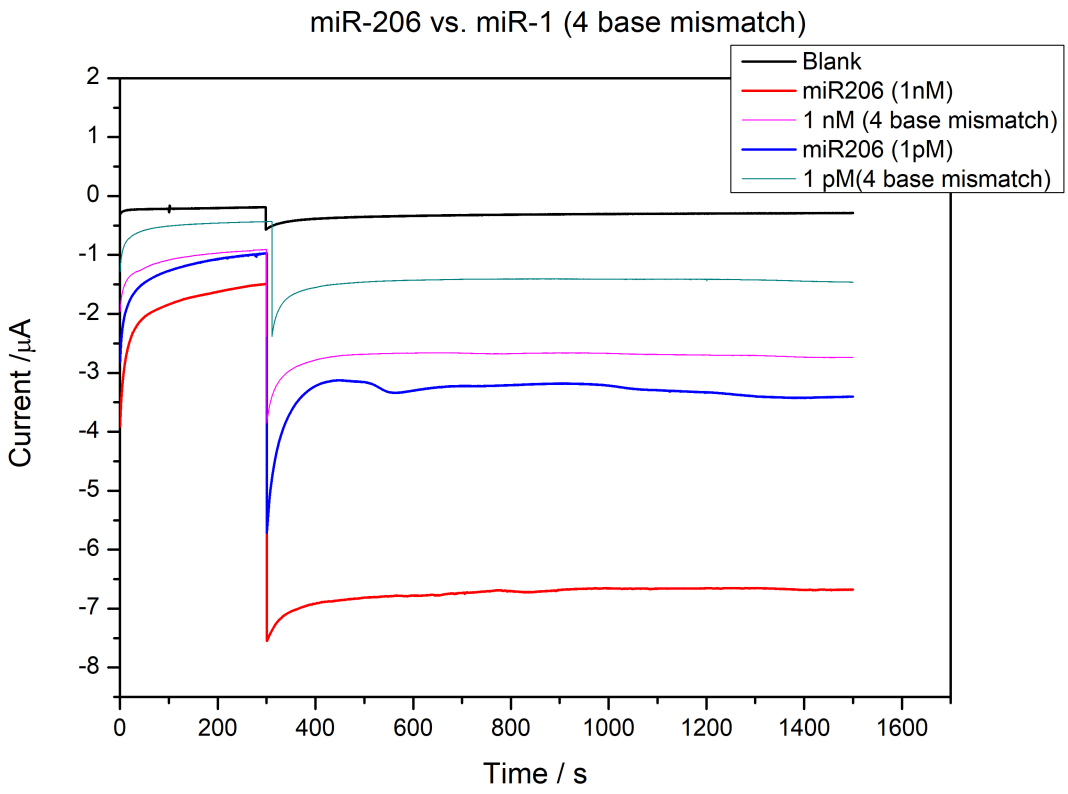


Figure 5.5. Chronoamperometric curves showing the current difference between a fully complementary strand at 1 nM and 1 pM (red and blue line) and a 4-base mismatches strand (pink and green line) at the same concentrations. The fully complementary assay was labelled with gold nanorods. Potential applied is -0.25 V in 0.01 M PBS. The difference in current before and after the addition of 400 µM hydrogen peroxide is displayed. Measurements were performed in triplicate.

Table 5.4. Comparison between the currents observed for a fully complementary nucleic acid strand and 4-bases mismatches. Average values and standard deviations were calculated by measurements performed in triplicate (n=3).

Concentration	$/\Delta i\ (\mu A)/$ Fully complementary (miRNA-206)	$/\Delta i\ (\mu A)/$ 4 base mismatches (miRNA-1)	% decrease
1 pM	2.43 ± 0.02	1.04 ± 0.02	57.01%
1 nM	5.39 ± 0.09	2.00 ± 0.02	62.89%

A possible explanation for the magnitude of the current signal being smaller than theoretically predicted is related to the position of the base mismatches in the miRNA sequence. It is important to note that the seed region, which is identical in both miRNA-1 and miRNA-206, plays a crucial role in determining miRNA-target specificity. This region typically contains the "seed match" for the target mRNA, ensuring selective binding to intended targets rather than non-target mRNAs with partially complementary sequences [33]. Despite the lower current signal than anticipated, it is still sufficient to prevent false positive responses and distinguish between targets with the similar structure.

Let- 7b

The biosensor's ability to distinguish between different members of the let-7 miRNA family was assessed by examining three representative members: let-7b (fully complementary : 3'-UUGG UGU GUU GGA UGA UGG AGU-5'), let-7g (one-base mismatch : 3'-UUGG UUU GUU GGA UGA UGG AGU-5'), and let-7f (two-base mismatch: 3'-UUGA UUU GUU GGA UGA UGG AGU-5').

Figure 5.6 displays the typical current signal responses of the functionalized fully complementary assay at the nM and pM scales, contrasted with the current signal response of the functionalized assay with (A) one-base mismatch and (B) two-base mismatches within the same concentration range. Table 5.5 shows the average current signals and the extent of signal decrease.

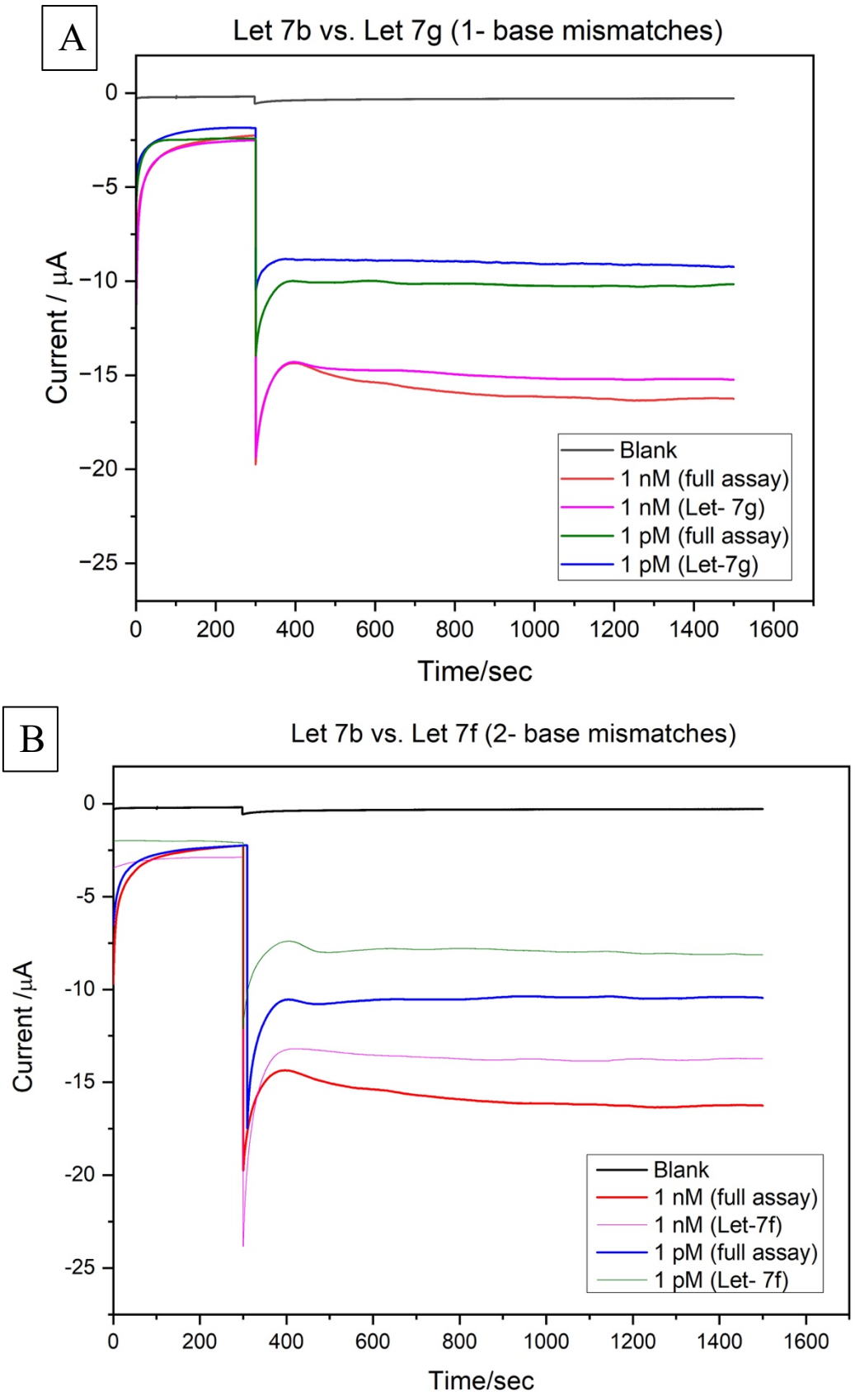


Figure 5.6. Representative chronoamperometric curves of the current difference between a fully complementary strand at nM and pM and a (A)1-base mismatches strand (and (B) 2-base mismatches

at the same concentrations (n=3). The fully complementary assay was labelled with platinum nanoparticles. Potential applied is -0.50 V in 0.01 M PBS. The difference in current before and after the addition of 400 µM hydrogen peroxide is displayed.

Table 5.5. Comparison between the current of a fully complementary let-7b assay and 1-base and 2 base mismatches. Average values and standard deviations were calculated by measurements performed in triplicate.

Concentration	$/\Delta i\ (\mu A)/$ Fully complementary (let-7b)	$/\Delta i\ (\mu A)/$ 1-base mismatch (let-7g)	$/\Delta i\ (\mu A)/$ 2-base mismatches (let-7f)	% decrease (1-base ; 2-base mismatches)
1 pM	8.22 ± 0.04	7.39 ± 0.03	6.49 ± 0.01	10.03% ; 21.05%
1 nM	14.20 ± 0.01	12.82 ± 0.02	11.30 ± 0.08	9.74% ; 20.42%

Based on the theorical calculation of association constants and in comparison with a fully complementary assay (K_a = 2.82 x 10^9), it is expected that a one base mismatch (K_a = 2.53 x10^9) will result in an approximately 8% decrease in current signal, while two-base mismatches (2.05 x 10^9) should lead to a 24% decrease in current signal. Consistent with these predictions, the amperometric i-t curves demonstrate a signal reduction of approximately 20% for both pM and nM concentrations for two base mismatches, and from approximately 10% for pM and nM concentrations of the one base mismatch.

The lower decrease in the current response despite the presence of base mismatches can be attributed to three main factors. Firstly, the shared seed region between the mismatches and the fully complementary assay, along with the specific characteristics of the mismatches, play a significant role. Additionally, the presence of G:U wobble pairs within the mismatches and the mismatches being located at the end of the sequence contribute to this phenomenon.

The seed region, spanning positions 2 to 7 from the 5' end of the miRNA molecule, acts as a guide for target recognition and binding . When a mismatch occurs in the seed region, it disrupts the complementarity between the miRNA and the target mRNA sequence. This disruption leads to a less stable binding complex and a decrease in the number of bonds formed between the miRNA and the complementary sequence on the target mRNA [33][34]. However, since the fully complementary assay and mismatches have an identical seed region, the binding process tends to proceed along the entire sequence in a similar way to the fully complementary target. Consequently, mismatches outside the seed region would be more challenging to detect as they have a moderate impact on the overall binding affinity.

In this case, the mismatches present as G:U wobble pairs. This type of mismatch occurs when a G nucleotide in the miRNA sequence pairs with a U nucleotide in the target mRNA sequence, despite the mismatch. The G:U wobble pair is partially tolerated within the sequence extension due to the formation of some hydrogen bonds, although fewer than the canonical Watson-Crick base pairs (G:C and A:U). As a result, the G:U wobble pair retains a certain level of interaction between the miRNA and the target mRNA, contributing to a lower decrease in binding strength [35].

Furthermore, when two base mismatches occur, with one being a wobble pair and the other located at the end of the sequence, the disruptive impact on pairing (i.e. binding efficiency) is diminished. Mismatches at the end of the sequence have a lower impact on the overall miRNA-target binding, further contributing to the observed lower decrease in the current response [36].

These factors collectively influence the binding affinity and stability of miRNA-target interactions, highlighting the crucial role of seed region complementarity in efficient miRNA-mediated gene regulation. It is essential to note that the assay is run under kinetic control conditions. The equilibrium constant determines the binding strength between the biosensor and the miRNA targets. In the case of mismatches, the changing equilibrium constant affects the stability of the binding complex, resulting in the observed variations in the current signal. Therefore, the equilibrium constant plays a crucial role in determining the impact of mismatches on the current response.

It is important to note that distinguishing between highly similar miRNA family members can be challenging, and a combination of multiple approaches, such as PCR, bioinformatics tools,

and high-throughput sequencing technologies, is often employed for accurate identification. The fact that the developed biosensor exhibits current variations within the range predicted by theoretical calculations demonstrates the selectivity of the screen carbon printed electrodes (SPCE) platform. Therefore, it not only can differentiate between false positives, but it can also accurately detect current values without the need for additional techniques.

miRNA-135a

The selectivity of the biosensor towards different members of the miRNA-135 family was evaluated using two representative members: miRNA-135a (3'-AGUGU AUC CUU AUU UUU CGG UAU-5'), which is fully complementary to the functionalized assay, and miRNA-135b, which contains a one-base mismatch (3'-AGUGU AUC CUA ACU UUU CGG UAU-5')

Figure 5.7 presents the standard current signal responses of the functionalized fully complementary assay at both the nM and pM scales, comparing them to the current signal response of the functionalized assay with a one-base mismatch within the identical concentration range. Table 5.6 provides the average current signals and the magnitude of the signal decrease.

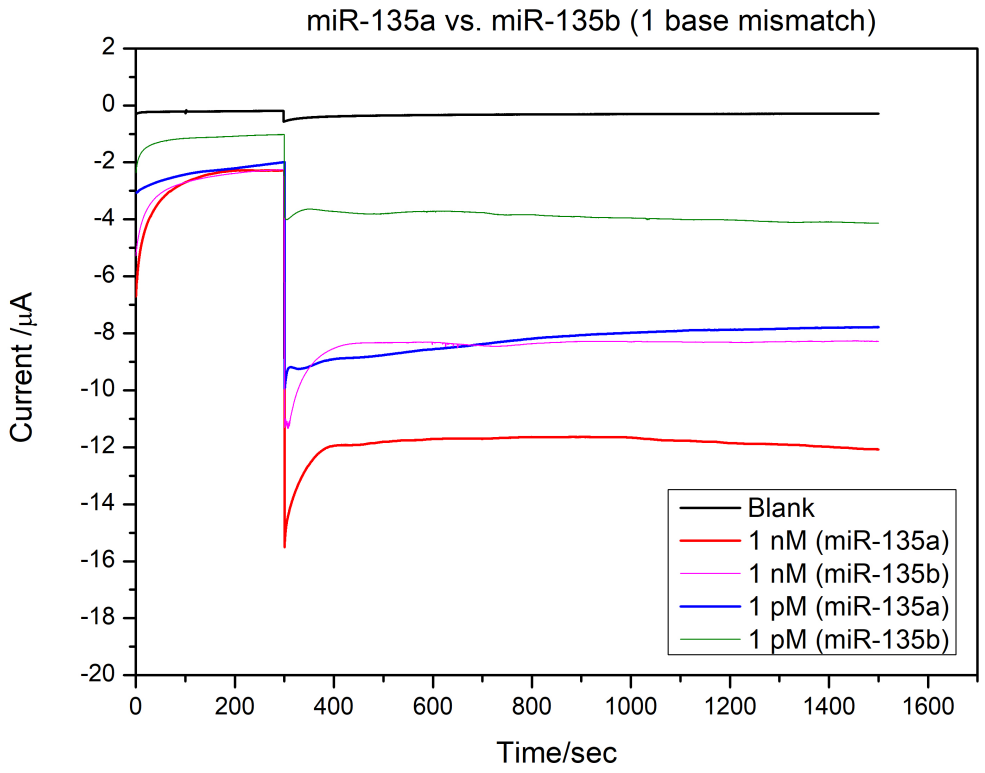


Figure 5.7. Chronoamperometric curves show the current difference between a fully complementary strand at nM and pM (red and blue line) and a 1-base mismatch strand (pink and green line) at the same concentrations (n=3). The fully complementary assay was labelled with palladium nanocubes. Potential applied is -0.375 V in 0.01 M PBS.The difference in current before and after the addition of 400 μM H_2O_2 is displayed.

Table 5.6. Comparison between the current of a fully complementary nucleic acid strand and 1-base mismatch. Average values and standard deviations were calculated by measurements performed in triplicate.

Concentration	$/\Delta i\ (\mu A)/$ Fully complementary (miRNA-135a)	$/\Delta i\ (\mu A)/$ 1 base mismatch (miRNA-135b)	% decrease
1 pM	5.98± 0.01	3.14± 0.04	44.19%
1 nM	10.50 ± 0.03	6.01± 0.04	42.76%

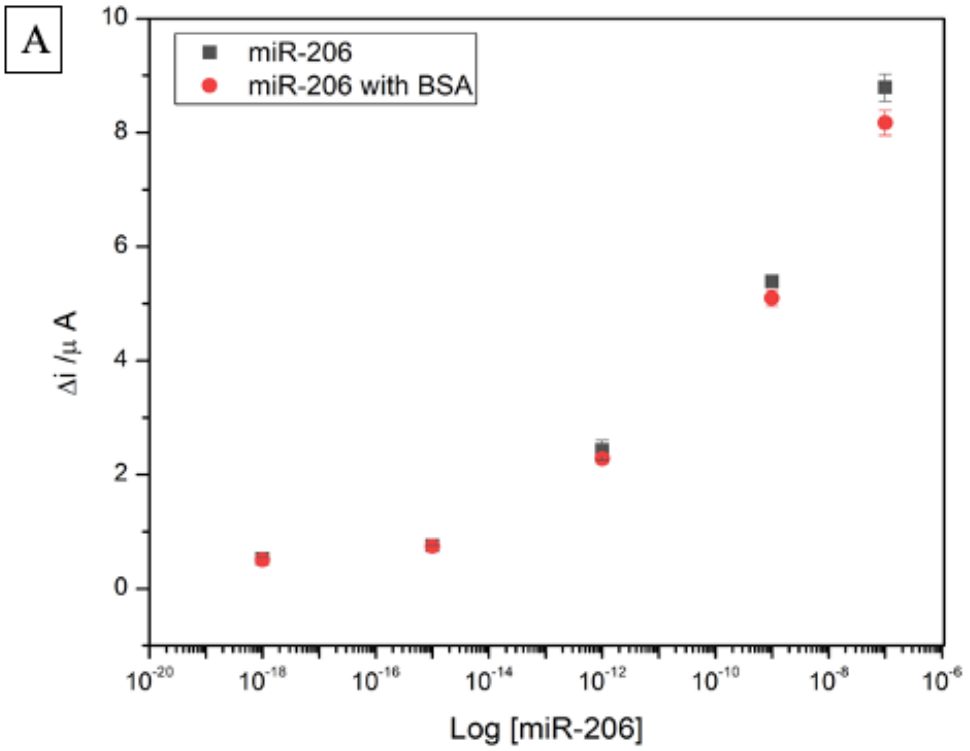
The variation in current signal (Δi) follows the anticipated pattern, with a higher variation observed when the miRNA target is fully complementary to the functionalized assay at both the nM and pM ranges. Conversely, a sequence containing a one-base mismatch results in a lower variation. The theoretical calculation of the association constants predicts that miRNA-135a has a K_a value of 2.74 x 10^9, while miRNA-135b has a value of 1.59 x 10^9. Thus, the binding of the functionalized assay to the mismatched sequence is expected to generate a reduction in current signal of 42%. The experimental results closely align with these predictions, showing a reduction from 43 to 44% at the high and low concentration ranges.

Considering the difference between the expected decrease in current and the obtained value is within 5%, the platform can be deemed highly specific for the detection of miRNA-135a, demonstrating sufficient sensitivity to differentiate between a fully complementary miRNA strand and one that contains a single mismatched base.

5.2.4 Non-specific binding of BSA

The sensor's performance regarding non-specific binding of proteins was evaluated using bovine serum albumin (BSA) as a surrogate for human serum albumin (HSA), which is naturally present in human plasma samples. Since the ultimate goal of this project is to employ the biosensor for miRNA detection in circulating blood, it is crucial to ensure its specificity against high-affinity molecules. If BSA binds non-specifically to the miRNA capture-probe or other assay components, it competes with the specific binding of the miRNA target, thereby reducing signal generated the miRNA-target interaction. This interference can result in several complications, including false-negative signals, reduced sensitivity, increased background noise, and compromised assay performance. These issues can introduce variability and inconsistencies in the results, making it challenging to derive meaningful conclusions from the assay data.

To obtain more realistic data on the impact caused by this protein, BSA was tested at a concentration that is close to the physiological concentration of HAS in blood, approximately 1 mM. Figure 5. 8 A-C illustrates the assessment of interference at various concentrations (ranging from 1 μM to 1 aM) of the target miRNA of interest (miRNA-206, miRNA-135a, let-7b). The obtained results were then compared to samples containing miRNA in the absence of BSA. Table 5.7; 5.8; and 5.9 provide a summary of the data obtained from these experiments.


A
miR-206
miR-206 with BSA
Δi /μ A
Log [miR-206]
10
8
6
4
2
0
10-20
10-18
10-16
10-14
10-12
10-10
10-8
10-6

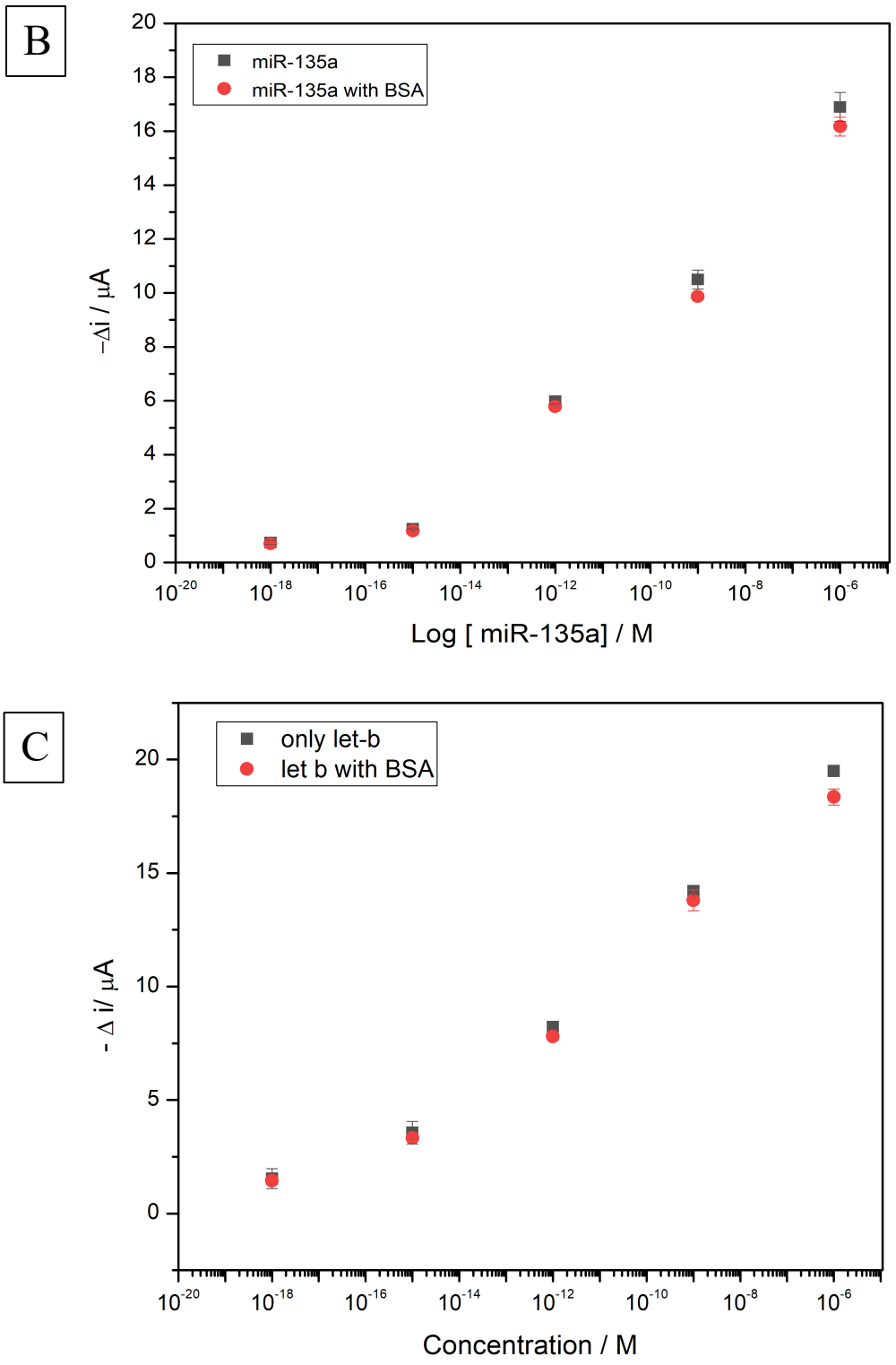


Figure 5.8. Calibration curves of functionalized assays at a range of concentrations (from 1μM to aM) of (A) miRNA-206; (B) miRNA-135a; (C)let-7b and 1 μM of miRNA reporter-probe without any interfering assay (black line) and in an environment where BSA is present (red line). The error bars were indicated on the curve (n = 3). Potential applied is (A) -0.25V; (B) -0.375 V; (C) -0.5V in 0.01M PBS.

Table 5.7. Comparison between the current of a functionalized fully complementary miRNA-206 assay with and without an environment of BSA. Average values and standard deviations were calculated by measurements performed in triplicate.

Concentration of miRNA-206 (M)	/Δi (μA)/ miRNA-206	/Δi (μA)/ miRNA-206 + BSA	% decrease
$1x10^{-7}$	8.79 ± 0.02	8.17 ± 0.02	5.70
$1x10^{-9}$	5.39 ± 0.01	5.10 ± 0.01	4.39
$1x10^{-12}$	2.43± 0.02	2.28 ± 0.01	2.56
$1x10^{-15}$	0.76 ± 0.02	0.74 ± 0.02	2.42
$1x10^{-18}$	0.52 ± 0.02	0.51 ± 0.03	3.24

Table 5.8. Comparison between the current of a functionalized fully complementary miRNA-135a assay with and without an environment of BSA. Average values and standard deviations were calculated by measurements performed in triplicate.

Concentration of miRNA-135a (M)	/Δi (μA)/ miRNA-135a	/Δi (μA)/ miRNA-135a + BSA	% decrease
$1x10^{-6}$	16.90 ± 0.05	16.20 ± 0.04	4.14
$1x10^{-9}$	10.50 ± 0.03	9.88 ± 0.01	4.40
$1x10^{-12}$	5.98± 0.01	5.78 ± 0.05	3.35
$1x10^{-15}$	1.25 ± 0.02	1.18 ± 0.07	5.60
$1x10^{-18}$	0.74 ± 0.08	0.69 ± 0.06	6.20

Table 5.9. Comparison between the current of a functionalized fully complementary let-7b assay with and without an environment of BSA. Average values and standard deviations were calculated by measurements performed in triplicate.

Concentration of Let-7b (M)	/Δi (μA)/ Let-7b	/Δi (μA)/ Let-7b + BSA	% decrease
$1x10^{-6}$	19.50 ± 0.01	18.35 ± 0.03	5.90
$1x10^{-9}$	14.20 ± 0.01	13.80 ± 0.05	2.82
$1x10^{-12}$	8.22± 0.04	7.79 ± 0.02	5.17
$1x10^{-15}$	3.56 ± 0.05	3.33 ± 0.01	6.46
$1x10^{-18}$	1.54 ± 0.04	1.44 ± 0.03	6.50

The amperometric response of the functionalized assays, specifically miRNA-206, miRNA-135a, and let-7b, demonstrated linearity across a wide concentration range from 1 μM to 1 aM. The decrease in current response observed in assays with non-specific binding compared to fully complementary assays was limited, with maximum reductions of 5.70% for miRNA-206, 6.20% for miRNA-135a, and 6.50% for let-7b.

These findings emphasize the strong resistance of the sensor to non-specific binding of BSA at different target concentrations. The change in current response (Δi) directly reflects the electrocatalytic reduction of hydrogen peroxide facilitated by the nanoparticles. This reduction occurs when the target miRNAs hybridize with the miRNA reporter-probe, forming a specific double helix structure. In cases where the miRNA reporter-probe fails to fully bind to the target miRNA sequence, a decrease in Δi values occurs. This decrease signifies a differentiation process by the system, allowing it to distinguish between different target miRNAs based on the extent of binding between the reporter-probe and the target sequence.

Importantly, despite the high BSA content in the samples, the sensor does not experience significant interference in miRNA detection. This result suggests that there is a low propensity for the biosensor to become fouled by non-specific adsorption of proteins that could disrupt its

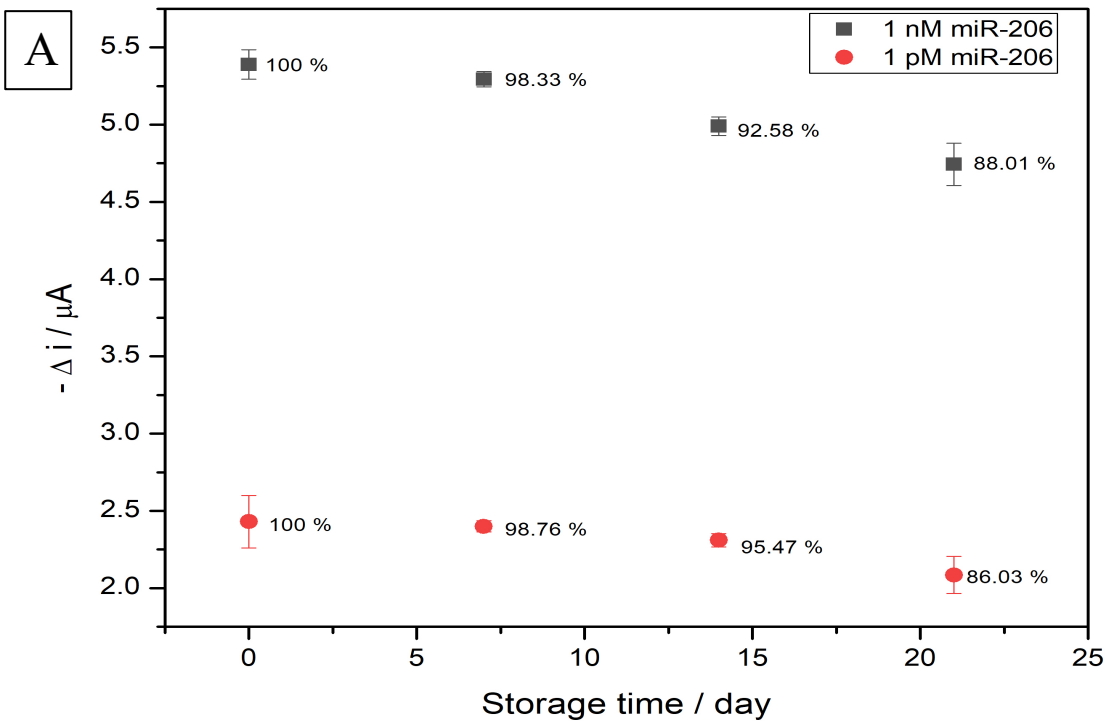
functionality. The sensor's ability to resist non-specific binding contributes to its reliability and suitability for accurate miRNA detection applications.

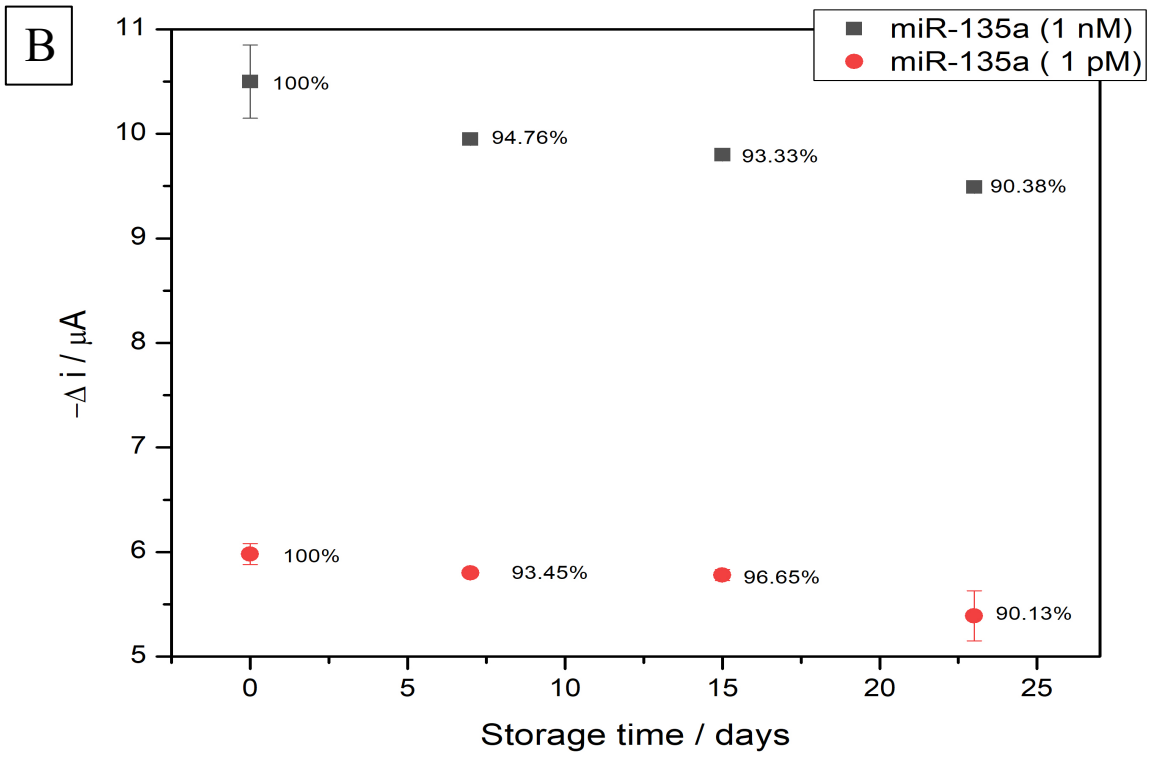
Additionally, the proposed biosensor offers significant advantages for routine miRNA analysis. Unlike existing miRNA assays that require highly purified RNA samples, this biosensor eliminates the need for chemical/biological ligation and PCR amplification [37]. Consequently, it enables direct profiling of miRNAs with minimal or no sample pre-treatment, streamlining the analysis process.

5.2.5 Stability of the biosensor

To investigate the stability of the developed biosensor, independent electrodes containing the sensing phase and miRNA capture-probes were prepared. These electrodes were stored in an immobilization buffer at 4 °C for 21 days. The study involved testing 9 fully complementary assays, with triplicate samples for each assay. The samples were functionalized with either AuNRDs, PdNCBs, or PtNPs and hybridized to miRNA-206, miRNA-135a, and let-7b, respectively. Amperometric analysis was conducted to study the behaviour of the platform at specific miRNA targets at nanomolar (nM) and picomolar (pM) scales, with measurements taken at 4-5 day intervals.

Figure 5.9 presents the variation in current response (Δi) of the 20% AuS SPCE platform hybridized with (A) miRNA-206, (B) miRNA-135a, and (C) let-7b during different storage times of the sensing phase.


A
1 nM miR-206
1 pM miR-206
100 %
98.33 %
92.58 %
88.01 %
100 %
98.76 %
95.47 %
86.03 %
- Δ i / μA
Storage time / day


B
miR-135a (1 nM)
miR-135a (1 pM)
100%
94.76%
93.33%
90.38%
100%
93.45%
96.65%
90.13%
–Δ i / μA
Storage time / days

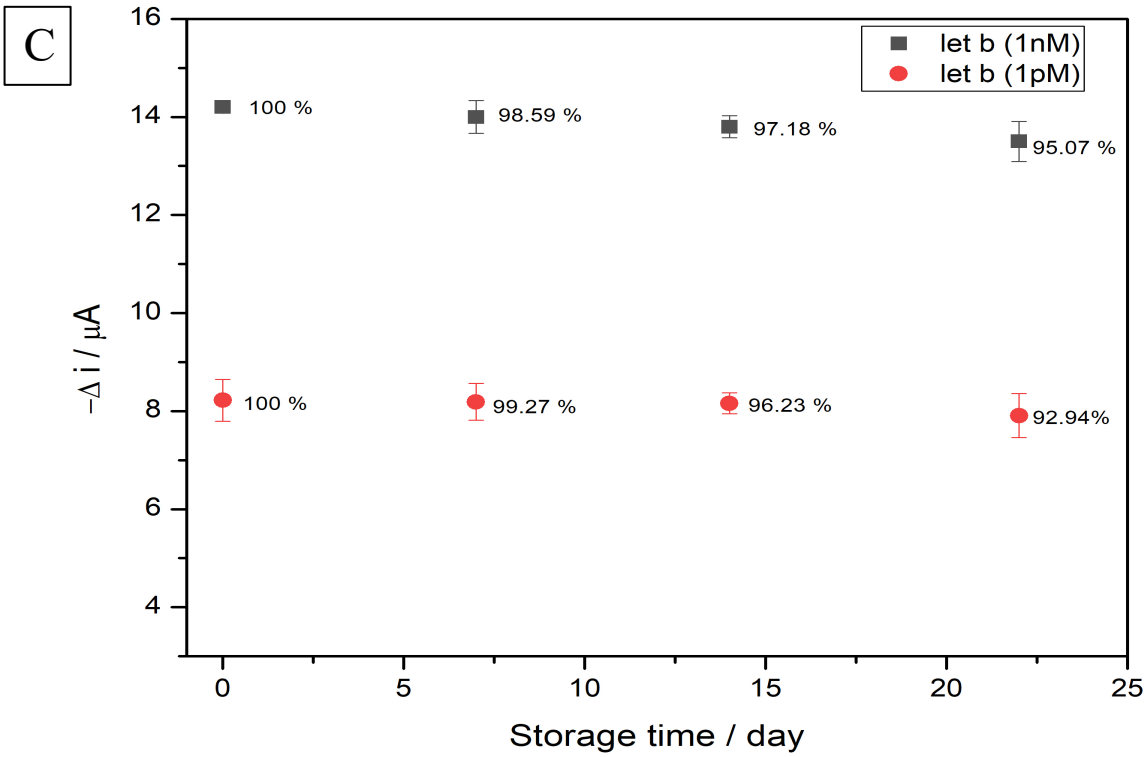


Figure 5.9. Time dependence of the amperometric current response of the biosensor to two different concentrations (1 nM and 1 pM) of (A)miRNA-206; (B) miRNA-135a; (C) let-7b after storage at 4 °C for 21 days. The number next to each data point represents the average percent of response compared to the freshly prepared biosensors. Errors bars estimated as triple of the standard deviations (n=3).

To assess the stability of the biosensor, the response after 21 days of storage was compared to the signal of freshly prepared biosensors. For the assay with 1 nM of miRNA-206, the biosensor's response after 21 days of storage was approximately 88% of its original signal. For the assay with 1 pM of miRNA-206 under the same storage conditions, the biosensor's response is approximately 86% of the original signal.

For the sensing phase stored for 21 days and hybridized to miRNA-135a, the current signal maintained from 90.13% (pM) to 90.38% (nM) of its original magnitude. Similarly, when the sensing phase was stored for 21 days and hybridized with let-7b, the current signal remained at 92.94% (pM) to 95.07% (nM) of its original value.

Based on these results, it is suggested that the monolayer formed by the miRNA capture-probe at the 20% AuS SPCE remains stable for several days. The biosensor retains good activity for

hybridization, indicating that the immobilized sensing phase retains its functionality over the storage period.

The decrease in current signal throughout the analysed period is likely caused by exogenous ribonucleases (RNAse) that decompose the capture-probe strands on the electrode surface. The varying stability of the nanoparticles immobilized to the miRNA-reporter reporter-probe also contributes to the decrease in current signal over time. This can be attributed to the fact that the binding reaction between the nanoparticles and the miRNA reporter-probe occurred on "day zero" in an Eppendorf and subsequent storage took place at 4 degrees Celsius in the fridge. For subsequent analyses, the previously prepared functionalized reporter-probe was utilized to complete the assay.

These results not only demonstrate the formation of a stable sensing platform but also highlight its significance in reducing analysis time and enabling the storage of biosensors for future use. This is particularly important in the context of point-of-care sensors, as they are required to have a satisfactory shelf-life. By establishing a stable sensing phase, the biosensors can be stored for extended periods and utilized whenever needed. This capability is crucial for point-of-care applications where immediate testing may not always be feasible, allowing healthcare professionals to rely on the biosensors even after a certain period of time has elapsed. Therefore, the development of a highly stable sensing platform addresses the need for both prolonged shelf-life and the convenience of utilizing biosensors at the point of care.

5.3 Conclusion

In conclusion, this study presents a proof-of-concept investigation of an innovative electrochemical platform designed for detecting biomarkers associated with neurological diseases. The development of a screen-printed carbon electrode incorporating 20% (w/w) gold microspheres in the carbon ink significantly advances the field of electrochemical biosensors. The inclusion of a small percentage of gold microspheres has notably increased the active surface area of the SPCE, surpassing that of conventional SPCE surfaces, resulting in improved miRNA capture-probe binding efficiency. Additionally, the incorporation of different-shaped metal nanoparticle labels, such as gold nanorods, platinum nanoparticles, and palladium nanocubes, enhances the biosensor's performance by amplifying the signal from the miRNA targets and generating distinguishable current signals. This approach allows for sensitivity

adjustment based on the selection of different nanoparticles, catering to the specific requirements of different miRNAs.

The biosensor exhibits a wide dynamic range, as indicated by the calibration curves. These curves display a linear relationship between the current and the logarithm of the analyte concentration across a broad range spanning 6 orders of magnitude for miR-206 and 9 orders of magnitude for miR-135a and let-7b. It demonstrates high sensitivity for detecting ultralow concentrations of the biomarkers, with LOD values of 0.6 fM for miRNA-206, 0.42 fM for miRNA-135a, and 1.17 fM for let-7b. When compared to other relevant electrochemical biosensors for miRNA detection, the proposed biosensor outperforms in terms of linear dynamic range, detection limit, and sensitivity.

The biosensor also demonstrates selectivity for the target miRNAs, as evidenced by higher current signals for the fully complementary assays compared to assays with one-base and four-base mismatches. Additionally, the biosensor's reproducibility falls within acceptable limits, with RSD values ranging from 1.95% to 3.95% for miRNA-206, 1.01% to 5.42% for miRNA-135a, and 1.07% to 5.80% for let-7b. The good reproducibility is attributed to the stability of the counter and reference electrodes, as well as the limited gold coverage on the working electrode surface.

The biosensor exhibits strong resistance to non-specific binding of BSA, with limited decreases in current response observed (~6%) when compared to fully complementary assays. This resistance indicates the biosensor's reliability and suitability for accurate miRNA detection application. Additionally, the biosensor offers advantages for routine miRNA analysis by eliminating the need for extensive sample pre-treatment thus streamlining the analysis process.

Furthermore, the developed biosensor exhibits good stability and functionality even after being stored for 21 days. Comparisons with freshly prepared biosensors reveal that it retains a significant portion of its original signal. The formation of a stable monolayer by the miRNA capture-probe on the 20% AuS screen-printed carbon electrode (SPCE) indicates the longevity and efficiency of the immobilized sensing phase. These findings highlight the practical significance of the highly stable sensing platform, reducing analysis time and enabling extended storage. The stability is particularly valuable in point-of-care applications, ensuring

a satisfactory shelf-life and enabling healthcare professionals to rely on the biosensors even after an extended duration.

Overall, the developed platform shows promising potential for multiplex detection. Its sensitive and selective detection of multiple miRNAs, exemplified by the successful detection of miRNA-206, miRNA-135a, and let-7b, positions it as an good platform for simultaneous detection of multiple miRNA targets. This capability significantly improves the accuracy of neurological disease detection, as miRNAs' multi-targeting ability correlates with disease diagnosis accuracy. Simultaneous detection of multiple targets is crucial for enhancing diagnostic precision. Additional design improvements could further enhance its potential application as a point-of-care device in clinical diagnostics.

5.4 References

[1] Thakur, K. T., Albanese, E., Giannakopoulos, P., Jette, N., Linde, M., Prince, M. J., Steiner, T. J., & Dua, T. (2016). Neurological Disorders. In V. Patel (Eds.), et al., Mental, Neurological, and Substance Use Disorders: Disease Control Priorities, Third Edition (Volume 4). The International Bank for Reconstruction and Development / The World Bank. Retrieved from https://www.ncbi.nlm.nih.gov/books/NBK361950/doi:10.1596/978-1-4648-0426-7_ch5.

[2] Shabaninejad, Z., Yousefi, F., Movahedpour, A., Ghasemi, Y., Dokanehiifard, S., Rezaei, S., Aryan, R., Savardashtaki, A., & Mirzaei, H. (2019). Electrochemical-based biosensors for microRNA detection: Nanotechnology comes into view. *Analytical biochemistry*, *581*, 113349. https://doi.org/10.1016/j.ab.2019.113349

[3] Renedo, O. D., Alonso-Lomillo, M. A., & Martínez, M. J. (2007). Recent developments in the field of screen-printed electrodes and their related applications. *Talanta*, *73*(2), 202–219. https://doi.org/10.1016/j.talanta.2007.03.050

[4] Paimard, G., Ghasali, E., & Baeza, M. (2023). Screen-Printed Electrodes: Fabrication, Modification, and Biosensing Applications. *Chemosensors, 11*(2), 113. https://doi.org/10.3390/chemosensors11020113

[5] Rasheed, P. A., & Sandhyarani, N. (2017). Electrochemical DNA sensors based on the use of gold nanoparticles: a review on recent developments. *Microchimica Acta, 184*, 981–1000. https://doi.org/10.1007/s00604-017-2143-1.

[6] Xia, N., & Zhang, L. (2014). Nanomaterials-Based Sensing Strategies for Electrochemical Detection of MicroRNAs. *Materials (Basel, Switzerland), 7*(7), 5366–5384. https://doi.org/10.3390/ma7075366

[7] Mistry, K. K., Layek, K., Mahapatra, A., RoyChaudhuri, C., & Saha, H. (2014). A review on amperometric-type immunosensors based on screen-printed electrodes. *The Analyst*, *139*(10), 2289–2311. https://doi.org/10.1039/c3an02050a

[8] Pimalai, D., Putnin, T., Waiwinya, W., Chotsuwan, C., Aroonyadet, N., & Japrung, D. (2021). Development of electrochemical biosensors for simultaneous multiplex detection of microRNA for breast cancer screening. *Microchimica Acta, 188*, 329. https://doi.org/10.1007/s00604-021-04995-8

[9] Niu, W., Zhang, L., Xu, G. (2010). Shape-Controlled Synthesis of Single-Crystalline Palladium Nanocrystals. *ACS Nano, 4* (4),1987-1996. https://doi.org/10.1021/nn100093y.

[10] Liu, B., & Liu, J. (2017). Methods for preparing DNA-functionalized gold nanoparticles, a key reagent of bioanalytical chemistry. *Analytical Methods, 9*, 2633. https://doi.org/10.1039/c7ay00368d

[11] Bard, A. J., & Faulkner, L. R. (2000). Electrochemical methods: fundamentals and applications (2nd ed.). John Wiley & Sons.

[12] Cai, X., , Tanner, E. E. L., , Lin, C., , Ngamchuea, K., , Foord, J. S., , & Compton, R. G., (2018). The mechanism of electrochemical reduction of hydrogen peroxide on silver nanoparticles. *Physical chemistry chemical physics*, *20*(3), 1608–1614. https://doi.org/10.1039/c7cp07492a

[13] Gao, Z., & Yang, Z. (2006). Detection of microRNAs using electrocatalytic nanoparticle tags. *Analytical Chemistry*, *78*(5), 1470-1477. https://doi.org/10.1021/ac051726m

[14] Morais, A., Rijo, P., Batanero, B., & Nicolai, M. (2022). Low Platinum-Content Electrocatalysts for Highly Sensitive Detection of Endogenously Released H_2O_2. *Biosensors, 12* (9), 672. https://doi.org/10.3390/bios12090672

[15] Ulusoy, U. (2023). A Review of Particle Shape Effects on Material Properties for Various Engineering Applications: From Macro to Nanoscale. *Minerals, 13*(1), 91. http://dx.doi.org/10.3390/min13010091

[16] Bishop, K. J., Wilmer, C. E., Soh, S., & Grzybowski, B. A. (2009). Nanoscale forces and their uses in self-assembly. *Small (Weinheim an der Bergstrasse, Germany)*, *5*(14), 1600–1630. https://doi.org/10.1002/smll.200900358

[17] Baloun, J., Bencurova, P., Totkova, T., Kubova, H., Hermanova, M., Hendrych, M., Pail, M., Pospisilova, S., & Brazdil, M. (2020). Epilepsy miRNA Profile Depends on the Age of Onset in Humans and Rats. *Frontiers in neuroscience*, *14*, 924. https://doi.org/10.3389/fnins.2020.00924

[18] Vangoor, V. R., Reschke, C. R., Senthilkumar, K., van de Haar, L. L., de Wit, M., Giuliani, G., Broekhoven, M. H., Morris, G., Engel, T., Brennan, G. P., Conroy, R. M., van Rijen, P. C., Gosselaar, P. H., Schorge, S., Schaapveld, R. Q. J., Henshall, D. C., De Graan, P. N. E., & Pasterkamp, R. J. (2019). Antagonizing Increased *miR-135a* Levels at the Chronic Stage of Experimental TLE Reduces Spontaneous Recurrent Seizures. *The Journal of neuroscience : the official journal of the Society for Neuroscience*, *39*(26), 5064–5079. https://doi.org/10.1523/JNEUROSCI.3014-18.2019

[19] Cattani, A. A., Allene, C., Seifert, V., Rosenow, F., Henshall, D. C., & Freiman, T. M. (2016). Involvement of microRNAs in epileptogenesis. *Epilepsia*, *57*(7), 1015–1026. https://doi.org/10.1111/epi.13404

[20] Kan, A. A., van Erp, S., Derijck, A. A., de Wit, M., Hessel, E. V., O'Duibhir, E., de Jager, W., Van Rijen, P. C., Gosselaar, P. H., de Graan, P. N., & Pasterkamp, R. J. (2012). Genome-wide microRNA profiling of human temporal lobe epilepsy identifies modulators of the immune response. *Cellular and molecular life sciences*, *69*(18), 3127–3145. https://doi.org/10.1007/s00018-012-0992-7

[21] Vangoor, V. R., Reschke, C. R., Senthilkumar, K., van de Haar, L. L., de Wit, M., Giuliani, G., Broekhoven, M. H., Morris, G., Engel, T., Brennan, G. P., Conroy, R. M., van Rijen, P. C., Gosselaar, P. H., Schorge, S., Schaapveld, R. Q. J., Henshall, D. C., De Graan, P. N. E., & Pasterkamp, R. J. (2019). Antagonizing Increased *miR-135a* Levels at the Chronic Stage of Experimental TLE Reduces Spontaneous Recurrent Seizures. *The Journal of neuroscience : the official journal of the Society for Neuroscience*, *39*(26), 5064–5079. https://doi.org/10.1523/JNEUROSCI.3014-18.2019

[22] Han, C. L., Liu, Y. P., Guo, C. J., Du, T. T., Jiang, Y., Wang, K. L., Shao, X. Q., Meng, F. G., & Zhang, J. G. (2020). The lncRNA H19 binding to let-7b promotes hippocampal glial cell activation and epileptic seizures by targeting Stat3 in a rat model of temporal lobe epilepsy. *Cell proliferation*, *53*(8), e12856. https://doi.org/10.1111/cpr.12856

[23] Torrente-Rodríguez, R. M., Montiel, V. C. R. - V., Campuzano, S., Farchado-Dinia, M., Barderas, R., Segundo-Acosta, P. S., Montoya, J. J., & Pingarron, J. M. (2016). Fast Electrochemical miRNAs Determination in Cancer Cells and Tumor Tissues with Antibody-Functionalized Magnetic Microcarriers. *ACS Sensors, 1*(7), 896–903.https://doi.org/10.1021/acssensors.6b00266

[24] Chand, R., , Ramalingam, S., , & Neethirajan, S., (2018). A 2D transition-metal dichalcogenide MoS_2 based novel nanocomposite and nanocarrier for multiplex miRNA detection. *Nanoscale*, *10*(17), 8217–8225. https://doi.org/10.1039/c8nr00697k

[25] Tran, H. V., Piro, B., Reisberg, S., Huy Nguyen, L., Dung Nguyen, T., Duc, H. T., & Pham, M. C. (2014). An electrochemical ELISA-like immunosensor for miRNAs detection based on screen-printed gold electrodes modified with reduced graphene oxide and carbon nanotubes. *Biosensors & bioelectronics*, *62*, 25–30. https://doi.org/10.1016/j.bios.2014.06.014

[26] Vargas, E., Torrente-Rodríguez, R. M., Ruiz-Valdepeñas Montiel, V., Povedano, E., Pedrero, M., Montoya, J. J., Campuzano, S., & Pingarrón, J. M. (2017). Magnetic Beads-Based Sensor with Tailored Sensitivity for Rapid and Single-Step Amperometric Determination of miRNAs. *International journal of molecular sciences*, *18*(11), 2151. https://doi.org/10.3390/ijms18112151

[27] Campuzano, S., Torrente-Rodríguez, R. M., López-Hernández, E., Conzuelo, F., Granados, R., Sánchez-Puelles, J. M., & Pingarrón, J. M. (2014). Magnetobiosensors based on viral protein p19 for microRNA determination in cancer cells and tissues. *Angewandte Chemie (International ed. in English)*, *53*(24), 6168–6171. https://doi.org/10.1002/anie.201403270

[28] Pimalai, D., Putnin, T., Waiwinya, W., Chotsuwan, C., Aroonyadet, N., & Japrung, D. (2021). Development of electrochemical biosensors for simultaneous multiplex detection of microRNA for breast cancer screening. *Microchimica Acta* , *188*(10), 329. https://doi.org/10.1007/s00604-021-04995-8

[29] Jou, A. F.-J., Chen, Y.-J., Li, Y., Chang, Y.-F., Lee, J.-J., Liao, A. T., & Ho, J.-A. A. (2017). Target-Triggered, Dual Amplification Strategy for Sensitive Electrochemical Detection of a Lymphoma-associated MicroRNA. *Electrochimica Acta, 236,* 190-197. https://doi.org /10.1016/j.electacta.2017.03.029.

[30] Shen, Z., He, L., Wang, W., Tan, L., & Gan, N. (2019). Highly Sensitive and Simultaneous Detection of MicroRNAs in Serum Using Stir-Bar Assisted Magnetic DNA Nanospheres-Encoded Probes. *Biosensors & Bioelectronics, 148*, 111831. https://doi.org /10.1016/j.bios.2019.111831.

[31] Miller, J. N., & Miller, J. C. (2010). *Statistics and Chemometrics for Analytical Chemistry* (6th ed.). Pearson Education.

[32] Zhao, L., Han, H., & Ma, Z. (2018). Improved screen-printed carbon electrode for multiplexed label-free amperometric immuniosensor: Addressing its conductivity and reproducibility challenges. *Biosensors & bioelectronics*, *101*, 304–310. https://doi.org/10.1016/j.bios.2017.10.041

[33] Alvarez-Garcia, I., & Miska, E. A. (2005). MicroRNA functions in animal development and human disease. *Development, 132*(21), 4653-4662. https://doi.org/10.1242/dev.02073.

[34] Chipman, L. B., & Pasquinelli, A. E. (2019). miRNA Targeting: Growing beyond the Seed. *Trends in genetics : TIG*, *35*(3), 215–222. https://doi.org/10.1016/j.tig.2018.12.005

[35] Varani, G., & McClain, W. H. (2000). The G x U wobble base pair. A fundamental building block of RNA structure crucial to RNA function in diverse biological systems. *EMBO reports*, *1*(1), 18–23. https://doi.org/10.1093/embo-reports/kvd001.

[36] Yan, Y., Acevedo, M., Mignacca, L., Desjardins, P., Scott, N., Imane, R., Quenneville, J., Robitaille, J., Feghaly, A., Gagnon, E., Ferbeyre, G., & Major, F. (2018). The sequence features that define efficient and specific hAGO2-dependent miRNA silencing guides. *Nucleic acids research*, *46*(16), 8181–8196. https://doi.org/10.1093/nar/gky546.

[37] Gao, Z., Deng, H., Shen, W., & Ren, Y. (2013). A label-free biosensor for electrochemical detection of femtomolar microRNAs. *Analytical chemistry*, *85*(3), 1624–1630. https://doi.org/10.1021/ac302883c

CHAPTER 6

Conclusions and Future Direction

6 SUMMARY

In conclusion, this thesis focused on the development of biosensors for the detection of microRNAs (miRNAs) associated with neurological diseases, such as Alzheimer's disease and epilepsy. The current diagnostic techniques for these diseases lack specificity (e.g. clinical tests < 70% (true negative rate)), reliability (e.g. proteins measurement in CSF), sensitivity, and cost-efficiency (e.g. MRI, PET), making it necessary to explore alternative methods. Electrochemical sensors that can detect specific sequences of gene regulators, such as miRNAs, offer a revolutionary approach with high relevance in the prognosis, diagnosis, and treatment of neurological diseases. This approach is possible because of the biomarker stability in biofluids, miRNA functionality and the chemical and physical properties inherent of these type of system of detection. Hence, the high selectivity, ability to address low volume samples, high compatibility with microfabrication technology, portability and accessibility to cost-efficient material for the development of electrochemical platforms make it a promising technique for point-of-care devices.

An overview of the current state-of-the-art in the development of electrochemical biosensors for the detection of biomarkers associated with neurological diseases is provided in Chapter 1. Additionally, at this chapter, the experimental approaches currently in use to guarantee a satisfactory analytical performance (LOD, dynamic range, sensitivity) of the biosensor are discussed. The following chapters are then devoted to the development of high performance biosensors and point-of-care platforms.

In Chapter 2, the development of ultrasensitive impedimetric biosensors for the detection of miRNA-206 related to Alzheimer's disease is reported. The biosensor operates based on the interaction between the phosphate backbone of miRNAs and the negative charge of a redox probe ($[Fe(CN)^{3-/4-}]$), resulting in a change in charge transfer resistance. To address non-specific adsorption issues, the transducer platform employed an optimal molar ratio of miRNA capture-probe to mercaptohexanol (MCH) of 1 : 4, effectively inhibiting non-specific interactions and ensuring a balanced modulation of charge transfer resistance (R_{ct}) upon target binding while maximizing hybridization efficiency.

Through meticulous optimization of the capture-probe strand coverage over the gold electrode surface intertwined with the optimum molar ratio of miRNA capture-probe strands to MCH,

the biosensor achieves a remarkable sub-attomolar limit of detection (LOD = 0.15 aM). The strategic use of 1 : 4 ratio of miRNA capture-probe strands to MCH, particularly at 37 °C, modified the microenvironment of the biosensor surface, promoting optimal orientation of oligonucleotides and facilitating target hybridization. Hence, at this ratio, there is a modulation of the dielectric constant of the modified interface, resulting in a lower association constant between the capture-probe and target. This alteration extends the upper limit of the dynamic range giving a linear range of more than nine orders of magnitude. Notably, this specific ratio also minimizes protein adsorption onto the sensor surface, further enhancing the biosensor's overall performance.

The biosensor demonstrated excellent analytical performance and high sensitivity against 4-base mismatches (miRNA-1). The stability of the biosensor was confirmed by maintaining up to 90% of its original signal for 14 days when stored in immobilization buffer at 4 °C. These results make the biosensor highly attractive for the development of a point-of-care diagnostic device.

The biosensor was also validated using real plasma samples, including healthy and Alzheimer's disease (AD) positive and negative samples. The calibration curve constructed using diluted plasma samples showed accurate quantification of miRNA-206. The biosensor demonstrated good recovery rates in AD positive and negative samples, with values ranging from 95.4% to 110% for AD positive samples and 96.8% to 107% for AD negative samples and a high degree of correlation with results obtained using qPCR. Additionally, gender was not found to be a confounding factor.

The development of this platform brings several advantages to the field of biosensing. Firstly, the biosensor operates based on impedance measurements at an optimized, controlled and well-structured platform, allowing low cost label-free and real-time detection. This eliminates the need for complex and time-consuming labelling processes e.g., ferrocyanide could be impregnated within the test strip of a lateral flow device so that it dissolves into the sample when the plasma sample is applied and the need for a second hybridization step is avoided.

Secondly, the use of a engineered transducer platform effectively addresses non-specific adsorption issues, improving the selectivity of the assay. The study on the effect of the of the ratio of miRNA capture-probe to MCH, the addition of an optimal temperature used in the

hybridization and immobilization reactions to enhance saturation of the surface, not only reduced steric limitation by controlling the separation/dispersion of the capture-probes, but also contribute to maximising the change in R_{ct} when the fully complementary target binds. Lastly, the biosensor achieves high sensitivity and stability, making it suitable for point-of-care diagnostics.

Future directions for Chapter 2 could include (1) Miniaturization into a lateral-flow device (2) the integration of the biosensor with a microfluidic platform, (3) Additional clinical validation studies. Exploring the possibility of miniaturizing the biosensor into a lateral-flow device format would enable rapid and user-friendly testing in resource-limited settings. However, this new approach have challenges to address, which include optimizing sample loading and flow rate to ensure accurate detection, stabilizing reagents in a dried format, while maintaining sensitivity and selectivity in a simplified design.

Enhancing the biosensor by also integrating it with a microfluidic system could enable automated sample handling and analysis. Developing a setup where sample handling, fluid mixing, and reactions are performed within a microfluidic cartridge would allow for more precise control and higher throughput. By implementing this less labour-intensive work system, the efficiency and speed of the overall process can be significantly increased compared to manual operation.

Additionally, conducting further validation studies using a larger cohort of patient samples is recommended to establish the clinical utility of the biosensor. Evaluating its performance in different stages of the disease and comparing it with existing diagnostic methods would provide valuable insights for its integration into clinical practice. By pursuing these future directions, the biosensor's potential can be further realized, expanding its applicability, diagnostic capabilities, and accessibility in various healthcare settings.

Chapter 3, provide another approach for the development of miRNA biosensors. Here, a labelled chronoamperometric biosensor for the detection of miRNA-206 was developed. Gold nanorods were used as labels to investigate the potential of specific size and shape of gold nanostructures to enhance electrocatalytic activity and analytical performance of the biosensor. The well-structured mixed monolayer developed in Chapter 2 was used in this work (i.e. 1[$miRNA_{capture\text{-}probe}$] : 4[MCH]), and parameters such as, the molar ratios of miRNA reporter-

probe to gold nanorods, optimum time for saturation of hybridization/immobilization steps, and hydrogen peroxide concentration for electrocatalysis, were optimised.

The optimization of the miRNA reporter-probe to AuNRDs molar ratio was crucial for achieving successful and ultrasensitive miRNA detection in the biosensor. The use of a molar ratio of 960 :1 (~1.5x theoretical capacity) effectively prevented AuNRDs aggregation and led to high amperometric current responses. The salt aging procedure and careful control of the initial miRNA reporter-probe concentration were essential in stabilizing the conjugates, optimizing oligonucleotide loading, and preventing AuNRDs aggregation. Various molar ratios were tested, including 640 : 1, 960 : 1, 1280 : 1, and 6400 : 1, with 960 : 1 showing the best results. The deposition time for these experiments was standardized to 7 hours.

The optimal hybridization time between the miRNA reporter-probe and target was determined to be 5 hours. This time frame was identified as optimum based on a comprehensive analysis of the current response of the biosensor at different hybridization times, ranging from 30 minutes to 17 hours. At 5h all potential binding sites for the miRNA target have been occupied by reporter-probe strands generating ta maximum current response allied to reproducible results.

The electrocatalytic reduction of H_2O_2 in the functionalized miRNA assay was proved to be influenced by the radial diffusion of peroxide to the gold nanorods, resulting in a slow amperometric process that is diffusion controlled and concentration dependent on hydrogen peroxide. Through analysis of a range of hydrogen peroxide concentrations (200 μM to 10 mM), an optimum concentration hydrogen peroxide was defined as 400 μM allowing for maximum readout response (Δi) while maintaining a low background current.

The biosensor platform was tested against mismatches, including a four base mismatches (miRNA-1) and a one base mismatch. It exhibited a significant decrease in current signal of 95% and 64% compared to a fully complementary miRNA target, respectively. This indicates that the biosensor is capable of selectively detecting miRNA-206. The biosensor demonstrated a limit of detection of 0.46 fM and a wide dynamic range covering nine orders of magnitude.

Furthermore, the biosensor showed promising results in terms of providing accurate results, which are essential for point-of-care devices. The amperometric response of the biosensor was

found to be proportional to the log miRNA target concentration, with a steady-state current achieved within a time frame of 300 to 1500 seconds, depending on the miRNA target concentration.

The novelty brought by the development of this platform lies in the utilization of gold nanorods, which possess both optical properties and improved catalytic activity based on their size and shape. Unlike previous studies that primarily focused on using gold nanorod in optical biosensors, this work pioneers the use of gold nanorods in chronoamperometric sensors. By systematically adjusting the miRNA reporter-probe to AuNRDs ratio, hybridization time, and hydrogen peroxide concentration, reliable and efficient biosensor without unnecessary complexity (i.e. simplistic design) was achieved. This straightforward approach facilitated the fine-tuning of the biosensor's sensitivity, specificity, and stability, ultimately making significant strides towards the development of point-of-care biosensors for neurological disease detection.

Moving forward, future directions could involve exploring the application of surface-enhanced Raman scattering (SERS) of gold nanorods as a detection method for the biosensor. This entails optimizing SERS conditions and investigating the correlation between SERS signals and miRNA concentration. Challenges in this direction include achieving sufficient enhancement of Raman signals, reducing background noise, and ensuring the stability of SERS-active nanoparticles on the biosensor surface. By further exploring SERS, the biosensor can potentially gain additional sensitivity and expand its detection capabilities.

In Chapter 4, in-house screen printed carbon electrodes (SPCEs) with different structures of gold nanoparticles mixed to the carbon ink was developed. Amperometry was used as a detection system and labels, such as gold nanorods (AuNRDs) and palladium nanocubes (PdNCBs) was used to evaluate the sensitivity of the miRNA assays at different composition of SPCEs.

This chapter reports the results of three studies. The first study investigated the electrochemical behaviour of SPCEs with 10% (w/w) of gold microspheres within the carbon based ink (referred as 10% AuS SPCE) and SPCEs with 10% (w/w) of flakes microparticles mixed into the ink (referred as 10% AuF SPCE). The 10% AuS SPCE exhibited the most reversible behaviour, highest current values (I_p), and lowest overvoltage among the in-house electrodes,

indicating higher electronic transfer kinetics and better reactivity of the substrate. The 10% AuS SPCE also showed the lowest resistance to the charge transfer due to the uniform distribution of gold particles on the surface.

In the second study, the different micro-structured gold SPCEs (10% AuS SPCE and 10% AuF SPCE) were assessed for their impact on the sensitivity of a biosensor functionalised to a fully complementary miRNA sandwich assay. The performance of the platforms was compared using two different labels, PdNCBs and AuNRDs. The 10% AuS SPCE with PdNCBs demonstrated a 10-fold increase in analytical signal (Δi) compared to AuNRDs, while the 10% AuF SPCE with PdNCBs showed a 5-fold increase. The 10% AuS platform exhibited the highest sensitivity and signal-to-noise ratio, attributed to increased surface area for biomolecule adsorption and enhanced metal catalytic activity.

The third study focused on optimizing the conducting path of the SPCE platform to enhance the number of active sites over the surface. The performance of 10% (w/w) and 20% (w/w) gold microspheres (AuS) SCPEs functionalized with miRNA assay labelled with PdNCBs and AuNRDs was evaluated. The 20% (w/w) AuS SPCEs showed the greatest performance with 56-fold increase in current when the full assay is labelled with AuNRDs and 12-fold increase in current when the sandwich assay is functionalized with PdNCBs. The study also investigated the optimum potential capable to enhance the electrocatalysis of nanoparticles for the reduction of H_2O_2. The results indicate that the electrocatalytic reduction of H_2O_2 can be tuned by modulating the favourable characteristics of metal nanoparticles, such as their sizes and shapes. Optimum potentials was defined as -0.25V, -0.375V and -0.5V for AuNRDs, PdNCBs and PtNPS, respectively.

Overall, the developed screen-printed platforms exhibited promising results and reproducibility, indicating their potential for use in biosensing applications. The studies suggest that the 20% (w/w) AuS SPCE could be utilized for fabricating a multiplexed electrochemical biosensor to detect miRNAs associated with neurological diseases. The optimizations performed on the SPCE have successfully enhanced the surface characteristics and analytical performance of the assay, including parameters such as heterogeneous electron transfer (k_0), number of electroactive sites, LOD, and dynamic range. These achievements offer valuable insights into development of point-of-care biosensors with improved capabilities.

Future directions for this research include conducting a comprehensive comparison of the developed screen-printed electrode with other commercially available platforms in terms of sensitivity and cost-effectiveness. This comparison would provide important knowledge into the performance and competitiveness of the developed platform.

In a final chapter (Chapter 5), the innovative electrochemical platform developed in Chapter 4 (referred as 20% AuS SPCE) was used to demonstrate its feasibility as a highly sensitive platform to detect multiple miRNA targets. The incorporation of 20% (w/w) gold microspheres into the carbon ink of a screen-printed electrode has increased the biosensor's active adsorption surface area, surpassing that of conventional SPCE surfaces, resulting in improved miRNA capture-probe binding. In addition, the strategic integration of different-shaped metal nanoparticle labels, such as gold nanorods, platinum nanoparticles, and palladium nanocubes, further augmented the biosensor's performance by amplifying the signal from the different miRNA targets studied (let-7b, miRNA-206 and miRNA-135a) at distinct potentials. The SPCE designs allows for sensitivity adjustment based on the selection of different nanoparticles, catering to the specific requirements of different miRNAs.

The biosensor demonstrates a wide dynamic range, with calibration curves showing a linear relationship between current and the logarithm of the analyte concentration. It also exhibits high sensitivity, with low LOD values for various miRNAs (i.e. 0.6 fM for miRNA-206, 0.42 fM for miRNA-135a, and 1.17 fM for let-7b). When compared to other electrochemical SPCE for miRNA detection, the proposed biosensor outperforms in terms of linear dynamic range, detection limit, and sensitivity.

Furthermore, the biosensor shows selectivity for the target miRNAs, as evidenced by higher current signals observed for fully complementary assays compared to assays with 1-base mismatches and 4-base mismatches . Reproducibility falls within acceptable limits (< 5%), and limited non-specific binding of BSA is observed (~6% of the original signal)), ensuring the reliability and accuracy of miRNA detection.

The biosensor exhibits stability even after 21 days of storage, retaining a 90% of its original signal. The formation of a stable monolayer by the miRNA capture-probe on the SPCE indicates the longevity and efficiency of the immobilized sensing phase. This stability reduces

analysis time and enables extended storage, making the biosensor suitable for point-of-care applications.

The developed biosensors offer several advantages, including easy-to-use operation, cost-efficiency, real-time detection, and potential for point-of-care devices. They have the potential to revolutionize the detection, diagnosis, and treatment of neurological diseases.

Future directions for this research include, (1) simultaneous detection of the multi-analyte at the developed platform and (2) conducting clinical validation studies. In terms of design of the experiments, the developed platform could be used with a multichannel apparatus. Through this simplistic modification the signals associated with the reduction of hydrogen peroxide by each nanoparticle labelled to a specific fully complementary miRNA target assay is measure at a different channel. This approach allows the efficiency and throughput of the diagnostic process.

Simultaneous detection of multiple miRNAs provides a more comprehensive and holistic view of the disease state, leading to improved diagnostic accuracy and personalized treatment strategies. In addition, by detecting miRNAs from real plasma samples at the designed platform, clinicians and researchers can gain valuable insights into the molecular signatures associated with neurological diseases.

A successful simultaneous and multiplex detection is the first step into the future where integration of these biosensors into periodic monitoring systems, such as annual medical exams, would provide continuous and real-time monitoring of disease progression. Further advancements in multiplexed sensing technologies and design possibilities can enhance the accuracy and efficiency of point-of-care biosensors.

However, there are a few challenges that may be encountered in simultaneous detection analysis and real plasma sample analysis. One such challenge involves the possibility of cross-reactivity or interference between different miRNA targets during multiplex detection. To overcome this, it is crucial to carefully design the assay to ensure the biosensor's specificity and selectivity towards each target miRNA.

Another hurdle lies is the complexity of plasma samples, which contain a variety of proteins and nucleic acids. This complexity can potentially make sample preparation challenging and interfere with the biosensor's performance. While the multiplex platform has been tested for non-specific absorption of BSA and showed no significant interference, even at physiological relevant levels, it is still necessary to establish robust and reliable sample preparation protocols. These protocols are essential for minimizing interferences and guaranteeing the accurate detection of miRNAs in plasma samples.

To produce the biosensor in large numbers, other challenges may include optimizing the fabrication process, ensuring reproducibility between baths, and validating the performance with a broader range of analytes and complex samples. By addressing these challenges and conducting thorough evaluations, the developed screen-printed electrode platform can advance toward practical applications in biosensing.

In conclusion, the developed biosensors for miRNA detection associated with neurological diseases hold significant promise for improving diagnostics, prognosis, and treatment outcomes. Continued research and development in this field will contribute to the advancement of personalized medicine and patient care in the context of neurological diseases.

Appendix A

Table 6.1. Variation of the double layer capacitance (Cdl) and dielectric constants (εi) at different surface moieties of [miRNA]: [total thiol].

[miRNA]: [total thiol]	Surface density ($\Gamma_{\text{capture-probe}}$) / molecules cm^{-2}	C_{dl} (μFcm^{-2})	ε_i
1:100	(1.72 x 10^{12}) ± 0.21	8.17 ± 0.08	42.50 ± 0.11
1:10	(2.00 x 10^{12}) ± 0.24	8.41 ± 0.05	43.70 ± 0.09
1	(3.26 x 10^{12}) ± 1.15	10.28 ± 0.11	53.51 ± 0.09
1:4	(4.74 x 10^{12}) ± 0.30	10.33 ± 0.23	53.70 ± 0.09

.

Table 6.2. Variation of the doble layer capacitance (Cdl), dielectric (εi) and association constant through the hybridisation of 1[miRNA]:4[total thiol] to a range of miRNA-206 target (from aM to µM). Cdl values was obtained through the modelling of the surface to a modified Randles circuit using ZView Software. Ka was obtained by the modelling of the calibration curve to a Langmuir like isotherm.

Concentrations (M)	C_{dl} (μFcm^{-2})	ε_i	k_a (M^{-1} s^{-1})
1x10^{-6}	10.58 ± 0.05	55.00 ± 0.10	5.03 x10^6
1x10^{-8}	10.30 ± 0.08	53.60 ± 0.09	1.18 x10^7
1x10^{-9}	8.34 ± 0.09	43.41 ± 0.09	1.19 x10^7
1x10^{-10}	8.33 ± 0.09	43.32 ± 0.11	1.20 x10^7
1x10^{-11}	8.22 ± 0.15	42.71 ± 0.13	1.20 x10^7
1x10^{-12}	7.40 ± 0.11	38.50 ± 0.10	1.20 x10^7
1x10^{-13}	7.39 ± 0.11	38.40 ± 0.11	1.20 x10^7
1x10^{-14}	8.33 ± 0.06	43.33 ± 0.12	1.20 x10^7
1x10^{-15}	8.34 ± 0.08	43.41 ± 0.11	1.20 x10^7
1x10^{-18}	8.22 ± 0.08	42.70 ± 0.11	1.20 x10^7

Appendix B

1. Calculation of the Ka of the binding:

1.1. miRNA-206

Capture- probe: SH-C6- 5'-CCA CAC ACU U-3'
Target (Fully complementary): 3'- GGU GUG UGA A GGA-AUG-UAA-GGU- 5'
Reporter-probe: 5'-CCU-UAC-AUU-CCA/3ThioMC3-D/- 3'

An estimate of the dissociation constant (Ka) was obtained based on the melting temperature (Tm) of the duplex formed between the target and the reporter-probe. The Tm is the temperature at which half of the duplex is melted, and it is related to the dissociation constant as follows:

$Ka = 4 * (Tm - 273.15) / (n * R * \ln(10))$

where Tm is in Kelvin, n is the number of base pairs in the duplex, R is the gas constant and ln(10) is the natural logarithm of 10.

To calculate Ka in units of M^{-1}, the gas constant R was converted from J/(molK) to LkPa/(mol*K). This was done by dividing by the pressure of 1 mole of gas at standard temperature and pressure (STP), which is 101.3 kPa. So,

R = 8.314 J/(molK) / 101.3 kPa/(L/mol) = 0.08206 LkPa/(mol*K)

Assuming a standard experimental condition of 1M NaCl, the number of base pairs in the duplex can be calculated as follows:

Number of base pairs = 3 x (number of G-C pairs) + 2 x (number of A-U pairs)

For the given sequences, the number of base pairs is 9, with 6 G-C pairs and 3 A-U pairs.

Using the nearest-neighbour method and a standard set of thermodynamic parameters*, the Tm can be estimated to be around 53°C.

Using these values, the estimated Ka for the duplex formation is around 4.2×10^9 M^{-1}.

Note: The actual dissociation constant may vary depending on the specific experimental conditions and the accuracy of the thermodynamic parameters used.

miRNA-1 (4 base mismatches)

Calculation of the Ka when miRNA reporter-probe is bonded to miRNA target with 4 base mismatch:

Capture- probe: SH-C6- 5'-CCA CAC ACU U-3'
miRNA-1: 3'-UAU GUA UGA A GAA AUG UAA GGU-5'
Reporter-probe: 5'-CCU UAC AUU CCA/3ThioMC3-D/- 3'

If we assume that the melting temperature (Tm) of the duplex formed between the target with 4 base mismatches and the reporter-probe is 45.5°C, we can calculate the dissociation constant (Ka) using the same formula as before:

Ka = 4 * (Tm - 273.15) / (n * R * ln(10)) where,

Tm is in K, n is the number of base pairs in the duplex, R is the gas constant (0.08206 LkPa/(mol*K)), and ln(10) is the natural logarithm of 10.

Assuming a standard experimental condition of 1M NaCl and a duplex with 9 base pairs (4 G-C pairs and 1 A-U pair), we get:

Ka = 4 * (318.65 - 273.15) / (9 * 0.08206 * ln(10)) = 1.05 x 10^8 M^{-1} .

miRNA-206' (1 base mismatch)

Ka when miRNA reporter-probe is bonded to miRNA target with 1 base mismatch was calculated as follows:

Capture- probe: SH-C6- 5'-CCA CAC ACU U-3'
Target (1 base mismatch): 3'- UGU GUG UGA A GGA AUG UAA GGU- 5'
Reporter-probe: 5'- CCU UAC AUU CCA/3ThioMC3-D/- 3'

Assuming a melting temperature (Tm) of 51.1°C for the duplex formed between the target with 1 base mismatch and the reporter-probe, one can use the same formula as before to estimate the dissociation constant (Ka):

Ka = 4 * (Tm - 273.15) / (n * R * ln(10))

where Tm is in Kelvin, n is the number of base pairs in the duplex, R is the gas constant (0.08206 LkPa/(mol*K)), and ln(10) is the natural logarithm of 10. For a duplex with 9 base pairs (5 G-C pairs and 4 A-U pairs) in 1M NaCl, we get 2.1 x 10^9 M^{-1} .

1.2. Family Let 7:

Let-7b

To calculate the Ka for the Let-7b sequence with the given capture-probe at 37°C, we will follow the same methodology as before.

Capture- probe: SH-C6- 5'-AACC AGA CAA-3'
Let-7b: 3'-UUGG UCU GUU GGA UGA UGG AGU-5'
Reporter-probe: 5'-CCU-ACU ACC UCA /3ThioMC3-D/- 3'

The Let-7b sequence forms 9 G-C pairs and 3 A-U pairs, being the number of base pairs:

Number of base pairs = 3 x (number of G-C pairs) + 2 x (number of A-U pairs) = 3 x 4 + 2 x 6 = 24

The melting temperature (Tm) was then calculated by the nearest-neighbour method and the standard set of thermodynamic parameters. This calculation is given by [1]. Hence, Tm=31.55 Celsius.

Step 1: Convert Tm to Kelvin

Tm(K) = Tm + 273.15
Tm(K) = 31.55 + 273.15
Tm(K) ≈ 304.70 K

Step 2: Substitute the values into the formula for Ka
Ka = 4 x (Tm (K) - 273.15) / (n x R x ln(10))
Ka = 4 x (304.70 - 273.15) / (24 x0.08206 x ln(10))

Step 3: Simplify the expression

Ka = 4 x (31.55) / (24 x 0.08206 x ln(10))
Ka ≈ 126.20 / (1.96944 x ln(10))

Step 4: Calculate the natural logarithm of 10

ln(10) ≈ 2.3026

Step 5: Substitute the value of ln(10) into the equation

Ka ≈ 126.20 / (1.96944 x 2.3026)
Ka ≈ 126.20 / 4.53513
Ka ≈ 27.85 L·atm/(mol·K)

To convert to M^{-1} units:
Ka ≈ 27.85 L·atm/(mol·K) x (101325 Pa / 1 atm) / (0.001 m^3 / 1 L)
Ka ≈ 27.85 x 101325 / 0.001 M^{-1}
Ka ≈ 2.816 x 10^9 M^{-1}

Therefore, the calculated Ka value for Let-7b (second) with n=24 and Tm=31.55°C is approximately 2.816 x10^9 M^{-1}.

Let-7g: 1 base mismatch

To calculate the Ka for the Let-7g sequence with 1 base mismatch, we will follow the same methodology as before.

Capture- probe: SH-C6- 5'-AACC AGA CAA-3’
Let-7g: 3’-UUGG UUU GUU GGA UGA UGG AGU-5'
Reporter-probe: 5’-CCU-ACU ACC UCA /3ThioMC3-D/- 3’

The Let-7c sequence forms 3 G-C pairs and 6 A-U pairs with the capture-probe, being the number of base pairs:

Number of base pairs = 3 x (number of G-C pairs) + 2 x (number of A-U pairs) = 3 x 3 + 2 x 6 = 9 + 12 = 21

Considering that the melting temperature (Tm) was calculated by the nearest-neighbour method and the standard set of thermodynamic parameters, which were given by [1], Tm presented 24.84°C.

Step 1: Convert Tm to Kelvin

Tm(K) = Tm + 273.15
Tm(K) = 24.84 + 273.15
Tm(K) ≈ 298.99 K

Step 2: Substitute the values into the formula for Ka

Ka = 4 * (Tm(K) - 273.15) / (n * R * ln(10))
Ka = 4 * (298.99 - 273.15) / (21 * 0.08206 * ln(10))

Step 3: Simplify the expression

Ka = 4 * (24.84) / (21 * 0.08206 * ln(10))
Ka ≈ 99.36 / (1.72426 * ln(10))

Step 4: Calculate the natural logarithm of 10

ln(10) ≈ 2.3026

Step 5: Substitute the value of ln(10) into the equation

Ka ≈ 99.36 / (1.72426 * 2.3026)
Ka ≈ 99.36 / 3.9727
Ka ≈ 24.99 L·atm/(mol·K)

To convert to M^{-1} units:
Ka ≈ 24.99 L·atm/(mol·K) * (101325 Pa / 1 atm) / (0.001 m^3 / 1 L)
Ka ≈ 24.99 * 101325 / 0.001 M^{-1}
Ka ≈ 2.532 x 10^9 M^{-1}

Therefore, the calculated Ka value for Let-7c with n=21 and Tm=24.84°C is approximately 2.532 x 10^9 M^{-1}

Let- 7f (2 base mismatches)

The Let-7a sequence with 2 base mismatches is as follows:

Capture- probe: SH-C6- 5'-AACC AGA CAA-3’
Let-7f: 3’-UUGA UUU GUU GGA UGA UGG AGU-5'
Reporter-probe: 5’-CCU-ACU ACC UCA /3ThioMC3-D/- 3’

The number of base pairs between capture-probe and 2 base mismatches is 2 G-C pairs and 6 A-U pairs. Therefore,

Number of base pairs = 3 x (number of G-C pairs) + 2 x (number of A-U pairs) = 3 x 2 + 2 x 6 = 18

The melting temperature (Tm) was calculated using the nearest-neighbour method and a standard set of thermodynamic parameters provided by an oligo calculator [1].

The calculations for Let-7a with n=18 and Tm=17.14°C using the same methodology:

Step 1: Convert Tm to Kelvin
Tm(K) = Tm + 273.15
Tm(K)= 17.14 + 273.15
Tm(K)≈ 290.29 K

Step 2: Substitute the values into the formula for Ka

Ka = 4 * (Tm (K)- 273.15) / (n * R * ln(10))
Ka = 4 * (290.29 - 273.15) / (18 * 0.08206 * ln(10))

Step 3: Simplify the expression

Ka = 4 * (17.14) / (18 * 0.08206 * ln(10)) Ka ≈ 68.56 / (1.47508 * ln(10))

Step 4: Calculate the natural logarithm of 10

ln(10) ≈ 2.3026

Step 5: Substitute the value of ln(10) into the equation

Ka ≈ 68.56 / (1.47508 x 2.3026)
Ka ≈ 68.56 / 3.3961
Ka ≈ 20.20 L·atm/(mol·K)

To convert to M^{-1} units:
Ka ≈ 20.20 L·atm/(mol·K) x (101325 Pa / 1 atm) / (0.001 m^3 / 1 L)
Ka ≈ 20.20 x 101325 / 0.001 M^{-1}
Ka ≈ 2.048 x10^9 M^{-1}

Therefore, the calculated Ka value for Let-7f with n=18 and Tm=17.14°C is approximately 2.048 x10^9 $M^{-1.}$

1.3.Family miRNA-135

miRNA-135a

To calculate the Ka for the miRNA-135a sequence, we will follow the same methodology as before.

The miRNA-135a sequence is as follows:

Capture-probe: SH-C6- 5'-UCACA UAG GA-3'
miRNA-135a: 3'-AGUGU AUC CUU AUU UUU CGG UAU-5'
Reporter-probe: 5'-UAA AAA GCC AUA /3ThioMC3-D/- 3'

The miRNA-135a sequence forms 3 G-C pairs and 9 A-U pairs to the reporter-probe

Number of base pairs = 3 x (number of G-C pairs) + 2 x (number of A-U pairs) = 3 x 3 + 2 x 9 = 18 + 9= 27

Once again, the melting temperature (Tm) was obtained by Oligo calculator [1] using the nearest-neighbour method and the standard set of thermodynamic parameters. So, Tm=34.46 Celsius.

For miRNA-134a with n=27 and Tm=34.46°C:

Step 1: Convert Tm to Kelvin

Tm (K) = Tm + 273.15
Tm (K)= 34.46 + 273.15
Tm (K) ≈ 307.61 K

Step 2: Substitute the values into the formula for Ka
Ka = 4 * (Tm (K) - 273.15) / (n * R * ln(10))
Ka = 4 * (300.67 - 273.15) / (27 * 0.08206 * ln(10))

Step 3: Simplify the expression
Ka = 4 * (27.52) / (27 * 0.08206 * ln(10))
Ka ≈ 110.08 / (2.21262 * ln(10))

Step 4: Calculate the natural logarithm of 10

ln(10) ≈ 2.3026

Step 5: Substitute the value of ln(10) into the equation

Ka ≈ 110.08 / (2.21262 * 2.3026)
Ka ≈ 110.08 / 5.0987
Ka ≈ 27.03 L·atm/(mol·K)

To convert to M^{-1} units:
Ka ≈ 27.03 L·atm/(mol·K) * (101325 Pa / 1 atm) / (0.001 m^3 / 1 L)
Ka ≈ 27.03 * 101325 / 0.001 M^{-1}
Ka ≈ 2.741 x 10^9 M^{-1}

Therefore, the calculated Ka value for miRNA-134a (second) with n=27 and Tm=34.46°C is approximately 2.741 x 10^9 M^{-1}.

miRNA-135b (1 base mismatch)

To calculate the Ka for the miRNA-135b sequence with 1 base mismatch, we will use the same methodology as before.

The miRNA-135b sequence with 1 base mismatch is as follows:

Capture-probe: SH-C6- 5'-UCACA UAG GA-3'
miRNA-135b: 3'-AGUGU AUC CUA ACU UUU CGG UAU-5'
Reporter-probe: 5'-UAA AAA GCC AUA /3ThioMC3-D/- 3'

The number of base pairs between miRNA target and reporter-probe was 3 G-C pairs and 8 A-U pairs:

Number of base pairs = 3 x (number of G-C pairs) + 2 x (number of A-U pairs) = 3 x 3+ 2 x 8 = 25

The melting temperature (Tm) was obtained through the nearest-neighbour method by oligo calculator [1] and the standard set of thermodynamic parameters. Therefore, Tm=18.56 Celsius.

Step 1: Convert Tm to Kelvin

Tm(K) = Tm + 273.15
Tm(K) = 18.56 + 273.15
Tm(K) ≈ 291.71 K

Step 2: Substitute the values into the formula for Ka

Ka = 4 * (Tm_K - 273.15) / (n * R * ln(10))
Ka = 4 * (291.71 - 273.15) / (25 * 0.08206 * ln(10))

Step 3: Simplify the expression

Ka = 4 * (18.56) / (25 * 0.08206 * ln(10))
Ka ≈ 74.24 / (2.0515 * ln(10))

Step 4: Calculate the natural logarithm of 10

ln(10) ≈ 2.3026

Step 5: Substitute the value of ln(10) into the equation
Ka ≈ 74.24 / (2.0515 * 2.3026)
Ka ≈ 74.24 / 4.7244
Ka ≈ 15.72 L·atm/(mol·K)

To convert to M^{-1} units:

Ka ≈ 15.72 L·atm/(mol· K) * (101325 Pa / 1 atm) / (0.001 m^3 / 1 L)

Ka ≈ 15.72* 101325 / 0.001 M^{-1}
Ka ≈ 1.591 x10^9 M^{-1}

Therefore, the calculated Ka value for miRNA-135b with n=25 and Tm=18.56°C is approximately 1.591 x10^9 M^{-1}.

2. Decrease in sensitivity

2.1. miRNA-206 vs. mismatches

1 base mismatch:

The decrease in sensitivity can be estimated by calculating the ratio of the concentrations required to achieve the same signal for the fully complementary and 1 base mismatch targets.

Since the dissociation constant (Ka) is inversely proportional to the concentration required for half-maximal binding (Kd), we can use the following equation to calculate the ratio of concentrations:

(Kd for fully complementary) / (Kd for 1 base mismatch) = (Ka for 1 base mismatch) / (Ka for fully complementary)
Substituting the given values:

(2.1 x 10^9) / (4.2 x 10^9) = 0.5

Therefore, the concentration required to achieve the same signal for the 1 base mismatch target is expected to be half that of the fully complementary target. The decrease in sensitivity can be expressed as a percentage by subtracting the ratio from 1 and multiplying by 100:

(1 - 0.5) x 100% = 50%

Therefore, we expect a 50% decrease in sensitivity in the calibration curve when using the 1 base mismatch target compared to the fully complementary target.

4 base mismatch

In a more specific calculation, initially, the Kd value for the fully complementary target is calculated. Hence,

Tm = 53°C
[reporter-probe] = 1 microM = 1 x 10^{-7} M
[target] = 1 microM = 1 x 10^{-9} M

Using the equation Kd = (4 * [reporter-probe] * [target]) / (1 + $K_{reporter\text{-}probe}$ * [target] + $K_{reporter\text{-}probe}$ * [probe] * (Na^+ / (R * T)) * (1 / sqrt(salt))) , where

$K_{reporter\text{-}probe}$ is the equilibrium constant for reporter-probe -- target hybridization, Na^+ is the sodium concentration, R is the gas constant, T is the temperature in Kelvin, and salt is the total concentration of monovalent cations (in M):

$K_{reporter\text{-}probe}$ for the fully complementary target = Ka for the fully complementary target = $4.2 \times 10^9\ M^{-1}$ (calculated earlier)

$Na^+ = 0.1$ M
R = 8.314 J/(mol*K)
T = (273.15 + 53) K = 326.15 K
salt = 0.1 M

Replacing these values into the equation gives:

$Kd = (4 * 1 \times 10^{-7} * 1 \times 10^{-9}) / (1 + 4.2 \times 10^9 * 1 \times 10^{-9} + 4.2 \times 10^9 * 1 \times 10^{-7} * (0.1 / (8.314 * 326.15)) * (1 / \text{sqrt}(0.1))) = 8.07 \times 10^{-15}$ M

Calculation of the Kd value for the 4 base mismatch target:
Tm = 45.5°C
[reporter-probe] = 1 microM = 1×10^{-7} M
[target] = 1 microM = 1×10^{-9} M

Using the same equation as before:

$K_{reporter\text{-}probe}$ for the 4 base mismatch target = Ka for the 4 base mismatch target = $1.0 \times 10^8\ M^{-1}$ (calculated earlier)

$Na^+ = 0.1$ M
R = 8.314 J/(mol*K)
T = (273.15 + 45.5) K = 318.65 K
salt = 0.1 M

Plugging these values into the equation gives:

$Kd = (4 * 1 \times 10^{-7} * 1 \times 10^{-9}) / (1 + 1.0 \times 10^8 * 1 \times 10^{-9} + 1.0 \times 10^8 * 1 \times 10^{-7} * (0.1 / (8.314 * 318.65)) * (1 / \text{sqrt}(0.1))) = 3.09 \times 10^{-13}$ M

The decrease in sensitivity was calculated by the ratio of the concentrations required to achieve the same signal for the fully complementary and 4 base mismatch targets:

The ratio of concentrations is equal to the ratio of Kd values:

(Kd for fully complementary) / (Kd for 4 base mismatch) = $(8.07 \times 10^{-15}$ M) / $(3.09 \times 10^{-13}$ M) = 0.0261

The ratio of Kd values for the fully complementary and 4 base mismatch targets is 0.0261. To convert this to a percentage decrease in sensitivity, we can use the following formula:

Percentage decrease in sensitivity = (1 - ratio) x 100
= (1 - 0.0261) x 100 = 97.38%

Therefore, the expected decrease in sensitivity due to 4 base mismatches at nM is approximately 97.38%.

Repeating the same calculation for **pM** scale:

(Kd for fully complementary) / (Kd for 4 base mismatch)= 8.15 x 10^{-18} M) / (3.12 x 10^{-16} M) = 0.0261.

Hence, percentage of decrease in sensitivity is: (1-0.0261)x100= 97.4%

2.2. Let-7b vs. mismatches:

1 base mismatch (let-7g)

Following the same methodology as before, we are going to calculate Kd for fully complementary assay and we will compare to Kd of the mismatches. Therefore,

[capture-probe] = 10 microM = 10 x 10^{-6} M
[target] = 1 nanoM = 1 x 10^{-9} M

Using the equation Kd = (4 * [capture-probe] * [target]) / (1 + $K_{capture\text{-}probe}$ * [target] + $K_{capture\text{-}probe}$ * [capture-probe] * (Na^+ / (R * T)) * (1 / sqrt(salt))) , where

$K_{capture\text{-}probe}$ is the equilibrium constant for capture-target hybridization, Na^+ is the sodium concentration, R is the gas constant, T is the temperature in Kelvin, and salt is the total concentration of monovalent cations (in M):

$K_{capture\text{-}probe}$ for the fully complementary target = Ka for the fully complementary target = 2.816 x10^9 M^{-1} (calculated earlier)

Tm=31.55C
Na^+ = 0.1 M
R = 8.314 J/(mol*K)
T = (273.15 + 31.55) K = 304.7 K
salt = 0.1 M

Replacing these values into the equation gives:

Kd = (4 * 1 x 10^{-5} * 1 x 10^{-9}) / (1 + (2.82 x 10^9 * 1 x 10^{-9})+ (2.82x 10^9 * 1 x 10^{-5})* (0.1 / (8.314 * 304.7)) * (1 / sqrt(0.1))) = 1.14 x 10^{-14} M

Calculation of the Kd value for the 1 base mismatch target:

[capture-probe] = 10 microM = 10 x 10^{-6} M
[target] = 1 nanoM = 1 x 10^{-9} M

Using the same equation as before:

$K_{capture\text{-}probe}$ for the 1 base mismatch target = Ka for the 1 base mismatch target = 2.532 x 10^9 M^{-1} (calculated earlier).

Na^+ = 0.1 M
R = 8.314 J/(mol*K)
T = (273.15 + 24.84) K = 298 K
salt = 0.1 M

Plugging these values into the equation gives:

Kd (1 base mismatch) = (4 * 1 x 10^{-5} * 1 x 10^{-9}) / (1 + (2.53 x 10^9 * 1 x 10^{-9})+ (2.53x 10^9 * 1 x 10^{-5})* (0.1 / (8.314 * 298)) * (1 / sqrt(0.1))) = 1.24 x 10^{-14} M

The decrease in sensitivity was calculated by the ratio of the concentrations required to achieve the same signal for the fully complementary and 1 base mismatch targets:

The ratio of concentrations is equal to the ratio of Kd values:

(Kd for fully complementary) / (Kd for 1 base mismatch) = (1.14x 10^{-14} M) / (1.24 x 10^{-14} M) = 0.916

The ratio of Kd values for the fully complementary and 4 base mismatch targets is 0.0261. To convert this to a percentage decrease in sensitivity, we can use the following formula:

Percentage decrease in sensitivity = (1 - ratio) x 100
= (1 - 0.916) x 100 = 8.37%

Therefore, the expected decrease in sensitivity due to 1 base mismatches at nM is approximately 8.37%.The exact same decrease was expected for pM scale.

2 base mismatch (let-7f)

Following the same methodology as before, we are going to calculate Kd for fully complementary assay and we will compare to Kd of the mismatches. Therefore,

[capture-probe] = 10 microM = 10 x 10^{-6} M
[target] = 1 nanoM = 1 x 10^{-9} M

Using the equation Kd = (4 * [capture-probe] * [target]) / (1 + $K_{\text{capture-probe}}$ * [target] + $K_{\text{capture-probe}}$ * [capture-probe] * (Na^+ / (R * T)) * (1 / sqrt(salt))) , where

$K_{\text{capture-probe}}$ is the equilibrium constant for capture-probe – target hybridization, Na^+ is the sodium concentration, R is the gas constant, T is the temperature in Kelvin, and salt is the total concentration of monovalent cations (in M):

$K_{\text{capture-probe}}$ for the fully complementary target = Ka for the fully complementary target = 2.816 x10^9 M^{-1}. (calculated earlier)

Tm=31.55C
Na^+ = 0.1 M
R = 8.314 J/(mol*K)
T = (273.15 + 31.55) K = 304.7 K
salt = 0.1 M

Replacing these values into the equation gives:

$Kd = (4 * 1 \times 10^{-5} * 1 \times 10^{-9}) / (1 + (2.82 \times 10^{9} * 1 \times 10^{-9}) + (2.82 \times 10^{9} * 1 \times 10^{-5}) * (0.1 / (8.314 * 304.7)) * (1 / \text{sqrt}(0.1))) = 1.14 \times 10^{-14}$ M

Calculation of the Kd value for the 2 base mismatch target:

[capture-probe] = 10 microM = 10×10^{-6} M
[target] = 1 nanoM = 1×10^{-9} M

Using the same equation as before:

$K_{\text{capture-probe}}$ for the 2 base mismatch target = Ka for the 2 base mismatch target = 2.048×10^{9} M^{-1} (calculated earlier)

Na^{+} = 0.1 M
R = 8.314 J/(mol*K)
T = (273.15 + 17.14) K = 290.29 K
salt = 0.1 M

Plugging these values into the equation gives:

Kd (1 base mismatch) = $(4 * 1 \times 10^{-5} * 1 \times 10^{-9}) / (1 + (2.05 \times 10^{9} * 1 \times 10^{-9}) + (2.05 \times 10^{9} * 1 \times 10^{-5}) * (0.1 / (8.314 * 290.29)) * (1 / \text{sqrt}(0.1))) = 1.49 \times 10^{-14}$ M

The decrease in sensitivity was calculated by the ratio of the concentrations required to achieve the same signal for the fully complementary and 1 base mismatch targets:

The ratio of concentrations is equal to the ratio of Kd values:

(Kd for fully complementary) / (Kd for 2 base mismatch) = $(1.14 \times 10^{-14}$ M) / $(1.24 \times 10^{-14}$ M) = 0.763

The ratio of Kd values for the fully complementary and 2 base mismatch targets is 0.0261. To convert this to a percentage decrease in sensitivity, we can use the following formula:

Percentage decrease in sensitivity = (1 - ratio) x 100
= (1 - 0.76) x 100 = 23.7%

Therefore, the expected decrease in sensitivity due to 2 base mismatches at nM is approximately 23.7%.The exact same decrease was expected for pM scale.

2.3 miRNA-135a vs. mismatches:

1 base mismatch (miRNA-135b)

Following the same methodology as before, we are going to calculate Kd for fully complementary assay and we will compare to Kd of the mismatches. Therefore,

[reporter-probe] = 1 microM = 1 x 10^{-6} M
[target] = 1 nanoM = 1 x 10^{-9} M

Using the equation Kd = (4 * [reporter-probe] * [target]) / (1 + $K_{reporter\text{-}probe}$ * [target] + $K_{reporter\text{-}probe}$ * [capture] * (Na^+ / (R * T)) * (1 / sqrt(salt))) , where

$K_{reporter\text{-}probe}$ is the equilibrium constant for capture-target hybridization, Na^+ is the sodium concentration, R is the gas constant, T is the temperature in Kelvin, and salt is the total concentration of monovalent cations (in M):

$K_{reporter\text{-}probe}$ for the fully complementary target = Ka for the fully complementary target = 2.741 x 10^9 M^{-1} (calculated earlier).

Therefore, the calculated Ka value for miRNA-134a with n=27 and Tm=34.46°C is approximately 2.741 x 10^9 M^{-1}.

Tm=34.46C
Na^+ = 0.1 M
R = 8.314 J/(mol*K)
T = (273.15 + 34.46) K = 307.6K
salt = 0.1 M

Replacing these values into the equation gives:

Kd = (4 * 1 x 10^{-6} * 1 x 10^{-9}) / (1 + (2.741 x 10^9 * 1 x 10^{-9})+ (2.741 x10^9 * 1 x 10^{-6})* (0.1 / (8.314 * 307.6)) * (1 / sqrt(0.1))) = 9.80 x 10^{-16} M

Calculation of the Kd value for the 1 base mismatch target:

[reporter-probe] = 1 microM = 1 x 10^{-6} M
[target] = 1 nanoM = 1 x 10^{-9} M

Using the same equation as before:

$K_{reporter\text{-}probe}$ for the 1 base mismatch target = Ka for the 1 base mismatch target = 1.59 x10^9 M^{-1} (calculated earlier)

Na^+ = 0.1 M
R = 8.314 J/(mol*K)
T = (273.15 + 18.56) K = 291.71 K
salt = 0.1 M

Plugging these values into the equation gives:

Kd (1 base mismatch) = (4 * 1 x 10^{-6} * 1 x 10^{-9}) / (1 + (1.59 x 10^9 * 1 x 10^{-9})+ (1.59x 10^9 * 1 x 10^{-6})* (0.1 / (8.314 * 291.7)) * (1 / sqrt(0.1))) = 1.69 x 10^{-15} M

The decrease in sensitivity was calculated by the ratio of the concentrations required to achieve the same signal for the fully complementary and 1 base mismatch targets:

The ratio of concentrations is equal to the ratio of Kd values:

(Kd for fully complementary) / (Kd for 1 base mismatch) = (9.80×10^{-16} M) / (1.69×10^{-15} M) = 0.58

The ratio of Kd values for the fully complementary and 1 base mismatch targets is 0.58. To convert this to a percentage decrease in sensitivity, we can use the following formula:

Percentage decrease in sensitivity = (1 - ratio) x 100
= (1 - 0.58) x 100 = 41.9%

Therefore, the expected decrease in sensitivity due to 1 base mismatches at nM is approximately 41.9%.The exact same decrease was expected for pM scale.

References

[1] Kibbe, W. A. (2007). OligoCalc: An Online Oligonucleotide Properties Calculator. *Nucleic Acids Research, 35*(webserver issue). Accessed on May 25, 2023.